

KATHOLIEKE UNIVERSITEIT
LEUVEN

Arenberg Doctoral School of Science, Engineering & Technology
Faculty of Engineering
Department of Electrical Engineering

IMPROVING DATA-DRIVEN EEG-FMRI ANALYSES FOR THE STUDY OF COGNITIVE FUNCTIONING

Katrien VANDERPERREN

Dissertation presented in partial fulfillment of the requirements for the degree of Doctor in Engineering Sciences

December 2011

IMPROVING DATA-DRIVEN EEG-FMRI ANALYSES FOR THE STUDY OF COGNITIVE FUNCTIONING

Katrien Vanderperren

Jury :
Prof. dr. A. Bultheel, chairman
Prof. dr. ir. S. Van Huffel, promotor
Prof. dr. ir. M. Moonen
Prof. dr. ir. L. De Lathauwer
Prof. dr. ir. D. Vandermeulen
Prof. dr. ir. B. Vanrumste
Prof. dr. P. Stiers (Universiteit Maastricht)
Prof. dr. S. Debener (Universität Oldenburg)

Dissertation presented in partial fulfillment of the requirements for the degree of Doctor in Engineering Sciences

December 2011

© Katholieke Universiteit Leuven – Faculty of Engineering
Kasteelpark Arenberg 10, B-3001 Leuven (Belgium)

Alle rechten voorbehouden. Niets uit deze uitgave mag worden vermenigvuldigd en/of openbaar gemaakt worden door middel van druk, fotokopie, microfilm, elektronisch of op welke andere wijze ook zonder voorafgaande schriftelijke toestemming van de uitgever.

All rights reserved. No part of the publication may be reproduced in any form by print, photoprint, microfilm or any other means without written permission from the publisher.

D/2011/7515/158
ISBN 978-94-6018-458-1

Dankwoord

Het schrijven van een doctoraat is zoals het beklimmen van een berg. Je hebt dragers nodig om je bagage mee naar boven te sleuren en als je het onderweg of net voor de top, even niet meer ziet zitten, is er altijd wel iemand die je een duwtje in de rug wil geven. Mijn dragers en duwtjes-gevers wil ik dan ook graag allemaal bedanken. Maar omdat andere mensen het soms beter kunnen uitleggen dan ik, laat ik hen telkens eerst aan het woord.

No matter what accomplishments you make, somebody helped you.
Althea Gibson

Eerst en vooral wil ik graag mijn promotor, prof. Sabine Van Huffel, bedanken. Sabine, bedankt voor het vertrouwen dat je in mij gesteld hebt, bedankt voor de steun en bedankt voor het geven van de duwtjes die ik meer dan eens nodig had. Bedankt ook voor het creëren van de sfeer, die zo uniek is aan onze BioMed groep. Ik ben ervan overtuigd dat de jaarlijkse etentjes in je huis en je enthousiasme bij onze eigen initiatieven, de groep gemaakt hebben tot wat die nu is.

Verder wil ik ook graag de leden van mijn jury bedanken. Prof. Peter Stiers en prof. Bart Vanrumste, jullie stonden mee aan de wieg van ons EEG-fMRI IDO project. Bedankt voor jullie interesse in mijn werk en jullie voortdurende aanmoedigingen. Peter, de eerste keer dat je kritische blik over mijn BCG artikel ging, moest ik even slikken, maar achteraf was ik dankbaar en ik kan alleen maar zeggen dat ik heel veel van je geleerd heb. Bart, bedankt om me binnen te loodsen in het NeuroMath project, dit heeft me veel extra kansen gegeven en het was ook altijd een plezier om met jou op conferentie te gaan. Prof. Lieven De Lathauwer, bedankt om te willen deel uitmaken van mijn jury en bedankt ook dat ik steeds bij jou terechtkon met mijn vragen over tensoren.

Ik zou ook graag prof. Dirk Vandermeulen en prof. Marc Moonen willen bedanken voor het zetelen in mijn jury. Ook aan prof. Adhemar Bultheel een oprechte dankuwel om als voorzitter te willen optreden. Prof. Stefan Debener, already since the very beginning of my PhD, your numerous EEG-fMRI papers drew my attention. It is a big honor that you accepted to be a member of my commission.

Mijn dankbaarheid gaat ook uit naar het Instituut voor Wetenschap en Technologie (IWT) Vlaanderen voor de financiële steun aan mijn onderzoek. Daarnaast bedank ik ook graag Ida, Ilse, Elsy, Evelyn, Eliane, Lut, John, Mimi, Maarten, Liesbeth en alle medewerkers van de systeemgroep en het magazijn voor alle administratieve en logistieke steun.

No one can whistle a symphony. It takes a whole orchestra to play it.

Halford E. Luccock

Toen ik bezig was aan het overzicht van samenwerkingen, realiseerde ik me pas met hoeveel verschillende groepen en onderzoekers ik de gelegenheid heb gehad om samen te werken. Graag zou ik dan ook al deze mensen willen bedanken.

Eerst en vooral, alle professoren betrokken bij het EEG-fMRI IDO project: prof. Bea Van den Bergh, prof. Johan Wagemans, prof. Stefan Sunaert en prof. Lieven Lagae. Samen met Sabine, Peter en Bart, hebben jullie dit project opgestart en mij de kans gegeven hierop te werken en van elk van jullie te leren. Bedankt hiervoor! Jennifer en Nikolay, het werken met simultane EEG-fMRI data verliep in het begin niet van een leien dakje, maar met ons drietjes en de vele hulp van anderen, zijn we er uiteindelijk toch in geslaagd de nodige kennis op te bouwen. Het was steeds fijn met jullie samen te werken!

Daarnaast bedank ik alle mensen met wie ik in de loop van de voorbije jaren van kortbij of veraf heb samengewerkt. In het kader van simultane EEG en fMRI waren dat o.a. Maarten Mennes, Bart Machilsen, Simon Tousseyn, prof. Wim Van Paesschen en prof. Patrick Dupont. Ook een dikke dankjewel aan Ron Peeters voor het oplossen van onze talloze problemen tijdens de metingen. In addition, it was a pleasure to work together with Jan Van den Stock, prof. Mathieu Van den Bulck, Guy Nagels, Sara Assecondi and the other people from the MEDISIP group in Ghent, the people from the neurophysiology lab of prof. Marc Van Hulle and Borís Burle and his co-workers from Marseille.

Finding good players is easy. Getting them to play as a team is another story.

Casey Stengel

If there is one thing I will regret when going to work somewhere else, then it will be that I have to leave behind the nice atmosphere in our BioMed group. Especially in the last years, we have built up a real team, that can "play" together without any additional effort. Many of you have become real friends in the meanwhile. I would like to say thank you for all the support, the nice moments in Alma, on birthday, bachelor and wedding parties and all the fun we made on all possible occasions. Ben, Jan, Kirsten, Laure, Vanya, Jean-Baptiste, Ivan, Vladimir, Joachim, Ninah, Diana, Maria, Anca, Mariya, Aileen, Rosy, Kris, Devy, Milica, Alex, Carolina, Ann-Sofie and Thijs: thanks, dank u, merci, danke, gracias, köszönöm, mulţumiri,

hvala, ... ! In addition, a special thanks goes to the people I shared the office with. Maarten, bedankt voor de kritische blik, die me soms tot wanhoop dreef, maar uiteindelijk mijn resultaten en artikels alleen maar beter maakte. Hulp zoals die van jou is zeldzaam, vandaar dat er in ruil nog altijd een (bijna even zeldzame) West-Vleteren op je staat te wachten. Wouter, samen begonnen, alleen was jij een heel stuk sneller, waarschijnlijk om de bij momenten bijna onhoudbare hitte van ons bureau te ontvluchten. Het was een plezier om met jou een bureau te delen! Bori, köszönet a rengeteg támogatásért, kiváltképp az utolsó embert próbáló hónapokban. Egy igazi barátra leltem benned. Bogi, hvala ti za podršku, prijateljstvo i sve trenutke u kojima si me zasmejavao. Zahvaljujući tebi, rad na doktoratu je postao mnogo zabavniji. Ukratko, 'fala ti onoliko!

Happiness is time spent with friends and looking forward to sharing time with them again.

Lee Wilkinson

Niet alleen de collega's hebben gezorgd voor de nodige ontspanning en afleiding tussen het doctoraatswerk door, ook de vrienden wil ik hiervoor graag bedanken.

Eerst en vooral de vrienden van de studies, onze zogenaamde Elek2006 groep. Bedankt voor de vele activiteiten, feestjes en weekendjes. Het was steeds een plezier bij jullie te zijn. Een speciaal woordje van dank hierbij aan mijn maatje Steven. Samen met je vrouw Lies heb je me dit jaar een ongelofelijk mooi cadeau gegeven en een echt gebaar van vertrouwen, door mij meter te maken van jullie zoon Milo. Ik kijk er echt naar uit om hem samen met jullie te zien opgroeien en de vele mooie momenten met jullie te delen. Daarnaast wil ik in het bijzonder ook Jan bedanken, die mij, ondanks alles, voor 200% is blijven steunen. Woorden zijn niet voldoende om je te bedanken voor alles wat je voor me gedaan hebt.

Veerle, Laura, Laurence, Sofie en Joke, bedankt voor de vriendschap en de gezellige etentjes, waar mannen alleen welkom zijn als ze klein zijn en schattig, en leven op melk of fruitpap. Hopelijk kan ik mijn schade van de voorbije maanden snel weer inhalen nu! Daarnaast wil ik ook graag alle anderen bedanken: mijn fijne medestudenten van de Spaanse les, Liesbeth en Miek, Christine en al diegenen die ik hier nu vergeet. Als ik weer eens wat te langzaam reageerde op jullie mails of niet kon afspreken, dan weten jullie hopelijk vandaag waarvoor dit was en kan ik het snel weer goedmaken.

Children learn to smile from their parents.

Shinichi Suzuki

Last but not least, zou ik mijn ouders, mijn zus Leen en haar vriend Dimi en mijn broer Pieter willen bedanken. Bedankt voor alle steun, liefde, aanmoedigingen en alle kansen die jullie mij gegeven hebben. Dat jullie vandaag trots op mij zijn, is mijn grootste beloning.

If the human brain were so simple that we could understand it, we would be so simple that we couldn't.

Emerson M. Pugh

Abstract

Understanding the cognitive processes that are going on in the human brain, requires the combination of several types of observations. For this reason, since several years, neuroscience research started to focus on multimodal approaches. One such multimodal approach is the combination of electroencephalography (EEG) and functional magnetic resonance imaging (fMRI). The non-invasive character of these two modalities makes their combination not only harmless and painless, but also especially suited for widespread research in both clinical and experimental applications. Moreover, the complementarity between the high temporal resolution of the EEG and the high spatial resolution of the fMRI, allows obtaining a more complete picture of the processes under study.

However, the combination of EEG and fMRI is challenging, not only on the level of the data acquisition, but also when it comes to extracting the activity of interest and interpreting the results from integrated analyses. This thesis, therefore, describes the setup of a typical EEG-fMRI study in detail and addresses the different steps to be taken in a full EEG-fMRI analysis. More specifically, a number of data-driven approaches that can be used at several stages of an EEG-fMRI study are optimized and validated. In this context, the work presented in this thesis can be subdivided in three main parts.

First, preparatory to any further analysis, the EEG and fMRI data need to be preprocessed and artifacts caused by the simultaneous acquisition need to be removed from the EEG data. The removal of these artifacts, and especially of the ballistocardiogram (BCG) artifact, is not straightforward. Despite considerable effort on this issue, no consensus has yet been reached on the best removal method. Therefore, this thesis investigates some of the most widely used methods for BCG artifact removal. More in detail, this work specifically focuses on the method parameters and on an accurate validation based on different task conditions and single trial event-related potentials (ERPs).

Further, the use of parallel factor analysis (PARAFAC) for the extraction of task-related characteristics from ERP data, is shown. It is demonstrated that PARAFAC can distinguish between different task-related conditions on a single

trial level, by employing the PARAFAC trial signatures for classification. Also, an evaluation of the robustness of the method against noise is presented, by including data measured inside the scanner. Although the obtained accuracies are lower in the latter case, PARAFAC proves to perform better than a classification based on raw data single trial characteristics.

Finally, two different approaches for EEG-fMRI integration (and more specifically, the integration of fMRI with the ERP data) are assessed. First, the single trial ERP information obtained with PARAFAC is used for the analysis of fMRI data. Second, average ERPs and fMRI from different subjects are combined in a so-called JointICA analysis. These two obviously distinct methods in fact address two different advantages of combined EEG-fMRI studies. Whereas the single trial analysis allows interpreting the possible connection between fluctuations in EEG and fMRI on a single trial level, JointICA enables the generation of a full spatiotemporal picture of the ongoing processes.

As such, this thesis confirms the usefulness of data-driven methods in the analysis and integration of EEG and fMRI, thereby extending results of earlier studies in the same research field.

Samenvatting

Het begrijpen van cognitieve processen, vereist de combinatie van verschillende soorten observaties. Om deze reden zijn multimodale benaderingen de laatste jaren steeds populairder geworden. Eén dergelijke multimodale methode is de combinatie van het elektro-encefalogram (EEG) en functionele magnetische resonantie beeldvorming (fMRI). Het niet-invasieve karakter van deze twee meettechnieken maakt hun combinatie niet alleen onschadelijk en pijnloos, maar ook in het bijzonder geschikt voor wijdverspreid onderzoek in zowel klinische als experimentele toepassingen. De complementariteit tussen de hoge temporele resolutie van EEG en de hoge spatiale resolutie van fMRI, laat bovendien ook toe een meer volledig beeld te vormen van de bestudeerde processen.

De combinatie van EEG en fMRI is echter een serieuze uitdaging, niet alleen op het vlak van data-acquisitie maar ook bij het extraheren van de relevante informatie en het interpreteren van de resultaten van de geïntegreerde analyses. In deze thesis wordt daarom de opbouw van een typische EEG-fMRI studie in detail beschreven, met aandacht voor de verschillende stappen die bij een volledige EEG-fMRI analyse moeten genomen worden. Meer bepaald worden een aantal datagedreven technieken, die gebruikt kunnen worden in verschillende fases van de EEG-fMRI studie, geoptimaliseerd en gevalideerd. Dit werk kan worden opgedeeld in drie grote delen.

Ten eerste dienen de EEG- en fMRI-data voorbewerkt te worden, voorafgaand aan elke verdere analyse. Hierbij moeten ook de artefacten die veroorzaakt worden door de simultane acquisitie, verwijderd worden uit het EEG. De verwijdering van deze artefacten, en in het bijzonder van het ballistocardiogram (BCG) artefact, is echter niet eenvoudig. Aangezien nog geen consensus bereikt is over welke methode de beste resultaten oplevert, worden in dit werk een aantal veelgebruikte methodes onderzocht. Hierbij wordt specifiek geconcentreerd op de methode-parameters en op een gedetailleerde validatie, gebaseerd op verschillende taakcondities en op enkelvoudige (niet-uitgemiddelde) gebeurtenis-gerelateerde potentialen (*event-related potentials* of ERP's).

Verder wordt getoond hoe *parallel factor analysis* (PARAFAC) kan worden

gebruikt voor het extraheren van taak-gerelateerde karakteristieken uit de ERP-data. Er wordt bewezen dat PARAFAC in staat is het onderscheid te maken tussen verschillende taak-gerelateerde condities op het niveau van enkelvoudige stimuli. Dit wordt aangetoond met classificatieresultaten gebaseerd op de PARAFAC-componenten. Ook wordt de robuustheid van deze methode tegen ruis geëvalueerd, door dezelfde analyses uit te voeren op data opgemeten binnenin de scanner. Hoewel in dit geval de verkregen performantie lager is, werkt PARAFAC toch duidelijk beter dan wanneer de classificatie gebaseerd wordt op ruwe data eigenschappen.

In een laatste onderdeel van dit werk, worden twee verschillende benaderingen voor EEG-fMRI integratie (en meer specifiek, voor het combineren van de fMRI- met de ERP-data) geëvalueerd. In de eerste methode wordt de hierboven verkregen taak-gerelateerde ERP-informatie gebruikt in de analyse van de fMRI-data. Een tweede aanpak maakt gebruik van uitgemiddelde ERP- en fMRI-data van verschillende subjecten die gecombineerd worden in een zogenaamde JointICA-analyse. Deze twee duidelijk verscheiden methodes richten zich in feite op twee verschillende voordelen van gecombineerde EEG-fMRI studies. Waar de eerste analyse toelaat om de mogelijke link tussen EEG- en fMRI-fluctuaties op het niveau van enkelvoudige gebeurtenissen te bekijken, maakt JointICA het mogelijk de interacties tussen spatiale activaties in de tijd te lokaliseren.

Op basis van de resultaten kan worden besloten dat deze thesis de bruikbaarheid van datagedreven methodes voor zowel de analyse als de integratie van EEG en fMRI bevestigt en een uitbreiding is van de resultaten van eerdere studies in hetzelfde onderzoeksdomein.

Nomenclature

Symbols

$a, b, \ldots$	scalars
$\mathbf{a}, \mathbf{b}, \ldots$	vectors
$\mathbf{A}, \mathbf{B}, \ldots$	matrices
$\mathcal{A}, \mathcal{B}, \ldots$	tensors
$\mathbf{A}^T$	transpose of the matrix $\mathbf{A}$
$\mathbf{A}^{-1}$	inverse of the matrix $\mathbf{A}$
a_{ijk}	element of three-way tensor $\mathcal{A}$ at position (i, j, k)
$[\mathbf{a}\,\mathbf{b}]$	matrix with columns $\mathbf{a}$ and $\mathbf{b}$
$\sum$	sum
$\otimes$	Kronecker product $\mathbf{A} \otimes \mathbf{B} \stackrel{\text{def}}{=} [a_{ij}\mathbf{B}]$.
$\odot$	Khatri-Rao product $\mathbf{A} \odot \mathbf{B} \stackrel{\text{def}}{=} [\mathbf{a}_1 \otimes \mathbf{b}_1 \ldots \mathbf{a}_R \otimes \mathbf{b}_R]$

Metrics

Hz	Hertz
ms	milliseconds
mV	millivolt
μV	microvolt
s	seconds

Abbreviations

AAS	Average Artifact Subtraction
ANOVA	ANalysis Of VAriance
BA	Brodmann Area
BCG	BallistoCardioGram
BCI	Brain Computer Interface
BOLD	Blood Oxygen Level Dependent
BSS	Blind Source Separation
BVA	Brain Vision Analyzer
CANDECOMP	CANonical DECOMPosition
CCA	Canonical Correlation Analysis
CNS	Central Nervous System
ECG	ElectroCardioGram
ECoG	ElectroCorticoGram
EEG	ElectroEncephaloGram
EMG	ElectroMyoGram
EPI	Echo-Planar Image
ERP	Event-Related Potential
EOG	Electro-OculoGram
FID	Free Induction Decay
FASTR	fMRI Artifact Slice Template Removal
fMRI	functional Magnetic Resonance Imaging
FWHM	Full Width at Half Maximum
GLM	General Linear Model
HRF	Hemodynamic Response Function
ICA	Independent Component Analysis
IDO	InterDisciplinair Onderzoeksprogramma (Interdisciplinary research program)
ISI	Inter-Stimulus Interval
ITPC	Inter Trial Phase Coherence
JADE	Joint Approximate Diagonalization of Eigenmatrices
LDA	Linear Discrimimant Analysis
LFP	Local Field Potential
LOC	Lateral Occipital Complex
LVF	Left Visual Field
MEG	Magnetoencephalogram
MNI	Montreal Neurological Institute
MPRAGE	Magnetization Prepared RApid Gradient Echo
MR	Magnetic Resonance
MRI	Magnetic Resonance Imaging
NIRS	Near InfraRed Spectroscopy
NMR	Nuclear Magnetic Resonance
N-PLS	Multiway Partial Least Squares

OBS	Optimal Basis Set
PARAFAC	PARAllel FACtor analysis
PCA	Principal Component Analysis
PET	Positron Emission Tomography
PNS	Peripheral Nervous System
PSD	Power Spectral Density
PSP	PostSynaptic Potential
ROI	Region Of Interest
RR	R peak to R peak
RF	Radio Frequency
RVF	Right Visual Field
SNR	Signal to Noise Ratio
SOBI	Second Order Blind Identification
SPM	Statistical Parameter Mapping
SVD	Singular Value Decomposition
SVM	Support Vector Machine
TC	Topographic Components
TE	Echo Time
TMS	Transcranial Magnetic Stimulation
TR	Repetition Time

Thesis-specific symbols and abbreviations

CE	CEntral (stimulus)
DET	DETection task
DL	Down Left
DR	Down Right
GNG	Go/NoGo task
NPC	Number of Principal Components
PTP	Peak-To-Peak value
UL	Upper Left
UR	Upper Right

Contents

Dankwoord i

Abstract vii

Samenvatting ix

Nomenclature xi

Contents xv

1 Introduction 1

1.1 Background 1

1.1.1 The human brain 2

1.1.2 Electroencephalography 3

1.1.3 Functional Magnetic Resonance Imaging 9

1.1.4 Combination of EEG and fMRI 15

1.1.5 Physiological relation between EEG and fMRI 17

1.1.6 Overview of integration approaches 19

1.2 Aims of the thesis 21

1.3 Chapter-by-chapter overview 21

1.4 Collaborations 23

1.5 Personal contributions 24

1.6 Conclusion 27

2 Data acquisition **29**

2.1 Simultaneous acquisition of EEG and fMRI 29

2.1.1 Equipment 30

2.1.2 Data acquisition parameters 31

2.2 Experimental data 33

2.2.1 Task paradigms 33

2.2.2 Overview of acquired data 38

2.3 Conclusion 39

3 Preprocessing of the data **41**

3.1 EEG preprocessing 41

3.1.1 Gradient artifacts 41

3.1.2 Heartbeat detection 45

3.1.3 Removal of ballistocardiogram artifacts 52

3.1.4 Use of independent component analysis 55

3.2 fMRI analyses 55

3.2.1 Preprocessing of the fMRI data 55

3.2.2 Statistical analyses 60

3.3 Conclusion 62

4 Removal of ballistocardiogram artifacts **63**

4.1 Introduction 63

4.1.1 Origin of the ballistocardiogram artifact 64

4.1.2 Characteristics of the ballistocardiogram artifact 65

4.1.3 Overview of ballistocardiogram artifact removal methods . 67

4.1.4 Aims of this chapter 68

4.2 Materials and methods 69

4.2.1 Experimental data 69
4.2.2 Simulation study 69
4.2.3 EEG preprocessing 70
4.2.4 OBS method 70
4.2.5 ICA method 71
4.2.6 OBS-ICA method 75
4.2.7 Validation criteria 76
4.2.8 Statistical analyses 79
4.3 Results 80
4.3.1 Outside results 80
4.3.2 Simulation results 81
4.3.3 OBS results 81
4.3.4 ICA results 84
4.3.5 Comparison of OBS with ICA 89
4.3.6 OBS-ICA results 93
4.4 Discussion 94
4.5 Conclusion 100

5 Single trial ERP reading based on Parallel Factor Analysis 101

5.1 Introduction 101
5.2 Materials and methods 103
5.2.1 Experimental data and preprocessing 103
5.2.2 PARAFAC 104
5.2.3 Application of PARAFAC to single trial ERP data 104
5.2.4 Evaluation of the results 106
5.3 Results 110
5.3.1 Illustration of the PARAFAC approach 110
5.3.2 Single trial left-right classification of outside data 110

5.3.3 Single trial quadrant classification of outside data 112
5.3.4 Single trial left-right classification of inside data 115
5.3.5 Single trial quadrant classification of inside data 116
5.3.6 Relation with fMRI data 117
5.4 Discussion 121
5.5 Conclusion 125

6 ERP-fMRI integration based on subject variability: a validation study 127
6.1 Introduction 127
6.2 Materials and methods 129
6.2.1 Experimental data: acquisition and preparation 129
6.2.2 JointICA 130
6.2.3 Application of JointICA 131
6.3 Results 132
6.4 Discussion 136
6.5 Conclusion 138

7 Conclusions and further research 139
7.1 General conclusions 139
7.1.1 Optimization of data quality 139
7.1.2 Extraction of single trial ERP information 140
7.1.3 Integration of EEG and fMRI 141
7.2 Future work and open problems 141
7.2.1 Using ERP information to create a time dimension for the fMRI spatial activations: grouping study 141
7.2.2 EEG-fMRI integration based on trial-by-trial fluctuations . 146
7.2.3 Other multimodal approaches and applications 148

Appendix 151

Bibliography **155**

Publication list **175**

Curriculum vitae **181**

Chapter 1

Introduction

This chapter aims at introducing the physiology of the human brain and the advantages of combining different neuroimaging methods to study neurological processes. Section 1.1 therefore focuses on providing the reader with some general background about the different aspects important for this thesis. First, a short description is given about the anatomy and working of the human brain in §1.1.1. Subsequently, in §1.1.2 and §1.1.3 the two neuroimaging methods used for this work are introduced and explained. §1.1.4 then explains the motivation behind the integration of these two methods and the advantages and disadvantages of this approach. Brief overviews of studies investigating the physiological relation between EEG and fMRI and of the most widely used integration methods are respectively given in §1.1.5 and §1.1.6. In addition to this background, the general aims of the thesis are defined in Section 1.2 and the structure of the thesis is outlined in Section 1.3. Finally, collaborations and personal contributions are summarized in respectively Section 1.4 and Section 1.5 and some conclusions are listed in Section 1.6.

1.1 Background

To fully understand the analyses and results presented in this thesis, some basic knowledge on the human brain and the employed neuroimaging methods is needed. This short introduction goes, therefore, more deeply into several of these physiological and methodological aspects.

1.1.1 The human brain

Based on [172], an introduction to brain anatomy is given.

The human brain is the centre of the human nervous system, a network of cells specialized for the reception, integration and transmission of information. More specifically, the brain forms a part of the central nervous system (CNS), as opposed to the peripheral nervous system (PNS) which comprises the sensory and motor nerve fibers that enter and leave the CNS or are completely outside the CNS. Besides the brain, the CNS also includes the spinal cord, lying within the vertebral column, and the retina.

Enclosed within the skull, the human brain has the same general structure as that of other mammals, but is over three times larger than the brain of a typical mammal with an equivalent body size [111]. Globally, the human brain (visualized in Figure 1.1) consists of three major parts: the brainstem (connecting the brain with the spinal cord), the cerebellum (attached to the brainstem) and the diencephalon and cerebrum. As can be seen in the figure, the brainstem is composed of the medulla oblongata, the pons and the midbrain, while the thalamus, subthalamus and hypothalamus form together the diencephalon. The cerebrum encompasses the right and left cerebral hemispheres, which are connected by the corpus callosum.

The brain contains more than 10^{10} nerve cells or neurons. Although these neurons are rather diverse in size and shape, they are usually composed of the following parts: grey dendrites, a grey cell body, a white myelinated axon and synaptic terminals (Figure 1.2(a)). The cell body or soma contains the nucleus, responsible for the synthesis of proteins for export to the axon. Also the other parts of the neuron play an important role in the transmission of information: the axon sends signals from the cell body to distant targets, the synaptic terminals transmit these signals to other cells and the dendrites receive the signals from other cells.

Brain tissue is divided into two tissue types: grey matter and white matter. This distinction can be clearly seen on an axial cross-section of the brain (Figure 1.2(b)). The grey matter is composed of the (grey) cell bodies and dendrites and is found on the surface of the brain, called the cortex, and in some deeper structures. The axons, on the other hand, form the white matter constituting the larger inner part of the brain.

The cerebral cortex is folded into gyri (the "bumps") and sulci (the "grooves"), thereby increasing the surface area. The deepest sulci are called fissures. Mainly based on the location of sulci and fissures, the cortex on each hemisphere is divided into four lobes: the frontal, temporal, parietal and occipital lobes (illustrated in Figure 1.3). More detailed anatomical names for subdivisions of these lobes are then based on the location of the gyri within these lobes (e.g., superior temporal

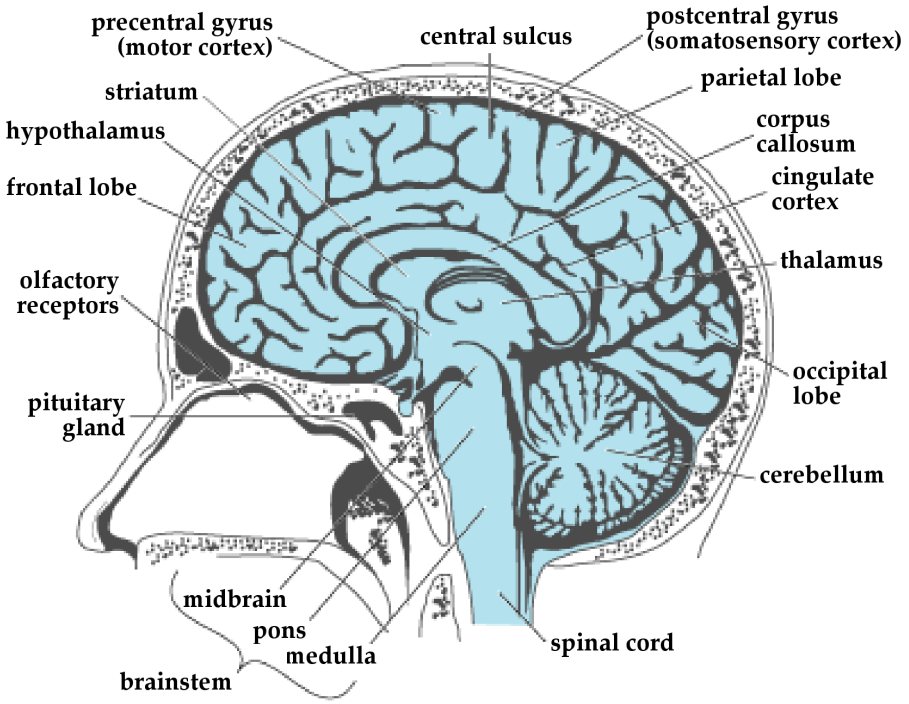

Figure 1.1: *Schematic representation of sagittal cross-section of the human brain with indication of major anatomical parts (adapted from [99]).*

gyrus) or their position with respect to one of the sulci or fissures (e.g., precentral gyrus).

Another division in brain areas has been presented by Brodmann, classifying the areas of the cortex according to the structure of their brain cells. An illustration of these so-called Brodmann areas is shown in Figure 1.4. Although originally, these areas were defined based solely on their neuronal organization, many are now known to be closely related to diverse cortical functions. This functionality actually provides another way to name the different parts of the cortex, thereby emphasizing the relation of these areas to their role in vision, audition, motor performance, etc.

1.1.2 Electroencephalography

Ever since the first human electroencephalogram (EEG) recordings by Hans Berger in 1924 [21], EEG has been widely used for measuring electrical brain activity and it has nowadays become one of the most popular tools for both clinical

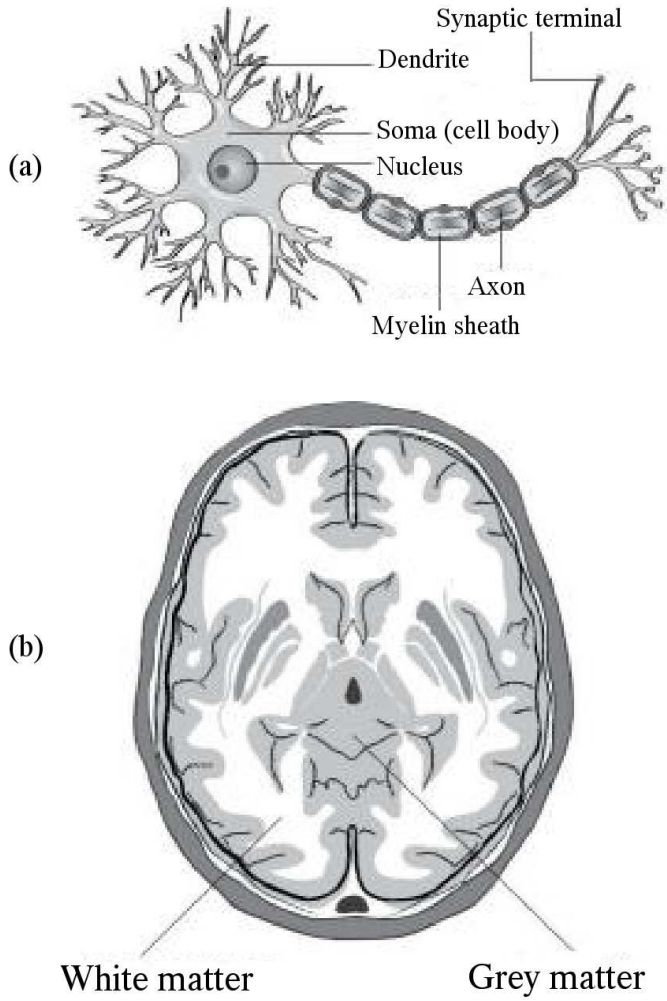

Figure 1.2: *(a) Schematic representation of a neuron; (b) Axial cross-section of the brain allows distinguishing grey and white matter (adapted from [100]).*

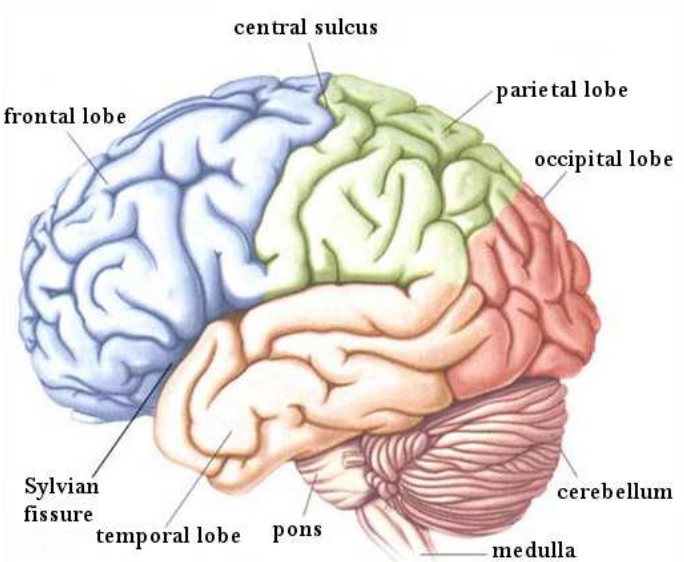

Figure 1.3: *Schematic representation of the left cerebral hemisphere with indication of the four lobes.*

and experimental neuroimaging purposes. In this section, the origin of electrical brain activity and the different aspects related to its measurement with EEG are addressed, based on [45, 51, 159, 177].

Electrical brain activity

The unequal distribution of Na^+, K^+ and Cl^- ions across the cell membrane of neurons, causes their interior to be negatively charged with respect to their exterior. This potential difference is called the resting potential and lies typically around -70 mV.

When cells communicate with each other, they release chemicals, called neurotransmitters, at the synaptic terminals. These neurotransmitters travel from pre- to postsynaptic regions, thereby causing a change in the resting potential or a so-called postsynaptic potential (PSP). These potential changes can range up to several millivolts (mV) and last for about 10 ms. As every neuron has many synapses connecting to different neurons, the actual potential over a cell membrane is given by the spatial or temporal summation of the PSPs. When there is a depolarization (a decrease in negativity) beyond a critical level, an action potential is generated that proliferates along the axon. Arriving at the synapse, this action potential can on its turn release neurotransmitters to communicate

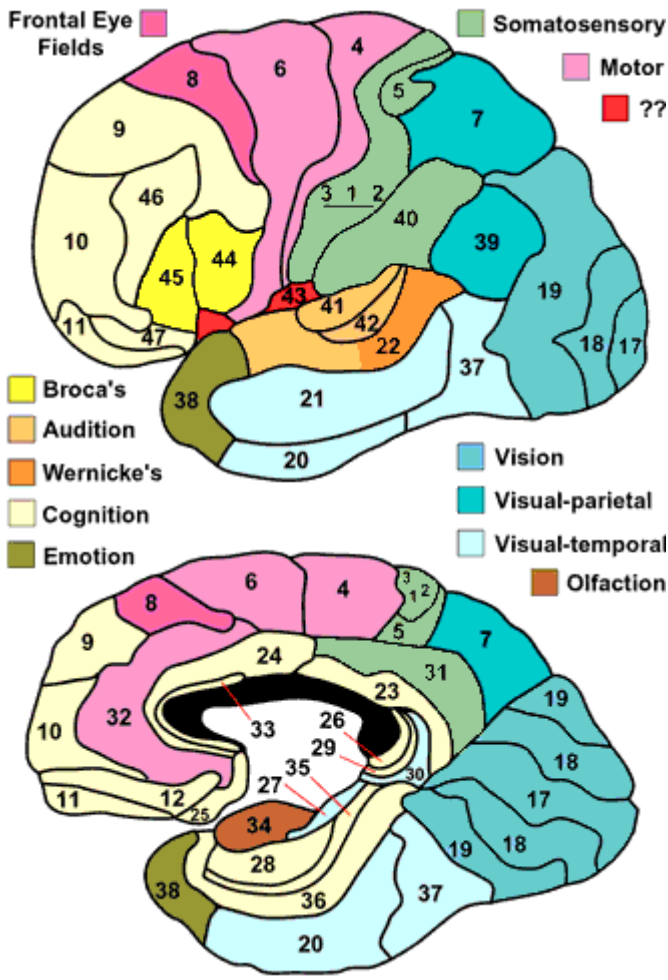

Figure 1.4: *Schematic representation of the division of the cerebral cortex into Brodmann areas. The functionality of the areas is indicated in different colors (adapted from [98]).*

with the next set of neurons. However, not all PSPs will contribute to an increased depolarization of the cell membrane. Those PSPs that do so and eventually lead to action potentials, are called excitatory PSPs. The so-called inhibitory PSPs, on the contrary, will take part in the suppression of action potentials.

Measurement of EEG signals

From the previous section, it becomes clear that neurons possess specific electrical properties which cause their activity to produce electrical fields. These fields may be recorded by means of electrodes either at a short distance from the sources (local field potentials or LFPs), either from a longer distance, at the cortical surface (electrocorticogram or ECoG) or at the subject's scalp. The latter is most commonly called the EEG and provides a measure for the electrical communication between neurons as a function of time. However, the occurring potential changes can only be detected if many neurons synchronously de- or hyperpolarize. Therefore, it is believed that the EEG is specifically generated by the synchronous firing of many vertically oriented large pyramidal cells in the cortex. These cells are aligned in such a way that they amplify each other's extracellular field [78]. A small fraction of the summation of the resulting currents penetrates through the meningeal coverings, spinal fluid and skull to the scalp, causing different parts of the scalp to be at different potential levels. By putting electrodes on the scalp, these potential differences can be measured as a function of time, thereby yielding the EEG.

To position the electrodes on the scalp, the International Federation of Societies for Electroencephalography and Clinical Neurophysiology has recommended a standardized electrode setting, commonly called the international 10-20 system [109, 170]. This system, illustrated in Figure 1.5, proposes electrode placement based on intersections at 10 or 20% intervals of distances between specific anatomic landmarks on the head. As such, 21 electrode positions are obtained, each indicated with a combination of two or three letters an/or digits. The first letter normally corresponds to the specific region the electrodes are located on. As such, F indicates electrodes on the frontal lobe, P on the parietal, T on the temporal and O on the occipital lobe. The letter C indicates the electrodes on the central line. For most electrodes, a second letter or a digit is added to this letter; a Z for all electrodes on the midline and odd and even numbers for electrodes on the left and right hemisphere, respectively. For setting a larger number of electrodes on top of these 21 positions, additional electrodes are equidistantly placed in between the above electrodes and the same naming approach is preserved.

Since the aim of EEG is to measure potential differences on the scalp, one or several reference electrodes have to be used. Different reference electrode placements have been used in literature, such as using the vertex (Cz), linked-ears, average

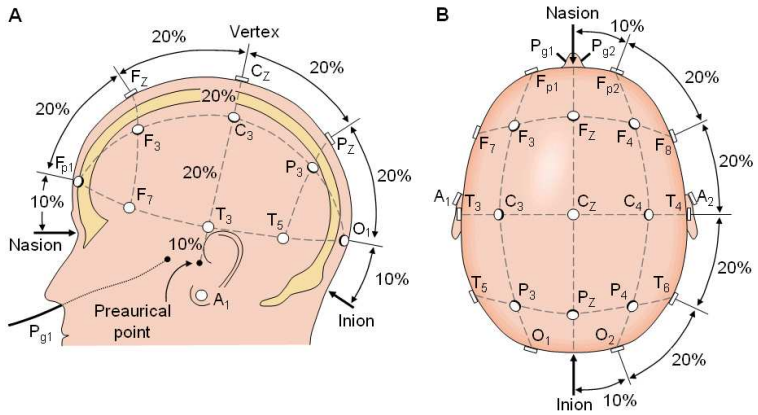

Figure 1.5: *Side and top view of the standard EEG electrode placement according to the 10-20 international system. The placement is based on a grid of lines, generated by connecting specific anatomical landmarks such as the nasion, inion and preauricular points, that mutually intersect at 10 and 20% intervals of their length. The electrodes are put at these intersections (from [137]).*

reference, etc.

Typical EEG rhythms and artifacts

One of the advantages of EEG is that it is a reasonably cheap and simple way to measure brain function. Its typical patterns are relatively well studied, which allows diagnosing several brain disorders based on visual inspection of the EEG. A number of these typical patterns are specifically characterized by their different frequency ranges. Brain rhythms between 0.5 and 4 Hz are called delta waves, those between 4 and 7.5 Hz theta and the oscillations between 8 and 13 Hz alpha waves. Further, also beta waves ranging from 14-26 Hz and gamma waves at frequencies above 30 Hz exist. In healthy adults, the amplitudes of these brain rhythms can change over states such as sleep and wakefulness or even evolve with age.

Looking at the other side of the picture, EEG also suffers from a number of limitations. First, from the above explanation about the generation of electrical brain activity, it may have already become clear that scalp EEG measurements record only a portion of the underlying brain activity. In addition, the spatial resolution of EEG is rather low, due to the limited number of electrodes only present on the scalp.

Another problem of EEG lies in the fact that it measures potential differences,

without making a distinction between brain and other sources. These recorded potentials not generated by the brain, are called artifacts and can sometimes completely deteriorate the brain activity of interest. Origins of these artifacts can be twofold: physiological and non-physiological. Non-physiological artifacts are mainly related to power line interference or malfunctioning of the recording equipment, while physiological artifacts are caused by parts of the body itself. This latter category includes, among others, artifacts coming from eye blinking and eye movement and artifacts caused by muscle contraction. Fortunately, signal processing techniques are successfully used to remove or suppress these artifacts and recover the underlying brain signals [46, 52, 145].

Event-related potentials

EEG is used in many applications that require a measure for brain function. It has shown its value for the analysis of sleep disorders, long-term monitoring of epilepsy patients and research in the field of neuropharmacology. One particular field for which EEG has been used extensively is the study of event-related potentials (ERPs), responses in the brain to specific motor, sensory or cognitive events [132]. These ERPs are rather small, especially compared to the background EEG activity. Therefore, procedures for extracting the ERPs from the EEG signals are needed. The most straightforward approach to achieve this, is to simply average over a set of event trials, thereby emphasizing the activity of interest and canceling out the other ongoing neural processes and noise (visualized in Figure 1.6). This approach, however, assumes that the brain is always reacting in exactly the same way to a certain stimulus. As this might not be true because processes like learning and habituation can influence the brain's responses, recent ERP studies focus more on single trial ERP data as to obtain more information about the brain's behavior. Obtaining these single trial ERPs, however, requires more advanced signal processing techniques.

ERP signals can be characterized by the amplitude, latency and spatial distribution of specific ERP components. These ERP components are the positive and negative deflections constituting the ERP waveform. They are usually represented by the letter P or N, depending on their polarity, plus a number indicating their latency or order. The most common ERP components are also indicated in Figure 1.6.

1.1.3 Functional Magnetic Resonance Imaging

Functional magnetic resonance imaging (fMRI) is a non-invasive technique that allows localizing active brain regions. It is not only used in experimental research for assessing brain function in, e.g., visual or cognitive tasks but also in pre-surgical

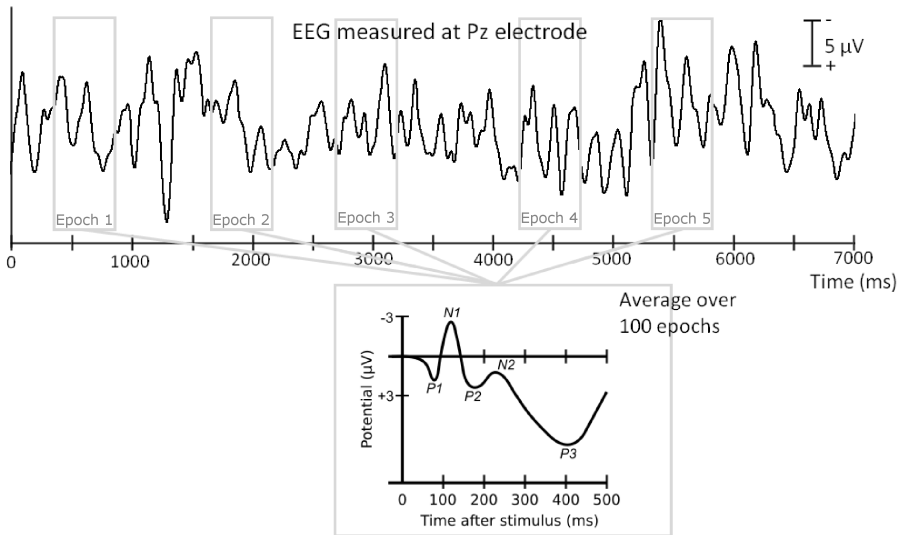

Figure 1.6: *Illustration of averaging procedure for the extraction of ERPs. Stimuli are presented to the subjects and the resulting responses are averaged. The most common ERP components are also indicated in the figure.*

examinations. Its physical basis is the phenomenon of nuclear magnetic resonance (NMR) or simply called magnetic resonance (MR). In the following sections, first the physics of MR will be briefly described, after which the principles of both MRI and fMRI will be explained. This explanation is based on [83, 162, 173], but for a more detailed background the reader is directed to specific MRI literature, such as [110, 167].

Physical basis of magnetic resonance

The hydrogen atom is the most relevant atom for MRI and fMRI, due to its abundance in the human body as a part of water molecules. The nucleus of this hydrogen atom consists of one single proton, that is characterized by a certain mass, a positive electrical charge and, like all protons and neutrons, an angular momentum or a spin. Since moving electrical charges produce a magnetic moment, also the spinning, positively charged hydrogen nuclei will possess such a moment and, therefore, interact with an externally applied magnetic field B_0. At the atomic level, some of the protons will align with the field (lower energy state) and others will align against the field (higher energy state), as such canceling each other out. However, a slight majority will align with the field so that the net result is an alignment with the external field. The larger this external field, the bigger will be

the difference in energy levels and the larger the majority aligned with the field. The total magnetic field of the excess protons is called the magnetization M_0. In addition, the external magnetic field B_0 will also cause the protons to precess or rotate around the field direction. The frequency of this precession is called the Larmor frequency and is directly proportional to the strength of B_0.

Applying a second oscillating magnetic field B_1 (also referred to as a electromagnetic radio frequency (RF) pulse) tuned to the Larmor frequency, transmits energy to the nuclei, causing some of the protons to jump to the higher energy state. In addition, the precession of the nuclei will be brought in phase. As a result, at the macroscopic level, the magnetization vector M_0 (that we consider originally aligned with B_0 along the Z-direction), spirals down to the XY-plane (with B_1 in the X-direction). This is illustrated on the left in Figure 1.7, where the magnetization vector is presented in a rotating frame (as such, ignoring the precession movement).

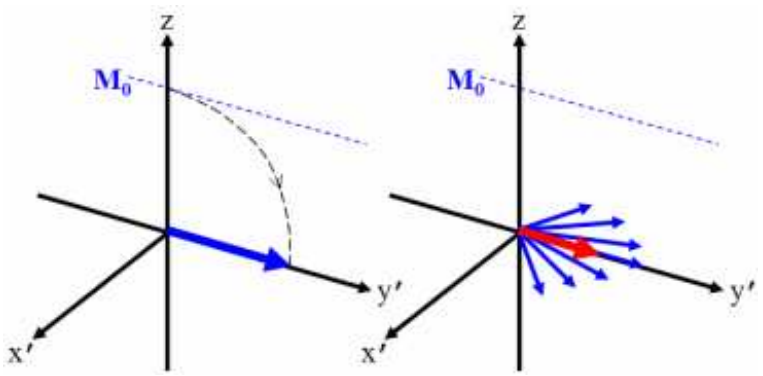

Figure 1.7: *Schematic representation of the magnetization going down to the XY-plane when an oscillating magnetic field is applied (left part) and the dephasing in the XY-plane due to nuclei interactions and field inhomogeneities (right part). Figure from [102].*

Removing the RF pulse causes some of the protons to return back to the lower energy state, thereby releasing a photon. On the macroscopic level, this corresponds to the magnetization vector recovering back to M_0 along the Z-direction at the expense of the component in the XY-plane. This releases the originally absorbed RF energy, partly as electromagnetic radiation, partly heating up the surrounding tissue. The recovery of the Z-component to M_0 is called T_1 relaxation, because its time course is characterized by an exponential curve with a time constant T_1. This T_1 is unique for every tissue and indicates the time after the excitation pulse when 63.2% of the magnetization is again aligned with B_0.

As explained above, applying the oscillating magnetic field B_1 brings the precession of the protons in phase. The precession rate of these protons depends on the

strength of the magnetic field they experience. However, due to interactions between their magnetic fields, the precession rate of certain protons will be altered, resulting in a loss in phase. As a consequence, the XY-component of the magnetization component will reduce. This process is called spin-spin or T_2 relaxation, related to the T_2 time constant of the corresponding exponential curve. Unlike T_1 values, these T_2 values are unrelated to field strengths, although they are also unique for each tissue type.

However, not only proton interactions cause the precession to go out of phase, also field inhomogeneities have this effect. The time constant taking these into account, together with the above described proton interactions, is called T_2^*. The dephasing is illustrated on the right in Figure 1.7. By applying different RF pulses in different sequences, both T_1, T_2 and T_2^* can be measured and as such give an idea about the tissue under study. During MR experiments, it will be the signal generated by the XY-component of the magnetization, called the Free Induction Decay (FID) that can be recorded by the coil placed around the subject inside the MR scanner.

Acquisition of anatomical images

The above explained time constants are tissue dependent and can thus be used to make brain images allowing to distinguish between different anatomical regions and tissue types. These time constant maps are obtained by selecting appropriate recording parameters such as the most optimal pulse sequence and a proper repetition (TR) and echo time (TE). The TR is the time between two consecutive RF pulses while TE is related to specific pulse sequences like the spin-echo and gradient-echo sequences. To spatially encode the maps, strong magnetic field gradients are applied. These gradients, provided in all directions, cause nuclei at different locations to rotate at different speeds. Since these spatially varying rotation frequencies are known, they can be used to accurately determinate spatial location. More information on the acquisition of MRI can be found in [110, 167]. An example of a T_1-weighted image is given in Figure 1.8. The size of the voxels (three-dimensional version of a pixel) in this image is $3 \times 3 \times 3$ mm.

Acquisition of functional images

fMRI is based on blood flow and blood oxygen concentration as measures for brain activity. These phenomena will be explained in this section together with the way how they are captured in MR images.

The BOLD signal Neurons in the brain consume oxygen. This oxygen is continuously supplied to the neurons by the blood in which the oxygen is attached

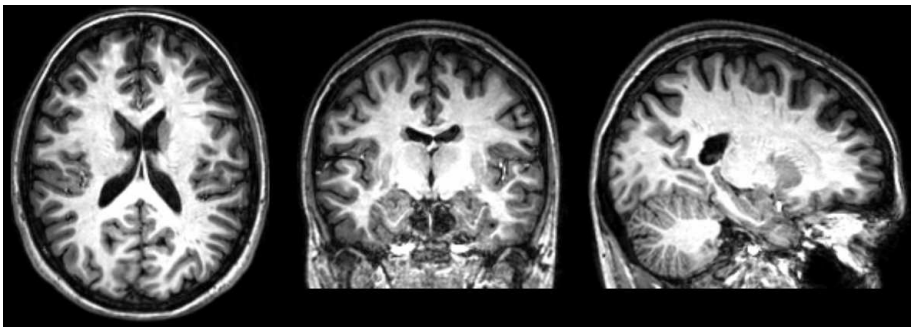

Figure 1.8: *Example of a T_1-weighted MR image, with from left to right: an axial, a coronal and a sagittal slice.*

to hemoglobin molecules. When neuronal activity increases, also more oxygen is needed. This additional oxygen is provided by an increased blood flow, leading to an increased concentration of oxygenated blood in the capillaries surrounding the active brain areas. Since oxygenated and deoxygenated blood have different magnetic properties, their difference in concentration can be measured with an MR scanner. More specifically, the oxygen concentration in the blood affects the magnetic environment of the hydrogen nuclei. As a consequence, low oxygen concentrations will cause faster dephasing of the protons and thus a lower T_2^* time constant. MR images reflecting T_2^* will therefore be brighter in active brain areas (longer T_2^*), an effect that is called the blood oxygen level dependent (BOLD) effect. These MR images are obtained with the gradient echo planar imaging sequence, which is especially sensitive to the T_2^* constant.

In reality, the signal time course following neuronal activation, is not limited to a simple increase and decrease. It follows a specific pattern, the so-called hemodynamic response, that can be visualized with the hemodynamic response function (HRF). The physiology behind the course of this response (illustrated in Figure 1.9) is, however, only partially understood.

Detecting active brain regions The identification of active brain regions with fMRI is, however, complicated by the fact that the increase in BOLD response related to neuronal activation is only 2-5% of the total signal. As such, the images need to be carefully preprocessed (see Chapter 3) and statistical analyses are needed to detect regions with an increased blood flow. One of the most widely used methods in this context, is based on generating a general linear model (GLM) for the fMRI signal. This GLM is constructed by creating a signal based on time points of interest (e.g., time instances of presented stimuli) and convolving this signal with a model for the HRF. The fMRI signal in each voxel is then statistically compared with this GLM and the resulting statistical map can be thresholded to

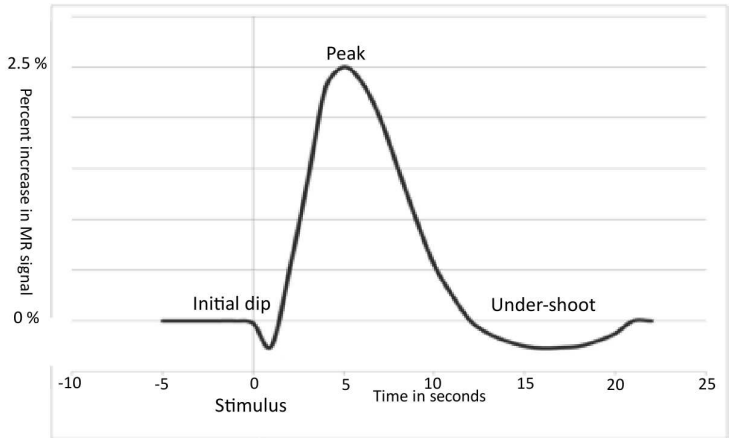

Figure 1.9: *Illustration of the hemodynamic response after the perception of a specific stimulus (adapted from [101]).*

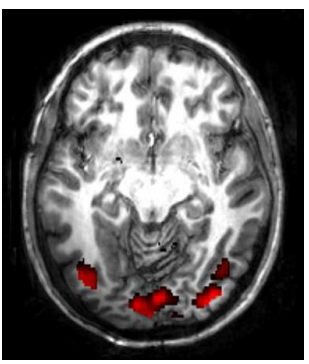

Figure 1.10: *Illustration of activation of visual areas obtained with fMRI on axial slice of MRI image.*

retrieve the activated brain areas. An example of activated brain areas is shown in Figure 1.10.

Next to this GLM-based approach, also blind source separation (BSS) methods like independent component analysis (ICA) and canonical correlation analysis (CCA) have been applied to fMRI data [28, 83]. These methods have the advantage that no model of the HRF has to be assumed and no timing information about the origin of activation is needed.

1.1.4 Combination of EEG and fMRI

To obtain a complete picture of how the human brain works, a combination of different types of observations is needed. For this reason, multimodal approaches are gaining more and more popularity in neuroscience research. One such multimodal approach is the combination of EEG and fMRI. The non-invasive character of these two modalities makes their combination not only harmless and painless, but also especially suited for widespread research in both clinical and experimental applications [24, 54, 159, 200].

Besides their non-invasiveness, the integration of EEG and fMRI has several advantages which, at the same time, represent the motivation behind their integration. The first advantage of EEG and fMRI lies in their complementary properties, visualized in Figure 1.11. As explained above, EEG measures electrical responses with a millisecond precision, but suffers from limited spatial accuracy due to the electrode positions restricted to the scalp surface. fMRI, on the other hand, yields very accurate spatial images based on local changes in brain hemodynamics. This hemodynamic response is, however, a slow signal and fMRI images are only acquired every few seconds. This is far below the brain reaction time to externally applied stimuli, thus complicating the analysis of detailed temporal brain changes. For this reason, it is believed that the complementarity between the high temporal resolution of EEG and the high spatial resolution of fMRI can provide deeper insight into brain function and dysfunction [12].

Another benefit of EEG-fMRI is its potential use for the validation of new methodologies [54]. As new EEG and fMRI processing techniques constantly emerge, established results from one of them can be used to prove the performance of a new technique applied to the other. E.g., the spatial localization obtained with specific source localization techniques (methods that aim at recovering the sources of measured EEG activity) can be validated looking at the brain areas activated during a corresponding fMRI experiment (e.g., [90]).

A third advantage of bringing EEG and fMRI together, is related to the fact that some events that occur in the brain are best observed in one modality while also their effect in the other modality can be of great interest [159]. The most typical example of this can be found in the field of epilepsy imaging and forms in fact the original motivation for integrating both modalities. Since interictal spikes (short epileptiform discharges occurring in between two seizures) can only be detected in the EEG, only the combination of EEG and fMRI allows mapping their hemodynamic correlates non-invasively.

Although the first two motivations for EEG-fMRI do not strictly impose this, the latter argument does require the EEG and fMRI to be simultaneously acquired. As shown in [20], this simultaneous approach has several important advantages. First of all, it ensures that both modalities are being measured under exactly the

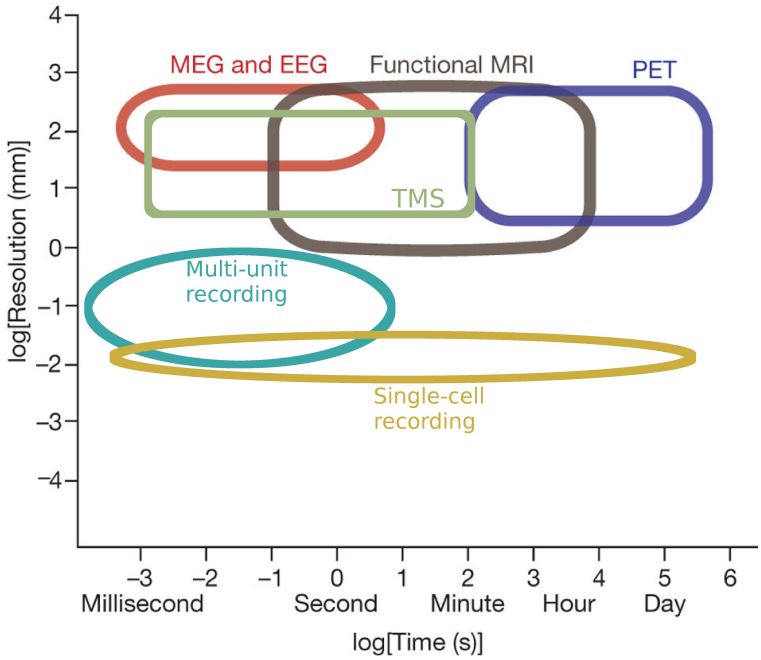

Figure 1.11: *Spatial and temporal resolution of several neuroimaging techniques. EEG and fMRI clearly show complementary spatial and temporal resolution properties. The other presented techniques are Positron Emission Tomography (PET), Transcranial Magnetic Stimulation (TMS) and intracranial electrophysiological recordings like multi-unit and single-cell recordings (adapted from [147]).*

same circumstances and conditions. For example, Novitski et al. [168] showed that the loud noise of the scanner can have an influence on how the brain reacts to certain stimuli. Secondly, simultaneously recording EEG and fMRI allows studying the brain in the same state of arousal, attention and habituation which can be related to, e.g., preparation time and time of the day [219]. Finally, it enables the investigation of relationships between trial-to-trial changes in event-related activity and changes in the BOLD response.

Despite the clear benefits of simultaneous acquisition, there are also some important disadvantages. This approach is not only more expensive due to the specialized equipment needed to perform the measurements and ensure patient safety, but it also has a major impact on the data quality. On the one hand, the MR images can be distorted by susceptibility artifacts and noise related to the presence of conductive materials and insufficient shielding of the EEG equipment [89, 92, 117, 127]. Fortunately, by using appropriate MR-compatible materials and appropriate shielding, this distortion can be minimized. On the other hand, when

acquired in the MR scanner, EEG data are highly contaminated with two major artifacts. Firstly, gradient artifacts occur due to switching magnetic fields during fMRI acquisition. Several procedures have been proposed to remove this type of artifact from the EEG (e.g., [187]). Nevertheless, since this artifact is invariant over time, most studies nowadays are consistent in using a subtracting procedure based on an average artifact template [3]. A bigger challenge is faced with the ballistocardiogram (BCG) artifact, produced by cardiac pulse-related movement of the scalp electrodes inside the magnetic field. The exact cause of this movement is still a matter of investigation (e.g., [222]) and also the removal of this artifact is a problematic issue, reported in many simultaneous EEG-fMRI studies (e.g., [56]). The simultaneous acquisition of EEG and fMRI will be more extensively discussed in Chapter 2, while the origin and removal of the artifacts will be further explained in Chapter 3 and Chapter 4.

The advantages of EEG-fMRI integration have already been exploited in numerous applications. For instance, the combination of EEG and fMRI allows localizing epileptic activity based on spike-triggered fMRI [19, 119, 128, 182]. Other possible applications are the study of ongoing brain rhythms [86, 87, 122, 155] and cerebral activation during sleep [43, 130, 178]. Also the analysis of event-related brain responses based on multimodal information [57, 58, 72, 154, 157] becomes more and more popular. This latter application will benefit especially from a meaningful combined approach since event-related responses are low amplitude signals highly sensitive to experimental conditions and brain state.

1.1.5 Physiological relation between EEG and fMRI

The obvious advantages of combining EEG and fMRI have been clearly described in the previous section. Their combination, however, assumes that both modalities reflect at least partly the same phenomena. As explained in Section 1.1.2, EEG is a measure of the electrical activity of the brain and, more specifically, is thought to be mainly related to synaptic activity. fMRI, on the other hand, is a more indirect measure of neuronal activity, as it is based on changes in metabolic and hemodynamic signals. To understand the physiological relation between EEG and fMRI, it is, therefore, crucial to understand how exactly the fMRI BOLD signal relates to changes in neuronal activity. A brief description of such relationship is given here, based on [184], to which we also refer the reader for a more detailed overview.

Unraveling this relationship is, nevertheless, not straightforward, as there are different aspects complicating this issue. First, in the temporal domain, the BOLD signal can be seen as a slow, delayed version of the neurophysiological response [184]. This causes the vascular responses to subsequent stimuli to partially overlap and as such, influence each other [123]. Second, only within

a limited range of stimulus conditions, hemodynamic signals are linearly related to neuronal activity [184]. In some networks, either the hemodynamic or the electrophysiological responses can saturate, introducing a partially nonlinear and thus more complex relation (e.g., [65]). Third, also the lower signal to noise ratio (SNR) of hemodynamic compared to neurophysiological signals, can complicate the interpretation of the fMRI data [131].

In the description of electrical brain activity in Section 1.1.2, a distinction was made between synaptic activity and action potentials (spiking activity). The question is now which of these two types of activity is reflected in the fMRI data. In literature, both studies reporting a relationship between spiking activity and hemodynamics signals, and studies indicating the BOLD signal being correlated with synaptic activity, can be found (for an overview, see [184]). This confusing situation is, however, not surprising, since the high local connectivity of the cortex results in a high correlation between synaptic activity and action potential rates. As such, these two types of neuronal activity need to be dissociated in order to identify which one of them is connected to the fMRI signal. Findings from studies that succeeded in this spatial segregation, suggest that the BOLD contrast primarily reflects the presynaptic and postsynaptic signals, and this mainly in the gamma frequency range (e.g., [131, 164]). Nevertheless, also spiking activity can be linked to the BOLD signal, but such coupling depends on whether the employed paradigm causes the neurons to be strongly correlated [166].

Apart from the positive BOLD responses to specific events or phenomena, as investigated in the above-mentioned studies, negative responses and spontaneous fluctuations in fMRI signals exist. Also these two can be associated with certain changes in neuronal activity. Negative BOLD responses have been shown to be coupled with a reduction in neuronal activity [186], although part of their origin is thought to be vascular [93]. Spontaneous fluctuations in fMRI data are not only due to respiration [22] and vasomotion [143], but also to fluctuations in locally measured neuronal activity [185].

So far, we mainly described which types of neuronal activity are coupled to the BOLD signal and how this relation looks like. Underlying the coupling between neuronal and hemodynamic changes, are the mechanisms known as "neurovascular coupling" [184]. A so-called "neurovascular unit", consisting of neurons, glia and cerebral blood vessels, is thought to be responsible for causing and controlling changes in cerebral blood flow related to neuronal activity [106]. More specifically, various vasoactive agents, such as ions, metabolic by-products and neurotransmitters, are released due to an increase in neuronal activity. The resulting vasodilation is then further propagated upstream, probably via a specific type of signalling within the vascular wall [69].

It should be clear that the relation between EEG and fMRI and their integration cannot be seen as separate problems. On the one hand, combining simultaneously

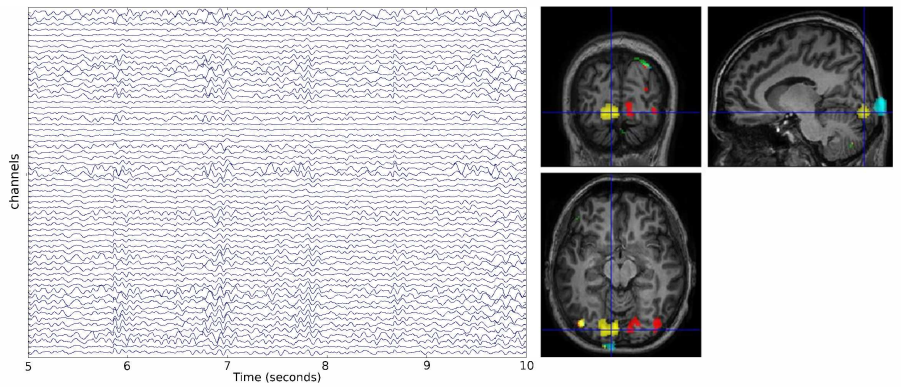

Figure 1.12: *Illustration of typical set of EEG data (left) after the removal of the scanner-related artifacts (cf. Chapter 3 and 4) and activated brain regions (right) obtained from simultaneously recorded fMRI data (cf. Chapter 3).*

measured EEG and fMRI data can give more information about their exact coupling. On the other hand, more knowledge on this coupling might improve the integration methods by including more detailed and accurate models of their underlying neural activity. One such neuronal model for EEG-fMRI integration has, e.g., been described in [113]. Although the proposed model was very simple, it allowed confirming some earlier found correlations between EEG and fMRI.

1.1.6 Overview of integration approaches

Despite all the research performed on EEG and fMRI (an illustration of both types of data is given in Figure 1.12), their exact coupling still remains an open question (see the previous section for a brief discussion). This complicates the integration of the two modalities, which can be performed on several levels. These levels of integration subdivide the integration approaches in several categories, as also explained in [24, 159]. A brief overview of different methods is given here, but for a detailed comparison of different methods, the reader is referred to [159, 200].

Maybe the simplest approach to combine EEG and fMRI is comparing the results obtained with each modality independently. This level of integration relates to the second benefit of EEG-fMRI, allowing the validation of new techniques in one of the modalities. As said earlier, results of EEG source localization techniques can, e.g., be validated with fMRI results [90]. However, a weak (spatial) correspondence between the results of such *coregistration* approaches does not automatically imply that there is something wrong with the techniques under study. In fact, there are several possible explanations for such poor resemblance, since some studies

reported about so-called EEG-blind fMRI sources and fMRI-blind EEG sources [8, 96, 175].

A more advanced integration approach is to use the data from one modality as prior knowledge in the analysis of the other modality. This type of integration approaches is considered *asymmetric* since the data flow occurs in one specific direction. Basically, two types of approaches can be distinguished: EEG-informed fMRI analysis and fMRI-informed EEG analysis. In EEG-informed fMRI analysis, time information from the EEG is used to build up a model for the fMRI data, with the aim of obtaining hemodynamic correlates of certain brain processes. E.g., many studies are based on the incorporation of specific aspects of ERP signals on a single trial level in the fMRI model [20, 74]. Both amplitudes and latencies of ERP components can be used for this purpose and in addition, ICA is often used as a preprocessing tool [57, 58]. Also the identification of brain areas correlated with the occurrence of epileptic spikes [118, 119, 216] or with spontaneous changes in typical EEG brain rhythms [87, 122, 155] is based upon similar principles. fMRI-informed EEG analysis, on the other hand, usually comes down to using the obtained brain areas from fMRI as constraints in EEG source localization analyses (e.g., [11]).

The most interesting integration approaches are, without doubt, based on *symmetric* data fusion. One such possibility is the use of Parallel ICA, as proposed in [72]. This algorithm extracts components from both modalities, applying spatial ICA to fMRI data of different subjects [30], and temporal ICA to single trial ERP data. After extracting the independent components from both modalities, the components are matched based on trial-by-trial correlations. In this Parallel ICA, however, EEG and fMRI are first analyzed separately before matching their results. A strategy that overcomes this limitation, is the JointICA method [29, 154]. In this method EEG and fMRI are combined in one common data space and a joint ICA model is applied to these data. This method can be employed both with single trial ERP-fMRI data and with averaged data from different subjects, in both cases aiming at connecting the different ERP peaks to their corresponding brain activations. In addition to ICA, also other BSS methods have been introduced in the EEG-fMRI context. In [42], e.g., the authors propose the use of multi-set CCA to decompose EEG and fMRI based on a trial-by-trial covariation between the two. Following this approach, they identify brain regions from the fMRI with a similar behavior as the trial-to-trial amplitudes modulations in the ERPs. These symmetric approaches can even be taken a step further by including higher-order decomposition methods in the analysis. This is the strategy followed in [141] where components related to different brain rhythms are retrieved with the multiway partial least squares (N-PLS) method.

1.2 Aims of the thesis

The aim of this thesis is the development and optimization of data-driven approaches for the analysis of EEG, fMRI and the combination of both. More specifically, from the EEG, ERPs are extracted in order to investigate specific sensory and cognitive processes. As should be clear from the above introduction, the integration of EEG (or ERPs) and fMRI is a complex field, not only for reasons of data quality but also because of the completely different nature of the two modalities. For this reason, the exact objective of this work is threefold.

1. The acquired data need to be preprocessed and the above explained scanner-related, and other artifacts need to be removed. To this end, different methods are examined and validated based on data from established experimental paradigms.
2. The ERP data are further analyzed in order to extract meaningful trial-by-trial information about their characteristics. This is carried out with specific higher-order decomposition techniques.
3. Patterns from the ERP and fMRI data are integrated. In particular, both single trial and averaged data will be used for this purpose and different approaches will be validated.

1.3 Chapter-by-chapter overview

A complete EEG-fMRI study consists of several steps, starting from the acquisition of the data and finally aiming at obtaining a complete spatiotemporal picture of the cognitive processes under study. A summary of the most important steps of such a study, is given in Figure 1.13. The contents of the successive chapters nicely follow this stepwise procedure and, as such, their correspondence is also indicated.

Chapter 1 introduces the physiology of the nervous system and the working of the human brain. In addition, the two modalities that are used in this work to measure brain activity, namely EEG and fMRI, are explained. Also the advantages and disadvantages of their combination are addressed together with a brief overview of currently proposed integration approaches. As such, the relevant background to understand the analyses and results presented in this thesis, is provided. Furthermore, the objectives of this thesis work are summarized, together with an overview of the presented chapters, the collaborations and personal contributions.

Chapter 2 explains the technical challenges of the simultaneous acquisition of EEG and fMRI data and the recording parameters for both modalities. In

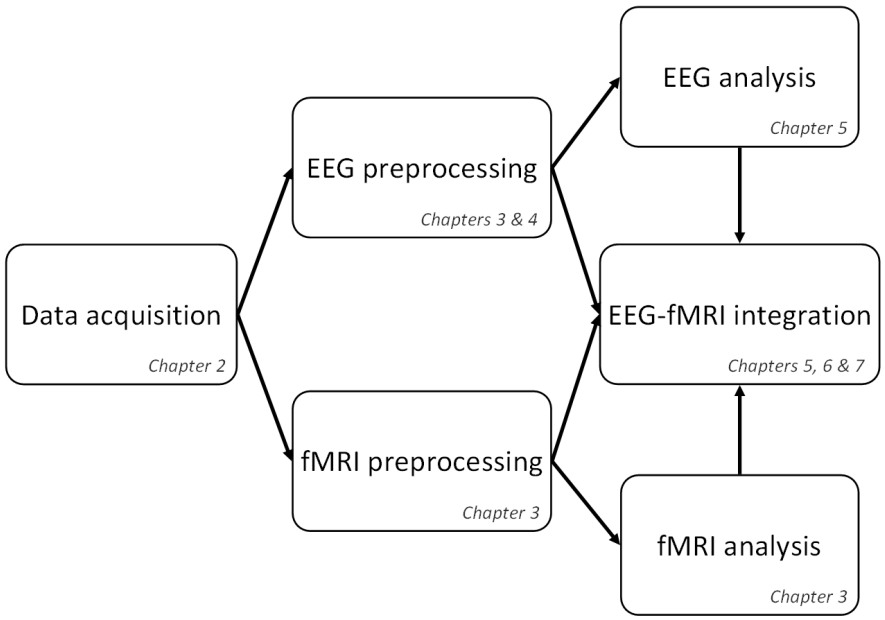

Figure 1.13: *Overview of a typical EEG-fMRI study, ranging from data acquisition until a complete integration of EEG and fMRI data. The chapters of this PhD thesis in which each of these steps are (partly) addressed, are marked as well.*

addition, the experimental tasks which are used to generate ERPs and specific brain activations, are described. An overview of the available datasets is given.

Chapter 3 describes the necessary preprocessing steps for simultaneously acquired EEG data. More specifically, the removal of the gradient artifacts is addressed, after which the detection and correction of the QRS onset times (necessary for BCG artifact removal) is discussed in detail. The reduction of the BCG artifact, on the other hand, is only shortly introduced since it is the main topic of Chapter 4. For the fMRI data, preprocessing as well as standard GLM analyses to obtain activated brain regions are explained.

Chapter 4 presents the results of an extensive validation study on BCG artifact removal. First, the origin of the BCG artifact is explained and its characteristics are illustrated for different examples. For the removal, some of the most widely used reduction methods are evaluated and compared. Their parameters are optimized based on different criteria derived from average and trial-by-trial characteristics of ERPs.

Chapter 5 proposes a new approach for extracting trial-by-trial variability

information from ERP data. Since ERPs are hidden in the ongoing EEG activity and noise, specific signal processing techniques are needed to retrieve them. Our approach is based on higher-order source extraction and is validated on data from 27 subjects acquired in different circumstances. By varying the employed data and also looking at more severely distorted signals, the possibilities and limitations of this approach are clearly shown. In addition, obtained variability measures are also used to analyze a small set of fMRI data.

Chapter 6 gives a brief overview of a validation study performed with the so-called JointICA EEG-fMRI integration method. This method can work with averaged ERP and fMRI data and will, as such, suffer less from data quality issues than the above explained use of single trial ERP measures. Nevertheless, also here, a distinction will be made between data of different quality levels. In addition, the idea is to find out how exactly, meaningful spatiotemporal pictures are obtained with JointICA.

Chapter 7 summarizes the work presented in the previous chapters and gives the general conclusions. Moreover, specific suggestions for future work are formulated and illustrated.

1.4 Collaborations

The work included in this thesis was initiated within the context of the K.U.Leuven EEG-fMRI IDO project (Interdisciplinary Research Program - 05/010) with several partners. Although this project has been finalized in the meanwhile, these collaborations have been of great importance for different aspects of the presented study. An overview of the involved partners and their current affiliations will now be given:

- Prof. Dr. Johan Wagemans and co-workers from the Laboratory of Experimental Psychology
- Prof. Dr. Peter Stiers, Maastricht University, Faculty of Psychology and Neuroscience
- Prof. Dr. Stefan Sunaert and co-workers from the Department of Radiology
- Prof. Dr. Lieven Lagae and co-workers from the Department of Pediatric Neurology
- Prof. Dr. Bea Van den Bergh, Tilburg University, Department of Psychology
- Prof. Dr. Ir. Bart Vanrumste, K.H.Kempen University College, Biosciences and Technology Department

With their expertise in the design, execution and interpretation of neurocognitive tests, the partners from the different psychology departments were mainly involved in the development and setup of the experimental paradigms and the interpretation of the obtained results. The neurology department also supported the setup and interpretation of the experiments, but, in addition, they were particularly involved in the optimization of the EEG acquisition. The people from radiology were not only responsible for the installation and optimization of the equipment setup for simultaneous EEG-fMRI acquisition, but also assisted in the analyses and interpretation of the fMRI data.

In addition to this IDO project, we also took part in the COST action NeuroMath (BM0601), dedicated to *Advanced methods for the estimation of human brain activity and connectivity*. Through this action, we started a collaboration with Dr. Borís Burle and his co-workers from the Laboratoire de Neurobiologie de la Cognition in Marseille, France. This joint work was focused on the removal of muscle artifacts from EEG data acquired during spoken language production. Apart from this project, our group also participated actively in the different NeuroMath workshops, of we which we organized one ourselves in Leuven in March 2009. A special issue of the journal Biomedizinische Technik/Biomedical Engineering dedicated to NeuroMath, was published on this occasion and, as co-organizer of the NeuroMath workshop, I became one of the issue's guest editors [209].

Other collaborations in the context of short-term projects and master theses, will be described in the next section.

1.5 Personal contributions

My own contribution in this work in fact ranges from the initial data acquisition until the final interpretation of the obtained integrated results. In addition, I was involved in several other studies which were not included in this thesis in order to preserve a certain coherence. Also these studies will be listed below.

In the initial phase of this project, data acquisition was performed by people from collaborating groups (cf. Section 1.4). However, already before the official end of our K.U.Leuven EEG-fMRI IDO project (05/010), I also got involved in the recordings and these became my responsibility after the other co-workers had left.

Prior to the removal of the BCG artifacts, the QRS onset times need to be accurately detected. We used the tools provided by the FMRIB toolbox [163] for this purpose, but some serious problems persisted. For this reason, we improved the toolbox's correlation based correction, in order to take into account specific problems that can occur with simultaneously acquired data. We included this

improved correlation approach in a stepwise guide, especially suited for newbies in the field (see Section 3.1.2).

One of the main topics of this work, was the study and removal of BCG artifacts (Chapter 4). We started this study with an investigation of the BCG artifact's characteristics, which was presented at the 1st NeuroMath workshop in Rome in December 2007 [207] and eventually published in a special issue of the *International Journal of Bioelectromagnetism* [206]. Afterwards, an extensive validation study based on ERP data acquired inside the MR scanner, was performed and published in *NeuroImage* [203]. In parallel, another BCG removal method based on canonical correlation analysis was validated on our datasets by Sara Assecondi from the Medical Imaging and Signal Processing (MEDISIP) group of the Department of Electronics and Information Systems of the University of Ghent. This work, in which I was involved in the setup of the analyses and the interpretation of the results, was published in *Clinical Neurophysiology* [10].

Another personal contribution was the extraction of single trial ERP information, which is the objective of the analyses explained in Chapter 5. The use of PARAFAC on single trial ERP data was introduced and validated with a classification procedure based on different conditions in the experimental paradigm. Some preliminary results of the possibilities of PARAFAC for ERP data were presented at the Biosignal conference in Berlin, Germany [202], while the eventual single trial extraction has been submitted to *Psychophysiology* [205].

The validation study on JointICA (cf. Chapter 6) was initially performed by my colleague Bogdan Mijović. Nevertheless, I was involved in acquiring the data, preprocessing the EEG signals and summarizing and interpreting the results. This study has been submitted in revised form to *NeuroImage* [148]. Another integration study conducted within our EEG-fMRI IDO project, was based on single trial P1 and N1 information. The results of this work indicated that simultaneous EEG-fMRI can separate visual processing at 100-200 ms after stimulus onset from the rest of the information processing in the brain. More details have not been included in this thesis, but can be found in a paper published in *NeuroImage* [169].

The ongoing study of which preliminary results are presented in Chapter 7, was developed in close collaboration with Bart Machilsen and professor Johan Wagemans of the Laboratory of Experimental Psychology. In this work, I have been mainly involved in data acquisition, analysis and interpretation. To facilitate further studies on EEG and fMRI, a K.U.Leuven EEG-fMRI website was also created, focusing on different aspects of the combination of the two modalities (www.esat.kuleuven.be/scd/eegfmri). A detailed manual describing the recording setup and different data analyses, is available on this website.

Thanks to the experience gained in the course of the above-mentioned studies and my participation to several NeuroMath workshops, I also got the opportunity to

write a review paper on simultaneous EEG-fMRI together with several experts in the field [24]. In addition, in the context of a master thesis, we collaborated with the group of professor Anna Bianchi (Dipartimento di Bioingegneria, IIT Unit, Politecnico di Milano, Milan, Italy) to study BOLD correlates of EEG alpha and beta rhythms observed during a motor task [41]. Under co-supervision of Dr. Guy Nagels from the multiple sclerosis centre in Melsbroek, other students also worked on the combination of EEG and fMRI, in this case distinguishing between healthy subjects and patients in different levels of multiple sclerosis. The two theses resulting from this work, were granted a Cera award, thereby emphasizing their relevance with regard to both social and technical aspects.

With the group of professor Mathieu Vandenbulcke and Jan Van den Stock (Division of Psychiatry), we also investigated the combination of fMRI with another electrophysiological measure, the electromyogram (EMG). As will be explained in Chapter 7, this application is mainly complicated by the removal of the gradient artifacts.

Next to the above work on several aspects of the combination of EEG and fMRI, I was also involved in a number of studies addressing other issues in neuroimaging research. One of these topics is artifact removal, since also non-simultaneously measured EEG data suffer from several types of contamination (cf. Section 1.1.2). For this reason, we worked on the removal of muscle artifacts from data acquired during spoken language production in collaboration with the group of Borís Burle in Marseille. As explained in Section 1.4, this work was started up thanks to, and continued throughout, the NeuroMath action. Preliminary results were shown at the 2nd NeuroMath Workshop in Jena, Germany [208] and the full study was published in *Neuroinformatics* [52].

An often overlooked type of brain-related distortion, specifically for ERP data, is alpha activity. Although this activity is often of interest in EEG studies, it can severely diminish the ability to identify ERP components, even after applying the averaging procedure. For this reason, we applied the PARAFAC method (presented in this thesis in the context of single trial ERP extraction) for the removal of alpha distortion and presented this work at the 4th European Congress of the International Federation for Medical and Biomedical Engineering (ECIFMBE) in Antwerp [204].

Other work was performed in the field of brain computer interface (BCI) systems, in which a mind speller, based on steady state visual evoked potentials, was developed [183]. Also this study was conducted in the context of a master thesis, in collaboration with the Computational Neuroscience Research Group of professor Marc Van Hulle.

1.6 Conclusion

In this chapter, first, the necessary physiological and methodological background for this thesis was summarized. In particular, the working of the human brain and the neuroimaging methods that can be used to visualize this brain activity, were described. The starting point for this work, which is the combination of simultaneously acquired EEG and fMRI data, was also motivated and an overview of current methods was given. Afterwards, specific objectives were formulated and the chapters in which these were addressed, listed. Both collaborations with other groups and personal contributions were summarized.

Chapter 2

Data acquisition

The aim of this chapter is to describe in detail the acquisition system and the different datasets employed in this work. First, in section 2.1, the simultaneous acquisition of EEG and fMRI will be discussed. More specifically, the equipment necessary for this type of measurements will be described, after which the selected acquisition parameters will be listed. Section 2.2 will tell something more about the datasets that will be further analyzed in the next chapters. Next to specific information about the tasks that were investigated, a detailed overview of the acquired data will be given. Section 2.3 will close the chapter with some conclusions.

2.1 Simultaneous acquisition of EEG and fMRI

As explained in the previous chapter, many EEG-fMRI applications benefit from simultaneously acquiring both modalities. A major breakthrough in this context was accomplished by Ives et al. [108], when they showed for the first time the feasibility of acquiring EEG data inside an MR scanner. Since then, much progress has been made, such that nowadays several EEG systems for simultaneous EEG-fMRI acquisition are commercially available. Nevertheless, to come to this point, a number of technical and safety-related challenges had to be conquered. The resulting acquisition setup and some related technical aspects will be highlighted in this section (based on [159, 200], without going into details). In addition, the specific acquisition parameters adopted in this study, will be discussed.

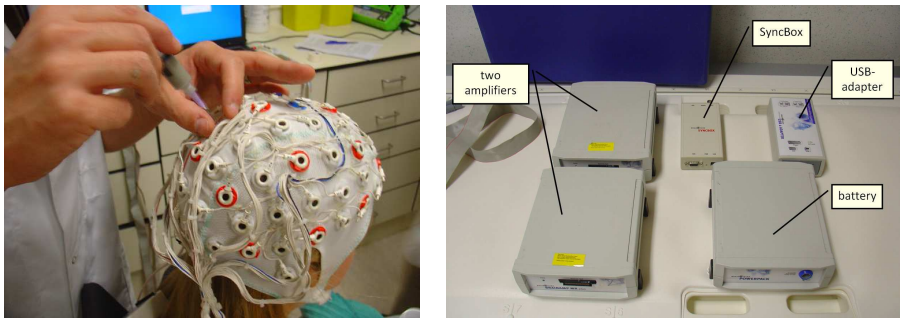

(a) (b)

Figure 2.1: *(a) Picture of an electrode cap (BrainCap MR) with 64 ring electrodes. Electrolyte gel has to be used to optimize the signal quality during measurements; (b) Picture of different parts of the BrainAmp MR+ system. Two battery powered amplifiers are used and connected to the computer via the USB adapter. In addition, the synchronization box allows synchronizing the EEG data with the clock of the MR system.*

2.1.1 Equipment

Standard EEG instrumentation consists of a set of electrodes, an acquisition system to amplify and digitize the EEG signals, a system (e.g., a computer) to visualize and analyze the recordings and a number of leads and wires to connect all these components. The electrodes can be stuck to the subject's scalp or can be mounted in an electrode cap, as illustrated in Figure 2.1(a). To ensure good signal quality during the EEG measurements (i.e., minimize the impedances), the EEG electrodes must be filled with a conductive electrolyte gel.

The bore of the MR scanner can be seen as a "hostile" environment for recording the EEG data [200]. More specifically, all elements of the EEG hardware are exposed to both a constant and a varying magnetic field and to the RF pulses emitted during fMRI acquisition. Different approaches can be adopted to cope with this "hostility", thereby dividing the currently available MR-compatible EEG systems into two main categories. In addition, any use of ferromagnetic materials has to be avoided.

A first category of systems are the ones of which the biggest part is located in the scanner control room. A clear advantage of this approach is that putting the amplifier system outside the strong magnetic field avoids the necessity of a specific MR-compatible design for the amplifiers. However, this setup requires the use of long electrode leads and an opening for these leads in the MR filter panel, respectively causing bigger gradient artifacts and possibly leading to leakage of RF energy.

In this study, a system based upon the second approach is used. More specifically, the EEG data were collected using the BrainAmp MR+ system (BrainProducts, Munich, Germany), of which some parts are visualized in Figure 2.1(b). The battery powered amplifiers of this system are positioned inside the scanner bore, as such reducing the amount of gradient artifacts related to long electrode wiring. In addition, the signals going from the amplifiers to the recording computer are fed through fiber optical cables, which have the advantage of being immune against magnetic or RF coupling. The amplifiers of this system are specifically designed to be used in the MR environment while all other electrically critical components of the EEG system can be put in the control room. When attaching the electrodes to the amplifiers, sandbags can be used to fixate the corresponding leads in order to avoid additional movement artifacts.

Regardless of the followed approach, a number of small details also have to be taken care of. First of all, the selected imaging sequence can have an effect on the subject's safety, since a badly chosen sequence can cause serious heating at the border between the scalp and the electrolyte gel [146]. Moreover, any type of loops that could cause additional currents, albeit in the electrode leads or in any other cable, should be avoided [63]. It has also been shown that synchronizing the EEG-amplifier clock to the MR scanner control-device clock improves the removal of the gradient artifacts [5, 38, 138]. Therefore, the BrainAmp MR+ System also includes a synchronization box, as can be seen in Figure 2.1(b).

Furthermore, to prevent head movements and resulting distortion of both EEG and fMRI data, it is important to take care of the subject's comfort. Therefore, when a subject is lying supine in the scanner, a cushion is used to minimize the pressure of the electrodes on the head. In addition, the subject is provided with earplugs to avoid harmful effect from the scanner's acoustic noise.

2.1.2 Data acquisition parameters

Besides the above-mentioned synchronization aspect, also the detection of the true onset of the gradient artifacts is essential for fully capturing their shape. This is important since a successful removal of the artifacts highly depends on an accurate construction of the artifact template. The gradient artifacts cover a broad frequency spectrum ranging from very low frequencies until several thousand Hertz [3]. To avoid aliasing and at the same time capture the major part of these artifacts, EEG data were measured using an analog hardware filter between 0.1 and 250 Hz and a sampling rate of 5 kHz.

The experiments were performed at two locations, the University of Maastricht (Maastricht, The Netherlands) and the University Hospital Gasthuisberg of the Katholieke Universiteit Leuven (Leuven, Belgium). For validation purposes, the EEG data were acquired in three different situations: inside the MR scanner

simultaneously with fMRI, inside the MR scanner without simultaneous fMRI acquisition and in the scanner control room. Regardless of the situation, the EEG data were collected from 62 standard scalp sites using the above explained BrainAmp MR+ system (with a distinct system for each location). Since the exact distribution of the electrodes over the scalp differed between the two locations, the setup is explained below for both locations separately. In both cases, electrode impedances were kept below 10 kΩ. Also the MR scanner and the fMRI acquisition parameters are detailed for each location individually.

Location 1: University of Maastricht (Maastricht, The Netherlands)

In this setup, the 62 unipolar electrodes were placed equidistantly. Their location with respect to the international 10-20 system is indicated with black circles in Figure 2.2. Two additional electrodes were placed below the left eye and on the right lower back to monitor eye blinks (with electro-oculography or EOG) and electrocardiograms (ECGs), respectively. All 64 channels were recorded with Cz as reference and POz as ground.

For the measurements inside the MR scanner, a Siemens 3T Allegra scanner (Siemens, Munich, Germany) was used. 160 echo-planar images (EPI) composed of 32 slices of $3.5 \times 3.5 \times 4$ mm voxel size were recorded with ascending slice order with a repetition time of 2 seconds during each experimental block. For anatomical reference a full brain anatomical image was obtained with the magnetization prepared rapid gradient echo (MPRAGE) imaging sequence (192 slices, TE = 2 ms, TR = 2.25 s).

Location 2: University Hospital Gasthuisberg of the Katholieke Universiteit Leuven (Leuven, Belgium)

The 62 unipolar electrodes employed in this setup were arranged according to the international 10-20 system (see Figure 2.2). In addition, the EOG was measured below the left eye and an ECG electrode was put on the left scapula. All 64 channels were recorded with FCz as reference and Iz as ground.

The simultaneous measurements were performed in a Philips 3T Intera whole-body scanner (Royal Philips Electronics, Amsterdam, the Netherlands). 160 EPI images composed of 28 slices of $3 \times 3 \times 4.5$ mm voxel size and 4.8 mm slice thickness were recorded with ascending slice order with a TR of 1.95 s (for the detection and Go/NoGo task) and a TR of 2 s (for the grouping task). Also here the MPRAGE sequence was used to acquire anatomical images (230 coronal slices, TE = 4.6 ms, TR = 9.7 s).

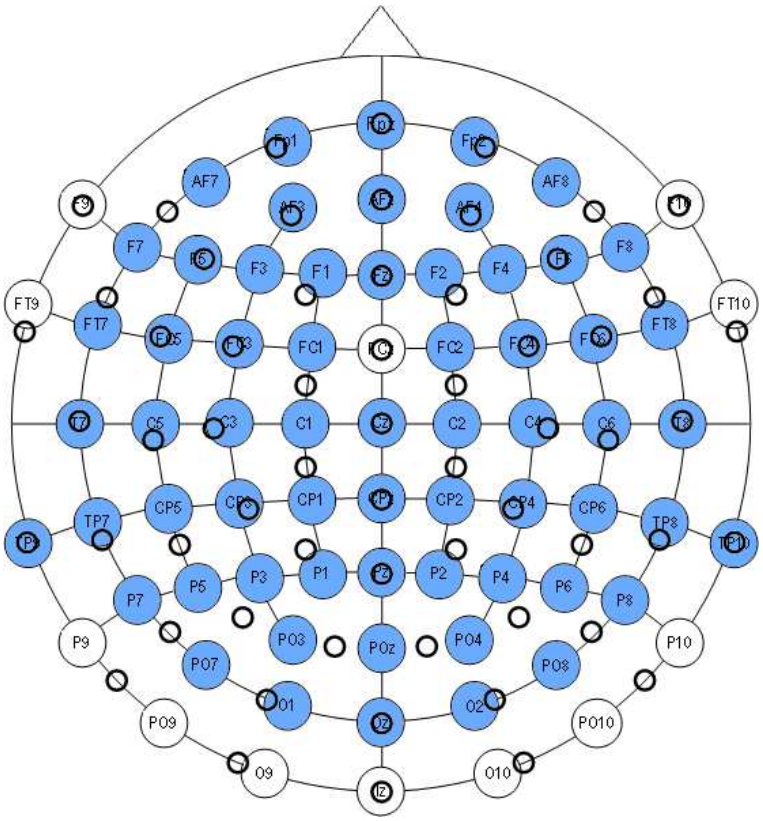

Figure 2.2: *Schematic representation of electrode distribution of 74 electrodes following the international 10-20 system. The 62 equidistant electrodes used in the Maastricht setup are indicated with small black circles while the 62 electrodes in the Leuven setting are colored.*

2.2 Experimental data

First, the employed task paradigms will be described after which the actual available data will be listed.

2.2.1 Task paradigms

The different stimulation paradigms were generated and presented to the participants with the Presentation software (Neurobehavioral Systems, Albany, CA, USA).

Detection task

The first task was a visual detection paradigm with segments of circular black-and-white checkerboard stimuli presented one at a time in randomized sequences to one of the four quadrants of the visual field [67]. As such, there are upper left (UL), upper right (UR), down left (DL) and down right (DR) stimuli. In addition, a large circular black-and-white checkerboard was presented as a central stimulus (CE) on the middle part of the screen. Subjects were instructed to fixate the cross in the middle of the screen and to press a button upon detection of each of these stimuli. In the simultaneous measurements, also empty events were used in order to provide a baseline for the fMRI event-related analysis. The figure during empty events was not different from the inter-stimulus interval, i.e., a grey screen with a fixation cross. More details about the stimulus presentation can be found in [169].

Concerning the number of stimuli and their presentation, in fact two different versions of the detection task were used. In the original version (visualized in Figure 2.3), the stimuli were presented in four blocks and per run 100 stimuli (20 of each type) were shown to the participants. In each condition the stimulus was presented for 150 ms and the inter-stimulus interval (ISI) varied between 900 ms and 2400 ms. In the alternative version a longer ISI was used, more specifically varying between 2250 and 5000 ms. In this case, stimuli were presented in six blocks of 70 trials (14 of each type). This simple detection task was selected as it is known to evoke robust P1 and N1 components, not only useful for validating the artifact removal but also for assessing the potential of more advanced analysis approaches.

Go/NoGo task

The second task included in this work, is a cognitive control task. More specifically, a visual Go/NoGo paradigm was employed to investigate the mechanisms between generating and withholding responses [25, 76, 165]. This task is illustrated in Figure 2.4 and requires fast, simple responses to Go stimuli (red square) and inhibition of any responses to NoGo stimuli (red circle). Each run consisted of 100 trials of which 80 were Go trials. In each condition the stimulus was presented for 150 ms. The ISI varied between 850 ms and 5850 ms. The Go/NoGo task has led to the identification of ERP components such as the NoGo N2 and P3 that are strongly augmented on NoGo-trials, as compared with Go trials, particularly at frontocentral sites.

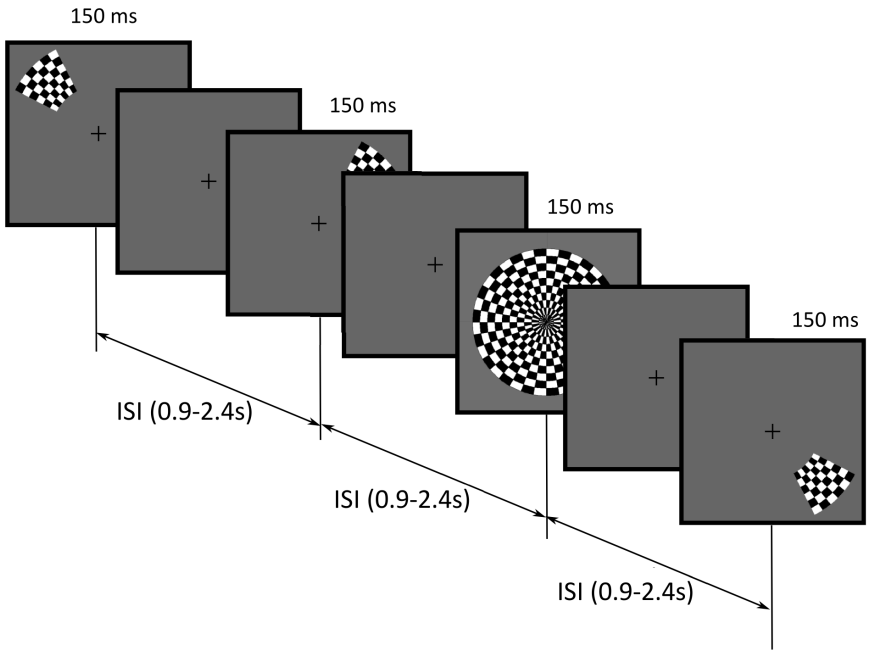

Figure 2.3: *Schematic representation of fragment of detection task paradigm. Five types of stimuli are alternated with empty events and with an ISI between 900 and 2400 ms.*

Grouping task

The purpose of this third task was to obtain a better understanding of the mechanisms underlying two-dimensional shape perception. In the early twentieth century, a number of local and global grouping principles that contribute to visual perception have been postulated [116, 218]. By using stimuli of which the structure detection involves local and global grouping, we hope to reveal the processes behind these grouping principles.

The employed stimuli were arrays of oriented and non-overlapping Gabor elements (see Figure 2.5), created with MATLAB and GERT, the Grouping Elements Rendering Toolbox [62]. The stimuli were presented centrally on a uniform grey screen with a randomized alternation between structure, non-structure and catch stimuli. Non-structure stimuli were dense matrices of isolinear non-structure elements as shown in Figure 2.5(a). Catch stimuli looked similar but included a small circle in the Gabor array (Figure 2.5(b)). There were two types of structure stimuli, thereby distinguishing between two versions of task blocks. In version

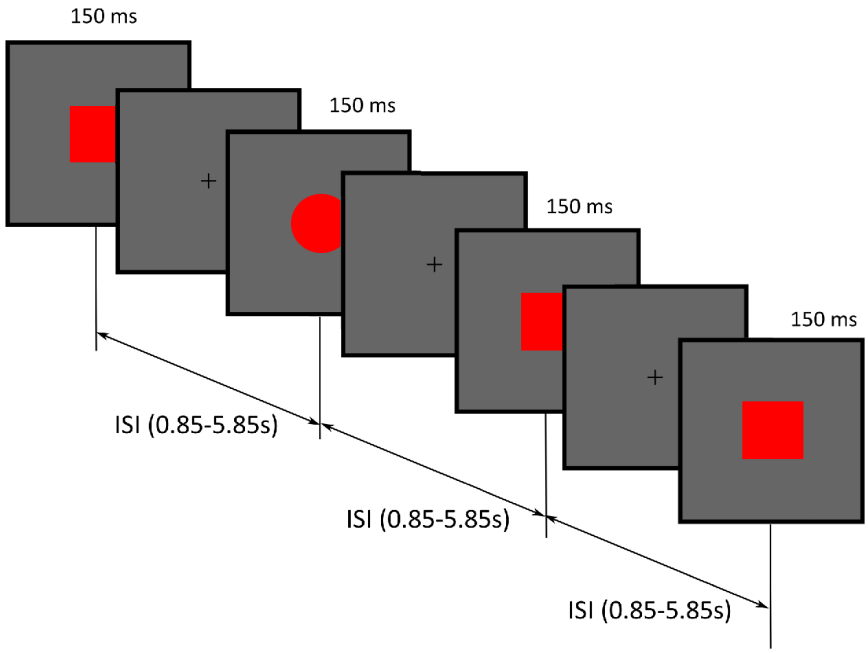

Figure 2.4: *Schematic representation of fragment of Go/NoGo task paradigm. Go (red squares) and NoGo (red circles) stimuli are presented with an ISI between 850 and 5850 ms.*

A, structure stimuli were dense matrices with curvilinear contour elements and isolinear non-structure elements (Figure 2.5(c)). Version B of the task showed structure stimuli corresponding to dense matrices with alternating curvilinear and orthogonal contour elements and isolinear non-structure elements (Figure 2.5(d)). Version A and B of the task differ in the fact that only global (version B) or both global and local grouping processes (version A) are involved in the detection of the structure stimuli. For more details on similar stimulus construction, see [133].

Subjects were asked to perform four blocks of each task version. They were instructed to focus on the fixation cross in the middle of the screen and press a button upon appearance of each of the catch stimuli. These catch stimuli were introduced to ensure that the participants' attention was kept to the screen. To avoid that participants would only focus on a small region of the display, we randomized the position of the circles across trials. In addition to the different stimuli explained above, also a number of blank events were included, for the same reason as the empty events in the detection task. The number of blank events and structure, non-structure and catch stimuli was randomized between task blocks.

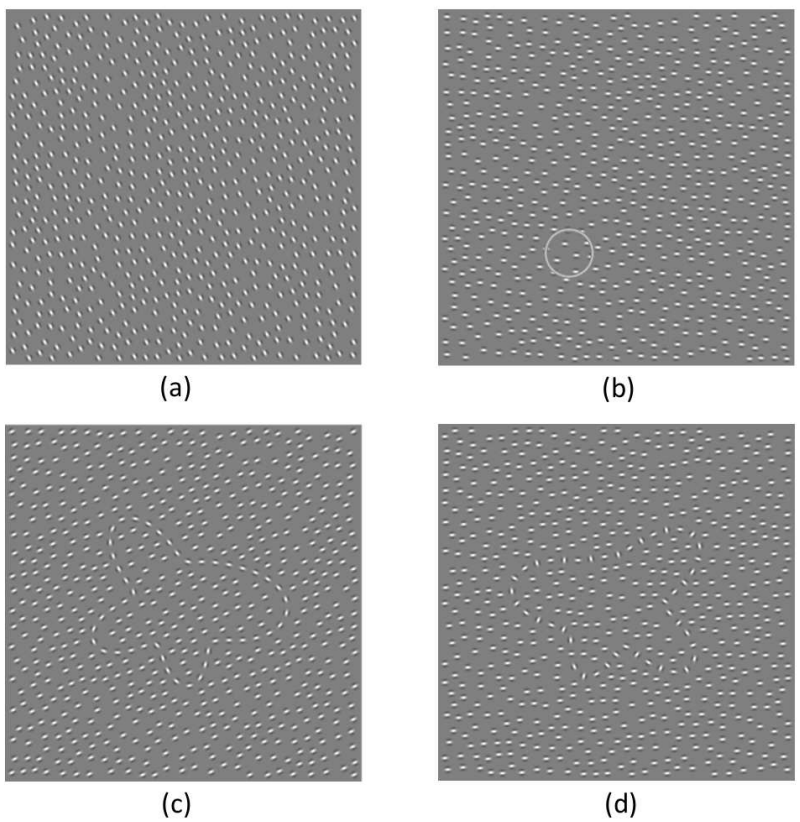

Figure 2.5: *Different types of stimuli used in the grouping task: (a) Non-structure stimuli; (b) Catch stimuli; (c) Global and local structure stimuli; (d) Global structure stimuli.*

The same task blocks were, however in a different order, used for every subject. As such, the total number of stimuli is equal for all subjects, yielding 500 trials for the version A task and 500 for the version B task, of which 8% were catch stimuli, 24% structure and 48% non-structure. The ISI varied between 2 and 2.4 seconds (in steps of 40 ms) and stimuli were shown for 200 ms.

2.2.2 Overview of acquired data

Because the detection and the Go/NoGo task were part of one study in which for several subjects both tasks were performed alternately, the subjects involved in this study and the resulting sets of data will be discussed together.

Study 1: Detection and Go/NoGo task

27 healthy subjects (11 female and 16 male, aged 18-44) with no history of neurological or cardiological disorders participated in this study. Written informed consent was obtained in accordance with the local ethical committee guidelines of the institution where the data were recorded. A detailed overview of the available datasets can be found in Table A.1 in the Appendix. As explained before, experiments were performed both inside and outside the MR scanner and in the former case, with and without simultaneous fMRI acquisition.

In total, there were fourteen subjects performing both the detection and the Go/NoGo task. Among these, five subjects performed the tasks in the three situations in Maastricht and in a simultaneous EEG-fMRI setting in Leuven while one subject was only measured in the three situations in Maastricht. Two other subjects did exactly the opposite, performing both tasks in three situations in Leuven and during a simultaneous experiment in Maastricht. For one subject a simultaneous and an outside experiment were performed in Leuven and for the five remaining subjects only simultaneous experiments were conducted, only in Leuven (one subject) or in both locations (four subjects). The remaining thirteen subjects just performed the detection task in Leuven. Ten of them were asked to perform this task twice, both simultaneously with fMRI and outside the scanner, the three remaining subjects were only measured in the simultaneous setting. Among these ten former ones, there were six for which the alternative version of the detection task was used (with higher ISI values).

Study 2: Grouping task

This study was performed in Leuven and only simultaneous EEG-fMRI data were acquired. 16 subjects (7 female and 9 male, aged 23-44) with no history of

neurological or cardiological disorders were included. Written informed consent was obtained in accordance with the local ethical committee guidelines. Four of the original 16 datasets had to be eventually discarded due to insufficient signal quality or problems during acquisition, resulting in 12 datasets for further analyses.

2.3 Conclusion

In this chapter, the simultaneous acquisition of EEG and fMRI was introduced by going deeper into the difficulties rising when acquiring EEG data inside the highly magnetic environment of the MR scanner. In addition, details were given about the datasets that were acquired in the course of this work. More specifically, a visual detection task, a Go/NoGo task and a grouping task were employed. For validation purposes, part of the subjects not only performed the tasks during simultaneous EEG-fMRI measurements, but also inside the MR scanner without fMRI and outside the scanner room. In the next chapters, the analyses performed on these different datasets will be discussed.

Chapter 3

Preprocessing of the data

This chapter aims at summarizing the most important preprocessing steps in both EEG and fMRI analyses. More specifically, for the EEG (Section 3.1), we go deeper into the removal of the gradient artifacts and the detection of the heartbeats from the ECG. The latter is important for the removal of the BCG artifacts, which will only be shortly discussed here, since it is the main topic of Chapter 4. In addition, the use of ICA for eye artifacts will be addressed. Next, Section 3.2 will shed more light on the preprocessing and standard statistical analysis of the fMRI data.

3.1 EEG preprocessing

As explained in Chapter 1, when acquired simultaneously with fMRI, EEG data are contaminated with both gradient and BCG artifacts. In addition, also eye movements can cause undesired EEG signal fluctuations. The origin and removal of these different kinds of artifacts will be discussed in this section and for BCG artifacts also further detailed in Chapter 4. A major part of the discussed preprocessing techniques is included in the EEGLAB toolbox [61] for MATLAB (The Mathworks Inc, Natick, Massachusetts, USA).

3.1.1 Gradient artifacts

First, the origin of the so-called gradient artifacts will be discussed based on [159, 200]. Next, several methods for its removal will be explained after which the approach adopted in this study will be illustrated.

Origin and characteristics

From Faraday's law of induction, it is known that a change in magnetic field will cause an electrical potential across a conductor subject to this field. The conductor can experience this magnetic change in two ways: either the magnetic field itself is modified or the conductor moves within the field. In the context of MRI acquisition, the presence of a time-varying magnetic field is inevitable. As explained in Section 1.1.3, the application of varying magnetic field gradients is essential for spatially encoding the MRI signals and RF pulses are used for spin excitation. Take this together with the conductivity of the leads, electrodes and other parts of the EEG equipment and the origin of so-called imaging artifacts becomes clear.

Two types of imaging artifacts can be distinguished: gradient and RF artifacts. The RF artifacts will, however, not further be discussed since they have much higher frequency than the EEG signals and will thus effectively be suppressed with the analog lowpass-filter explained in Section 2.1.2. As such, the major source of imaging artifact distorting the obtained EEG data, is the gradient artifact.

Gradient artifacts can have amplitudes 10 to 100 times larger than those of EEG signals and will therefore render any visual data inspection almost impossible. This is illustrated in Figure 3.1 showing a 5 seconds frame of simultaneously acquired EEG data on 62 channels. The artifacts follow the acquisition of each image slice (see the enlargement) and clearly obscure all underlying data. Furthermore, contrary to RF distortion, gradient artifacts occur at frequencies covering a broad frequency spectrum including the EEG's frequency range of interest (< 100 Hz). For this reason, simple lowpass-filtering will not suffice [3] and specific artifact correction techniques have to be applied.

Gradient artifact removal

The easiest way to overcome the problem of gradient artifacts in simultaneous measurements is to simply avoid the artifacts during certain periods of the acquisition. This can be achieved by using interleaved EEG-fMRI protocols, such as EEG-triggered fMRI (e.g., [181, 195, 216]) or periodic interleaved scanning (e.g., [86, 108, 120]). Nevertheless, although this kind of approaches can be useful for certain forms of brain activity, they are usually considered to be less flexible and less experimentally efficient than continuous measurements [159]. The latter implies, however, that gradient artifacts are present and need to be removed.

For this purpose, the most widely applied correction technique is the approach of average artifact subtraction (AAS) [3]. This method creates an artifact template for each channel by averaging consecutive artifact occurrences and subtracts the template from the data in this channel. This approach does not only assume that

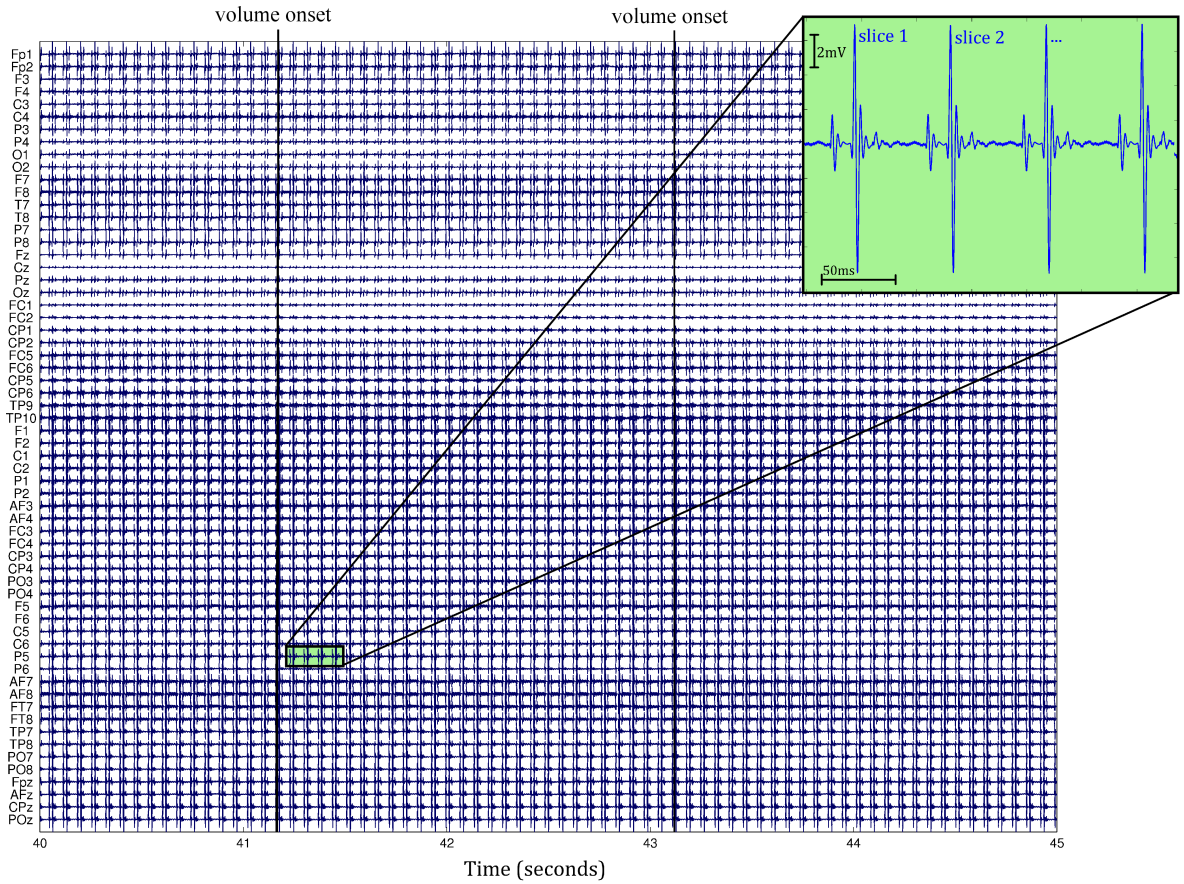

Figure 3.1: *Illustration of a short fraction of EEG data showing gradient artifacts, which can have amplitudes in the order of mV. The timing of the acquisition of each new volume is known and indicated on the data.*

the artifacts are linearly superimposed on the underlying data but also that their morphology and amplitude are similar over time. However, as mentioned above, the movement of a conductor within a magnetic field can cause additional potential changes. Although the subject's head is fixated and the subject is asked to move as little as possible, some small head movements are unavoidable. As such, random variations in the gradient artifact shape can occur and complicate the artifact correction [126, 159]. For this reason, several modifications of the AAS method have been proposed, mainly differing in the selection of artifact occurrences for the template and their weighting.

A simple adjustment of the AAS approach is to exclude outliers from the template construction based on a decreased correlation with an initial artifact shape [3]. In this way, single uncommon artifact occurrences cannot deteriorate the quality of the artifact template. In addition, the template can further be improved by using a moving average procedure thereby accounting for small but continuous alterations in the artifact's characteristics. This can be combined with a certain type of weighting, as also proposed in [3]. Weighting can, e.g., be based on exponential decay functions [15] or Fourier spectrum-based similarity measures [82]. Also the BrainVision Analyzer (BVA) software (BrainProducts, Munich, Germany) offers different template estimation methods, relying on moving averages or correlation-based artifact selection.

The above adaptations are, nevertheless, not sufficient in the case of abrupt head movements causing a sudden change in artifact properties [121]. For this reason, another modification of the template procedure has been proposed, in which realignment parameters from the fMRI analysis (for more information, see Section 3.2.1) are taken into account in the template creation. This realignment parameter-informed algorithm [156], freely available in the Bergen EEG-fMRI EEGLAB plug-in, avoids averaging over discontinuities in artifact properties.

Another important aspect for the template creation is that the onsets of the artifacts can be precisely located in time, in order to avoid systematic errors in the artifact template. Many acquisition setups, therefore, offer the possibility of saving the onset timings of each new volume acquisition together with the EEG data (as illustrated in Figure 3.1). However, in cases of asynchrony between the MR system and the EEG recording computer, some temporal jitter can still occur. To correct for this jitter, several techniques have been proposed. Possibilities are, e.g., upsampling the data combined with temporal alignment [15, 163] or selective average subtraction [88]. In [163], the artifact template is also refined based on principal component analysis (PCA), as to account for temporal variations in the artifact's shape. This algorithm is publicly available under the name of fMRI artifact slice template removal (FASTR) as a part of the FMRIB plug-in for EEGLAB. In addition, also software solutions exist for cases where no volume onset information is available. An automatic detection of these volume onsets can be performed with the BVA software or with the above-mentioned Bergen plug-in

[156]. Nevertheless, correction for temporal jitter becomes less important with synchronization, as explained in Chapter 2.

Regardless of the applied artifact correction technique, residual artifacts might still contaminate the EEG data. One solution for this, is the use of ICA to separate the artifacts from the brain signals [139]. Also PCA [161, 163], adaptive noise cancellation (ANC) [3] and spatial beamformer techniques [27] have been investigated for the same purpose. Moreover, although the objective of this section is not to list all possible methods for gradient artifact removal, we do want to mention some alternatives for the widely used template subtraction, more relying on frequency characteristics. In this light, in [188, 212], adaptive filters were used but also comparing the frequency content in simultaneous and non-simultaneous measurements is possible [97]. A completely different approach has been proposed by Anami et al. [5], who adapted the fMRI sequence parameters such that the gradient artifacts would be minimized at the time instants where the EEG data are sampled.

The current study employs the AAS method based on a moving average including 25 volumes as implemented in the Bergen EEG-fMRI EEGLAB plug-in [156]. An example of the same portion of EEG data as in Figure 3.1 after the application of this method is given in Figure 3.2.

From this figure it is clear that some high frequency residuals remain after artifact correction. For this reason, a lowpass-filter at 30 Hz is applied to the data. This is combined with a highpass-filter at 1 Hz, as to avoid slow drifts in the data. Next, since the high sampling rate was only necessary to capture the gradient artifacts which have now been removed, the data are downsampled to 250 Hz. The result of the filtering and downsampling is shown in Figure 3.3, again on the same piece of data as before.

3.1.2 Heartbeat detection

More than standard EEG studies, combined EEG-fMRI measurements strongly benefit from the simultaneous acquisition of ECG data. The reason for this can be found in the second major artifact present in simultaneously acquired EEG data, namely the BCG artifact. As will be explained in more detail in Chapter 4, this artifact is caused by subtle head movements related to the cardiac cycle. For this reason, in most cases, its removal requires knowledge about the occurrence of consecutive heartbeats in the ECG. The detection of these heartbeats will be explained in this section, based on the method proposed in [163] and implemented in the EEGLAB FMRIB plug-in. Also a small improvement of the applied correction procedure will be discussed, together with some practical guidelines to apply the method.

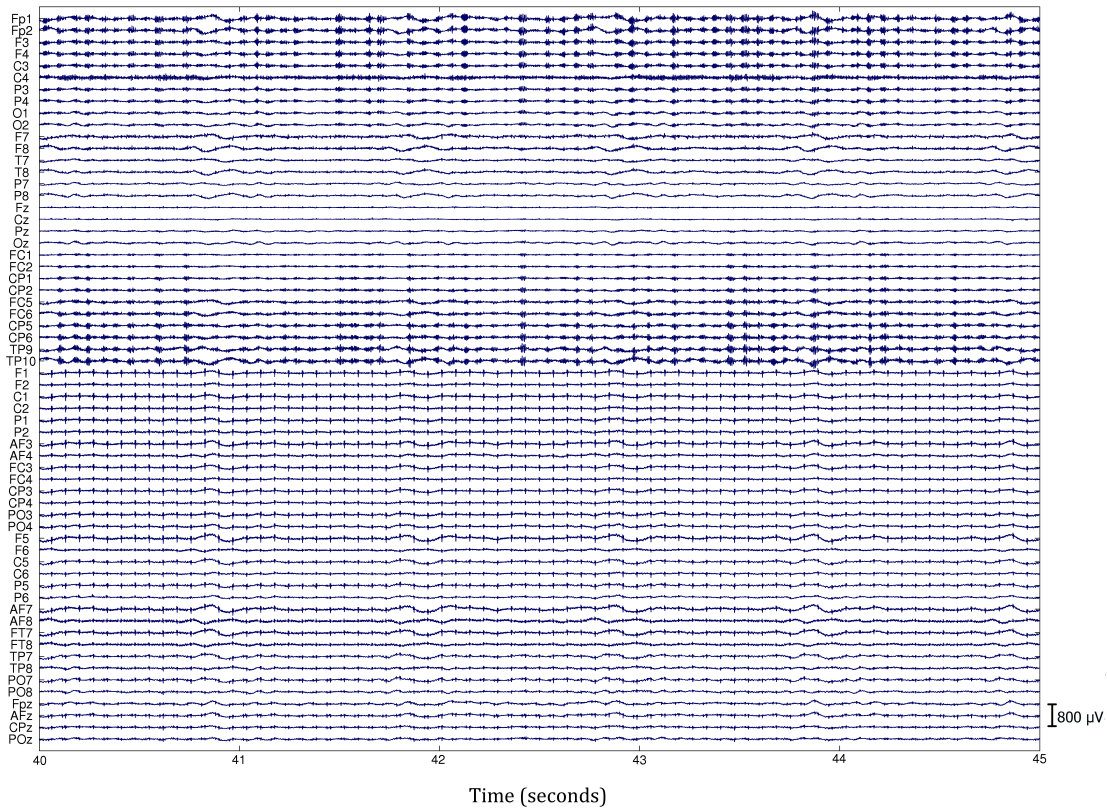

Figure 3.2: *Illustration of a short fraction of EEG data after removal of the gradient artifacts with the Bergen EEG-fMRI toolbox. Amplitudes have clearly reduced compared to the originally acquired data but some high frequency residuals are still present.*

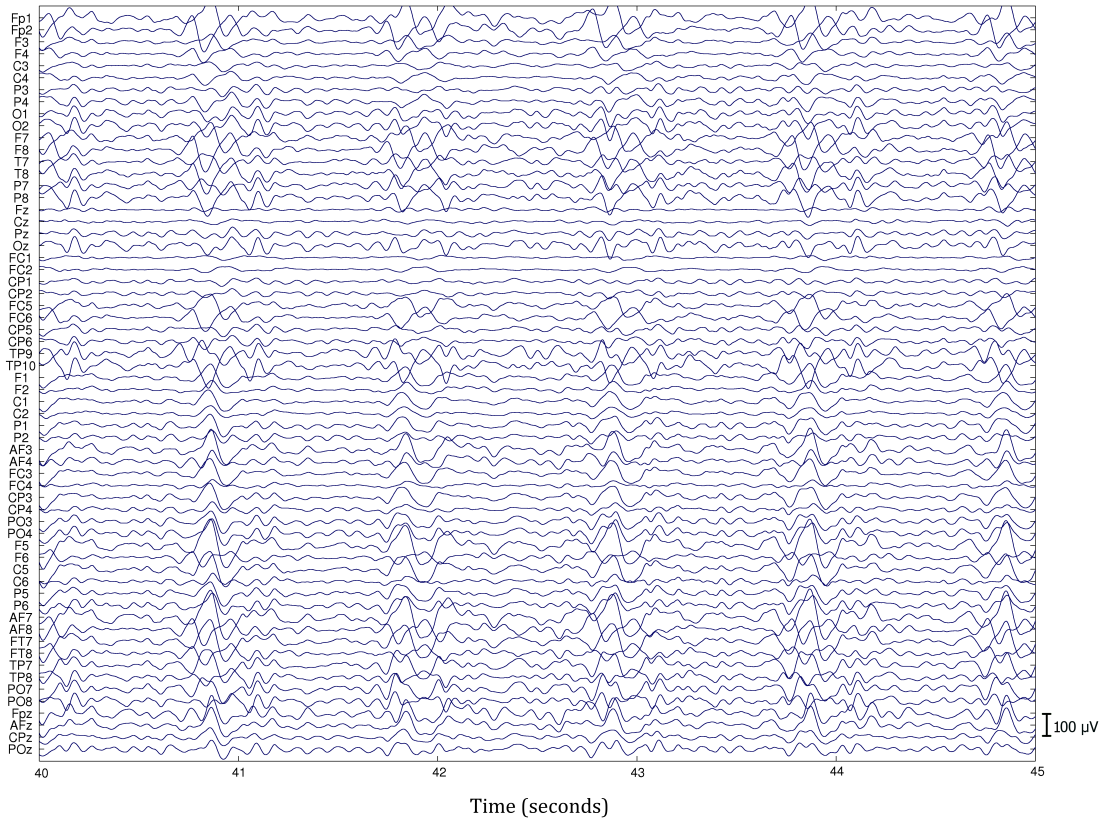

Figure 3.3: *Illustration of a short fraction of EEG data after removal of the gradient artifacts with the Bergen EEG-fMRI toolbox and filtering between 1 and 30 Hz. The additional filtering removed the high frequency residuals of the gradient artifacts.*

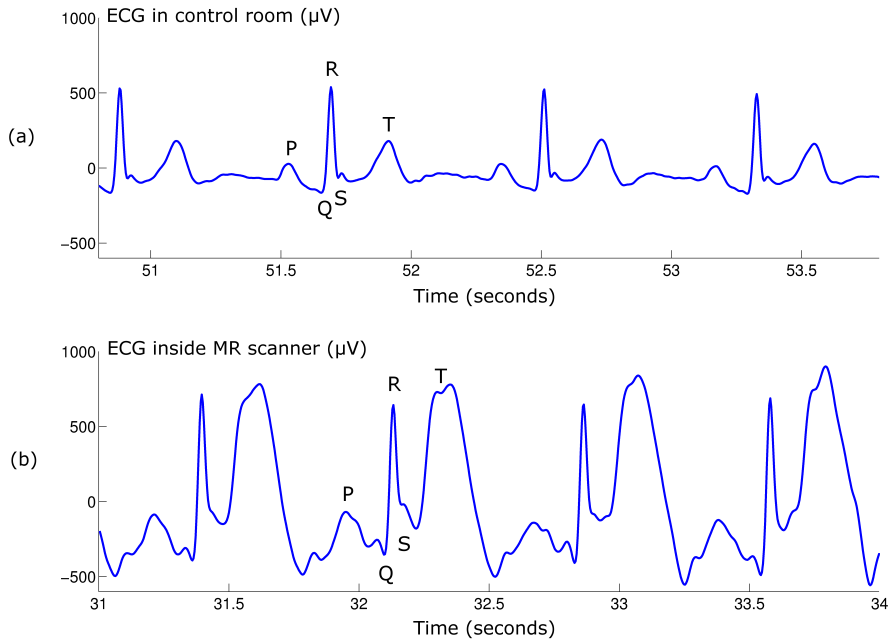

Figure 3.4: *Illustration of a short fraction of ECG data measured in normal circumstances (a) and inside an MR scanner (b). In both cases, the names of the typical deflections are indicated on the ECG trace.*

Apart from the FMRIB toolbox, also other software solutions, such as BVA, provide ways to perform the heartbeat detection. The FMRIB toolbox is, nevertheless, widely used since it is freely available and easy to use. For this reason, it is also the method used in this work, but we would like to make clear that we do not claim that the other methods would not suffice.

Detection and correction of QRS events with FMRIB toolbox

Exactly like the EEG measuring the electrical activity of the brain, the ECG represents the electrical activity of the heart. A typical ECG signal shows for each cardiac cycle a number of deflections, named with the letters P to T. An example of such an ECG signal acquired in the scanner control room is shown in Figure 3.4(a). The P wave, the Q, R and S waves composing the QRS complex and the T wave are indicated in this figure. Detecting the heartbeats from the ECG data usually comes down to the detection of the R peaks or QRS complexes.

ECG acquired inside the MR scanner, however, shows a somewhat different time course as can be seen in Figure 3.4(b). The most apparent difference between this ECG trace and a normal ECG is the augmented T wave caused by the conductivity of blood [217]. For this reason, simple thresholding methods or typical QRS detection algorithms like Pan-Tompkins [171], cannot be used. The QRS detection method in the FMRIB plug-in [163] is therefore based on combined adaptive thresholding [35] and a Teager energy operator [114].

The method can be summarized as follows. After filtering the ECG data, a so-called complex ECG lead is constructed by applying the k-Teager energy operator. As such, a specific frequency, in this case the 10th harmonic of the heartbeat frequency, is emphasized. Next, three thresholds M, F and R are computed from this lead and QRS peaks are detected whenever the amplitude exceeds the sum of these three thresholds. Further details can be found in [35, 163].

In addition to this optimized QRS detection, the FMRIB plug-in also includes several steps to correct the obtained QRS timings. Both false positives and false negatives are taken care of by searching for respectively too short or too long RR intervals (time between two consecutive R peaks). Moreover, the QRS complexes around the obtained onset timings are also aligned based on a correlation with an average QRS segment. This alignment is performed twice, but in both cases with the original average QRS shape as template.

Improved version of correlation-based QRS correction

Despite the high specificity and sensitivity values presented in [163], for several datasets in the current work, the above explained correction procedure did not seem to correct all mistakes in the QRS detection. More specifically, artifacts were still partly misaligned, possibly indicating some minor shortcomings in the correlation-based alignment approach.

After closer inspection of the obtained misalignments, two problems were identified. First, the alignment proposed in [163] is only based on the ECG lead. Even when the ECG electrode is carefully placed, it is still possible that its quality is far below that of the other channels. This is illustrated in Figure 3.5(a), showing a short fragment of ECG data of which the quality is obviously lower than the one shown earlier in Figure 3.4(b). A second problem might be the fact that an average template is used for the correlation and that this template is not updated in between the two alignment steps. In cases where many QRS onsets are misaligned, the average template will be more smoothed and, as such, less representative for the individual QRS events.

In this thesis, an improved version of the correlation-based correction is therefore applied. This version not only allows including other channels than the ECG in

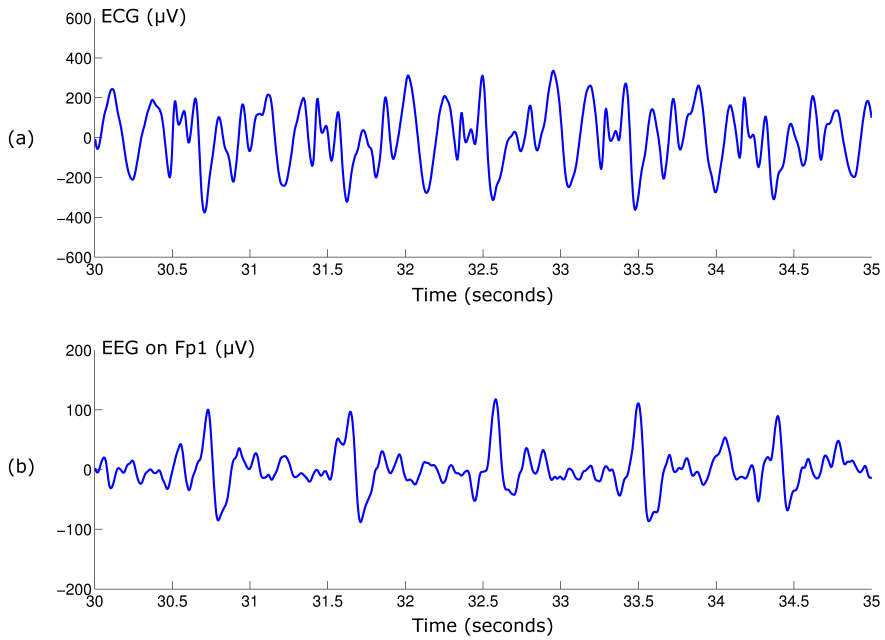

Figure 3.5: *(a) Illustration of a short fraction of ECG data measured inside the MR scanner after removal of the gradient artifacts. On this ECG trace the heartbeats are difficult to distinguish; (b) EEG signal on channel Fp1 measured simultaneously, after removal of the gradient artifacts. On this trace the cardiac cycle is easier to follow.*

the correlation procedure, but also provides the possibility of using specifically selected individual artifact or QRS occurrences for the template. The benefit of not only relying on the ECG channel becomes clear from Figure 3.5(b) where the EEG is shown on channel Fp1, with the cardiac rhythm being much more apparent than on the ECG signal above.

Figure 3.6 shows the effect of the proposed modifications on a five seconds data fragment measured simultaneously with fMRI (after the removal of the gradient artifacts and consecutive filtering). Although the QRS complexes can hardly be distinguished in this ECG, the occurrence of new heartbeats is still clear and it can be seen that the original detection (Figure 3.6(a)) shows several misalignments. After applying alignment, based on correlating the artifact occurrences with one selected occurrence in all channels, the misalignments are, however, solved.

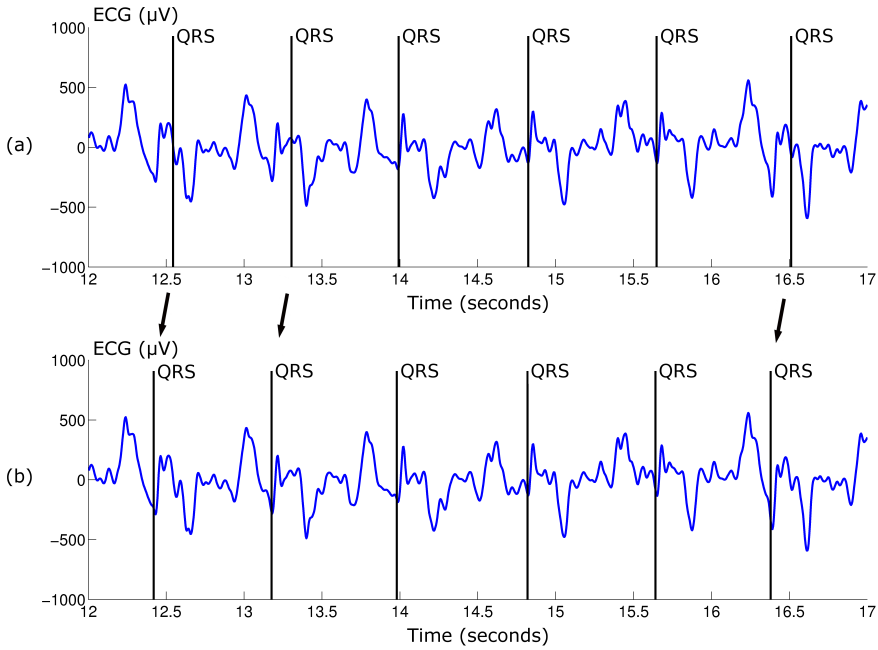

Figure 3.6: *(a) Five seconds fragment of ECG data with marks corresponding to detected QRS complexes obtained with the FMRIB toolbox. Half of the detections in this data piece are differently aligned compared to the other half; (b) Same ECG fragment with new QRS timings obtained by following the step-by-step correction procedure.*

Step-by-step guide for obtaining correct QRS detection

In the course of analyzing different datasets with the FMRIB QRS detection algorithm, not only misalignments occurred, but also other problems arose, such as missing and redundant detections. For this reason, from experience gained during the processing of the datasets included in this work, a step-by-step guide for obtaining a correct QRS detection was constructed. The different steps are relatively simple, but the presented schedule proved to be a useful checklist, especially for researchers with less experience in the field. Nevertheless, as explained above, also other software solutions, such as BVA, exist, but the step-by-step guide presented here, is tailored to the application with the FMRIB plug-in.

The different steps to be followed, are illustrated in Figure 3.7. First, the FMRIB plug-in is applied as recommended in the accompanying manual. This means that the ECG channel is identified and used for QRS detection and correction, as explained earlier in this section. A first visual check of the resulting detections

is performed. If the detection appears to be bad due to a low quality ECG measurement (e.g., more than 20% of the QRS complexes is wrongly detected), the initial application of the algorithm can be repeated with one of the EEG channels as input.

A next, more detailed, visual inspection aims at identifying problems for individual QRS occurrences. Very useful for this purpose is to additionally check the course of consecutive RR intervals, which can be plotted for each dataset separately. If missing QRS events are observed, these events can be added either manually or via an automatic approach based upon the mean RR distance. Redundant QRS peaks can also occur and need to be removed. Further, misaligned detections can be corrected for, based on our improved QRS correction procedure.

Following this step-by-step guide, the subsequent BCG removal step becomes more efficient. This is demonstrated in Table 3.1. After the QRS detection, the Optimal Basis Set (OBS) method from this same FMRIB toolbox [163], is applied to remove BCG artifacts (more information about this method will be given in Chapter 4). The quality of the obtained datasets is then assessed by determining the number of task-related data segments that remain after thresholding. This thresholding is performed at 50, 100 and 150 μV.

The number of available segments after thresholding at 50 μV is significantly better in the case with additional QRS correction compared to the case without (p-value of Wilcoxon signed rank test = 0.00001). Also at 100 μV and 150 μV there is a significant increase in number of segments (respectively $p = 0.00015$ and $p = 0.029$). As such, we can conclude that the improved QRS correction method together with the step-by-step procedure for optimizing the detection, improves the quality of the resulting datasets.

3.1.3 Removal of ballistocardiogram artifacts

The ballistocardiogram or BCG artifact is the second type of artifact that typically occurs during simultaneous EEG-fMRI measurements. This artifact is related to the cardiac cycle and is encountered whenever a (large) constant magnetic field is present. This is the case in the MR scanner, even when no fMRI data are acquired. As such, also in interleaved EEG-fMRI protocols, this artifact would contaminate the data.

Since the origin of this artifact is still a matter of investigation and its removal is considered to be more complicated than that of the gradient artifact, the BCG artifact will be discussed in more detail in Chapter 4.

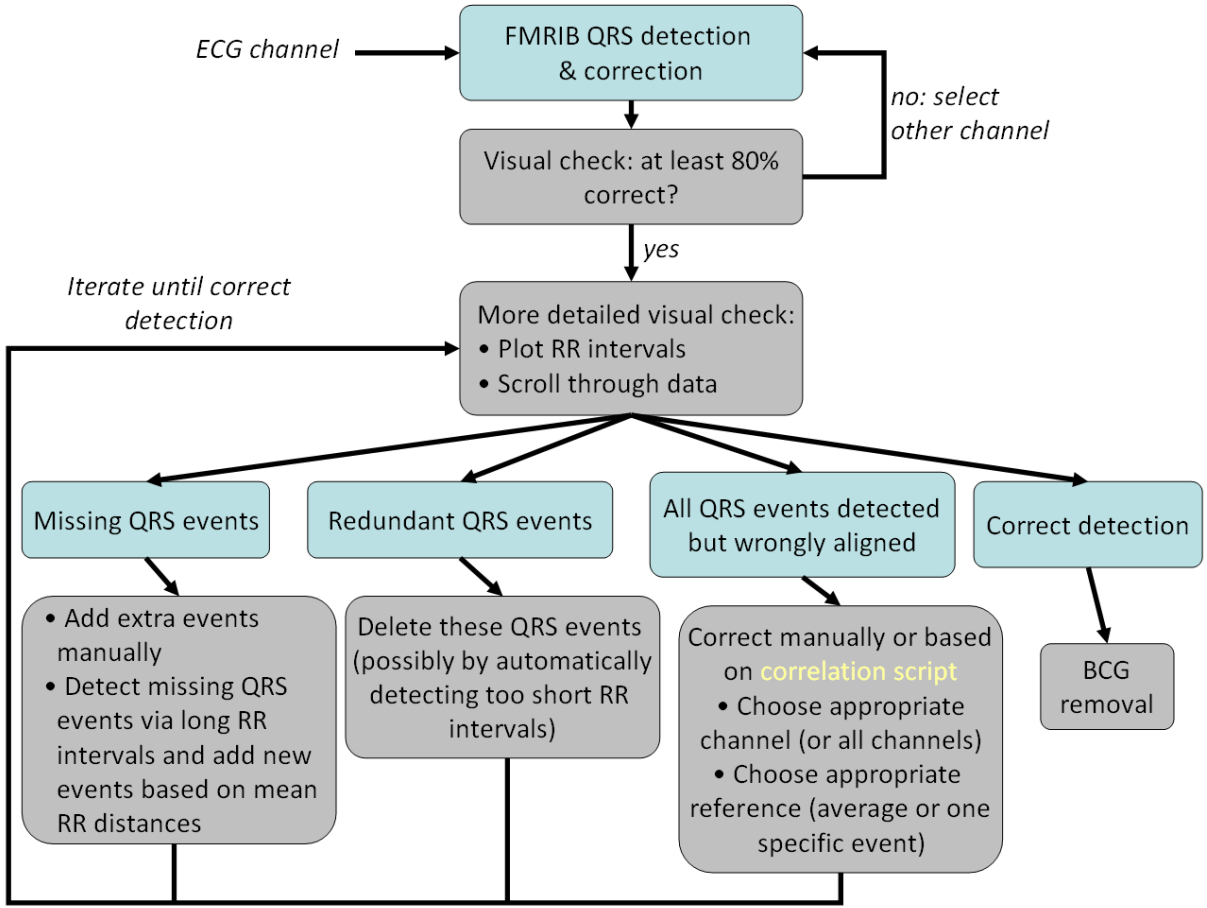

Figure 3.7: *Step-by-step procedure to improve the QRS detection obtained with the FMRIB plug-in.*

Table 3.1: *Comparison of number of segments that remain after thresholding between data of which BCG artifacts have been removed based on the FMRIB plug-in and data of which the QRS detection has been improved with the above explained procedure and additional correction. Three thresholds are investigated: 50, 100 and 150 μV.*

Subject	Number of segments						
	Total	Without correction			With correction		
		50μV	100μV	150μV	50μV	100μV	150μV
1	400	146	344	371	166	358	379
2	400	128	331	370	175	338	370
3	400	0	326	394	0	325	396
5	400	143	328	380	166	328	380
6	400	117	382	397	145	388	398
7	400	155	347	382	168	350	382
8	400	310	389	394	315	389	397
9	400	198	363	391	202	364	390
10	400	330	387	394	339	388	393
11	400	176	377	398	201	384	397
12	400	237	364	388	239	366	390
13	400	222	378	393	237	381	393
14	420	268	405	412	294	408	412
15	420	379	420	420	390	420	420
16	420	34	307	384	66	348	399
17	420	366	410	417	372	412	417
18	420	268	377	406	278	380	407
19	420	139	370	414	176	389	413
20	400	201	393	397	206	393	397
21	400	250	384	398	281	389	399
22	400	150	373	390	165	374	392
23	400	344	395	400	346	395	400
24	400	312	380	393	334	382	395
25	400	237	390	398	238	396	400
26	400	255	380	396	260	381	396
27	400	224	361	378	229	360	376
Mean	405	230	371	394	246	376	396

3.1.4 Use of independent component analysis

The technique of ICA has already been mentioned several times in the previous chapters, e.g., for the analysis of fMRI data or as a part of specific EEG-fMRI integration approaches. ICA is also widely used for the removal of different kinds of artifacts, since it is known to allow the separation of data into its underlying sources, in this case, both brain and non-brain sources. One possible application of ICA in this context, is the removal of (residual) BCG artifacts. As these artifacts are discussed in more detail in Chapter 4, also the application of ICA for this purpose, will be addressed there.

Another possibility of ICA, is the removal of eye artifacts. These artifacts are caused by eye blinking and horizontal and vertical eye movements and are most pronounced on frontal EEG channels, which is obvious since these are closer to the eyes. An example of a fragment of EEG data showing many eye artifacts, is shown in Figure 3.8(a). Several studies have demonstrated the usefulness of ICA for the removal of these artifacts [112, 145]. In this work, the ICA algorithm JADE is applied to the data (more information on different ICA algorithms will be given in Chapter 4). The temporal and spatial patterns of the sources are then visually inspected and compared to the EOG trace. A "clean" EEG signal is obtained by reconstructing the data without the eye-related sources, as shown for the same EEG fragment in Figure 3.8(b).

3.2 fMRI analyses

Chapter 1 (Section 1.1.3) already addressed some difficulties when searching for activated brain regions, based on fMRI data. These difficulties are related to the fMRI's low signal to noise ratio (SNR). For this reason, careful preprocessing and further statistical analyses are needed to retrieve the spatial activations. In this work, fMRI analyses were performed with the statistical parametric mapping software (SPM5, Wellcome Department of Cognitive Neurology, London, UK). The specific analysis steps (illustrated in Figure 3.9) are briefly discussed in this section. For more details, the reader is directed to [84].

3.2.1 Preprocessing of the fMRI data

Because statistical parameter mapping (SPM) is a voxel-based method, it is possible that unwanted variance components in the voxel time-series compromise the effects of interest. Such variance can, e.g., be related to movement, causing a voxel to be connected to different brain regions in the course of the measurements. The aim of fMRI preprocessing is, therefore, to reduce this undesired variation in

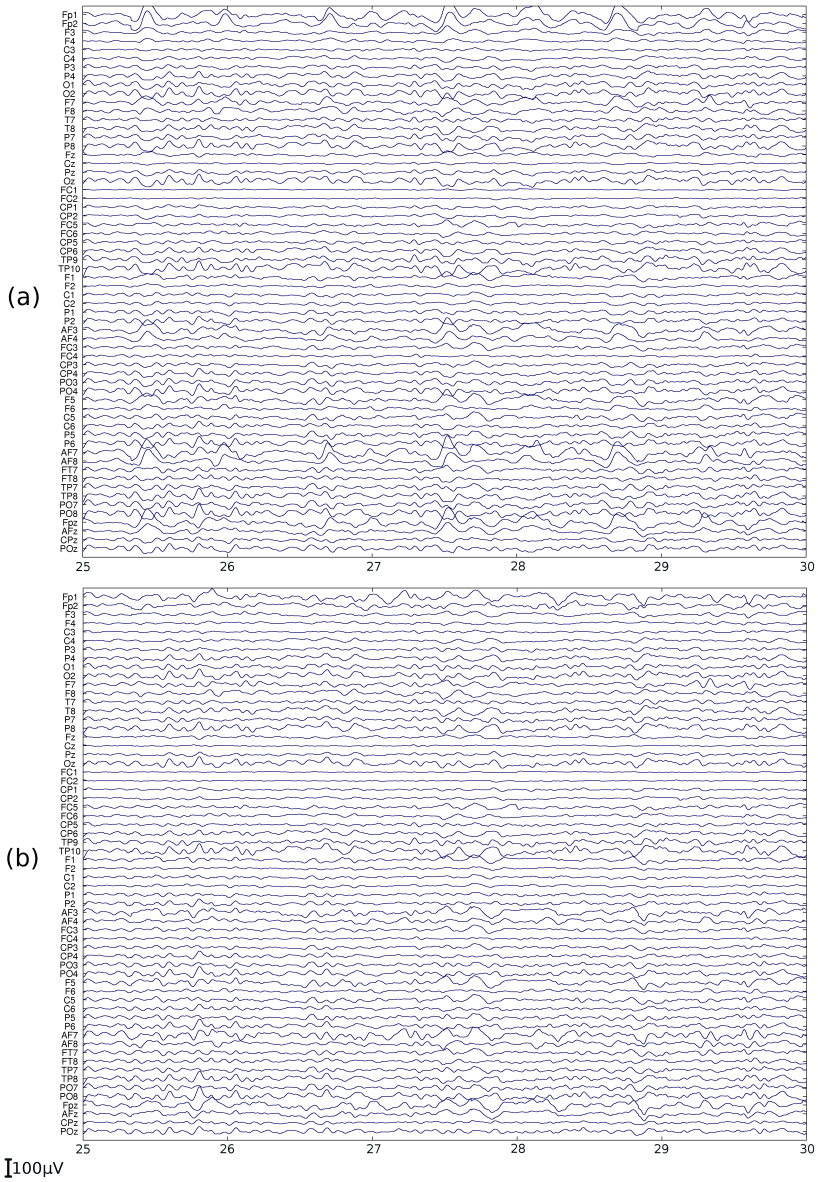

Figure 3.8: *(a) Five seconds fragment of 62 channel EEG data with clear eye artifacts mainly present on frontal channels; (b) Same EEG fragment after reduction of the eye artifacts with ICA.*

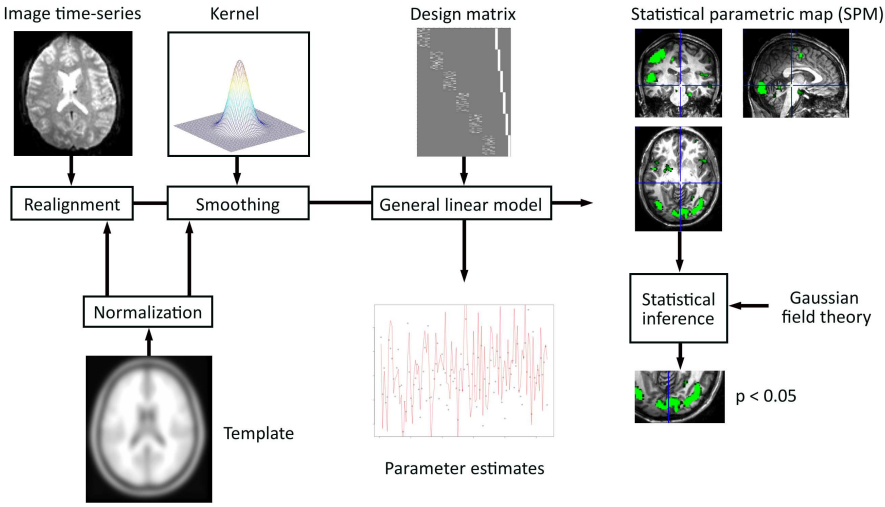

Figure 3.9: *Schematic representation of analysis steps that need to be followed to obtain a quantification of activated brain regions, based on raw fMRI images (based on [84]). The images are first slice-time corrected (not shown), realigned and co-registered with their anatomical image. Subsequently, normalization is applied by aligning the images to a template and finally the images are smoothed based on a Gaussian kernel. To analyze the fMRI data, a general linear model is constructed and fitted to the data. Applying statistics to the resulting parameter estimates, yields so-called statistical parametric maps which can be thresholded to investigate the activated brain regions in detail.*

the fMRI signals. The different steps to be taken for this purpose, are explained in this section.

Slice time correction

The acquisition of one complete fMRI volume requires the successive acquisition of a specific number of slices. This means that differences in slice acquisition time occur, or, in other words, that not all slices per brain volume are obtained at exactly the same time stamp. To correct for these differences, all slices are temporally realigned to one selected time point (via interpolation), a process called slice time correction. In the current work, the first slice is chosen as reference time point.

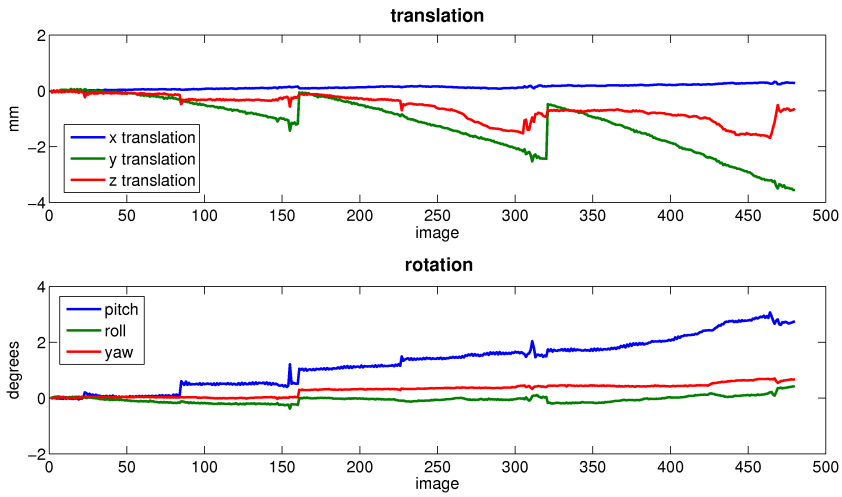

Figure 3.10: *Evolution of the six spatial realignment parameters used for movement artifact correction of the fMRI data. Both the three parameters for translation and the three for rotation, are shown.*

Spatial realignment

As already addressed in Section 3.1.1, even when all measures are taken against head motion, displacements up to several millimeters can still occur. These displacements can cause voxels to exhibit unwanted changes in signal intensity over time and have thus to be corrected for. This correction is called spatial realignment and is performed as follows. First, six parameters of an affine (rigid body) transformation, mapping all successive scans to one specific reference scan, are calculated. In our study, the first scan is chosen as reference scan. The exact estimation of the six movement parameters can be found in [84], but shortly said, an iterative least squares approach is used. Next, the transformation is applied via resampling based on interpolation. Figure 3.10 shows the evolution of the six realignment parameters (three for translation, three for rotation) over scans. These same realignment parameters are the ones included in the realignment-informed gradient artifact removal in the Bergen toolbox (see earlier in Section 3.1.1).

Co-registration

Since it is useful to visualize the activations that can be obtained with fMRI data by overlaying them onto the anatomical brain images, functional and anatomical images have to be co-registered. This is necessary, not only because both types of

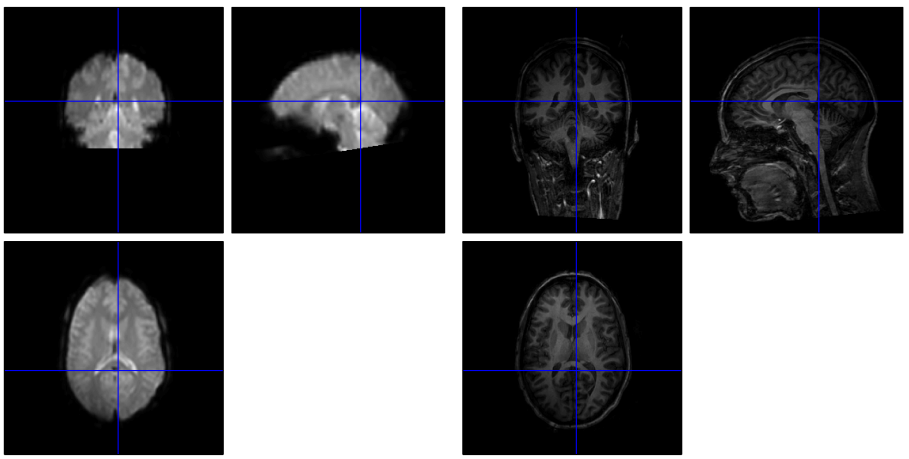

Figure 3.11: *Illustration of the correspondence between functional (left) and anatomical (right) images after the application of co-registration.*

images have a different resolution, but also because they are acquired in separate scans and subjects might have moved in between. A rigid-body transformation is used for co-registration, including three translations and three rotations along the different axes. This transformation is estimated by maximizing the mutual information between both image types. An illustration of the images after co-registration, is given in Figure 3.11.

Normalization

Human brains differ in size and shape. As such, it is understandable that one location in one subject's brain image does not necessarily correspond to the same location in another subject's brain image. However, in order to compare data from several scans and subjects, all acquired images have to be in the same three-dimensional space. For this reason, SPM includes a step called spatial normalization, in which the obtained images are mapped into a certain standard space. In the current work, this space is defined by the Montreal Neurological Institute (MNI) template. The MNI template is defined as a representation of a standard brain, generated by using MRI scans from a large number (> 150) of normal young controls. An illustration of this MNI template together with an anatomical image normalized correspondingly, is shown in Figure 3.12.

Normalizing the images to this template, is performed by minimizing the sum of squares of their difference. For this purpose, a 12-parameter affine transformation and a number of nonlinear deformations are combined. In fact, for both this

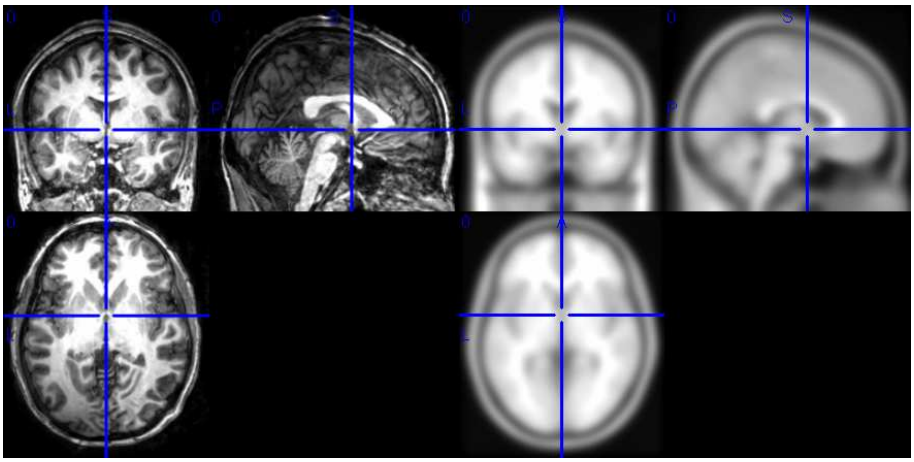

Figure 3.12: *Illustration of an anatomical MNI template (right) and an acquired anatomical image, normalized to this template (left).*

step and the previous step of co-registration, the transformation parameters are estimated for the average functional image (obtained in the realignment step) and only afterwards applied to all individual images.

Spatial smoothing

In order to suppress noise and effects related to residual differences between functional and anatomical images and across subjects, the last preprocessing step applied to fMRI data, is usually spatial smoothing. It is also used to enhance the correspondence between neighboring voxels, in order to facilitate subsequent statistical analyses (see below). Smoothing is achieved by convolving the images with a Gaussian kernel (see illustration in Figure 3.9) of a specified width. The width is characterized by the full width at half maximum (FWHM) and is chosen according to the shape of the expected signal change. Here, this parameter is set to 6 millimeters (in each direction).

3.2.2 Statistical analyses

The aim of statistically analyzing the preprocessed fMRI data, is to identify voxels showing a significant change in oxygenation over time. As such, brain regions activated by the process or stimulus under study, are obtained. As already mentioned in Chapter 1 (Section 1.1.3), the statistical analysis used in SPM for

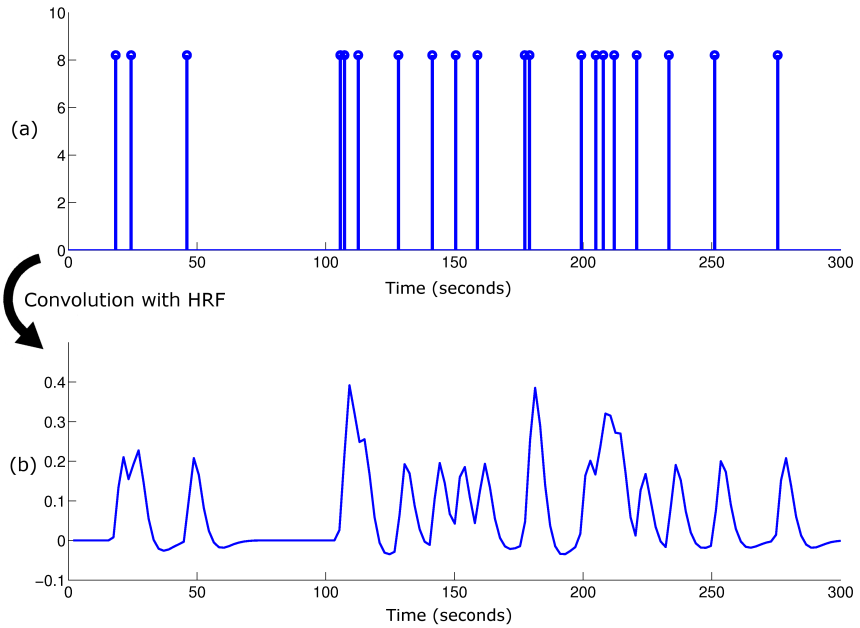

Figure 3.13: *(a) Illustration of a stick-function corresponding to the upper-left stimulus in one task block of the detection task. The values at the onsets of the stimuli are multiplied with a fixed scaling factor; (b) Result of the convolution of this stick-function with an HRF model.*

fMRI data is a mass-univariate approach based on a general linear model (GLM). The different steps that have to be taken, will now briefly be explained.

First, a design matrix is specified in which information about the experimental design and the variables of interest, is stored. More specifically, this matrix comprises one row per scan and one column for each regressor or stimulus function. For event-related designs, as is the case in this work, stimulus functions are usually constructed as stick-functions, having ones at stimulus onset times and zeros otherwise. These stick-functions are then convolved with a model for the HRF. An example of such a stick-function and the result after convolution, are shown in Figure 3.13.

Next, a GLM is created based on the design matrix and fitted to each voxel separately using classical or Bayesian approaches. The GLM is defined as $\mathbf{Y} = \mathbf{X} \cdot \boldsymbol{\beta} + \mathbf{U}$ with $\mathbf{Y}$ the data, $\mathbf{X}$ the design matrix and $\mathbf{U}$ the model error or noise. $\boldsymbol{\beta}$ contains the model parameters which are estimated during the fit and are a measure for the "goodness of fit" of the model. In other words, if the signal

change in a voxel is related to a certain stimulus, then a model based on this stimulus will show a higher estimated β value in this voxel.

Finally, the obtained β values are statistically evaluated based on, e.g., t-tests for each voxel. These t-tests will compare the β values with the uncertainty on their estimation and, as such, decide whether they are significantly different from zero. The resulting maps are the so-called statistical parametric maps. The t-tests do not only allow assessing the relation between the data and a certain stimulus, but also whether one stimulus is more relevant for a certain voxel than another. To identify the activated brain regions, the statistical maps can be thresholded, but given the large number of voxels, a correction for multiple comparison is needed.

3.3 Conclusion

The aim of this chapter, together with the next chapter addressing the issue of BCG artifacts more in detail, consisted in "preparing" the EEG and fMRI data for further analyses. More specifically, for EEG, the different preprocessing steps have been discussed. These included the removal of the scanner-related artifacts, i.e., the gradient and BCG artifacts (see also Chapter 4), and the reduction of possible eye artifacts. In the context of BCG artifact removal, it is also useful to retrieve the onsets of the heartbeats from the ECG signal. For this purpose, an improvement of an existing QRS detection approach together with a number of practical guidelines has been presented.

For the fMRI data, first the different preprocessing steps have been discussed, in which undesired fluctuations in the signal intensity in specific voxels were corrected. This was done with the SPM5 software, allowing the EPI time series to be slice-time corrected, realigned, co-registered with anatomical images, normalized to a template and smoothed with a 6-mm FWHM Gaussian kernel. Next, the statistical analyses necessary for obtaining the activated brain regions, were introduced. The relation of the signal change in each voxel to the stimulus or process of interest, was investigated with statistical parametric maps based on a general linear model.

Chapter 4

Removal of ballistocardiogram artifacts

This chapter addresses the issue of the ballistocardiogram artifact. In particular, Section 4.1 will first describe the origin and characteristics of this artifact after which the most important methods that have been proposed for its removal, will be explained. Next, Section 4.2 will go deeper into the BCG removal methods that have been investigated in this work and the validation criteria that are used to assess their performance. The results of these analyses will be summarized in Section 4.3 and further discussed in Section 4.4. To end, Section 4.5 will give some conclusions.

4.1 Introduction

Besides the gradient artifact, another type of scanner-related EEG distortion has already been mentioned several times in the previous chapters: the ballistocardiogram or BCG artifact. Figure 3.3, showing EEG data after the removal of the gradient artifacts and successive filtering, already gave an idea on how this artifact could look like.

In this section, the origin and characteristics of the BCG artifact will shortly be discussed and the motivation behind the BCG removal study performed in this chapter will be explained, based on the state-of-the-art of BCG removal methods.

4.1.1 Origin of the ballistocardiogram artifact

Despite almost two decades that have passed since the first observations of a heartbeat-related artifact in EEG recordings inside an MR scanner [108], the origin of this artifact is still under discussion. Nevertheless, several hypotheses have been formulated of which, according to [55, 222], the following three are the most plausible.

First of all, a subject lying supine in an MR scanner, will experience axial body motion due to the acceleration and abrupt reversal of blood flow in the aortic arch [6, 103, 160]. This motion will cause a "nodding" head rotation and, as such, a movement of the electrodes and wiring within the magnetic field. Recalling Faraday's law of induction (cf. Section 3.1.1), we know that such movement of conductive material in the magnetic field can give rise to electrical potentials.

Second, another possible mechanism behind the BCG artifact, is the pulsatile movement of the scalp caused by the expansion and contraction of adjacent blood vessels [55]. This scalp movement will cause the electrodes and cables to move, thereby also inducing voltage changes according to Faraday's law.

Third, since blood itself is a conductive material, a phenomenon called the Hall effect, can also play a role in the generation of BCG artifacts. The Hall effect is the production of a voltage difference across a conductor, carrying an electrical current within a magnetic field. As such, the movement of blood in certain blood vessels can induce electrical potentials, picked up by electrodes close to these vessels [3, 197].

Only a limited number of studies have investigated the validity of the above hypotheses in detail. Debener et al. [55, 159, 200] performed an experimental study based on a spherical phantom simulating both axial head rotation and lateral electrode expansion, the latter using inflating balloons. In [222], on the other hand, analytic expressions and simulations based on a physical model of BCG sources were proposed, focusing on head rotation and the Hall effect related to blood flow. Despite the different nature of these studies, their outcomes were to a large extent similar. Axial head rotation was found to be the dominant cause of BCG artifacts, explaining most of their spatial variability. Nevertheless, the other two possible sources, related to localized scalp movements and the Hall effect, were also thought to contribute, albeit in smaller proportions. The interaction between these two sources and the major contribution of head rotation is, however, not clear, since not enough is known about their temporal behavior. For this reason, further studies are needed to reveal the complete BCG origin picture.

It has to be noted here, that ballistocardiography is in fact the name for techniques measuring body movements in relation to the heartbeat [64]. The name was adopted for cardiac-related movement artifacts in EEG data in [174]. Since the

studies initially reporting about the heartbeat-related artifact inside magnetic fields, interpreted them as caused by blood flow-related body motion [103], the term BCG was also adopted here. Several authors, however, prefer to use a name which does not exclude other mechanisms behind the artifact and, therefore, call it the pulse artifact (e.g., [4]).

4.1.2 Characteristics of the ballistocardiogram artifact

Related to its complex and yet not fully uncovered origin, the morphology of the BCG artifact also shows a rather complicated dynamic behavior. Nevertheless, the artifact's synchrony with the cardiac rhythm, allows an easy identification of its occurrence within the EEG data. In this section, some of the temporal, spatial and spectral characteristics of the BCG artifact will be discussed and illustrated. Since the artifact is also visible in the absence of fMRI acquisition, two EEG datasets measured non-simultaneously inside the MR scanner, were used for this purpose.

To study temporal characteristics, the filtered EEG data were segmented based on the QRS peaks (detected on the ECG channel with the algorithm explained in Chapter 3) and averaged over these segments per channel. The obtained signals are shown for two subjects and channels FC3, AFz, F4, C6, F1, AF4, FC6 and CP4 in Figure 4.1 with an average reference. From this figure, it becomes clear that the artifact's shape and amplitude do not only differ between channels but also between subjects (see full and dashed lines). This is consistent with the description of the BCG's characteristics in [159, 200]. In addition but not shown in this figure, it should be noted that the amplitude of the artifact can also change slightly over time.

The spatial variation of the BCG artifact is represented by means of the topographical distribution of the intensity of the BCG-related segments at specific latencies. To this end, the same averaged BCG segments as explained above, are used. In Figure 4.2, the potential distribution of the amplitude of these BCG segments at latencies of 200 (a), 350 (b) and 500 ms (c) is shown. In correspondence with [56], an opposite polarity at the two sides of the head, is observed, reversing polarity in the course of the artifact.

In the frequency spectrum, the artifact causes a peak at the heart rate frequency and at several harmonics. In Figure 4.3, the normalized power spectral density on channel Fp8 is shown for a subject with a heart rate frequency of around 0.85 Hz. The peaks at this frequency and at several higher harmonics are clearly visible. Several of these frequencies overlap with the EEG's frequencies of interest, which makes the artifact removal more challenging.

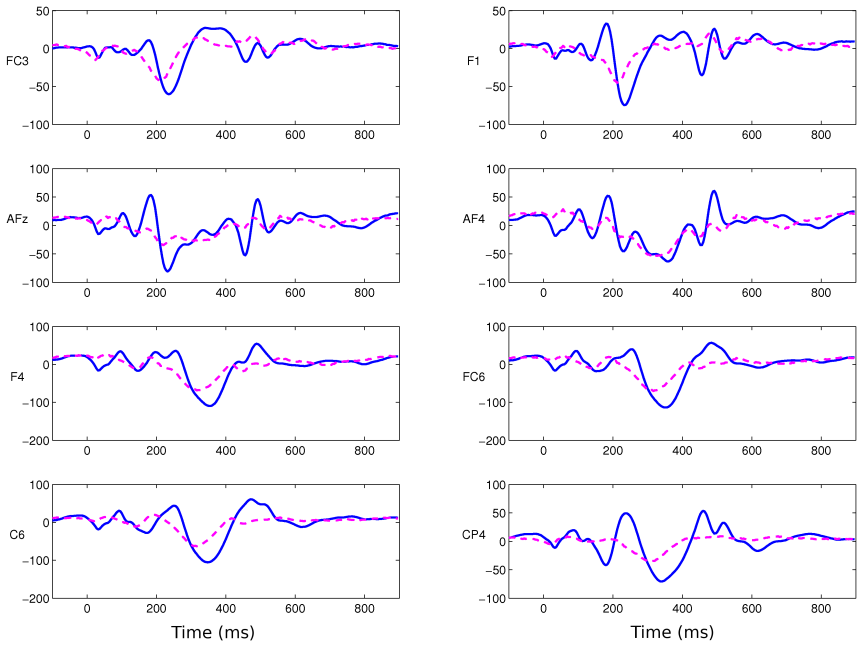

Figure 4.1: *Temporal BCG artifact representation by segmenting on QRS peaks and averaging. The temporal pattern of the artifact clearly differs between different channels (see different panels) and different subjects (see full and dashed lines).*

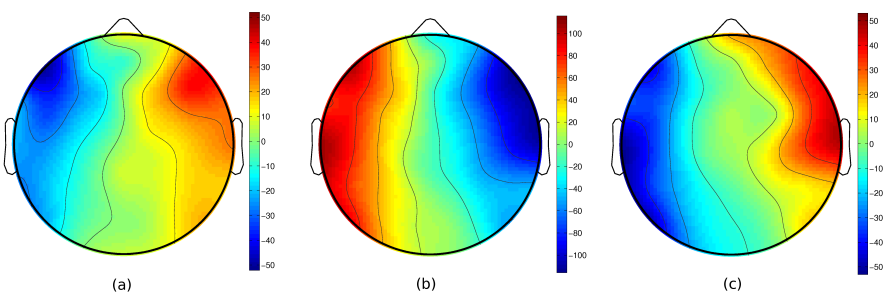

Figure 4.2: *Spatial BCG artifact representation with scalp distribution of specific values from averaged BCG-related segments: (a) value at latency of 200 ms; (b) value at latency of 350 ms; (c) value at latency of 500 ms. The BCG artifact has an opposite polarity at the two sides of the head which reverses in the course of the artifact.*

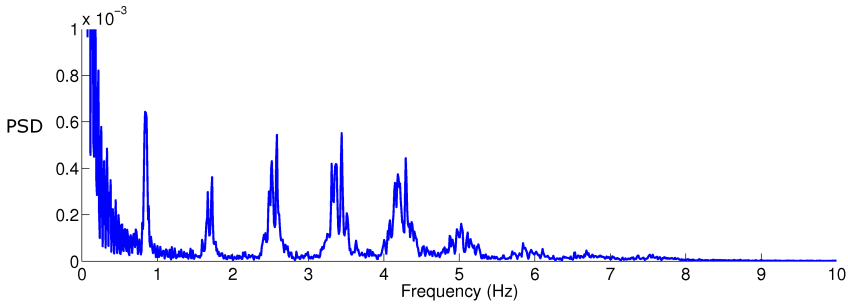

Figure 4.3: *Spectral BCG artifact representation with normalized power spectral density on channel Fp8. There is a clear peak at the heart rate frequency of 0.85 Hz and at several of its harmonics.*

4.1.3 Overview of ballistocardiogram artifact removal methods

From Section 4.1.1, we already know that the exact origin of BCG artifacts is still a matter of investigation. Furthermore, also their removal is a problematic issue, reported in many simultaneous EEG-fMRI studies (e.g., [56]). As a consequence, various BCG removal methods have been suggested. Roughly, these methods can be subdivided into two main categories.

The first category of methods for BCG artifact removal is based on the channel-wise subtraction of an artifact template. The methods differ in the way this template is generated. One of the first methods to be introduced, was similar to the procedure later adopted for gradient artifacts, employing a dynamic average artifact template [4]. Subsequently, variations on this average template were developed based on median-filtering [75] and Gaussian weighted averaging [86]. More recently, it was suggested to use an optimal basis set (OBS) of principal components for the template creation [163]. This technique relies on the idea that PCA applied to all artifact occurrences in each channel separately, makes it possible to capture the temporal variations of the BCG artifact. In addition to OBS, also other channel-by-channel correction approaches exist that try to improve the template construction. Bonmassar et al. [26], e.g., used an adaptive Kalman filter based on a motion signal that has to be additionally acquired during the measurements. Alternatives for the measurement of this motion signal were also proposed in [107, 142]. More recently, wavelet-based methods [213] and a moving general linear model approach [211], were introduced. More research is, however, needed to assess the usefulness of these latter two approaches [159].

The second category of methods is based on blind source separation. There are several ways to perform this separation (see Section 4.2) and many have already been suggested for the removal of the BCG artifact. Assecondi et al. [9], for

instance, make use of CCA to perform blind source separation. The most widely reported blind source separation technique for BCG artifact removal, however, is ICA [19, 139, 192]. This is a signal processing technique that can be used to recover sources from a set of simultaneously recorded signals, assuming that they result from a linear mixing of independent source signals [39]. ICA applied to EEG data contaminated with BCG artifacts, can potentially identify both brain- and artifact-related sources, given that they are independent, thereby cleaning up the EEG by removing the artifactual sources.

As will be explained in more detail in Section 4.2, most ICA algorithms assume stationarity of the sources. Since we know from Section 4.1.2 that the BCG artifact shows a considerable spatial variation across its occurrence [206], satisfying this assumption can be problematic. For this reason, it was suggested to apply OBS prior to ICA [58] instead of applying ICA directly to the EEG data. This approach would combine the strengths of both methods, removing the major part of the artifact with OBS and its residuals with ICA.

4.1.4 Aims of this chapter

Despite the numerous approaches suggested, there is so far little consensus on what method gives the best data quality [55, 139]. Grouiller et al. [91] made an attempt to evaluate different methods by comparing their effect on continuous EEG data. However, since the study of event-related responses with simultaneous EEG-fMRI measurements is a growing field, the performance of the methods should also be investigated there. In [56], the two most popular methods (OBS and ICA) and their combination (OBS-ICA) were compared on auditory ERPs. It was concluded that OBS and OBS-ICA could efficiently remove BCG artifacts and substantially improve the quality of the auditory responses. Although this study has led to a better understanding of the performance of OBS and ICA for BCG artifact removal, only little attention has been paid to the different method-dependent parameters to be selected and validation has only been performed with average measures. The present chapter aims, therefore, at furthering the selection of the most appropriate method by investigating these remaining uncertainties.

To be more precise, the aim of this chapter is to clarify the confusion that arises due to the manifold of current approaches. Our first aim was, therefore, a direct comparison of the quality of artifact removal of the most widely used methods, namely OBS, ICA and OBS-ICA, applied to ERP datasets. More specifically, data with ERPs from visual tasks were investigated, both in two in vivo datasets and in a carefully controlled simulation study. The application on visual ERPs has, to our knowledge, only got little attention so far. Furthermore, the combination of both in vivo and simulation data provides us with a more profound understanding of the performance of the BCG removal methods on realistic experimental data as well as

a precisely controlled situation. Secondly, we set out to establish for each of these methods, the optimal parameter settings, yielding the best possible performance. This issue has been somewhat disregarded in previous studies, although an optimal choice of parameters is essential for the quality of the results. Thirdly, we set out to evaluate the effect of these optimized methods at all relevant levels of EEG datasets, ranging from average measures comparing the ERPs inside and outside the magnetic field to statistical power in discriminating experimental conditions in the ERPs. Hence, the six validation criteria included, not only account for a good artifact removal but also for an accurate recovery of the underlying data.

4.2 Materials and methods

In the following subsections, first, the utilized sets of in vivo experimental data are discussed after which the construction of simulated datasets is explained. Subsequently, the employed methods for BCG artifact removal are described, together with the applied validation criteria.

4.2.1 Experimental data

As this chapter focuses on BCG artifacts, the data used were restricted to EEG data measured in the MR scanner without simultaneous fMRI acquisition and EEG data measured outside the scanner room, for validation purposes. More specifically, five subjects (subjects 1 to 5 in Table A.1) were included for which both detection and Go/NoGo data were available. As can be deducted from Table A.1, these data were measured in the Siemens scanner in the Maastricht setup. The reason for selecting the detection and the Go/NoGo task, was their ability to evoke respectively robust P1 and N1 and reliable NoGo N2 and P3 components, useful for validating the artifact removal.

4.2.2 Simulation study

To generate a set of simulated signals, a short fragment of continuous EEG data was acquired from one (additional) subject (male, aged 46), who did not perform any task while lying in the scanner. For practical reasons, these measurements were restricted to 5 minutes and conducted in the Philips scanner of the Leuven setup. This dataset can be assumed to contain background EEG contaminated with realistic BCG artifacts and instrumental noise.

Subsequently, Go and NoGo grand average ERPs obtained during outside measurements were added to this dataset. These grand average ERPs were

retrieved from Go/NoGo data acquired outside the scanner on subjects 7-9 (see Table A.1), and were used as models for Go and NoGo single trial responses. To extract the grand average ERPs, data were epoched on Go and NoGo stimuli and averaged after baseline removal and extreme value rejection.

The contribution of the background EEG and BCG artifacts with respect to the ERPs, was amplified with a varying factor, to obtain different SNR values. The results of this simulation study were validated with the square root of the mean squared values of the differences between the original grand average ERPs and the ERPs obtained after BCG removal.

4.2.3 EEG preprocessing

Since the EEG data were measured without simultaneous fMRI acquisition, only filtering and downsampling were applied prior to the BCG removal, combined with a detection of the QRS complexes (as explained in Chapter 3). In the following paragraphs, the actual methods for BCG removal are explained together with the parameters to set for each method. For a better understanding, an overview is given in Figure 4.4.

4.2.4 OBS method

As stated in [163], OBS is based on the assumption that each BCG artifact occurrence in each channel is independent of any previous occurrence. Furthermore, following the same principle, all artifact occurrences are assumed to be sampled from an unknown set of possible variations. To capture these principal variations, OBS uses PCA, applied to all artifact occurrences per channel. The first step of OBS [163] consists in shifting all QRS complex timings forward in time by 210 ms. This time period is chosen because it is known as the standard delay between QRS complexes and the corresponding BCG artifact occurrences. Next, for each channel, a matrix of BCG artifact occurrences is constructed and PCA is performed. The BCG artifact template is created based on a selected number of the resulting principal components, called the Optimal Basis Set. In order to obtain the cleaned data, the OBS per channel is fitted to, and subtracted from, each artifact occurrence.

In this study, the OBS method was performed as available in the EEGLAB plug-in FMRIB. One parameter needs to be selected, namely the number of principal components (NPC) used to create the artifact template. Most studies use the recommended value of 3 for this parameter, but, as one of the aims of this chapter is to investigate the effect of each parameter, this number was varied between 1 and 7 (with a step size of 1).

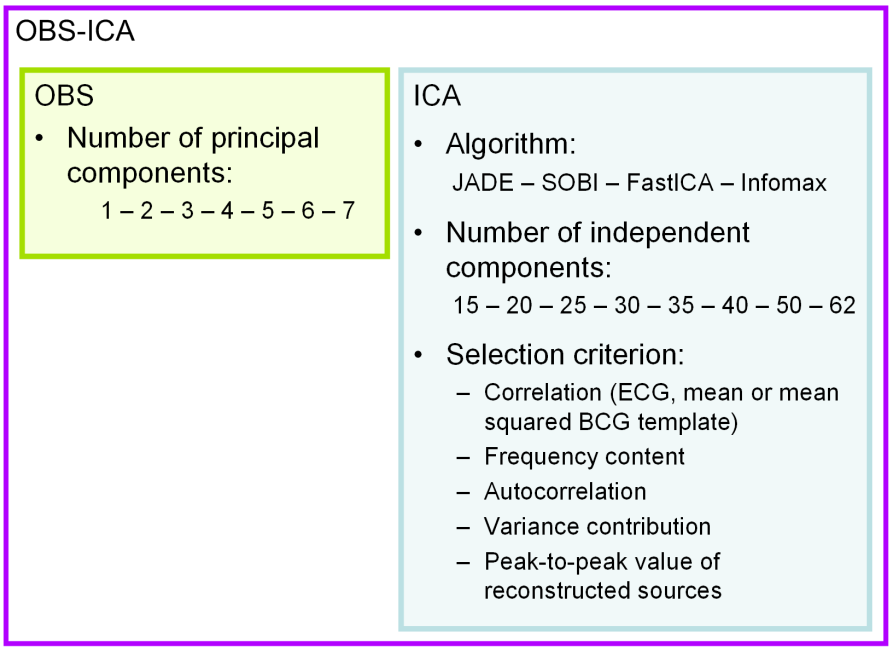

Figure 4.4: *Overview of methods evaluated in this study for the removal of the BCG artifact, together with the parameters investigated for each method. For the combined approach OBS-ICA, all parameters from both OBS and ICA were included.*

4.2.5 ICA method

The EEG represents a complex combination of numerous sources of neural activity. Because EEG is acquired with a number of electrodes on different positions on the scalp, each electrode will measure a weighted sum of these different sources. Mathematically, this can be represented with

$$\mathbf{X} = \mathbf{A} \cdot \mathbf{S} + \mathbf{N} \tag{4.1}$$

where $\mathbf{X}$ is the matrix of acquired signals $x_i(t)$ and $\mathbf{S}$ the matrix of source signals $s_i(t)$. The coefficients of $\mathbf{A}$ determine the contribution of the individual sources $s_i(t)$ in the measured signals and $\mathbf{N}$ represents the Gaussian noise. The aim of blind source separation comes down to the determination of the source signals $s_i(t)$ from the measured signals $x_i(t)$. These $s_i(t)$ can be estimated as

$$\mathbf{S} = \mathbf{W} \cdot \mathbf{X} \tag{4.2}$$

with $\mathbf{W}$ the unmixing matrix. However, since both coefficients and sources are unknown, it is generally impossible to determine them without imposing additional

constraints. Therefore, several possible assumptions about the sources have been proposed in order to obtain a unique decomposition. The most well-known is the constraint of statistical independence as imposed in ICA. As indicated in the introduction, ICA is a signal processing technique that recovers independent sources from a set of simultaneously recorded signals that result from a linear mixing of the source signals [39]. In [139] and [192], the ability of ICA to identify and remove BCG-related independent components has been shown.

During the application of ICA however, several choices need to be made. Not only several ICA algorithms exist, but also it is necessary to decide how many components should be retrieved. Once these components are obtained, a third important aspect is the approach followed to select the artifact-related components. In this study, these three mentioned choices were regarded as ICA parameters and will be discussed in more detail in the following sections.

Algorithm

In order to extract independent sources, various ICA algorithms can be used. In this study, four different implementations, namely Joint Approximate Diagonalization of Eigenmatrices (JADE), Second Order Blind Identification (SOBI), FastICA and extended Infomax ICA were compared. These algorithms were selected because they are well-known and most widely used in neuroscience applications [112, 134, 194].

JADE is one of the earliest ICA implementations and has a procedure based on higher-order statistics [33]. It diagonalizes the fourth-order cumulant matrices of the estimated sources. In [201], JADE proved to be effective for removing artifacts from EEG data.

SOBI [18] uses second order statistics to decompose the measurements and is employed in numerous EEG studies (e.g., [196]). It is based on a joint diagonalization of correlation matrices. SOBI is most appropriate for sources that are individually correlated in time, but mutually uncorrelated. In a recent study of Klemm et al. [115], SOBI proved to be among the best methods for separating EEG data.

FastICA on the other hand, is described as a computationally efficient method for performing the estimation of ICA [105]. It uses a so-called fixed-point iteration scheme that has been proven to be 10-100 times faster than conventional gradient descent methods. The sources are extracted one-by-one based on their kurtosis. FastICA was for the first time used for the removal of the BCG artifact in [139].

Infomax ICA performs the separation in independent sources based on the information maximization principle [17]. More specifically, the independent sources are retrieved by maximizing the entropy. Infomax is a very popular

algorithm for EEG decomposition and has previously been used in the BCG removal studies of Srivastava et al. [192] and Debener et al. [56]. In the current study, the extended Infomax approach, as proposed in [125], was applied.

To our knowledge, detailed comparisons of the effects of these different algorithms for BCG removal are so far lacking. In this chapter, we therefore investigated the effect of selecting a particular algorithm in more detail, by considering the four above-mentioned ICA implementations.

Number of components

In BSS problems, it is so far not possible to determine beforehand the exact number of sources generating the acquired signals. However, since the number of channels in our experiments is reasonably high (62) compared to other simultaneous EEG-fMRI studies [91, 139, 163], it is very well possible that the real number of sources underlying the measured data, does not equal the number of channels. As a consequence, reducing the dimensionality of the data before estimating the sources, might simplify the complexity of the problem for the actual iterative algorithm. In previous studies on ICA for BCG removal, the number of components was always chosen equal to the number of channels.

To investigate the effect of dimensionality reduction, this study did not rely on a fixed choice for the number of components but explored several possibilities. The number of components was varied among the following choices: 15-20-25-30-35-40-50-62. This selected range and sampling allowed us to determine the effect of this parameter.

Selection criteria

Once ICA has been performed and the underlying sources have been retrieved, it is crucial to carefully identify and select the artifact-related components. The first attempts to use ICA for BCG removal were mainly based on manual selection of the artifactual components (e.g., [104]). Subsequently, several automated selection criteria have been proposed in literature, the most important ones of which rely on correlation and variance properties [55, 139, 192]. In this work, we extended these selection criteria. In particular, we compared the accuracy of removal after selection based on correlation, frequency behavior, autocorrelation, variance and characteristics of reconstructed signals.

Correlation The most widely reported selection criterion is based on the amount of correlation of the resulting independent components with the ECG channel

[139, 192]. The BCG artifact, however, does not resemble the ECG pattern at all; therefore another reference signal might be more effective. Srivastava et al. [192] introduced the idea to use a template for the BCG artifact as reference signal. For this purpose averaged BCG artifacts were concatenated per channel and subsequently averaged over all channels. However, since BCG artifacts are known to have an inverse polarity at both sides of the head [56, 206], it is possible that by using an average over all channels for the BCG template, a substantial amount of the artifactual activity will be averaged out. Therefore, the BCG template might be improved by squaring these concatenated averaged artifacts before taking the mean over the channels, in order to emphasize the BCG artifacts. Furthermore, in order to take some temporal variation into account, the averaging per channel should be performed in windows.

In the present study, this latter procedure was compared with the two previously suggested ones. After correlating the ICA components with the suggested templates, a threshold was set on the correlation so as to identify all components with a higher correlation as artifact-related. For the actual threshold with all the three templates, it was chosen to start from 0.20, as this value is known from the literature (e.g., [139]), and to include the surrounding values 0.15 and 0.30.

Frequency content In Section 4.1.2 and [206], it has been shown that the presence of the BCG artifact is characterized by peaks in the frequency spectrum at the heart rate frequency and several of its harmonics. This property can also be exploited as a tool to select the artifact-related components from the ICA decomposition. To this end, the heart rate frequency was determined by computing the inverse of the average time between consecutive QRS complexes. Next, it was checked whether the frequency spectrum of every component (computed with a normalized power spectral density (PSD) based on a Welch window) showed a peak at this frequency and its first harmonic. If these peaks were present, the component was identified as BCG-related.

Autocorrelation Visually, the most apparent property of BCG-related independent components is their repetitiveness. A suitable measure for this repetitiveness is the autocorrelation function. The autocorrelation is the cross-correlation of a signal with a delayed version of itself and is often used for finding a repeating pattern in a signal (e.g., [59]). BCG-related components can thus be distinguished by the peaks shown in their autocorrelation at exactly the distance between two consecutive QRS complexes.

Variance contribution In [55], another alternative selection procedure has been suggested, based on the amount of artifact variance, explained by each of the independent components. Therefore, a matrix focusing on the artifactual activity

(by taking segments around the artifact occurrences) was used and the amount of variance explained in this matrix by every source was assessed with the EEGLAB function 'eeg_pvaf'. In the end, all variances were divided by their sum in order to retrieve variance contributions in terms of percentages which are easier to threshold. Minimal variance contributions of both 5 and 10% were eventually selected as a criterion for the BCG identification.

Peak-to-peak of reconstructed sources Another way to assess the characteristics of a specific source, is to look at the signals obtained by backprojecting this source to the signal space. The criterion proposed here, relies on the assumption that such backprojected signals should, if accounting for the BCG artifact, show patterns occurring at the same rhythm as the QRS complex in the ECG channel. Therefore, for each source, the reconstructed signals were epoched around the artifact occurrences and averaged. Of the resulting averages, peak-to-peak (PTP) values were computed as the difference between the maximal and the minimal value of these averages in every channel. These peak-to-peak values were then divided by the peak-to-peak values of the original signals and the maximal value over all channels was taken. The obtained percentages gave an idea on which sources specifically cause high artifact amplitudes in the data. As thresholds 15 and 25% of the relative peak-to-peak amplitude were selected in this study.

4.2.6 OBS-ICA method

Although the majority of the combined EEG-fMRI studies rely solely on one of the two above procedures, Debener et al. [58] proposed to combine them to optimize the artifact removal. More specifically, they suggested applying ICA to remove residual artifacts after BCG cleaning with OBS.

Because of the high quality of the results demonstrated with this combined approach, it was also included in our comparison study. Moreover, since the focus here was on an appropriate parameter selection, also the combination of all parameters needed to be investigated. These parameters are all the parameters explained in the separate OBS and ICA sections. Slight modifications of certain threshold values were, however, necessary because the preceding OBS alters the data properties, and were performed based on visual inspection of several examples. More specifically, for the correlation with the ECG channel, 0.07 and 0.15 were taken as thresholds and for the correlation with the mean and the mean squared BCG templates, 0.03 and 0.08 were chosen. Furthermore, we also wanted to account for subject-dependent differences in correlation, so a third threshold for the three correlation approaches was set on 75% of their maximal correlation. For the peak-to-peak value of the reconstructed sources 50 and 80% were chosen and for the variance contribution the thresholds became 5 and 15%.

4.2.7 Validation criteria

To assess the quality of the artifact removal and investigate the importance of the parameters, it is crucial to work with validation criteria that represent the different aims pursued with the data. Given the number of parameters, assessed validation was only feasible with quantified criteria. More specifically, for ICA alone, the number of evaluations per subject, task and block was 8 (possibilities for the number of components) x 4 (ICA algorithms) x 15 (selection criteria with different thresholds), equaling 480. For OBS-ICA this number needed to be multiplied by 7 (number of principal components), which resulted in 3360 possibilities.

The first objective of artifact removal is of course to remove the artifact as much as possible from the data. To this end, the peak-to-peak value of the artifact-related epochs and the variation among single trials were studied. Of equal importance, however, is the requirement that the artifact removal should not affect the data of interest, in this case the ERPs. Therefore, these ERPs were compared with the ones retrieved outside the scanner and their most important properties were studied. As opposed to previous similar studies, these properties were not only computed on averages over many trials, but also trial-to-trial characteristics were investigated.

Peak-to-peak value of artifact-related epochs

Our first validation criterion measures the amount of residual BCG artifact after the application of the different cleaning methods. A popular approach for this purpose is to look at certain properties of the averages of epochs retrieved around the QRS onset (e.g., [55, 139, 163]). Following [139], we extracted epochs from the EEG from 100 ms before until 900 ms after the QRS onset and subsequently averaged these. Then, the peak-to-peak amplitudes of the averaged epochs were computed by subtracting the minimal from the maximal value in each channel, and averaged over all channels. Finally, a ratio was calculated of the resulting values before and after BCG cleaning. As such, this criterion gives an idea on the reduction of the artifact compared to the original situation.

Single trial variation

A drawback of the above criterion lies in its assumption that the residual artifacts are not random and can thus be captured with an average measure. However, the residuals left by the algorithm can vary between occurrences [163]. Therefore, the use of a second criterion that pays more attention to this variability, is mandatory. We defined a measure based on the variability among task-related single trials. The approach relied on the assumption that, even though there can be small

differences, task-related single trials should be largely similar. The presence of the artifact however, which is randomly spread over these trials and has varying amplitudes, causes the single trials to be more diverse. Therefore, the better the artifact is removed, the smaller the single trial variation will become. This criterion was implemented in the following way. Firstly, epochs were extracted per stimulus for both the detection and the Go/NoGo task. From all epochs the mean of the prestimulus interval was subtracted (baseline subtraction) and the epochs were slightly shifted in time to fit with their average. This fit was defined as the maximal cross-correlation, in order to account for small inaccuracies in time. Next, the standard deviation over trials was computed and averaged over all time points and channels. The eventual criterion is the ratio of the resulting values before and after BCG removal.

ERP difference

The first criterion to assess the effect of artifact removal on the data of interest, compares the resulting ERPs with ERPs obtained with the same stimuli outside the scanner environment. To this end, Mantini et al. [139] defined a difference measure as the square root of the mean squared difference between all time points of the averaged ERPs inside and outside the scanner. In our specific case, it was chosen to retrieve ERPs from both the Go and NoGo stimuli in the Go/NoGo task and from the central stimulus and all stimuli together in the detection task. To create the ERPs, firstly data were re-referenced to the mastoids and all blocks per subject and task were taken together. Then, epochs were extracted and baseline subtraction was applied, after which trials with extreme values (above 200 μV) were removed and the average epoch computed. The difference measure was computed following the definition explained above (equation (7) in [139]), and this difference was averaged over all channels.

Signal-to-noise ratio

Assecondi et al. [10] show that ERPs from inside and outside the scanner, are not necessarily similar, although the exact cause of this dissimilarity still needs to be investigated. Therefore, the ERP difference might not be completely representative for the quality of the ERPs. For this reason, Debener et al. [56] proposed to use the SNR of peaks of interest in the averaged ERPs to assess the quality of the ERPs. They defined the SNR, following common clinical practice, as the amplitude of the selected peaks divided by the standard deviation of their prestimulus interval (200 ms before the stimulus onset). In the present study, the peaks used for this criterion were the P1 and N1 generated by the central stimulus in the detection task and the N2 and P3 generated by the Go and NoGo stimuli

in the Go/NoGo task. The exact procedure to create the average ERPs, was the same as for the ERP difference.

Task-related modulations

An important field of interest for ERPs, is the effect of the stimulus type on properties of typical ERP components. The feasibility to use data for this purpose, can therefore be considered as an additional criterion to evaluate the quality of the data. In the present study, two examples of these "modulations" were studied. Firstly in the detection task, we chose the difference between responses to left and right visual field stimuli, without making a distinction between upper and lower parts. More specifically, the focus was on the fact that the contralateral P1 (i.e., the P1 peak at the opposite side of the head as the stimulus) precedes the ipsilateral P1 [67]. To obtain a measure for this, averaged ERPs were created for both left and right stimuli and an average from 5 occipital channels on each side of the head was retrieved. Subsequently, the P1 was detected on the contralateral ERP and the amplitude of the ipsilateral ERP at the same latency was retrieved. A t-test was performed on the resulting contra- and ipsilateral amplitudes from all subjects to verify the significance of their difference. In Section 4.3, the average amplitude difference over all subjects is reported (as an indication for the effect size) together with the p-value from the performed t-test. For the Go/NoGo task, similar measures can be retrieved by looking at the N2 component on channel FCz. This N2 should be more pronounced in NoGo compared to Go conditions.

Trial-to-trial characteristics in the detection task

Traditionally, ERPs are extracted using an average over a large amount of trials. However, to fully exploit the advantages of combined EEG-fMRI measurements, it is more interesting to investigate the ERPs on a trial-to-trial basis. Since the above validation criteria are based on average ERPs, they cannot detect small method-related differences in data quality that might affect these trial-to-trial dynamics. For this reason, there is a need for an additional measure that investigates the quality of the data on a much lower level of averaging.

Novitskiy et al. [169] proposed to use single trial P1 and N1 amplitudes as regressors for fMRI analysis. More specifically, the amplitude differences in left and right hemisphere electrodes related to the position of the stimulus on the visual field were employed. A similar approach can be followed here to study the ERP quality in more detail. First of all, ERPs for both left and right stimuli were extracted, following the same procedure as in the modulation criterion, meaning that upper and lower stimuli on each side of the visual field were taken together. The set of trials after baseline removal and extreme value rejection was used in

two ways. First, the average over 5 left occipital channels for all right visual field stimuli was taken together with the average over 5 right occipital channels for the left visual field stimuli. As such, an average contralateral ERP was created allowing determining the latency of the contralateral P1. Secondly, the trial-to-trial quality of the set of trials was augmented by applying a Gaussian moving average (every window contained 11 trials). Afterwards, the amplitude of these trials at the P1 latency obtained in the first step was retrieved from the 5 left and 5 right occipital channels and averaged. As such, series of P1 amplitudes were obtained for both the left and the right hemisphere. Eventually, the right series were subtracted from the left. Since P1 amplitudes are known to be augmented on contralateral channels, the resulting values should be higher than zero for right visual field stimuli and lower than zero for the left ones.

The actual validation criterion measures for each stimulus type (left and right) the number of trials where the sign of the P1 difference value corresponds to the stimulus type, divided by the total number of trials. The resulting ratios represent two aspects of data quality. In the first place, the extreme value rejection removes all trials of insufficient quality by putting a threshold on the maximal amplitude of every trial. Therefore, the ratios will already be lower in cases with a lot of residual artifact. In the second place, both residual artifact and overcleaning of the data will deteriorate the relation between the P1 amplitude and the stimulus type and thus also lower the ratios.

To establish the meaningfulness of these classification ratios, also an additional ratio was investigated for both left and right stimuli. These ratios were defined as the number of correctly classified trials divided by the real number of trials that is subjected to the classification, i.e., after trial rejection. These ratios should be significantly higher than 50%, since otherwise these numbers could also be retrieved by chance.

4.2.8 Statistical analyses

Due to the size of the present study, several statistical tests were needed. First of all, to study the main effects of all parameters in each of the methods, a repeated measurements analysis of variance (ANOVA) was performed, using the SAS 9.2 GLM procedure (SAS Institute Inc., Cary, NC, USA). More specifically, univariate tests were used of which the outcome was adjusted with the Huynh-Feldt Epsilon (H-F) correction factor, to account for possible violation of the sphericity assumption [193].

In cases where only two sets of subject values had to be compared, paired two sample t-tests were used (after verification of normality and variance assumptions). More t-tests, but in a one sample version, were used to check whether the ratios of correctly classified trials divided through the number of good trials, were

significantly higher than 50%. These latter ratios were also evaluated on an individual basis through a proportion test, introduced in [220].

4.3 Results

The results are presented in different sections. Since two of our validation criteria have not yet been used in related studies, their values are first shown for data acquired outside the MR scanner. Subsequently, simulation results are presented for the three employed approaches. The two main approaches (OBS and ICA) are then evaluated each separately on the experimental data with focus on parameter selection. The next results section is devoted to the comparison of these two methods using each method's most optimal parameter settings. In the last section, also the additive benefit of applying OBS prior to ICA is investigated on the experimental data, with special attention to subject-related differences.

4.3.1 Outside results

Two of the validation criteria employed in this study, namely task-related modulations and numbers of correctly classified trials were new to validate BCG removal methods and therefore it was necessary to assess their performance and illustrate their values on data without artifacts. For the detection task data measured outside the MR scanner, the average modulation across subjects was found to be 1.46 μV with a p-value of 0.0017. For the outside data of the Go/NoGo task, this average modulation was 4.63 μV ($p = 0.0053$). These values show that task-related modulations should not only be present after good BCG cleaning, but should also be significant across subjects for both the detection and the Go/NoGo task.

As explained in Section 4.2, the last criterion studies the probability of predicting the side of stimulus presentation, based on trial-to-trial P1 amplitude asymmetry. For the left and right visual field stimuli, these percentages averaged over subjects, were respectively 74.34% and 73.75%. The p-values accounting for the fact that the pure classification part (i.e., the proportion of correctly classified trials in which only trials without extreme values are taken into account) should be better than chance (50%) were 0.0018 and 0.0181, respectively. These outside results demonstrate that data nicely cleaned from BCG artifacts, should correspond to high classification percentages, not retrieved by only pure chance. They also provide us with an upper limit of the classification performance of realistic single trial data.

4.3.2 Simulation results

To form an initial idea of the differences in performance between OBS, ICA and OBS-ICA, it is interesting to have a look at the results of our simulation study. Figure 4.5 shows the root mean squared values of the differences between the original ERPs and the ERPs obtained after BCG cleaning with OBS, ICA and OBS-ICA for different noise levels (different SNR values on the horizontal axis). For BCG cleaning with OBS, several numbers of principal components can be seen (ranging from 2 to 4) and for ICA and OBS-ICA small sets of parameter settings have been chosen as illustration. First of all, one can see that the presented curves show the expected behavior, in particular an increasing error for decreasing SNR values, up to some exceptions in the ICA graphs. For OBS, choosing different values for the number of principal components did not strongly affect the performance. Conversely, careful parameter selection appeared to be required for ICA since only with specific ICA parameters, errors could be found as low as with OBS. With OBS-ICA, these error values could even further be improved, on condition that proper parameter values were chosen.

The results from the validation on the realistic experimental data will now be discussed in the following sections.

4.3.3 OBS results

For pure OBS, we were mainly interested in knowing whether the recommended number of principal components for the BCG removal (NPC = 3) was a good choice and whether OBS resulted in ERP data of sufficient quality. For this purpose, the main effect of the number of principal components, evaluated with the first four validation criteria, is summarized in Table 4.1.

The effect of the number of principal components on the peak-to-peak value is also shown for all subjects in Figure 4.6 for the detection task. For the Go/NoGo task, the results looked similar.

The fact that for OBS the peak-to-peak value did not substantially decrease beyond 4 or 5 principal components, indicates that in the remaining principal components artifactual activity is no longer present. This finding is not inconsistent with the fact that the single trial variation continued decreasing beyond this point, since also by removing non-artifactual activity, the variation will decrease. The ERP difference was difficult to interpret here, since the effect of the number of principal components was dependent on the stimulus under study. For the SNR no significant effect of the number of principal components could be found.

For the fifth evaluation criterion, i.e., the quality of task-related modulations in both tasks, the effect of the number of principal components is summarized in the

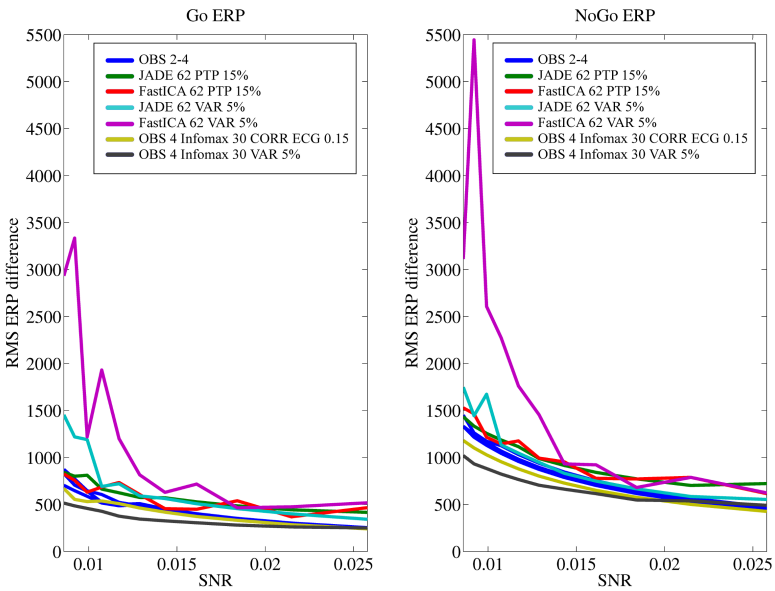

Figure 4.5: *Root mean squared value of the difference between the original ERPs and the averaged ERPs, obtained after BCG cleaning on simulated data with different noise levels. Values are shown for both the Go and the NoGo ERPs and for the OBS method (with number of principal components ranging from 2 to 4), the ICA approach and the combined approach OBS-ICA. For ICA, the algorithms JADE and FastICA are compared with 62 components and the variance contribution (VAR) and the peak-to-peak value of reconstructed sources (PTP) as selection criteria. For OBS-ICA, curves are shown for Infomax with 30 components performed after OBS with 4 principal components and with the correlation with the ECG (CORR ECG) and the variance contribution (VAR) as selection criteria.*

upper part of Table 4.2. In the lower part of this table, the effects according to the sixth criterion, the trial-to-trial behavior of the data in the detection task, can be found.

Based on the first four criteria, which bear closest resemblances to earlier studies, 2, 3 or 4 principal components would give the best results. However, according to the task-related modulation criterion, it can be concluded that only NPC = 3 and NPC = 4 yield a difference consistent over all subjects for the detection task. For the Go/NoGo task all selected numbers of principal components give significant differences but the best value is obtained with NPC = 2. For the trial-to-trial percentages, only with NPC = 2 and NPC = 3 values are found of which the pure classification part is significantly higher than 50% for both left and right visual

Table 4.1: *Effect of number of principal components (NPC) on the quality of the BCG removal with OBS, evaluated with the first four validation criteria. The right column gives the p-value of the main effects from a repeated measurements ANOVA.*

Validation criterion	Effect of increasing NPC	Significance
Peak-to-peak value	Strong decrease until NPC = 4 or 5	$p = 0.0002$
Single-trial variation	Strong decrease throughout whole range of NPC	$p < 0.0001$
ERP difference	Weak decrease throughout whole range of NPC	$p = 0.0024$
Signal-to-noise ratio	No significant effect (highest SNR with NPC = 2)	$p = 0.4704$

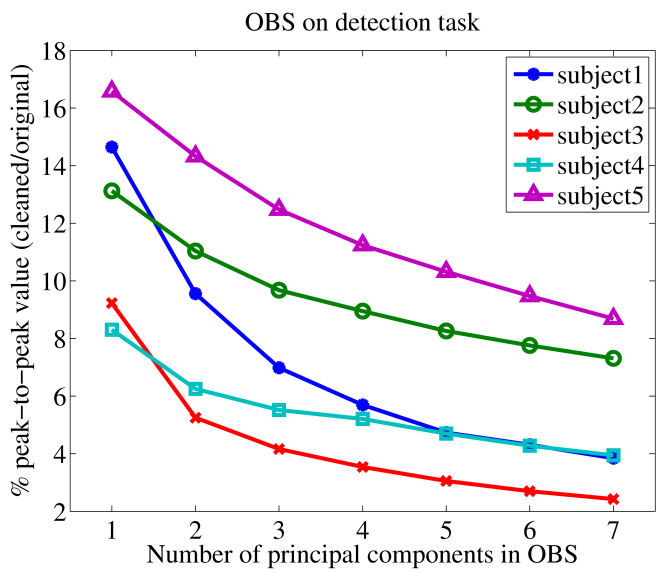

Figure 4.6: *Ratio (in %) of peak-to-peak values of BCG-related epochs after and before BCG cleaning with OBS. The results are shown for the detection task for the five subjects (in different colors) and for a number of principal components ranging from 1 to 7.*

Table 4.2: *Effect of number of principal components (NPC) on the quality of the BCG removal with OBS, evaluated with task-related modulation values and classification percentages. Upper part: Task-related modulation values (in μV) averaged over subjects for different numbers of principal components (NPC) with OBS. For the detection task, the presented values are the averages over subjects of the differences between the contra- and ipsilateral amplitudes at the latency of the contralateral P1. For the Go/NoGo task, the values represent the differences between the Go and NoGo amplitudes at the latency of the NoGo N2. Values in bold indicate a significant effect over all subjects. Lower part: Average percentages of trials in the detection task in which the P1 amplitude difference between left and right corresponds with the side of stimulus presentation. Percentages are shown for both left and right visual field stimuli (LVF and RVF). Note that the shown percentages indicate the portion of trials that are really useful, meaning computed on the total number of trials in the experiment. Bold indicates values for which the amount of trials correctly classified between left and right is significantly higher than half of the number of trials after removal of extreme values (over subjects).*

NPC	1	2	3	4	5	6	7
Detection (P1) [μV]	0.380	1.396	**1.373**	**1.305**	1.245	1.201	1.315
Go/NoGo (N2) [μV]	**6.736**	**6.826**	**5.428**	**5.485**	**4.794**	**4.884**	**4.168**
LVF stimuli [%]	**46**	**53.63**	**52.63**	**54.13**	**55.63**	**56.75**	53.38
RVF stimuli [%]	40.5	**54.25**	**54.88**	55.75	54.88	56.88	54

field stimuli. Thus, taken together the findings from all six criteria, only OBS with three principal components gives good and significant values for each of the criteria.

4.3.4 ICA results

First of all, it was tested whether performing ICA on selected (artifact-related) parts of the data instead of on the whole dataset, would improve or speed up the artifact removal. However, no significant effect with any of the proposed validation criteria could be found. Moreover, since BCG artifacts were prominent during nearly the whole time course of the data, this data selection did not give a significant time reduction either. Therefore, all presented results are based on ICA performed on the continuous EEG data.

To be able to extract the most interesting findings from the data, the evaluation

was performed in two stages. First, a subset of good parameter settings was generated based on the first four validation criteria and on visual inspection of grand average ERPs. Second, this subset was evaluated with the task-related modulation and the number of correctly classified trials.

The three parameters of interest in ICA were: algorithm, number of components and selection criterion. All three significantly affected each of the first four validation criteria in both tasks. To summarize these results in an insightful manner, thresholds were set on each criterion, distinguishing acceptable from really poor results. The thresholds were based on the values retrieved with the same criteria after OBS. More specifically, the lowest values retrieved with OBS were taken (as a kind of a worst case OBS), except for the peak-to-peak value for which a less stringent threshold was chosen. Afterwards, all parameter combinations that yielded values above the thresholds for all four of the validation criteria, were selected. The same parameter combinations were also evaluated with visual inspection of the grand average ERPs. Neither the values themselves nor the most optimal value are shown here quantitatively, since discussing them in detail would be too elaborate for the scope of this chapter. Moreover, optimal values seemed to differ between different criteria. Therefore, in Table 4.3 only the parameter combinations retained after these two steps (thresholding and visual inspection), are presented.

Of the remaining parameter combinations, Figure 4.7 shows the amplitudes of task condition induced ERP modulations together with their significance, for JADE (Figure 4.7a), SOBI (Figure 4.7b), FastICA (Figure 4.7c) and Infomax (Figure 4.7d) respectively. Also the number of correctly classified trials was evaluated and these cases where the proportion of correctly classified trials (relative to the number of trials after rejection of extreme values) was significantly higher than 50%, are presented in Table 4.4.

When the first four validation criteria are considered (Table 4.3), FastICA seems to require a higher number of components, while an optimal choice in selection criterion is less essential. This effect was confirmed by visual inspection, revealing that choosing a number of components lower than 50, completely deteriorates the results. For JADE and SOBI, the effect is rather the opposite: all numbers of components yield similar results as long as a proper selection criterion is used. Infomax seems to be less stringent in the choice of numbers of components and selection criteria. Only very low numbers of components (15 and 20) and two of the selection criteria (correlation with mean squared BCG channel and frequency content) give bad results. In all other cases, acceptable ERP signals can be retrieved, although in many cases the amplitude of the Go and NoGo peaks seems to be reduced (this is not shown here).

When looking at the task-related modulations (Figure 4.7), also JADE, SOBI and Infomax can only obtain better modulation results when using the highest

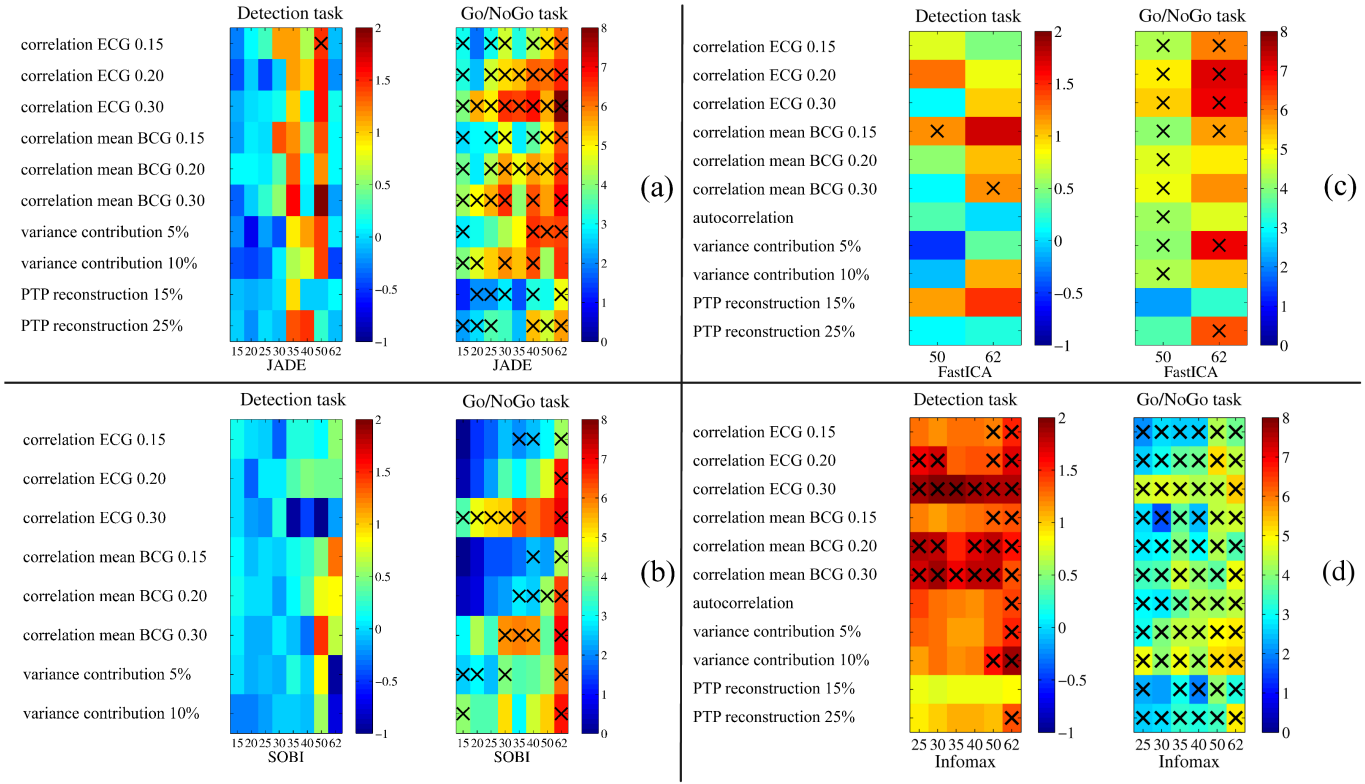

Figure 4.7: *Modulation values illustrated with color scale with* ***X*** *sign added if the shown modulation is significant over subjects. The values are shown for the selection criteria and number of components from the subset presented in Table 4 for (a) JADE; (b) SOBI; (c) FastICA; (d) Infomax and for both the detection task (left) and the Go/NoGo task (right).*

Table 4.3: *Subset of ICA parameters that remain after thresholding (based on minimal OBS values) on the first four validation criteria and after visual inspection of the grand average ERP.*

Algorithm	Number of components	Selection criteria
JADE	All possibilities	· Correlation with ECG and mean BCG channel · Variance contribution · Peak-to-peak value of reconstructed sources
SOBI	All possibilities	· Correlation with ECG and mean BCG channel · Variance contribution
FastICA	50 and 62	· Correlation with ECG and mean BCG channel · Autocorrelation · Variance contribution · Peak-to-peak value of reconstructed sources
Infomax	25, 30, 35, 40, 50 and 62	· Correlation with ECG and mean BCG channel · Autocorrelation · Variance contribution · Peak-to-peak value of reconstructed sources

number of components, thereby losing their advantage over FastICA. For all four ICA algorithms, the Go/NoGo N2 modulation is significant in many cases, regardless of a good parameter choice, which is in line with the OBS results. The P1 modulation in the detection task, however, is significant in only a few cases with JADE, SOBI and Infomax. This is probably because the P1 peak is much smaller than the Go/NoGo N2 and thus more sensitive to residual artifact and overcleaning. Infomax seems to better preserve the P1 modulation, but the amplitude differences of the N2 are reduced, which is in correspondence with the above-mentioned reduction of Go and NoGo peak amplitudes.

The sensitivity of the P1 peak is even further confirmed with the last criterion. Only five parameter combinations allowed significantly above chance classification

Table 4.4: *Evaluation of parameter possibilities from ICA subset with average percentages of trials of which the P1 amplitude difference between left and right corresponds with its stimulus type. Percentages are shown for both left and right visual field stimuli (LVF and RVF). Only those parameter combinations are included for which the ratio accounting for real classification performance between left and right (i.e., after removal of extreme-value trials) is significantly > 50% over subjects (see p-values in columns 5 and 7).*

Algorithm	Number of components	Selection criterion	%LVF	p(LVF)	%RVF	p(RVF)
JADE	40	Correlation mean BCG 0.15	55.4	0.0299	59.0	0.0424
SOBI	40	Correlation ECG 0.15	51.6	0.0223	53.13	0.0278
Infomax	62	Correlation ECG 0.20	57	0.0256	59.25	0.0088
Infomax	62	Correlation mean BCG 0.20	55.13	0.0359	56.63	0.0369
Infomax	62	Peak-to-peak of reconstructed sources 25%	56.63	0.0115	61.25	0.0065

of side of stimulus presentation, based on trial-to-trial P1 amplitude asymmetry (Table 4.4).

4.3.5 Comparison of OBS with ICA

An example of grand average ERPs obtained after OBS with 3 principal components, is given above in Figure 4.8 (panel a: Go/NoGo, panel b: Detection task). The corresponding grand averages for ICA are shown in the centre of Figure 4.8 (panels c and d). The ICA parameters (FastICA, 62 components and peak-to-peak value of reconstructed sources as selection criterion), were not the most optimal, but merely serve as an illustration, as one of the good parameter choices (Table 4.3). As a reference, also the grand average ERPs obtained outside the scanner are shown below in Figure 4.8 (panels e and f).

From these figures, it can be seen that both with OBS and ICA it is possible to obtain high quality grand average ERPs that show peaks and task-related modulations known from previous related studies. Moreover, the obtained components correspond to findings on data measured outside the scanner. Table 4.5 shows for each of the first four validation criteria a quantitative comparison between OBS and ICA with, for each ICA algorithm, parameters selected from the subset in Table 4.3. In particular, parameter sets were chosen for which the values of the ERP difference and the SNR of the ICA results are not significantly different from those of the OBS results. Apart from that, the presented parameter combinations are neither the most optimal nor the only good choices, but serve as an illustrative comparison of OBS and ICA. Table 4.5 shows that comparable results can be obtained with OBS and ICA for all validation criteria. Moreover, comparing Table 4.2 with Table 4.4 and with Figures 4.7a, 4.7b, 4.7c and 4.7d also reveals that similar values for task-related modulations and number of correctly classified trials can be found with OBS and ICA. It should be noted, however, that to obtain this quality of results with ICA, it is important to carefully optimize the parameter settings.

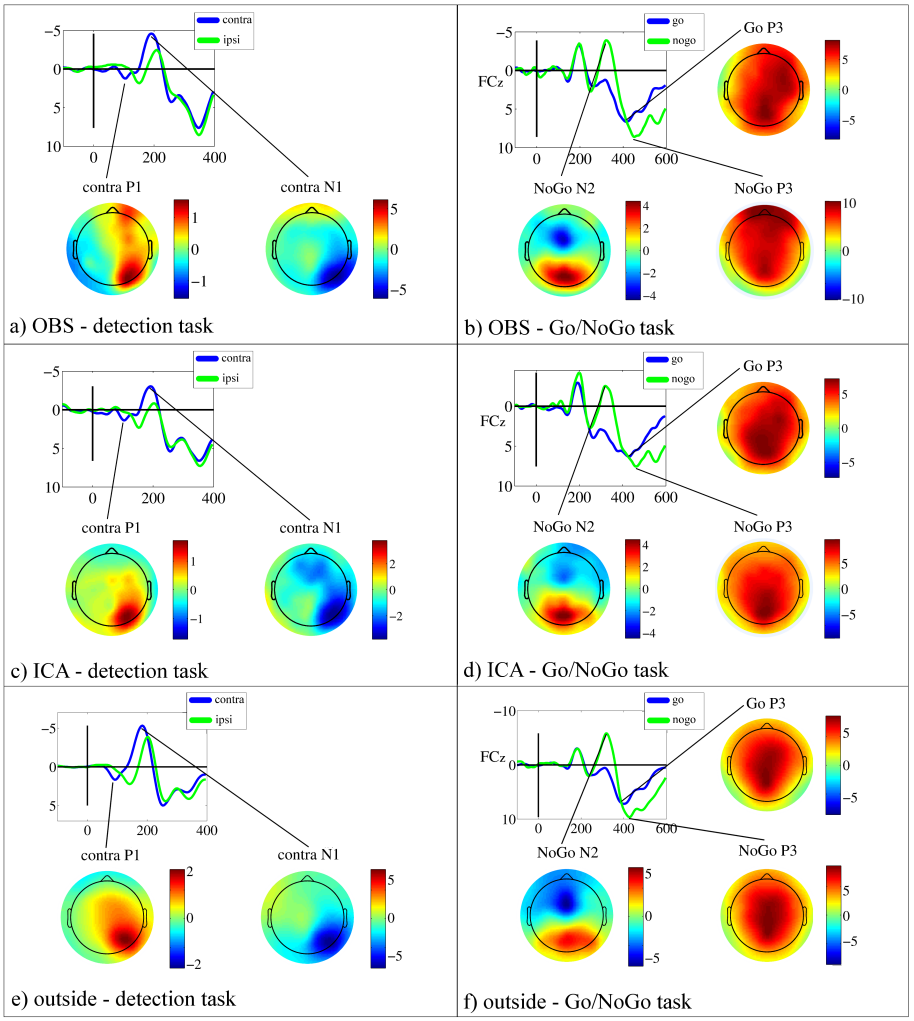

Figure 4.8: *Grand average ERPs (from five subjects) after OBS with number of principal components equaling 3 (upper figures (a) and (b)) and after ICA (FastICA, 62 components, peak-to-peak value of reconstructed sources 25%) (centre figures (c) and (d)) with scalp maps of specific ERP components. Figures (e) and (f) show the same grand average ERPs and scalp maps obtained from the data measured outside the scanner. Figures (a), (c) and (e): contra- (blue) and ipsilateral (green) ERPs for detection task in which five occipital channels on the left and right hemisphere were pooled together. Scalp maps are shown for the contralateral P1 and N1; (b), (d) and (f): Go (blue) and NoGo (green) ERPs for Go/NoGo task on frontocentral channel FCz with scalp maps of the NoGo N2 and P3 and the Go P3.*

Table 4.5: *For one good parameter combination per algorithm from the ICA subset from Table 4.3, a comparison is made between OBS and ICA with the first four validation criteria. The peak-to-peak value (PTP) of the BCG epochs and the single-trial variation (ST var) are indicated in percent for both the detection (DET) and the Go/NoGo task (GNG). The ERP difference (ERP ≠) is given for the central stimulus (centr) and all stimuli together (all) from the detection task (DET) and for both Go and NoGo ERPs from the Go/NoGo task (GNG). The SNR values are shown for the P1 and N1 peaks in the detection task and the NoGo N2 and P3 and the Go P3 in the Go/NoGo task.*

Method (and parameters)	PTP (DET)	PTP (GNG)
OBS (NPC=3)	7.76%	7.82%
FastICA (62 - PTP value of reconstructed sources 15%)	17.37%	16.64%
JADE (25 - correlation with mean BCG 0.15)	22.71%	17.54%
SOBI (35 - PTP value of reconstructed sources 15%)	7.55%	8.03%
Infomax (40 - variance contribution 5%)	34.53%	33.94%

Method (and parameters)	ST var (DET)	ST var (GNG)
OBS (NPC=3)	57.02%	53.82%
FastICA (62 - PTP value of reconstructed sources 15%)	38.35%	38.78%
JADE (25 - correlation with mean BCG 0.15)	45.72%	41.58%
SOBI (35 - PTP value of reconstructed sources 15%)	21.95%	22.73%
Infomax (40 - variance contribution 5%)	56.43%	56.13%

Continued on next page

Table 4.5: *(continued from previous page)*

Method (and parameters)	ERP ≠ centr DET	ERP ≠ all DET	ERP ≠ Go	ERP ≠ NoGo
OBS (NPC=3)	3.78 μV	2.83 μV	2.27 μV	2.62 μV
FastICA (62 - PTP value of reconstructed sources 15%)	3.05 μV	1.95 μV	2.07 μV	3.13 μV
JADE (25 - correlation with mean BCG 0.15)	3.18 μV	2.08 μV	2.20 μV	3.00 μV
SOBI (35 - PTP value of reconstructed sources 15%)	2.50 μV	1.45 μV	2.41 μV	3.50 μV
Infomax (40 - variance contribution 5%)	3.41 μV	2.34 μV	2.09 μV	2.85 μV

Method (and parameters)	SNR P1	SNR N1	SNR NoGo N2	SNR NoGo P3	SNR Go P3
OBS (NPC=3)	6.75	12.27	8.08	13.70	25.50
FastICA (62 - PTP value of reconstructed sources 15%)	3.55	12.31	6.81	12.90	21.49
JADE (25 - correlation with mean BCG 0.15)	5.41	7.69	6.92	12.20	20.36
SOBI (35 - PTP value of reconstructed sources 15%)	2.34	13.97	6.93	8.95	22.79
Infomax (40 - variance contribution 5%)	5.92	10.08	9.83	16.27	21.70

Table 4.6: *Subset of good OBS-ICA parameters based on SNR and task-related modulation. Specifically those parameters are retained where OBS-ICA has an SNR not significantly worse than that of OBS (number of principal components = 3) and modulation values significant for both the detection and the Go/NoGo task.*

Parameter	Choice	Remarks
Number of principal components	2-6	1 and 7 rarely give good results
Selection criterion	· Correlation with ECG · Correlation with mean channel · Correlation with mean squared channel (but not threshold 0.03) · Autocorrelation · Variance contribution	Using the frequency content does not remove any component after OBS
Algorithm and number of components	· JADE with ≥ 25 components · SOBI with ≥ 30 components · FastICA with 62 components · Infomax with ≥ 25 components	

4.3.6 OBS-ICA results

The additional application of ICA after OBS implied a vast amount of parameters to set and was therefore clearly more complicated than pure OBS. For this reason, the focus in this part was particularly on those OBS-ICA results outperforming those of OBS alone. The peak-to-peak value and single trial variation are not very useful for this purpose since we know that with OBS alone, already good values can be obtained. Moreover, the danger of the additional ICA is removing too much task-related signal from the data and this cannot be detected with these validation criteria. From our experience, also the ERP difference is not specific enough to pick up the differences and therefore it was decided to select a subset of suitable OBS-ICA parameters, based on the SNR and the modulation values. To this end, all parameter combinations were retrieved for which the SNR was not significantly worse than that of OBS and that yielded a significant task-related modulation for both the detection and the Go/NoGo task. The SNR may not be significantly worse since any additional ICA step should not decrease the amplitude of the peaks of interest. As such, the subset shown in Table 4.6 was retrieved.

Of this subset, the performance of classifying trials according to their P1 behavior was evaluated and all cases significantly better than in the pure OBS case, are listed

in Table 4.7. Significantly better is defined here as the fact that the minimum of the percentages of both left and right stimuli should be significantly higher than the corresponding percentage from OBS alone (e.g., if the percentage for the left stimulus is the lowest, then left percentages are compared) and the other percentage should not be significantly lower.

This table shows that it is indeed possible to obtain better trial-by-trial data quality by combining OBS and ICA but only with specific parameter settings. However, finding these parameter settings is not straightforward. Table 4.6 and 4.7 can give a general idea on which parameters to choose, but caution is recommended because, especially in Table 4.7, these parameters might be tuned specifically to our data. However, in our results, JADE, SOBI and Infomax were found to be effective, especially with correlation-based selection criteria.

It should be noted that the effect of an additional ICA step can largely depend on the individual under study. This is illustrated in Figure 4.9 for the trial-by-trial classification percentages. For each of the subjects and five different OBS-ICA parameter combinations, the differences between the OBS and OBS-ICA percentages are plotted for both the left and right visual field stimuli. However, five different parameter settings were chosen, each of them increasing the percentages for one subject, while decreasing them for most other subjects. A positive value here means that the percentages are higher with the additional ICA step, while a negative value indicates that the additional ICA step decreases the quality of the results. As such, this figure shows that choosing appropriate parameter settings is essential for the performance of ICA after OBS and that 'wrong' choices can completely deteriorate the results. The individual analyses were also performed for different numbers of principal components for pure OBS. However, in that case, the results were more consistent over subjects and similar trends as with OBS-ICA could not be found.

4.4 Discussion

In this study, we compared several existing methods and their parameter settings for BCG artifact removal from EEG data recorded inside an MR scanner. More specifically, OBS, ICA and OBS-ICA were used to clean ERP data from a visual detection and a Go/NoGo task. Validation of the BCG removal was performed with six different criteria, not only characterizing the residual artifact but, more importantly, also looking at the quality of the ERPs. We found that, although parameter settings strongly affected the performance of each method, no one method emerged as the best current approach. In general, OBS and ICA can yield comparable results, but the quality of the ICA results strongly depends on the choice of parameters. The need for careful parameter tuning makes ICA therefore less interesting for non-experienced users and also for experienced users,

Table 4.7: *Evaluation of parameter possibilities from OBS-ICA subset (Table 4.6) with average percentages of trials of which the P1 amplitude difference between left and right hemisphere corresponds with their stimulus type. Percentages are shown for both left and right visual field stimuli (LVF and RVF). p-values indicate whether the shown percentages are significantly better than the ones of pure OBS (with NPC = 3 see first row in the table). Only those combinations with at least one of both p-values (from left and right stimuli) lower than 0.05 are retained here. "Mean^2" stands for mean squared and "Nb comp" means number of components.*

NPC	Algorithm	Nb comp	Selection criterion	%LVF	p(LVF)	%RVF	p(RVF)
3	/(OBS alone)	/	/	52.63	/	54.88	/
2	SOBI	50	Correlation ECG, subject dependent	51.38	0.699	59.63	0.049
2	SOBI	62	Correlation mean, subject dependent	57.5	0.003	53.88	0.700
2	Infomax	62	Correlation mean, subject dependent	56.25	0.049	57.63	0.308
3	JADE	40	Correlation ECG, subject dependent	55	0.026	55	0.436
3	JADE	62	Variance contribution, 15%	50.63	0.769	56.63	0.022
3	SOBI	50	Correlation ECG, 0.15	52	0.746	57.8	0.032
3	Infomax	62	Correlation mean squared, 0.08	55.38	0.039	55.13	0.397
4	JADE	25	Correlation ECG, subject dependent	53.63	0.371	58.63	0.041
4	SOBI	40	Correlation mean^2, subject dependent	56	0.095	61.5	0.048
4	SOBI	62	Correlation ECG, 0.15	54.75	0.126	57.5	0.035
4	Infomax	30	Correlation mean, 0.03	54.88	0.184	58.25	0.011
4	Infomax	30	Correlation mean, 0.08	55.75	0.175	58.5	0.022
4	Infomax	30	Correlation mean, subject dependent	56.25	0.132	58.63	0.021
4	Infomax	40	Correlation mean, subject dependent	56.25	0.022	58.38	0.016
4	Infomax	50	Correlation mean, subject dependent	54	0.322	59.5	0.032
5	JADE	50	Correlation ECG, 0.07	57.25	0.034	57.25	0.017
5	SOBI	35	Correlation ECG, 0.07	52.75	0.446	58.5	0.024
5	Infomax	35	Correlation mean^2, subject dependent	51.88	0.629	59.63	0.031
5	Infomax	50	Correlation ECG, 0.07	59.25	0.077	59.75	0.042
5	Infomax	50	Correlation mean, subject dependent	52.88	0.46	60.63	0.015
6	JADE	50	Correlation mean^2, subject dependent	54	0.334	58.75	0.011
6	SOBI	50	Correlation mean^2, subject dependent	55.25	0.255	59.5	0.023
6	Infomax	50	Correlation mean, 0.03	55.13	0.197	58.88	0.019

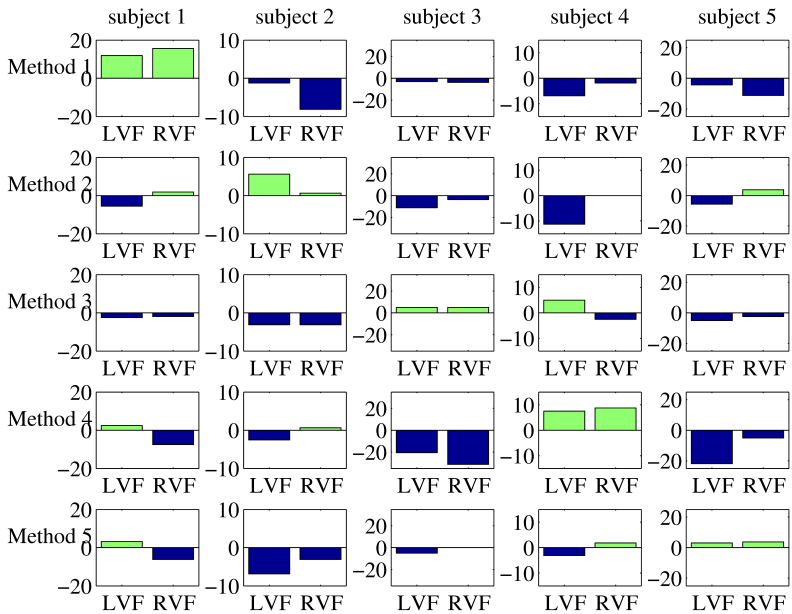

Figure 4.9: *Difference between classification percentages of OBS-ICA with five different OBS-ICA parameter combinations and OBS with three principal components. Each column represents a different subject and each row a different OBS-ICA parameter combination (= method). The percentage differences are shown for both left and right visual field stimuli (LVF and RVF). Negative and positive values are shown in different colors. Method 1 = OBS with three principal components - JADE with 35 components - correlation with mean squared BCG with 0.03; Method 2 = OBS with one principal component - JADE with 62 components - variance contribution 5%; Method 3 = OBS with four principal components - SOBI with 62 components - autocorrelation; Method 4 = OBS with four principal components - FastICA with 15 components - correlation with mean squared BCG with 0.08; Method 5 = OBS with three principal components - JADE with 35 components - correlation with mean BCG with 0.08.*

it is possibly very time-consuming. Combining OBS and ICA can increase data quality. However, we showed that, if wrong parameter choices are made, the additional ICA step might as well spoil the quality obtained with pure OBS.

The OBS approach, the most widely used subtraction method, uses PCA to create a template for each artifact occurrence in each channel. Our results show that the recommended value of three for the number of principal components is indeed most optimal. Subtracting more principal components will not remove much artifactual activity and less than three components do not capture the considerable temporal variation of the BCG artifact. Moreover, only NPC = 3 gives significant values for more detailed validation criteria (task-related modulation and trial-to-trial behavior), although the classification performance is still less than in the case of outside data.

The application of ICA for the removal of the BCG artifact, attempts to separate both artifact- and brain-related sources by decomposing the EEG into independent components. Decomposition can be performed into several numbers of components with different algorithms, and various selection criteria can be used to distinguish the artifactual from the other sources.

In their study on the comparison of OBS and ICA, Debener et al. [56] concluded that with OBS a better SNR could be obtained than with ICA. However, we found that by choosing the appropriate parameter settings, ICA can yield SNR values that are not significantly different from those of OBS. This is nevertheless not inconsistent with Debener's findings, since they already indicated themselves that the number of removed components was not optimized in their study. Trial-to-trial behavior and task-related modulation criteria further showed that identifying appropriate ICA parameter settings is not trivial. It is however important, because with many parameter combinations it would not be possible to retrieve the expected ERP waveforms. Although the results are not always straightforward, our study reveals important overall patterns. Reducing the dimensionality of the data before applying ICA appeared in many cases not to be beneficial and even harmful for the data quality, especially when using FastICA. With the other algorithms this effect was less prominent, although a solid explanation for this difference could not be found. Considering the selection of components, some selection criteria were preferable to others. Correlation-based measures proved to be effective for selecting the major artifact components, but also the variance contribution, as suggested in [55], and the peak-to-peak value of reconstructed sources are reliable selection criteria for ICA. Moreover, these three criteria have the advantage of yielding acceptable average results regardless of the chosen ICA algorithm. The nice performance of the variance contribution and the peak-to-peak value of reconstructed sources can probably be explained by the fact that BCG artifacts can be very effectively identified by looking at properties of the original data. The obvious rhythm of the BCG artifact (at the same rate as the ECG signal) is clearly not so pronounced in the artifactual independent components,

reducing the performance of the frequency content and autocorrelation criteria.

When comparing OBS and ICA, it should therefore be clear that the extensive parameter tuning makes ICA less attractive for BCG removal than OBS. With OBS, acceptable results are more easily obtained with the default number of principal components. OBS seems also more robust to different noise levels (see simulation study) than ICA. Furthermore, despite of all the effort and time spent in finding optimal ICA parameter settings, results were never significantly better than those of OBS.

We also investigated the combination of OBS and ICA. Confirming the findings of [56], the additional use of ICA after OBS can indeed increase the SNR. In addition, also for our other validation criteria OBS-ICA can yield an improvement compared to pure OBS. However, this improvement can easily turn into deterioration, as was illustrated with the individual results. Thus, when applying ICA after OBS, one should always carefully check the quality of the resulting ERPs. Automating this additional step is, therefore, not very obvious. Tracing back the individual differences in the additional ICA step to the characteristics of the BCG artifact in the data might have been useful in finding good parameter settings. As already indicated, the BCG artifact can largely depend on the subject and channel under study, as can also be retrieved with, e.g., global field power values [9, 189]. However, strong relations between such BCG characteristics and the performance of the methods could not be found.

Besides the actual comparison of methods, this study also revises and introduces validation criteria for the evaluation of new methods. Although the perfect removal of the BCG artifact is still not within reach, the used criteria show that acceptable EEG quality can be obtained with the existing methods. As indicated above, OBS combines good data quality with user-friendliness and is therefore preferred to ICA, which requires much more parameter tuning. A possible improvement can be obtained with the combination of OBS and ICA, but, in any case, our results show that it is essential to check in sufficient detail the obtained data quality.

A first important quality check is certainly the averaged ERP. To this end, Mantini et al. [139] proposed to use the difference between inside and outside ERPs. However, this ERP difference seems a rather rough measure for the quality of the ERPs, possibly due to the fact that components from inside and outside ERPs appear to have different latencies (as also shown by Assecondi et al. [10]). Therefore, the ERP difference might indicate only large differences in ERPs. Moreover, computing the ERP difference also requires EEG data from the same subjects measured outside the scanner environment, thereby increasing the recording time. The ERP difference was, however, included in this study in order to be able to compare our results with other, similar studies in the literature (e.g., [139]) and evaluate the adequacy of this previously suggested validation criterion. The SNR (as proposed in [56]) is a better validation criterion, although

residual artifacts could possibly wrongly be regarded as peaks of interest when automated peak detection is used. For this reason, studying the SNR should always be combined with visual inspection of the averaged ERPs.

Previous validation studies, using validation criteria based on averaged ERPs, were not able to reveal the benefit of using three principal components for OBS, as shown here. Furthermore, the importance of extensive parameter tuning in ICA would also not have been revealed with these average criteria. Therefore, in order to make a distinction between the methods under study clearer than what was previously possible, we included very detailed quality checks in our validation study. Although many ERP studies investigate properties of ERP components related to different conditions during the experimental task, preserving these task-related modulations was, to our knowledge, never employed before to investigate the quality of the BCG removal. Computing these same criteria on data acquired outside the magnetic field of the scanner, however, proved their ability to reveal good ERP data quality and indicated upper limits for what can be expected from these measures.

We believe that in most ERP studies, it should in general be possible to evaluate some kind of these task-related modulations on a trial-by-trial level, as was done in this study on the detection task data. Since single trial data already suffer from a low SNR outside the MR environment, additional denoising (with, e.g., the Gaussian average used in this study) might nevertheless be necessary. As shown in this chapter, the use of task-specific and trial-to-trial characteristics can therefore provide the user with a more widely validated quality assurance.

With our improved validation criteria, our findings extend the results of previous studies. For instance, Grouiller et al. [91] directly compared OBS and ICA, but their validation was performed on simulation data, alpha activity and epileptic spikes. Although the characteristics of these EEG patterns are completely different from those of ERPs, OBS proved to be a good choice in their study as well. This effect was strongest when the BCG artifact strongly contaminated the recordings, as is the case at the high field strength of 3T. Moreover, this is in agreement with the conclusions of our simulation study, namely that also high artifact amplitudes (low SNRs) still lead to reasonable error values with OBS.

The comparison of BCG removal methods in this study focuses on OBS- and ICA-based methods as these are most widely used. One of the first BCG removal methods, AAS might therefore seem not to be included in our comparison. However, since the first principal component obtained with OBS is always the average across artifact occurrences, using OBS with only one principal component can be seen as a type of AAS. It should nevertheless be noted that this implementation of AAS is not the most optimal one, since true AAS uses sliding windows, therefore partially accounting for the variability of the artifact.

Also other methods emerged recently, in particular the CCA-based BCG removal

method described in [9]. Since the latter method was not well established and validated on ERPs at the moment of setting up the study presented in this chapter, we decided not to include it here. However, to obtain a more complete picture on methods for BCG removal, this novel method was validated on the above datasets (extended with subjects 8 and 9) and compared with OBS and AAS in a separate study. The results of this work confirmed the good performance of OBS but also showed the usefulness for CCA, especially for capturing the variability of the BCG artifact. More information can be found in [10], where also the effect of the magnetic field on the characteristics of the ERPs is investigated.

4.5 Conclusion

Removing the BCG artifact from EEG data remains a major bottleneck for a successful integration of simultaneously recorded EEG and fMRI data, because the artifact shows a considerable variation over time and channels. Many attempts have been made, of which the most widely used ones, OBS and ICA as well as a combination of both, were compared in this study. Special care was taken to evaluate a large choice of possible parameter settings, combined with a comprehensive selection of informative validation criteria including task-related measures in single trial analysis. While the traditional validation criteria, based on average characteristics, were not specific enough to point out the difference between both methods, our task-specific criteria provided us with a much clearer distinction between OBS and ICA. The advantage of looking at stimulus-related ERP properties both on an average as on a trial-to-trial basis, is twofold. Firstly, we go beyond the typical averaging in ERPs, which improves data quality and smooths specific differences between methods. Secondly, these task-related modulations and the use of ERP data on a single trial basis are major research topics of interest for ERP scientists. Both OBS and ICA proved to yield equally good results, but since these results are much harder to obtain with ICA, OBS is a better choice for a good BCG artifact cleaning, in particular for beginners and less experienced users in the field. Indeed, OBS is less prone to inter-subject variations and more easy to use, thereby enabling automation and a more general use in clinical practice. However, since OBS also leaves some residual artifact, one might also consider using an additional ICA step after OBS. In this case it is essential to carefully monitor the removed activity and this for all subjects under study, because results might be very different between individuals. Applying ICA after OBS might as well improve as completely deteriorate the results.

In conclusion, these results provide important insights into how to optimize settings for OBS, ICA and OBS-ICA. These findings should yield enough informative guidelines for experts as well as newbies in the field to obtain the desired data quality in simultaneous EEG and fMRI measurements.

Chapter 5

Single trial ERP reading based on Parallel Factor Analysis

In the previous chapter, one of the validation criteria for BCG artifact removal, was the possibility to extract task-related ERP information on a single trial level. In the current chapter, an improved procedure for this single trial ERP reading will be presented, based on parallel factor analysis. In addition, the relationship of the obtained single trial ERP information with simultaneously measured fMRI data will be investigated. Section 5.1 will first explain the motivation behind the extraction of single trial fluctuations, after which the exact data and methods used in this chapter, will be summarized in Section 5.2. The results of these analyses will then be presented and discussed in respectively Section 5.3 and Section 5.4. Finally, some conclusions will be formulated in Section 5.5.

5.1 Introduction

As introduced in Section 1.1.2 and also taken into account in the validation of BCG artifact removal in Section 4.2.7, cognitive processes like attention and habituation can undermine the assumptions behind averaging EEG responses to obtain ERP signals. For this reason, it is interesting that recent improvements in analysis techniques make it possible to go beyond studying global effects with grand average ERPs and investigate fluctuations in single trial characteristics.

Moreover, a more particular interest in the extraction of information from single trial ERP data has risen since researchers began to focus on the relationship between these ERPs and fMRI data. As explained in Section 1.1.6, several studies

have included single trial ERP data in combined EEG-fMRI analyses. A major part of these studies are based on so-called integration-by-prediction analyses, using specific characteristics of ERP components on a single trial level as regressors in the analysis of fMRI data. Eichele et al. [74] for instance, extracted single trial N1, P2 and P3 amplitudes and used these, after convolution with a hemodynamic response function (HRF), to model the fMRI responses. Also other ways to correlate the single trial information from ERP and fMRI exist, but so far there is no golden standard for the estimation and validation of single trial responses. In this chapter, a validation procedure based on the distinction between different conditions in the task, will be adopted.

However, extracting information from single trial ERP data is not straightforward since the single trial ERPs are hidden in the ongoing neural activity and noise. For this reason, several studies have employed different BSS methods [40] in order to isolate task-related activity from the typical EEG mixture of brain and non-brain sources (e.g., [52, 152]). One of the earliest BSS methods that has been used in this context is PCA [70]. Also ICA has been applied, not only to extract single trial ERP information [135, 136], but also to relate this to simultaneously measured fMRI activations (e.g., [57, 58, 71]). As such, it was shown that ICA is a practical solution to identify functionally meaningful EEG activity on a trial-by-trial basis. Both PCA and ICA, however, can be applied in the spatial or in the temporal domain or in any other domain which is relevant for the data, but regardless of this choice, they come with the inherent drawback of being only applied to matrix data. Since not only the temporal course and the spatial localization of ERPs can be investigated, but also their variation across subjects, trials, conditions, etc. the above-mentioned methods do not allow to fully exploit all the information contained in the data.

A method that overcomes this problem, and has at the same time the advantage of being unique under very mild assumptions, is parallel factor analysis (PARAFAC) [94]. This method, also known as canonical decomposition (CANDECOMP) [34], allows decomposing multi-way data in a set of distinct atoms, which ideally represent distinct brain sources. PARAFAC has already shown its value for the analysis of EEG data, as, e.g., for the identification or suppression of activity in specific frequency bands [149, 204], the localization of the seizure onset zone in epileptic data [53] and the determination of the location of neonatal brain seizures [60]. It has also found its way to the study of ERP data where it was applied for the first time under the name of topographic components (TC) model in [152, 153]. Later, this work was extended and validated in, among others, [2, 77, 215]. In addition, Mørup et al. [151] used PARAFAC to investigate the ERP's inter-trial phase coherence (ITPC) obtained via wavelet transformation on the single trial ERP data.

Although these studies proved PARAFAC to be a useful alternative for the above-mentioned methods on matrix data, no single trial information was yet included

as PARAFAC was only applied to ERP measures which were averaged across trials. The current study, however, brings together the advantages of PARAFAC with the search for task-related information in single trial ERPs. For this reason, PARAFAC is used to extract sources from three-way data arrays with modes $channels \times time \times trials$. Compared to earlier studies [53, 149, 151], no wavelet transformation is applied prior to decomposing the data. As such, the PARAFAC decomposition will be based on characteristic temporal patterns rather than spectral behavior. This approach was, to our knowledge, never followed before with the aim of investigating the ERP's single trial characteristics and will be validated in this study on the data from the visual detection task explained in Chapter 2.

More specifically, to assess the potential of PARAFAC for this particular application on single trial ERP data, the performance of the method is investigated at different levels of increasing difficulty. First of all, the performance of PARAFAC in identifying different task-related conditions in the data is examined. To this end, also the importance of preprocessing the data is taken into account. Second, the same decomposition is also validated on ERPs from EEG data acquired simultaneously with fMRI data inside an MR scanner. Since these data are more severely contaminated with artifacts than the data measured in more optimal circumstances, this allows testing the robustness of the method. Third, based on the superior extraction of task-related information with PARAFAC compared to raw data, the resulting components are used to investigate the relationship between ERPs and fMRI.

5.2 Materials and methods

5.2.1 Experimental data and preprocessing

As mentioned above, this chapter is based on the data from the visual detection task. All 27 subjects mentioned in Chapter 2 and listed in Table A.1, have been included. Not only their data measured outside the scanner were used (subjects 1 to 19, measured in Leuven or Maastricht), but also data, measured simultaneously with fMRI in the Philips scanner in Leuven, were included in the study (subjects 1 to 27, except subject 4). In addition, for subjects 1, 5, 20, 21 and 23 also the data acquired in the Siemens scanner were employed for the presented analyses.

The reason why the simple detection task was chosen for this work is that it is known to evoke robust C1, P1 and N1 components, showing different properties, depending on the position in the visual field where the stimuli are shown. The most prominent difference is found between the ERPs for left versus right stimuli. In particular, the contralateral P1 is known to precede the ipsilateral P1 [67].

Although less pronounced, also stimuli shown in the upper and lower visual field cause differences in ERP components [37, 67, 214]. More specifically, these differences are found in the early C1 component (inverting polarity between upper and lower stimuli) and the amplitudes of the P1 and N1 components.

The acquired EEG data were subjected to the preprocessing steps that were explained in Chapter 3. From the simultaneously measured EEG signals, gradient and ballistocardiogram artifacts were removed. All data (also those measured outside the scanner) were filtered and ICA was performed to reduce residual BCG artifacts and eye blinks. Data were then rereferenced to the average of TP9 and TP10 (the closest electrodes to the mastoids in the present electrode setup). To extract task-related ERPs, the different task blocks per subject were merged together and data were then segmented from 100 ms before until 400 ms after stimulus onset. Baseline correction was performed based on the 100 ms pre-stimulus interval and low quality trials were rejected by thresholding trials on 50 or 100 μV for measurements inside and outside the scanner respectively.

For the fMRI data, images were slice-time corrected, realigned, co-registered with anatomical images, normalized to a template and smoothed, corresponding to the preprocessing procedure explained in Chapter 3. Further analyses will be based on the GLM approach, which was also explained in that same chapter.

5.2.2 PARAFAC

PARAFAC is a higher-order decomposition technique that can decompose multi-way signals into a series of distinct atoms or components [190]. Every atom is characterized by a certain distribution or course in each of the modes. For the three-way case, each element of the data array can be defined as follows:

$$x_{dft} = \sum_{k=1}^{N_k} a_{dk} \cdot b_{fk} \cdot c_{tk} + e_{dft} \tag{5.1}$$

with N_k the number of atoms, a_{dk}, b_{fk} and c_{tk} the signatures of every atom in each of the modes and e_{dft} the model error. In this study, PARAFAC was performed with the N-way toolbox [7], in which the decomposition is computed based on an alternating least squares algorithm [190].

5.2.3 Application of PARAFAC to single trial ERP data

This section explains how single trial ERP data are inserted in the PARAFAC analysis, and discusses the relevant parameters and preprocessing steps that need to be selected. Also the occurrence of so-called degeneracy, is addressed.

Basic approach

As mentioned above, in this study ERP data were arranged in tensors with modes $channels \times time \times trials$. More specifically, trials from all peripheral stimuli (upper left, upper right, down left and down right) were taken together in the three-way data array. Applying PARAFAC to this type of data arrays, results in a number of atoms, each characterized by a certain spatial distribution, a certain time course and a certain variation across trials. The number of atoms corresponds to the rank of the data array, but, as opposed to the two-way case, the exact computation of this rank is not straightforward. As such, the number of atoms has to be determined from the data. In this study, the performance of the method was therefore investigated for the number of atoms varying from 1 to 10 (with a step size of 1).

Furthermore, since the aim of applying PARAFAC in this study was to validate its feasibility in distinguishing between different task-related conditions, it was verified whether including prior knowledge about the expected task-related differences improved the results. Two types of prior knowledge were used for this purpose. First, the three-way data array was modified as to specifically contain those channels where the difference between the task-related conditions is known to be most pronounced. More specifically, to distinguish between left and right stimuli, five parietal-occipital channels in each hemisphere were chosen. To distinguish between all four quadrant stimuli, the selected occipital set of channels was extended with three channels on the midline (Pz, POz and Oz). Since for both cases the results clearly improved, all further analyses were only performed on this limited set of channels. We believe that such a subset of interesting channels can also be determined for most other experimental paradigms.

A second type of prior knowledge consisted in limiting the time period included in the three-way arrays, based upon a visual inspection of the average ERP waveforms. For the left-right differences, the selected time period was between 50 and 250 ms for data measured outside the scanner, and between 100 and 300 ms for data measured inside the scanner. This time period should include both the P1 and N1 components, known to show most of the difference between left and right stimuli (the difference in P1 and N1 latencies between the inside and outside the scanner data was previously discussed in [10]). For distinguishing between all four quadrant stimuli, the time period was chosen to start slightly earlier (around 30 ms), as to include the early C1 component, which is known to be relevant for upper-lower differences.

Centering and rescaling

Before fitting PARAFAC to a three-way dataset, the data need to be preprocessed. The importance of this preprocessing has been emphasized in [95] and its effect on the data has been discussed in detail in [77]. As mentioned in these studies, two ways of preprocessing the three-way data can be used: centering and rescaling. Centering is accomplished by subtracting the mean in a certain mode from the data whereas rescaling is performed by dividing the data by its standard deviation in one specific mode. In the current study, centering was applied over channels while rescaling was performed in the trial mode. Also the combination of both was investigated.

Orthogonality

A frequent problem occurring when fitting PARAFAC models is the so-called phenomenon of degeneracy [95]. This term is used for models in which the corresponding signatures of different atoms are mutually highly correlated or in which two or more atoms counteract one or more other ones. This causes components to be redundant and therefore difficult to interpret [77]. Moreover, degenerate solutions may involve convergence problems and may indicate the PARAFAC model as such, not being appropriate for the data. Field and Graupe [77] suggested to impose orthogonality in one of the modes in order to avoid degeneracy (as also proved in [95]). Since orthogonality constraints [191] were believed to be data-specific, their effect was investigated in the channel, time and in the trial mode separately. To check the incidence of degeneracy, correlations were verified based on the cross-product-based definition suggested in [77].

5.2.4 Evaluation of the results

To test the ability of PARAFAC to capture task-specific information, we checked the possibility to distinguish between different task-related conditions based on the PARAFAC trial mode. For comparison, a similar single trial classification was also performed based on specific peak amplitudes retrieved from the raw data. In addition, the fact that data from a simultaneous EEG-fMRI experiment were available, allowed searching for a relationship between the trial-by-trial modulations of the obtained PARAFAC components and the fMRI data.

Single trial classification based on raw data

As explained in Section 5.2.1, the employed detection task is composed of stimuli that cause differences in the characteristics of certain ERP components. These

differences can be quantified on a single trial level and as such yield a classification between single trial ERPs belonging to different task-related conditions.

The most prominent stimulus-dependent effect found in the ERP components of the detection task, is the difference in latency and amplitude of the P1 and N1 peak for left versus right stimuli. For reasons of simplicity, the classification of the single trials is based on the P1 peak properties. The following approach, as originally proposed in [169], was pursued, for each subject separately. First, the average latency of the P1 peak was determined based on an average contralateral ERP from 10 parietal-occipital channels. Next, from every trial a P1 difference measure was calculated by subtracting the mean from 5 right parietal-occipital channels of the average amplitude in a small window around the average P1 latency from the same mean value measured on 5 left parietal-occipital channels. Since it is known that the contralateral P1 should always precede the ipsilateral one, this P1 difference should be positive for stimuli shown on the right and negative for stimuli shown on the left visual field. Further, a linear discriminant analysis (LDA) was used for classifying these difference values in two groups corresponding to left or right visual field stimuli (without taking into account the upper-lower difference). For this purpose, half of the trials that remained after thresholding (50 or 100 μV), were used for training and the other half for testing. This half was selected randomly and the same analysis was repeated 1000 times, so as to finally obtain one average classification accuracy for every subject.

As explained above, in addition to these left-right differences, our detection task data also show ERP differences for upper versus lower stimuli. Therefore, it was also tested whether PARAFAC was able to separate all four quadrant stimuli. To obtain a classification in these four quadrants with the raw data, two features were combined. Apart from the P1 left-right difference measure, also a single trial estimation of the amplitude of the C1 peak on the POz lead was used. Since the P1 difference should show opposite polarities for left versus right stimuli and the C1 peak should show opposite polarities for upper versus down stimuli, this combination seemed a correct criterion for classifying the raw single trials into the four quadrants. For the classification itself, again LDA was used on the 1000 randomized training-test sets.

Single trial classification based on PARAFAC

A similar single trial classification was now aimed for with PARAFAC. In line with the classification based on the raw data, one feature was used for distinguishing between left and right stimuli and two features were included in the differentiation between all four quadrant stimuli. The features of interest were the PARAFAC trial modes.

For the left-right difference, the trial mode of each component was fed into the

LDA and, with the same repeated randomization as for the raw data, classified into two groups. This resulted in a classification accuracy for every component and for every number of extracted components and selected preprocessing steps. Afterwards, the best component and parameter-preprocessing combination were selected based on the classification accuracy computed on the training data.

For the quadrant-specific case, the best pair of trial modes was selected beforehand. To this end, all trial signatures were correlated with both a vector based on the true left-right separation and a vector based on the true upper-down difference. The two trial modes showing the highest correlation for either one of them, were fed together in the LDA and classified into four groups. The accuracy was evaluated in the same way as explained above for the left-right case.

Relation with fMRI data

As mentioned in Section 5.1, task-related information extracted on a single trial level can be used in the analysis of simultaneously acquired fMRI data. Therefore, we investigated whether the trial-by-trial fluctuations obtained with PARAFAC added additional information to the analysis of the fMRI. However, since the ERP data were thresholded to remove bad quality trials, not all trials that were originally acquired from every subject were included in the eventual PARAFAC analysis. Having the ERP information from all originally acquired trials is nevertheless essential for connecting these to their corresponding fMRI activation. The approach to overcome this problem is, therefore, first addressed after which the actual fMRI analysis is explained.

Extrapolation of the trial mode to all trials One solution for the limited trial information could be not to threshold the data prior to the application of PARAFAC. This approach would, however, include extremely bad trials in the analysis which could completely ruin the interpretability of the resulting components. Therefore, in this chapter, an alternative approach was used. This approach was inspired by a similar method followed with ICA described in [145], and comes down to the extrapolation of the obtained decomposition from a limited number of trials to all the trials originally acquired. To understand this, it is useful to take a look at the formulation of the PARAFAC model based on the Khatri-Rao product [190]. Assume $\mathbf{X}$ is the matricized version (dimensions $IJ \times K$) of the original tensor $\mathcal{X}$ ($I \times J \times K$) and $\mathbf{E}$ the matricized version of the model error obtained in the same way. $\mathbf{A}$, $\mathbf{B}$ and $\mathbf{C}$ collect the signatures a_{dk}, b_{fk} and c_{tk} (cf. equation 5.1). The PARAFAC model can then be written as:

$$\mathbf{X} = (\mathbf{A} \odot \mathbf{B}) \cdot \mathbf{C}^T + \mathbf{E} \tag{5.2}$$

with $\odot$ a representation for the Khatri-Rao product and $\mathbf{C}^T$ the transpose of the matrix $\mathbf{C}$. Rewriting this equation and ignoring the model error yields a formula

for the matrix of the third PARAFAC mode (in our case the trial mode):

$$\mathbf{C} = [(\mathbf{A} \odot \mathbf{B})^{-1} \cdot \mathbf{X}]^T \tag{5.3}$$

with $\mathbf{W}^{-1}$ the pseudoinverse of the matrix $\mathbf{W}$. The latter equation provides a way to extrapolate a given PARAFAC decomposition to more trials. Taken the obtained components in the first two modes (represented by $\mathbf{A}$ and $\mathbf{B}$) and replacing the data array $\mathbf{X}$ (with the limited number of trials) by the data array $\mathbf{X}_{new}$ (with all trials included) yields:

$$\mathbf{C}_{new} = [(\mathbf{A} \odot \mathbf{B})^{-1} \cdot \mathbf{X}_{new}]^T \tag{5.4}$$

As such an estimation $\mathbf{C}_{new}$ for the full trial mode based on a PARAFAC decomposition on a limited number of trials is obtained. This trial mode can then further be used for relating the ERP to the fMRI data.

Analyzing the fMRI data The aim of this analysis was to investigate the effect of including amplitude information from the PARAFAC trial mode in the analysis of the fMRI data. The followed approach will be illustrated here on data from five subjects showing good to very good classification accuracy (>78%) for distinguishing between left and right stimuli. The classification was performed here based on a K-means clustering approach (preferred here over LDA to avoid the necessity of a separate training set), clustering the trial mode of the extracted PARAFAC components into two groups. Since, however, stimuli were shown in the four quadrants of the visual field, the information whether they were upper or lower stimuli was taken from the original task implementation itself. We could also have used a clustering in four quadrants, but unfortunately, classification accuracy for that case on inside data (see Section 5.3) did not seem high enough for analyzing fMRI data.

Based on the above clusters, we wanted to verify whether single trial amplitude information from PARAFAC improved the model for the fMRI data. This was done by using one standard regressor based on task triggers and constructing two other regressors from the PARAFAC trial mode. For these latter two, regressors were created corresponding to each of the stimuli, thereby following the classification as explained above. However, while the first type of regressors only consisted of fixed values at the time instants of the trials (and zeros otherwise), the second type contained the actual normalized amplitude values obtained from the PARAFAC trial mode. The resulting signals were convolved with a HRF model and employed as regressors in the general linear model explaining the fMRI data (with the SPM5 software). Afterwards, a simple t-test was used to summarize the results over the five subjects.

5.3 Results

First, an illustration is given of the type of components obtained when applying PARAFAC to *channels* × *time* × *trials* data. Then, the task-related information contained in these components is discussed and quantified with a classification accuracy, both for data measured outside and inside the MR scanner. Also the importance of preprocessing and orthogonality constraints is addressed. To end with, the relation with the simultaneously acquired fMRI data is investigated.

5.3.1 Illustration of the PARAFAC approach

Figure 5.1 shows an illustration of applying PARAFAC to a three-way data array from one individual subject (subject 8). The data shown here, were measured outside the scanner and only the time frame around the P1 and N1 components was included in the analysis. Two components were retrieved of which the spatial distribution as well as its time course and trial-to-trial behavior, are shown.

The first component (shown on the left in figure 5.1) is left-right symmetrical over channels and corresponds to the ERP information common to left and right visual field stimuli. The second component on the other hand, represents the difference between left and right stimuli. This can be seen in the asymmetry of the spatial distribution and can be quantified by using the trial mode for classifying between left and right stimuli. The latter gives an average classification accuracy of 94.75%.

5.3.2 Single trial left-right classification of outside data

After thresholding the data at 100 μV, all 19 subjects performing the task outside the scanner retained at least 95% of their original number of trials. However, three out of them (subjects 3, 6 and 11) seemed to have more severely distorted channels, as for these three subjects between 8 and 40% of their data was removed when checking the data with a more stringent threshold of 50 μV.

Since narrowing the ERP time interval gives a small improvement, the influence of the number of extracted components, the choice of orthogonality and the exact preprocessing steps on the classification accuracy is shown in Figure 5.2 for the limited time frame (50-250 ms). For every case, the average classification accuracy over subjects is shown, together with its standard error (standard deviation divided by the square root of the number of subjects).

Without centering or rescaling, imposing orthogonality in the channel domain is the most efficient choice, since reasonable results are already obtained with only a few components (i.e., 80% on average with three components). Also

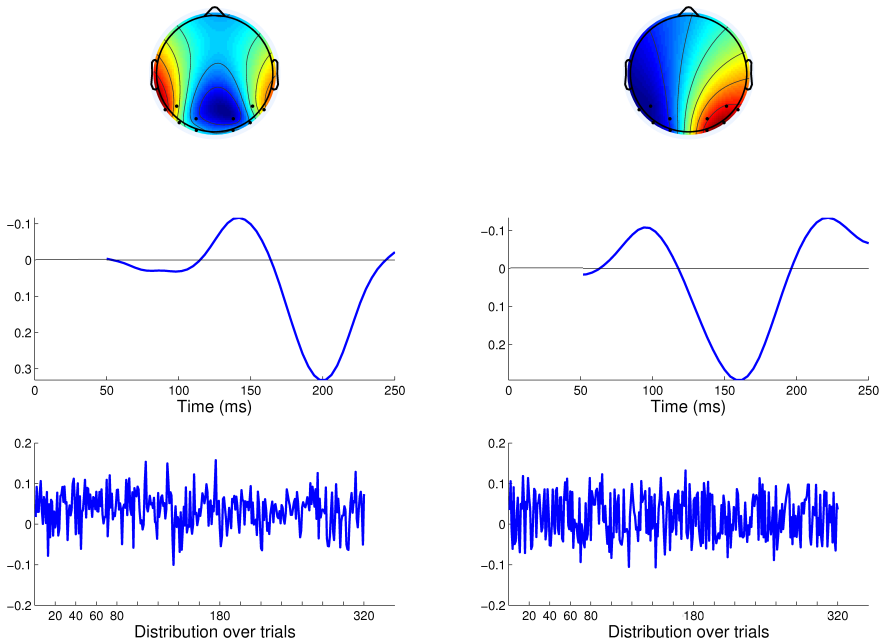

Figure 5.1: *Illustration of a PARAFAC decomposition on channels × time × trials data from one subject. Two components (orthogonal in the channel mode) have been retrieved from data from the detection task from 10 occipital channels and from a limited time frame. The upper part of the figure shows the spatial distribution of the components (only exact on the locations of the occipital electrodes, the rest of the scalp is extrapolated), the middle part of the figure shows the time courses and below, the distributions over trials can be found.*

orthogonality in trials or using no orthogonality at all can be useful, but the number of components to obtain a reasonable classification accuracy is higher. With centering or centering combined with rescaling, this dependence on the number of extracted components and orthogonality seems to almost disappear. Although there are still some small differences, the importance of careful parameter selection decreases to a great extent.

In Figure 5.3, the classification accuracy values from PARAFAC on the outside detection task data are compared with the ones retrieved from the raw data. For PARAFAC, not only the best individual results are shown, but also results obtained by using one fixed parameter-preprocessing set for all subjects. The choices made for the fixed parameter set are here using data with only the limited time frame (50-250 ms) included, applying centering and obtaining 5 components that are orthogonal in the channel domain. These choices were made, based upon

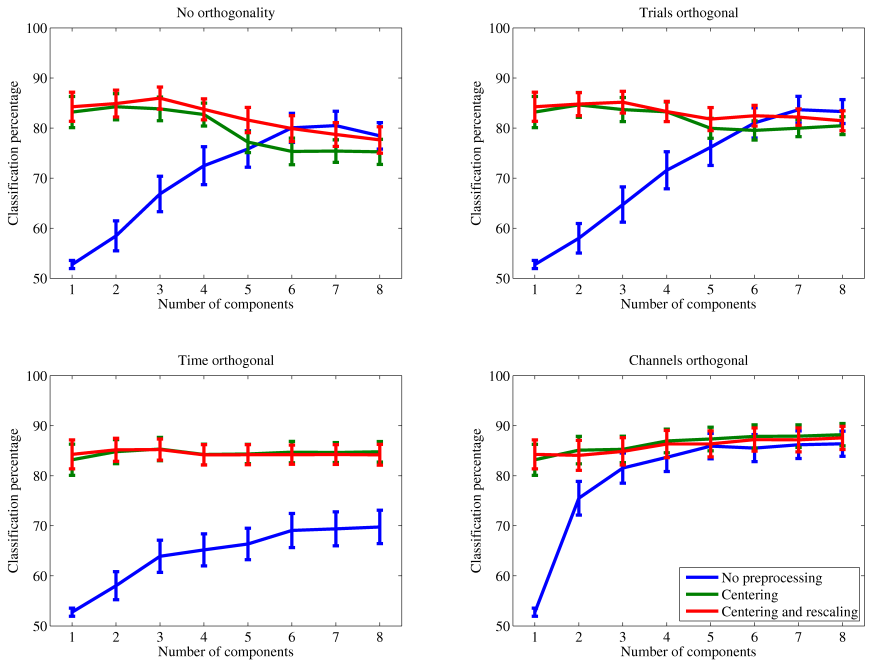

Figure 5.2: *Effect of centering and rescaling (in different colors), orthogonality (in different subplots) and the number of extracted components (on the horizontal axis) on the PARAFAC classification accuracy for the outside data. The shown values are average (lines) and standard error values (error bars) over subjects and correspond to the analyses including temporal prior knowledge (time frame of 50-250 ms). Regardless of the number of components extracted in each case, each time only one component was used for classification (selected based on the training data).*

the best average performance across subjects.

From this figure, it is clear that PARAFAC returns a higher classification accuracy than the raw data. The Wilcoxon signed rank test confirms this with a p-value of 0.0001 for both the individually optimal and the fixed parameter set.

5.3.3 Single trial quadrant classification of outside data

Classifying the single trials between left and right stimuli in fact ignores the other condition effect present in the current task paradigm, namely the one between upper and down stimuli. Including the investigation of this effect in the analysis,

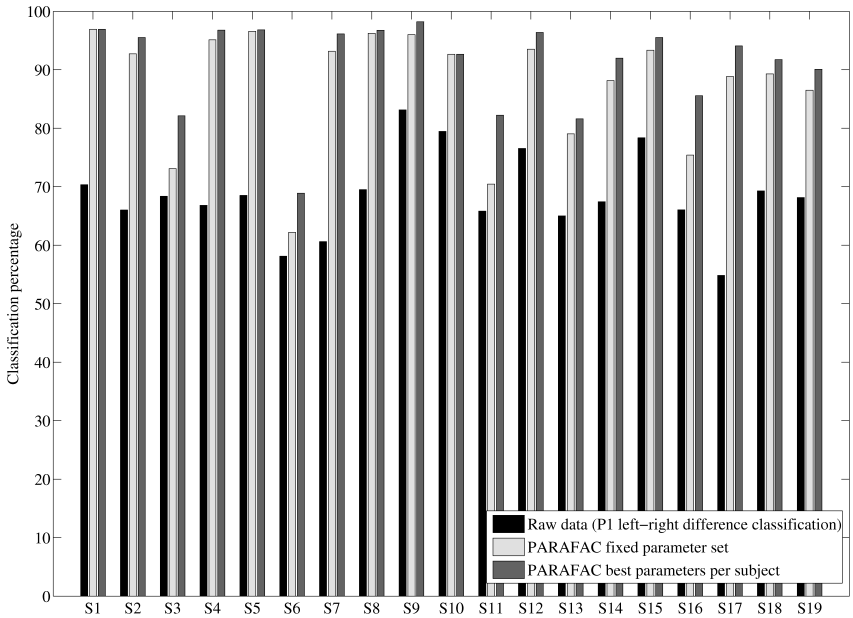

Figure 5.3: *Left-right classification accuracy values for all subjects (indicated with letter S) with both PARAFAC and raw data classification on the outside data. For PARAFAC, not only the best individual results are shown, but also results obtained by using one fixed parameter-preprocessing set for all subjects.*

allows a classification among the four quadrant stimuli. The employed data is the same as for the above left-right classification.

Concerning data preparation, centering seemed to give most improvement compared to the situation without any preprocessing. For orthogonality, there was a clear preference for applying no orthogonalization at all or imposing it in the trial mode. Extracting more components increased the performance of the classification, although this effect was not significant for every subject.

Contrary to the PARAFAC classification between left and right stimuli, when aiming at distinguishing between all four quadrant stimuli, the task condition information is no longer captured in only one PARAFAC component. More specifically, in most cases there are two components that need to be combined, one component explaining the difference between left versus right stimuli and another component related to the upper-down difference. An illustration of the combination of two PARAFAC components, revealing a clear distinction between the four stimuli is shown in Figure 5.4 (subject 5). The values on the axes

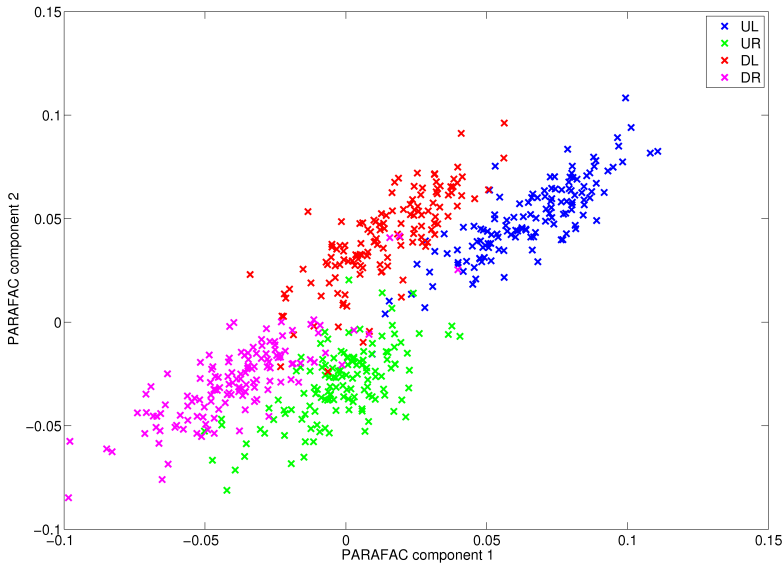

Figure 5.4: *Illustration of the combination of two PARAFAC components for distinguishing between the four quadrant stimuli in the detection task. The results are shown for subject 5 with centered data, orthogonality imposed in the channel mode and 10 components. The axes correspond to the trial modes of the two PARAFAC components while the colors of the marks denote the true stimulus type (UL = upper left, UR = upper right, DL = down left and DR = down right).*

correspond to the respective trial signatures of two components from a specific PARAFAC decomposition, whereas the colors indicate to which stimulus these points actually belong.

Figure 5.5 summarizes the results of classifying between all four quadrant stimuli based on both PARAFAC and the raw data. Similar to the results of the left-right classification, also here the best results are compared with the accuracy obtained when using one specific parameter set for all subjects. For this fixed parameter set, centering was used on the data with a limited time frame (30-250 ms), after which a decomposition in 10 components with orthogonalization in the channel mode was applied.

This figure clearly shows that PARAFAC outperforms the raw data classification also when used to separate all four peripheral stimulus types. This effect is confirmed statistically for both the best and fixed parameter set; the p-values of the Wilcoxon signed rank test are respectively $1.3 \cdot 10^{-4}$ and $1.6 \cdot 10^{-4}$.

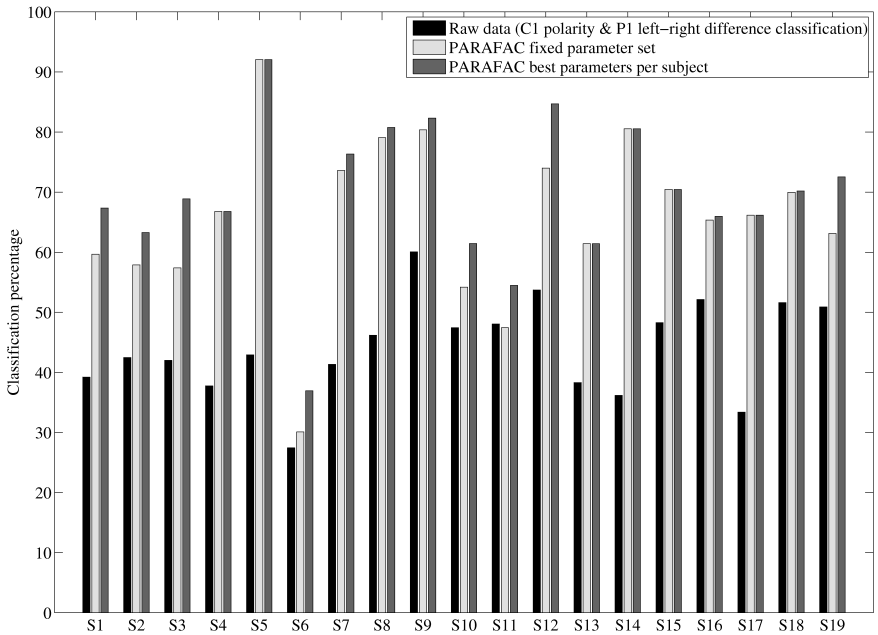

Figure 5.5: *Classification accuracy for all subjects (indicated with letter S) with both PARAFAC and raw data classification on the outside data, distinguishing the trials in the four quadrant stimuli. For PARAFAC, not only the best individual results are shown, but also results obtained by using one fixed parameter-preprocessing set for all subjects.*

5.3.4 Single trial left-right classification of inside data

As mentioned in Section 5.2.1, for the inside data another, more stringent, threshold was chosen. More specifically, trials were removed when their amplitude exceeded 50 μV. This hard thresholding was necessary since the simultaneous acquisition causes a more severe contamination of the data which, when not fully removed, can completely deteriorate the PARAFAC decomposition. However, as a consequence, the number of trials included in the inside PARAFAC classification is seriously reduced compared to the original number of trials and compared to the data outside the scanner.

For the 31 datasets (26 subjects of which 5 were measured in two different scanners), on average 67% of the trials were retained after thresholding. For all datasets but one this came down to at least 45% that could be used for further analyses. For the remaining dataset only 23% of the trials was used. All channels of this dataset were severely contaminated with residual BCG artifacts. Closer inspection of this dataset revealed uncommon patterns in the ECG lead which

caused unusual BCG shapes that were more complex to be removed.

Similarly to the data acquired outside the scanner, also here it was found that results improved by restricting the time range prior to the decomposition (100-300 ms). Centering and, to a lesser degree, rescaling, also seemed to have a positive effect on the classification accuracy. Imposing orthogonality in the channel mode seemed the poorest choice, but on an individual level results did benefit from orthogonal channels. The results got better when using more components, but with centering, less components had to be used to get a similar performance.

In Figure 5.6, classification accuracy values from PARAFAC on the inside data are compared with the ones retrieved on the raw data. For PARAFAC, not only the best individual results are shown, but also results obtained by using one fixed parameter-preprocessing set for all subjects. The choices made for the fixed parameter set are here using data with only a limited time frame included, applying centering and obtaining 9 components that are orthogonal in the trial mode.

The classification based on PARAFAC with the best parameters per subject is significantly better than the one based on the P1 left-right differences in the raw data ($p < 10^{-4}$). Although in this case it was more difficult to find one fixed parameter set, the results are also significantly better ($p = 0.0014$).

5.3.5 Single trial quadrant classification of inside data

In line with the distinction of trials in four quadrants performed on data measured outside the scanner, the results of this same analysis were also verified for inside data. Concerning data preparation, the differences between with and without centering and rescaling were very small, but there was a clear preference for imposing orthogonality in the trial mode. The results also clearly improved by extracting more components.

Figure 5.7 summarizes the results of classifying between all four quadrant stimuli based on both PARAFAC and the raw data. Also here the best results are compared with the accuracy obtained when using one fixed parameter set for all subjects. In this case, the time-limited data were centered and rescaled and 9 components that were orthogonal in the trial mode, were extracted.

Although the performance of single trial quadrant classification here is obviously lower than in the case of outside data, PARAFAC is still better than the raw data classification. This effect is confirmed statistically for both the best and the fixed parameter set (p-values of respectively $1.2 \cdot 10^{-6}$ and $5.9 \cdot 10^{-5}$).

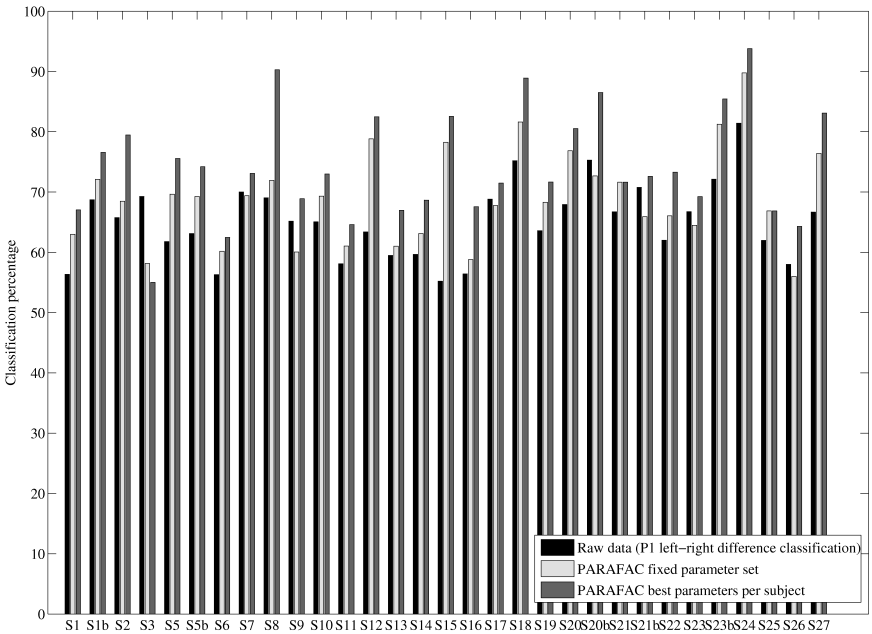

Figure 5.6: *Left-right classification percentages for all subjects (indicated with letter S) with both PARAFAC and raw data classification on the inside data. For PARAFAC, not only the best individual results are shown, but also results obtained by using one fixed parameter-preprocessing set for all subjects. For five of the subjects, also data measured in a Siemens scanner were included, these datasets are indicated with the letter b. Subject 4 is not included in this figure, since for this subject, only outside but no inside data were available.*

5.3.6 Relation with fMRI data

As explained above, the obtained task-related information was also used for analyzing the simultaneously acquired fMRI data. Results shown here, are based on data from five subjects. Three types of regressors were used (in separate analyses). The first one was a standard regressor based on the trigger information from the task, whereas the second one was based on the triggers according to the PARAFAC classification results. Finally, the third regressor included the amplitude information from the PARAFAC trial signatures (the c_{tk} values in equation 5.1) in the analysis. Activated regions obtained with the PARAFAC approach without amplitude information, are summarized in Table 5.1 for each of the four trial types.

The obtained activations not only nicely correspond to the findings when using

Table 5.1: *Regions obtained by using the classified trial information as input for the GLM analysis in SPM. The difference between upper and lower stimuli is based on the task itself, while the left-right classification is based on the PARAFAC output. As such, regions are retrieved for upper left (UL), upper right (UR), down left (DL) and down right (DR). For every region both its anatomical name and its Brodmann area (BA) are given.*

Trial type	Anatomical region	Brodmann area
UL	Right lingual gyrus	BA 18
	Right cuneus	BA 18
	Left middle occipital gyrus	BA 19
	Right precuneus	BA 7
	Left superior parietal lobule	BA 7
	Left precentral gyrus	BA 4
	Left postcentral gyrus	BA 3
	Left medial frontal gyrus	BA 6
	Right insula	BA 13
	Left and right cerebellum	/
UR	Left fusiform gyrus	BA 19
	Left middle temporal gyrus	BA 37
	Right middle temporal gyrus	BA 37
	Left postcentral gyrus	BA 3
	Left medial frontal gyrus	BA 6
	Left and right cerebellum	/
DL	Right cuneus	BA 17
	Left middle temporal gyrus	BA 37
	Right middle temporal gyrus	BA 37
	Left superior parietal lobule	BA 7
	Right precuneus	BA 7
	Left postcentral gyrus	BA 3
	Left medial frontal gyrus	BA 6
	Left and right insula	BA 13
	Left and right cerebellum	/
DR	Left lingual gyrus	BA 17
	Left middle temporal gyrus	BA 37
	Right middle temporal gyrus	BA 37
	Left superior parietal lobule	BA 7
	Right superior parietal lobule	BA 7
	Left precentral gyrus	BA 4
	Left medial frontal gyrus	BA 6
	Left insula	BA 13
	Left and right cerebellum	/

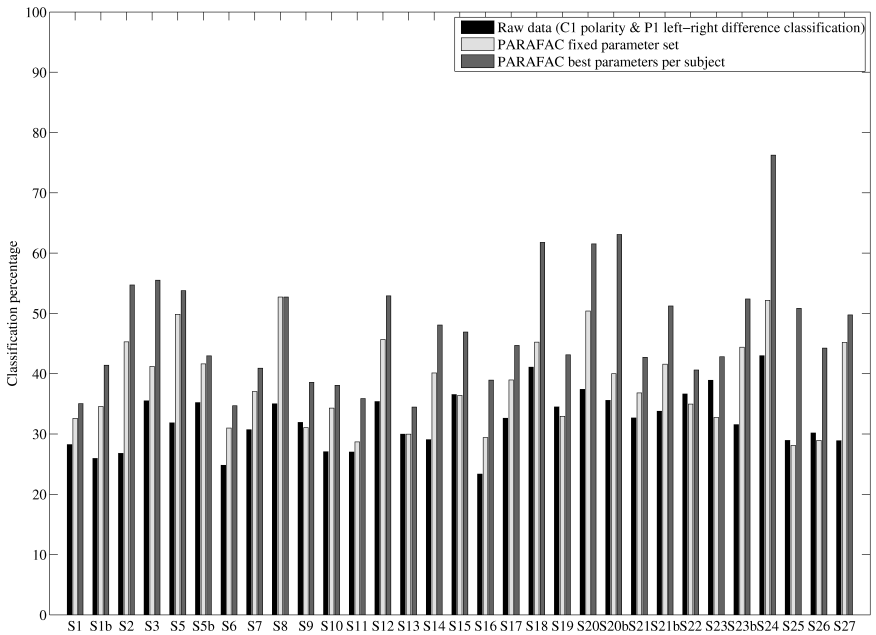

Figure 5.7: *Classification accuracy for all subjects (indicated with letter S) with both PARAFAC and raw data classification on the inside data, distinguishing the trials in the four quadrant stimuli. For PARAFAC, not only the best individual results are shown, but also results obtained by using one fixed parameter-preprocessing set for all subjects. For five of the subjects, also data measured in a Siemens scanner were included, these datasets are indicated with the letter b. Subject 4 is not included in this figure, since for this subject, only outside but no inside data were available.*

the original task triggers, but, moreover, also match the expected regions for this type of task. This can also be seen when comparing the obtained regions with the activations retrieved with JointICA, as shown in Chapter 6 [148]. First of all, the employed task requires visual detection, yielding activations both in the primary visual cortex (Brodmann area (BA) 17) and in the extrastriate visual areas (BA 18 and 19). Although this is not shown here, these activations also show the retinotopical mapping effect, meaning that their position around the calcarine sulcus is related to the position of the stimuli in the visual field. Also the lateral occipital complex (LOC - BA 37) is activated, an area involved in object recognition. Further, activations in the superior parietal lobule (BA 7) indicate involvement of spatial orientation. In addition, the task requires button press responses which activate areas in the primary motor cortex (BA 4), somatosensory cortex (BA 3) and premotor cortex (BA 6). Finally, for every trial type (upper left, upper right, down left and down right), also the insula (mostly contralateral)

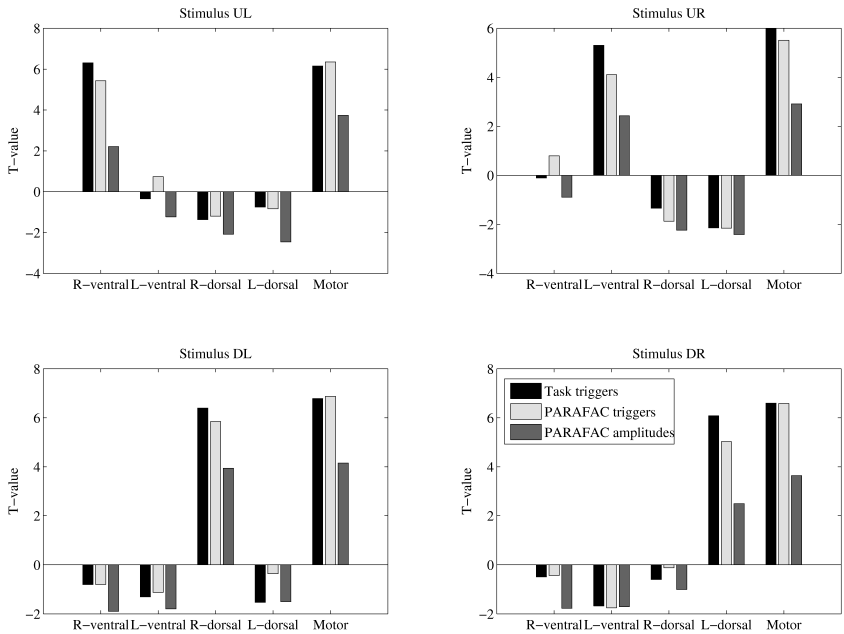

Figure 5.8: *t-values in five selected ROIs (four visual regions with their position around the calcarine sulcus indicated - R = right, L = left - and a motor region), averaged over voxels and subjects and for each of the stimuli (UL = upper left, UR = upper right, DL = down left and DR = down right). Values are shown for three different types of analyses: a standard GLM analysis based on the triggers from the task, a similar analysis based on the left-right classification obtained with PARAFAC and an analysis based on regressors including PARAFAC amplitude information.*

and both sides of the cerebellum are activated.

Using the regressors based on the PARAFAC amplitude information revealed the same regions. However, the obtained t-values in these regions were lower than in the case without amplitude information. This is illustrated in Figure 5.8. Five small regions of interest (ROIs) were defined for each subject, based on the activation obtained using the original task triggers. These ROIs were four locations in the early visual areas, each corresponding to one specific stimulus and a last ROI was defined in the motor area. For each location and each stimulus, the average t-value over all corresponding voxels and the five subjects, was calculated. As such, this t-value can be compared for analyses based on the task triggers, on the PARAFAC classification and on the PARAFAC amplitude values.

Because the extraction of the different ROIs is based on the standard fMRI analysis using task triggers, it is obvious that this analysis shows the expected activations

for each of the stimuli (blue). The analyses based upon PARAFAC (both with and without amplitudes), however, also yield these same regions.

Nevertheless, there is a clear decrease in t-values when comparing the activation based on the amplitude regressors with the activation obtained with the trigger information from the task or the PARAFAC classification. This is confirmed statistically, showing p-values above 0.45 when comparing the triggers from PARAFAC with the task, but resulting in p-values between 0.03 and 0.08 and between 0.007 and 0.05 when comparing the amplitude approach with the approaches based on task and classification triggers respectively. As such, it can be seen that using the amplitudes from the trial mode explaining most of the left-right differences, seems to deteriorate the fMRI results.

5.4 Discussion

In this study, we explored the ability of the higher-order decomposition method PARAFAC to extract specific task-related information from single trial ERP data. The results were validated by using the obtained components for classifying between different task-related conditions and by comparing these results with a similar classification based on raw data. Both data acquired in a control room and data acquired inside an MR scanner simultaneously with fMRI, were used. The latter not only allowed testing the robustness of the method on data with a lower signal quality, but also enabled including the obtained single trial amplitude values (from the PARAFAC signatures in the trial mode) in the analysis of the fMRI data.

Our results indicated that PARAFAC is indeed able to capture components reflecting task-related ERP differences on a single trial basis. This was clearly shown for both the left versus right stimuli and for the four quadrant stimuli. Careful parameter tuning was, however, needed. The results were significantly better than when only raw data characteristics were used for classification, possibly suggesting an improved denoising achieved with PARAFAC. Also the data measured inside the MR scanner allowed this classification, although the lower signal quality influenced the performance of the approach. In addition, one of the advantages of having simultaneously measured EEG and fMRI data available, is the possibility to investigate which features of the electrical and hemodynamic responses are related. Since the PARAFAC trial mode was found to be a meaningful representation of the task-related information, its amplitude information was also investigated within this context. However, although fMRI results based on the PARAFAC classification were similar to the ones based on standard analyses, including the amplitude values seemed to reduce the obtained activations.

When looking at the results, it becomes clear that there is not only a difference between the different stimuli that need to be distinguished, but also there exists a large inter-subject variability in the classification performance. This variability is thought to be mainly related to individual differences in data quality caused by, e.g., different amounts of residual artifact and noise. A clear illustration of this can be found in the fact that the classification accuracy for left-right differences in outside data was lower in subjects 3, 6 and 11. As explained in Section 5.3, these were exactly the subjects with an inferior data quality, as shown by their higher data loss after thresholding.

To verify the generalizability of the PARAFAC single trial extraction, we also tested whether we could distinguish between the Go and NoGo stimuli from the Go/NoGo task. The results of these analyses (performed on data from 9 subjects measured outside the scanner, cf. Chapter 2) are not included in detail in this chapter, but are briefly reported in this discussion as an additional argument for the usefulness of PARAFAC for single trial ERP extraction. The raw data classification (based on the N2 peak) resulted in an average classification accuracy of 60.33% $\pm$ 7.87% and with PARAFAC, accuracies of 71.29% $\pm$ 7.28% were obtained. Although these percentages are clearly lower than in the case of the left-right distinction in the detection task, the improvement of PARAFAC is still significant ($p = 0.0078$). The lower accuracies can possibly be attributed to the fact that the Go and NoGo ERPs are especially distinct in amplitudes, but less in spatial topography (as opposed to the left and right stimuli in the detection task).

Using PARAFAC for classifying between different conditions on a single trial basis, has certain advantages. First of all, the method is relatively fast, especially when extracting lower numbers of components. Since it was shown that centering reduced the number of required components to obtain a certain performance, it can be considered a crucial preprocessing step in cases where speed is important. Second, as opposed to the raw data classification, PARAFAC does not require detecting specific peaks or features from the ERP data. In our case, the raw data classification could maybe still have been improved by selecting other peaks or combining a set of peaks, but the need for peak detection and selection makes it a more laborious approach. For PARAFAC, prior knowledge concerning channels and time was used, but this selection was clearly less stringent than the one needed for the raw data classification.

A major disadvantage of the PARAFAC approach is, however, the need for parameter tuning and careful preprocessing. Our results clearly show that the most optimal preprocessing steps and choice in orthogonality and number of components are dependent on the stimuli and the subject under study. Nevertheless, this finding does not come as a surprise, since also for PARAFAC applied to average ERP data, these parameters had to be optimized for each dataset [77]. A possible way to do this (as also followed in this chapter), is to optimize the parameters based on training data. This of course requires the availability of a sufficient

amount of data.

One might also ask whether the trilinear structure of PARAFAC is the most appropriate model for ERP data and the condition-specific information. For this reason, Mørup et al. [150] proposed the use of so-called shifted PARAFAC for ERP data. The advantage of this approach would be that, e.g., small time shifts of certain components would not completely deteriorate the quality of the decomposition. This algorithm was, however, also tested on these data and did not yield any good results. A short simulation study (not shown here) revealed that this was probably caused by the amount of noise on the data, which the employed implementation of shifted PARAFAC (provided for MATLAB by the same authors) did not seem to be able to handle. Of course, this result does not exclude the fact that other higher-order methods (or another implementation of this shifted PARAFAC) might be more suitable for modeling the ERP data. E.g., the Tucker method [198, 199] has already been used on EEG data [1] and recently also other related methods have been proposed [47, 48, 49]. Since the structure of these models, however, allows more interaction between the obtained components, the interpretation becomes more difficult when compared to the PARAFAC model.

The obtained classification of single trial ERP data among several stimulus types, makes the presented PARAFAC application also a promising approach for use in real-time BCI applications. These BCIs are systems that use brain signals for the control of one or several external devices. The use of PARAFAC in BCIs is, however, not completely new. A number of studies investigated the potential of PARAFAC for distinguishing trial types, especially in the field of motor imagery tasks [36, 124] and also visually evoked potentials [129]. Nevertheless, to our knowledge, the majority of these studies work on a wavelet-transformed version of the acquired ERP data. In the current application, the shape (both amplitudes and latencies) of the ERP waveform is essential for the distinction between the different stimulus types. To capture this information in the decomposition, it is necessary to use the raw single trial data in the analysis. For this reason, we believe that the application of PARAFAC in $channels \times time \times trials$ modes, as presented here, might be a valuable alternative in specific BCI applications.

In addition, we want to state that we do not claim that our PARAFAC classification outperforms all the existing methods in the field of single trial classification. For that, we should compare them in an extensive validation study, which was not the objective of the current work. Moreover, we focused on the decomposition with PARAFAC delivering the features for classification, but the classification algorithm itself was not optimized. Using more advanced classifiers, based on, e.g., support vector machines (SVMs), instead of the currently used LDA or K-means methods, could further improve the obtained classification results.

The fact that the fMRI results obtained with PARAFAC triggers without amplitude information correspond to the results from a standard fMRI analysis,

may seem obvious in cases with high classification accuracy. They are, however, mainly shown for interpreting the difference between the task-trigger based and the PARAFAC amplitude-based analyses. In cases where the stimulus information would be unknown for a certain reason, the fMRI results could also serve as an alternative validation for the task-specificity of the obtained decomposition (as proposed in [54]).

In addition, in this context, it is also important to know which features correlate between EEG and fMRI. This information can be searched for on a single trial level when both modalities have been acquired simultaneously. In various EEG-fMRI studies, the aim was therefore to identify the BOLD correlates of the single trial amplitudes of specific ERP components, but findings of this type of analyses were rather diverse. On the one hand, applying the integration-by-prediction method yielded spatially distinct regions for single trial P2, N2 and P3 modulations in an auditory oddball task [74]. On the other hand, [13] and [144] did not find significant correlations with respectively single trial P1, and N1 and P2 amplitudes, but rather with ERP latencies [13] or time-frequency behavior [144].

According to [23], an essential step in finding the relationship between EEG and fMRI single trial variation, is to be able to distinguish between functionally significant trial-to-trial variability and variability that merely accounts for noise. Our PARAFAC approach yielded meaningful components that were related to task-specific conditions, significantly better than similar measures on raw data. For this reason, we wanted to compare the analysis of fMRI based on the PARAFAC trial signatures with the standard approach of using the trigger information from the task. The results, however, did not confirm any specific relation between the PARAFAC trial mode and the fMRI BOLD signal. This not only opens the question whether or not the amplitude variation across trials which is captured in PARAFAC is representative for the amplitude variability across evoked responses, but also whether single trial variability measures can always be expected to correspond between ERPs and fMRI.

Our combined "PARAFAC-fMRI" approach assumes that the single trial variability observed in the ERPs is reflected in the fMRI data. However, this is not necessarily true since EEG and fMRI can, e.g., differ in their sensitivity to experimental manipulations [57]. Moreover, in an empirical study of [210], functionally different hemodynamic and electrophysiological patterns were shown within the same task. For the fMRI data, it is known that its variability originates from coherent spontaneous fluctuations in brain activity [79, 80]. For the ERPs, several sources of variability have been discussed, ranging from ongoing alpha rhythms [16] to task manipulation and preparation mechanisms [180]. Studies specifically investigating the relationship between EEG and fMRI single trial fluctuations, reported relationships of the fMRI with alpha power (e.g., [14, 122]), alpha phase variability [179] and high-frequency oscillations in the gamma band [158]. The variability of such spontaneous brain rhythms might be so pronounced,

that it hides the functionally relevant variability of the evoked responses. It might be for this reason that the contribution found in a recent study of [50], of single trial ERP modulations to the link between EEG and fMRI, was very small. Further research is needed to obtain a a fuller understanding of the observed phenomena.

5.5 Conclusion

In this study, we showed the possibility of capturing task-specific information in single trial ERP data with PARAFAC. More specifically, the trial modes obtained when decomposing $channels \times time \times trials$ data with PARAFAC, can be used as features for a classification of the trials in several trial types. This was shown for data from a visual detection task measured both in a control room and inside an MR scanner. The presented results not only extend previous results with PARAFAC on ERP data, but are also promising for applications in BCI systems. Whereas earlier findings in this field were mostly based on averaged ERPs or wavelet-transformed single trial ERPs, our results show that it is possible to extract meaningful results from raw single trial ERP data.

Chapter 6

ERP-fMRI integration based on subject variability: a validation study

The extraction of task-related information on a single trial level with PARAFAC, allowed us in the previous chapter to search for a trial-by-trial relationship between ERPs and fMRI. However, also other approaches exist, e.g., retrieving peak-specific results based on similar ERP and fMRI characteristics across subjects. This chapter will, therefore, focus on the possibilities of such an alternative approach, namely JointICA. First, in Section 6.1, the assumptions and properties of JointICA will be introduced. Section 6.2 will then discuss in more detail the employed datasets and the application of JointICA to these data. An overview of the results will be given in Section 6.3, after which they will be discussed in Section 6.4. The chapter will end with some conclusions in Section 6.5.

6.1 Introduction

From the overview of possible integration methods presented in Chapter 1, it is clear that the fusion of EEG and fMRI is often performed at a single trial level. In line with these approaches, in Chapter 5, we also investigated the possibility of using the extracted task-related ERP information from PARAFAC in the analysis of fMRI data. As addressed in Section 5.4, however, there are certain issues that complicate the search for a trial-by-trial connection between EEG and fMRI. Not only the cause of variability in EEG and fMRI might be different [210], but also, it

is not straightforward to distinguish meaningful trial-by-trial variation from noise [23]. In simultaneous measurements which are necessary for single trial integration approaches, the latter becomes even more difficult, as was also reflected in the lower classification performance of PARAFAC on such data.

In contrast, another type of integration approach avoids these complications by not relying on trial-by-trial fluctuations for the data fusion but rather on a similar behavior of the two modalities across subjects. One such approach is JointICA [29]. As explained in Section 1.1.6, this method is based on the identification of independent components from EEG and fMRI simultaneously. Although this approach can also be used with single trial data [154], in this chapter we will investigate its possibilities on averaged ERP and fMRI signals. Using these averaged ERP and fMRI data, has the clear advantage of a superior data quality compared to single trial data.

JointICA is based on the assumption that the different components (peaks) of the ERP and the hemodynamic response corresponding to the same stimulus covary, either because they are generated in the same brain region [131], or because the BOLD active areas have participatory roles in ERP activity, but do not generate the signal themselves. Hence, it is believed that ICA will be able to disentangle these components and connect the electrical activations (ERP peaks) to their corresponding BOLD responses [29]. The hypothesis about this one-to-one relation between physiological origin and statistical dependence, however, is not necessarily true, since there is no particular mathematical reason to ensure capturing different ERP peaks always together with their corresponding fMRI activations. This has not only to do with the difficulty of assigning statistical independence to spatial activity patterns [44], but also with the very different nature of EEG and fMRI. Nevertheless, JointICA was shown to give meaningful results for integrated ERP and fMRI data in different applications [31, 32, 81, 221].

To further explore the possibilities of JointICA and, at the same time, address some of the unanswered methodological concerns regarding its assumptions, we validated the performance of the method on the data from the visual detection task. More specifically, we first assessed the relevance of the JointICA results by visually checking the obtained components and comparing them with findings from related studies [66, 68, 169]. In addition, we investigated the link between ERPs and fMRI by reassigning the ERPs and fMRI activation maps over participants, thus destroying the amplitude link between the two modalities. Moreover, the importance of the ERP-fMRI link was also examined by comparing the JointICA results with an individual ICA analysis on ERPs and fMRI separately. Finally, we investigated the importance of data quality by evaluating the use of data measured outside the scanner and we checked the required data volume.

The validation study performed in this chapter, mainly focuses on the relevance of the JointICA results and data quality issues. For a more elaborate discussion on

the assumptions behind JointICA and the effect of the employed ICA algorithm, the reader is referred to the JointICA study, described in [148]. The results presented here, also form a part of that study.

6.2 Materials and methods

In this section, the datasets used for this validation study will be described, after which the JointICA algorithm will be explained. Next, the analyses performed to investigate different aspects of the method, will be addressed.

6.2.1 Experimental data: acquisition and preparation

As mentioned above, this chapter is based on the data from the visual detection task (cf. Chapter 2 and Table A.1). More specifically, simultaneously acquired EEG and fMRI data from the Leuven session were included from 26 subjects (all subjects except subject 4). In addition, for 18 subjects (1 to 3 and 5 to 19), also the data measured outside the scanner (Leuven or Maastricht) were used.

The acquired EEG data (both inside and outside) were subjected to the same preprocessing steps as in the previous chapter, with the only difference that a sampling rate of 500 Hz was used (instead of 250 Hz). To create the ERPs, data were rereferenced to the average of TP9 and TP10, segmented from 100 ms before until 500 ms after stimulus onset, baseline corrected (-100 - 0 ms) and thresholded at 200 μV. Thereafter, an average ERP for each stimulus type was computed, and these averaged ERPs were fed into the JointICA analysis (see below).

For the application of the JointICA algorithm, the ERP data from the electrodes PO7 and PO8 were used to observe the activations corresponding to right and left visual fields respectively (one electrode per application of the method). The ERP belonging to the Oz electrode is additionally used to observe the C1 peak, corresponding to the activations in the primary visual cortex. As explained in the previous chapter, the use of Oz is needed since this ERP component will be mainly found on midline electrodes [66, 68, 140].

The fMRI data were slice-time corrected, realigned, co-registered with their anatomical image, normalized to a template and smoothed, corresponding to the preprocessing procedure explained in Chapter 3. A standard GLM fMRI analysis (cf. Section 3.2.2) was subsequently performed, based on stick-functions for each of the 5 stimulus locations (upper left, upper right, down left, down right and central). The 6 movement parameters (three for both translation and rotation) obtained during realignment, were inserted in the model as covariates of no interest. As a

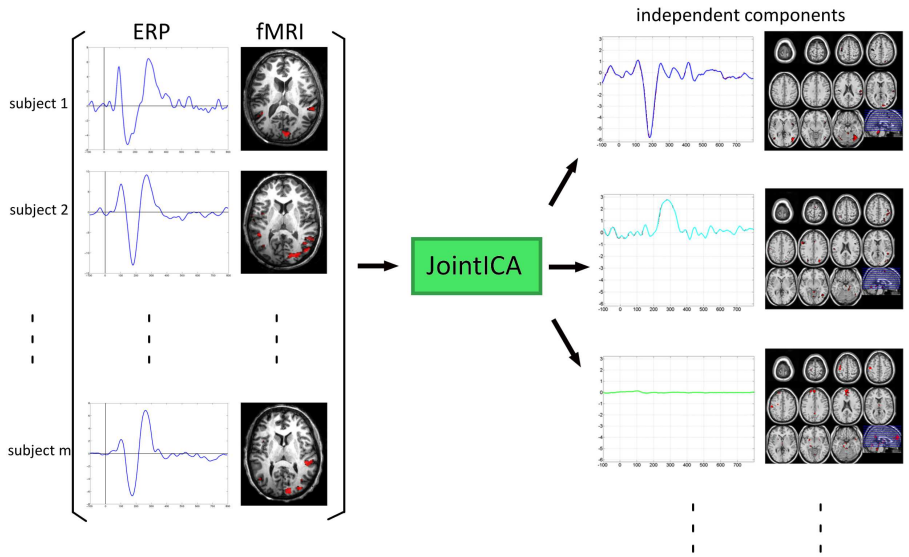

Figure 6.1: *Schematic representation of the application of the JointICA method to average ERPs and fMRI maps from m subjects. On the left the matrix with the concatenated ERP and fMRI data per subject is shown, which is (after upsampling of the ERPs and normalization) fed into JointICA. On the right some examples of resulting components are presented, each consisting of an ERP and an fMRI part.*

result, the design consisted of $5 + 6 = 11$ variables per experimental block per subject.

6.2.2 JointICA

JointICA was originally proposed in [29] and is freely available through the Fusion ICA Toolbox (http://icatb.sourceforge.net). As illustrated in Figure 6.1, it is applied as follows.

For every subject and stimulus, the fMRI activation map obtained with the SPM GLM analysis (explained above and in Section 3.2.2) has to be concatenated with the average ERP for this specific stimulus. However, to compensate for the disproportion between the number of voxels in the fMRI map and the number of time samples in the ERP signal, the ERP data are first upsampled using cubic spline interpolation. In addition, both ERP and fMRI data are normalized by subtracting their average and dividing by their standard deviation. The concatenated ERP-fMRI vectors for each subject, are then arranged together in

one matrix and fed into an ICA algorithm. The employed ICA algorithm (cf. Section 4.2.5) for this purpose was Infomax [17]. The equation of ICA, which has been explained in Chapter 4 (equation 4.1), can be modified as follows:

$$[\mathbf{X}^{\mathrm{fMRI}}\ \mathbf{X}^{\mathrm{ERP}}] = \mathbf{A} \cdot [\mathbf{S}^{\mathrm{fMRI}}\ \mathbf{S}^{\mathrm{ERP}}] + \mathbf{N} \tag{6.1}$$

Also here $\mathbf{X}$ and $\mathbf{S}$ represent the matrices of respectively acquired and source signals, but their superscripts indicate their correspondence to the fMRI or ERP matrix part. It is clear from this equation that the same mixing matrix $\mathbf{A}$ is assumed for both modalities. As such, the amplitudes of the ERP peak and of the BOLD response invoked by an activated area are expected to vary in a similar way across subjects. This corresponds to the above-mentioned assumption of JointICA that the electrical correlate of brain activation (expressed in the ERP components) and the hemodynamic response to brain activation (BOLD response) are generated by the same population of neurons. Additionally, JointICA will reveal regions that were not directly involved in the creation of the ERPs, but participated in their source activity, and therefore covariate strongly with a particular ERP wave.

As can be seen from Figure 6.1, the result from JointICA is a set of independent components represented by both a time course (ERP information) and a spatial map (fMRI information). For the employed data, the number of extracted components was investigated in detail in [148] and was eventually always chosen equal to the number of subjects included in the analysis.

6.2.3 Application of JointICA

To study different aspects of the JointICA approach, the following analyses were performed. First of all, JointICA was applied to the simultaneously recorded EEG and fMRI data from the 26 subjects. The relevance of the results was validated by comparing the resulting components for each stimulus with the activations that are expected from earlier studies [66, 68, 140, 169]. Subsequently, the same analyses were repeated, but now with ERP and fMRI data combined in a random order. By violating the mutual correspondence between ERP and fMRI data, these additional analyses should allow evaluating the above-mentioned JointICA assumption about similar ERP and fMRI patterns across subjects. Additionally, we also applied ICA to ERP and fMRI data separately to show the difference for both modalities compared to the JointICA analysis on the simultaneously acquired data. Based on these analyses we expect to understand whether the JointICA algorithm separates components and sources based on the interaction between both modalities, or whether the separation of one of the modalities is influenced (or driven) by the separation of the other one.

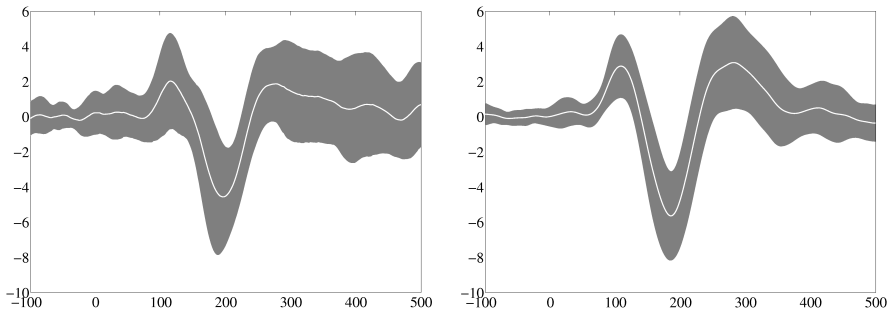

Figure 6.2: *Average ERPs (white), and the standard deviation (gray) of the simultaneously recorded ERP data from 26 subjects (left) and the ERP data recorded outside the scanner room from 18 subjects (right)*

Next, the importance of data quality was investigated by replacing the simultaneously recorded EEG data in the above analyses, with the EEG data acquired outside the scanner. As such, for each stimulus, a new data matrix with 18 rows (= 18 subjects) was obtained. This approach is justified, since with average ERPs, the signals should theoretically not differ between simultaneously and non-simultaneously measured sessions. The quality of the average ERPs measured outside the scanner is also clearly better, as illustrated with the standard deviation of these ERPs across subjects in Figure 6.2. Related to this data quality issue, we also checked to which extent the number of subjects affected the decomposition.

6.3 Results

As explained above, the JointICA method was first applied to the simultaneously recorded EEG and fMRI data from 26 subjects. In Figure 6.3, the resulting components for the down left stimulus are shown. More specifically, those components are presented, that explain 80% of the variance in the ERP time range between 50 and 350 ms. For each area, Brodmann areas (BA) and MNI coordinates are also given.

To further clarify the connection between specific ERP peaks and their corresponding activated brain areas, a summary of the most important findings is also given in the left panel of Table 6.1 (again for the down left stimulus). In this table, the activated brain areas are denoted with their anatomical name and their Brodmann area (BA). Some regions that are less relevant for the present research (like the cerebellum) are not included. The information about the C1 peak is obtained by using the Oz electrode, instead of PO8 as above.

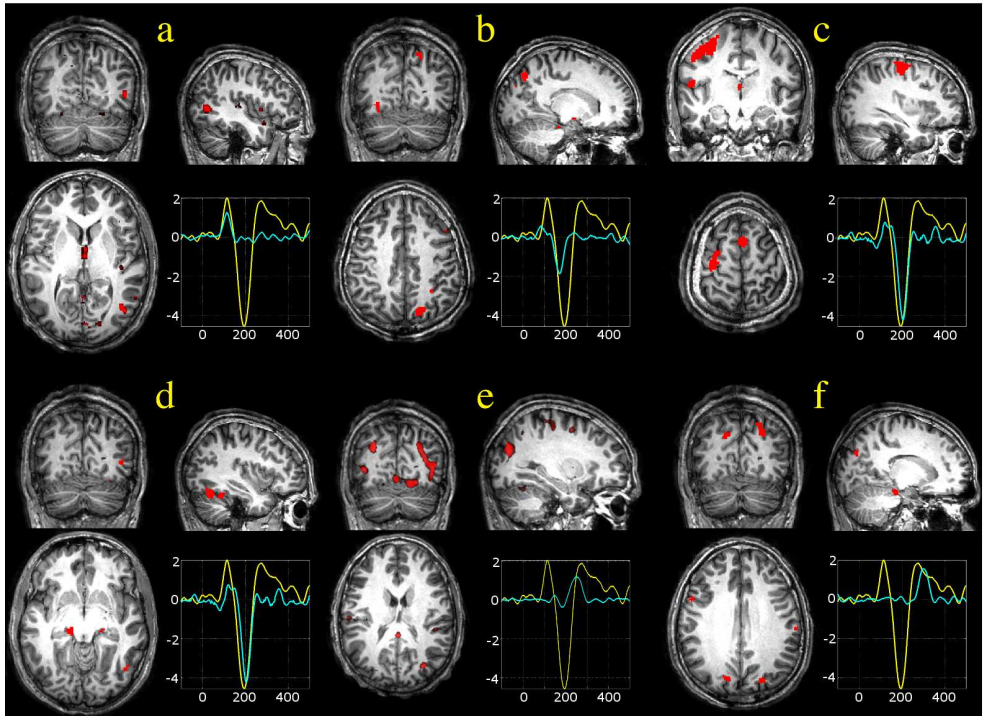

Figure 6.3: *Results of JointICA applied to simultaneously recorded EEG and fMRI data (channel PO8, down left stimulus). For every resulting component, the fMRI spatial map and the ERP time course are shown. (a) P1 ERP peak corresponding to activation in the right middle occipital gyrus (BA 37 - MNI [44 -70 4]) and right cerebellum (MNI [22 -70 -19]); (b) P1 (partly) and early N1 peak connected to activity in the right precuneus (BA 7 - MNI [16 -78 40]), cuneus (BA 19 - MNI [21, -79 43]) and left lingual gyrus (BA 18 - MNI [-31 -75 -8]); (c) P1 (partly) and late N1 peak linked to the right inferior temporal gyrus (BA 37 - MNI [47 -67 -3]) and right cerebellum (MNI [32 -63 -19]); (d) Same component (small P1 and late N1) visualized on other brain cross-section (revealing other fMRI areas): left postcentral (BA 1,2,3) and precentral gyrus (BA 4), insula (BA 13 - MNI [-56 -15 16]) and supplementary motor area (BA 6 - MNI [-47 2 50]); (e) Late N1 and early P2 peak associated to activation in the right and left cuneus (BA 19 - MNI [24 -83 36]), the right and left middle occipital gyrus (BA 19 - MNI [45 -77 9]), and the right cerebellum (MNI [17 -77 -15]); (f) P2 ERP component activating the right middle occipital gyrus (BA 18 - MNI [32 -86 2]), right and left cuneus (BA 18 - MNI [24 -83 36]) and right cerebellum (MNI [32 -68 -19]).*

Table 6.1: *Most important ERP peaks and their corresponding relevant activations retrieved from the simultaneously (left panel) and the non-simultaneously (right panel) recorded data for the down left stimulus. All ERP peaks were identified on channel PO8, except for the C1 peak of which the results were obtained with channel Oz. Regions like the cerebellum which are less relevant for the present research are not listed here, but they can be found in Figure 6.3 for the simultaneous data. The fMRI activations are presented with their anatomical name and their corresponding Brodmann area (BA).*

Simultaneous data			Non-simultaneous data		
ERP peak	Anatomical region	Brodmann	ERP peak	Anatomical region	Brodmann
C1	Right upper lingual gyrus	BA 17	C1	Right upper lingual gyrus	BA 17
P1	Right middle occipital gyrus	BA 37	P1 (early)	Right middle occipital gyrus	BA 19
				Right middle temporal gyrus	BA 37
				Left middle temporal gyrus	BA 37
			P1 (late)	Right fusiform gyrus	BA 19
N1 (early)	Right precuneus	BA 7	N1 (early)	Right precuneus	BA 7
	Right cuneus	BA 19		Right cuneus	BA 19
	Left lingual gyrus	BA 18		Right lingual gyrus	BA 18
N1 (late)	Right inferior temporal gyrus	BA 37	N1 (late)	Right middle occipital gyrus	BA 19
	Left postcentral gyrus	BA 1,2,3		Left postcentral gyrus	BA 1,2,3
	Left precentral gyrus	BA 4		Left precentral gyrus	BA 4
	Left medial frontal gyrus	BA 6		Left medial frontal gyrus	BA 6
P2	Right middle occipital gyrus	BA 18	P2	Right cuneus	BA 18
	Right cuneus	BA 18		Left cuneus	BA 18
	Left cuneus	BA 18			

From this table, it can be seen that the C1 peak is associated with early visual areas (BA 17), while the P1 is better connected to LOC (BA 37). The N1 peak on its turn, is not only linked to visual areas, but also to areas in the motor and somatosensory cortex (respectively BA 4 and BA 1, 2 and 3). The P2 component was found to correspond to extrastriate visual areas (BA 18). These activations are in line with results from previous studies as well as with the employed experimental paradigm (with button press).

Table 6.1 also summarizes the results of the JointICA analysis applied to the non-simultaneously measured data from 18 subjects (right panel). For comparison, also in this case, the results are shown for the down left stimulus from channel PO8 (and channel Oz for the C1 peak). As can be seen from this table, the independent components from simultaneous and non-simultaneous measurements largely overlap. Nevertheless, some small differences can be found, of which the most apparent one is the P1 activation of the right fusiform gyrus in the case of outside data. This activation makes the outside results slightly better, as it was expected based on earlier work [140].

When repeating the JointICA analyses for the simultaneously acquired data, but this time with the ERPs and fMRI in random combinations, the correspondence of the resulting components with the above findings becomes very small. The correlation of these components with the ones listed above is 0.4833 on average, with a standard deviation of 0.1802 (computed via Fisher's z-transform). In addition, when looking at the fMRI activations associated with certain ERP peaks, their correspondence is not in line with what is expected from the literature or the activation is not so easily interpretable. As such, it seems that the variation across subjects is indeed an important factor for the performance of JointICA.

We also compared the results from JointICA with those obtained by applying ICA solely to fMRI or ERP data. On average (computed via Fisher's z-transform), the individual ERP independent components had a higher correlation with the ERP parts of the JointICA results (0.7541 ± 0.3539) than the fMRI independent components (0.6065 ± 0.2205). This difference was statistically significant ($p = 0.0018$). However, despite the higher correlation of the ERP independent components, also the individual ERP decomposition is still significantly different from the result of JointICA. This implies that, although the ERP data seem to have the largest effect, the fMRI modality also influences the decomposition significantly.

To further investigate the issue of data quality, the amount of data included in the decomposition was also evaluated. To this end, the number of subjects for the analysis of the simultaneous datasets was reduced from 26 downward. As a result, once this number decreased below 20, the P1 peak was no longer uniquely identified and became associated to fMRI components which were no longer interpretable. This is illustrated in Figure 6.4, showing the components resulting from JointICA

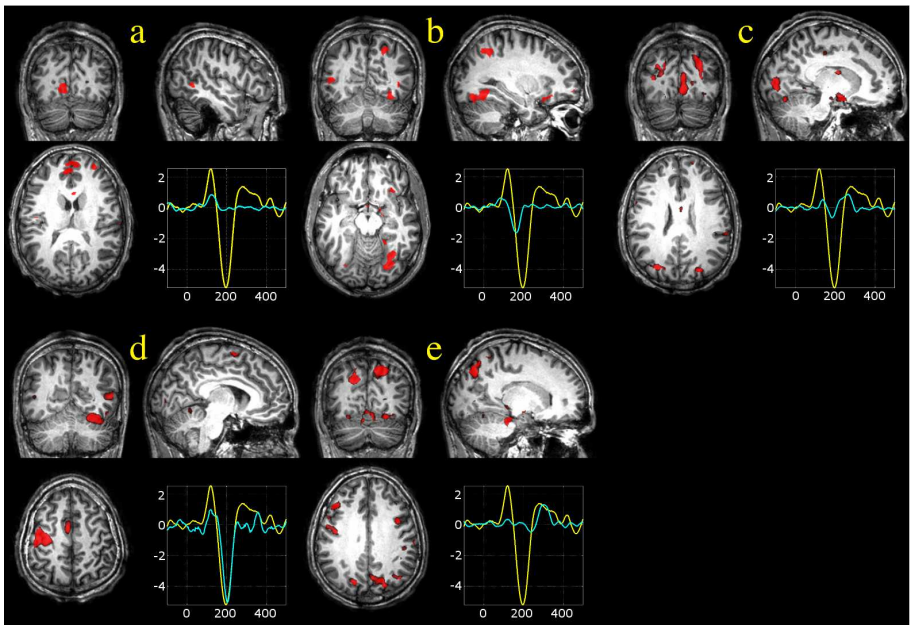

Figure 6.4: *The JointICA results of the simultaneously recorded data for 18 subjects (the same subjects as in the non-simultaneous case): (a) P1 ERP peak corresponding to activations in the left lingual gyrus (BA 18 - MNI [-11 -82 -3]) and right middle temporal gyrus (BA 37 - MNI [48 -64 7]), with some additional frontal lobe activation; (b) Early N1 peak associated to activity in the right fusiform gyrus (BA 19 - MNI [29 -76 -13]), right precuneus (BA 7 - MNI [19 -74 46]) and left middle temporal gyrus (BA 37 - MNI [-51 -69 9]); (c) Late N1 peak linked to activation around the calcarine sulcus and precuneus (bilaterally); (d) Late N1 peak with somatosensory activity in BA 3, 1 and 2 (postcentral gyrus), and in the primary motor cortex (precentral gyrus - BA 4). Also, visual activity is shown in inferior occipital gyrus (BA 19 - MNI [45 -72 -1]), and some cerebellum activity is found close to the right fusiform gyrus; (e) P2 related ERP activation mostly associated to the fMRI activation in right and left precuneus (BA 7).*

applied to the simultaneously acquired EEG and fMRI data for the down left stimulus from 18 subjects (the same 18 as in the non-simultaneous case). The obtained ERP and fMRI components are similar to the ones in Figure 6.3, except for the P1-related activation.

6.4 Discussion

In this study, we evaluated and presented the performance of JointICA, a recently proposed method for a symmetric integration of EEG and fMRI. We compared the

performance of this method for data from the visual detection task acquired both simultaneously and non-simultaneously and investigated the importance of the amount of data included in the analyses. Performing JointICA on simultaneously measured EEG and fMRI data, resulted in meaningful components. These components got, however, deteriorated when the subject-specific correspondence between ERPs and fMRI was violated or when less subjects were included in the analysis. Making use of EEG data measured outside the scanner room, slightly improved the interpretability of the results and yielded spatiotemporal activations which were more consistent with literature [66], especially for the P1 associated areas.

According to the literature and based on the characteristics of the presented task, the P1 and N1 peaks found in the ERPs are expected to correspond to extrastriate visual activations in fMRI [66]. In addition, our subjects were required to respond to the presented stimuli by pressing a button, which should evoke activation of the somatosensory and primary motor cortex, connected to the N1 peak [29, 148]. The results obtained with the JointICA analysis both on simultaneously and non-simultaneously acquired data confirm these expectations to a certain extent, hereby confirming the performance of this method as shown previously [29, 31, 32, 81, 221].

However, as opposed to the case with outside data, the simultaneous results with 26 subjects did not show the expected activation in the fusiform gyrus. In addition, all meaningful P1 activation disappeared when reducing the simultaneous data to the same 18 subjects as included in the outside data. Even after careful artifact removal and averaging, there is still a clear quality difference between inside and outside data (cf. Figure 6.2). Hence, data quality seems a major issue for JointICA. Therefore, acquiring EEG and fMRI data in separate sessions might be a good procedure in certain circumstances, and may yield better results with less participants. Nevertheless, there are many cognitive studies in which processes, such as habituation and arousal state [57, 58], play an important role, and thus simultaneous measurements have to be performed. Especially for these datasets, an optimized preprocessing procedure (as described in Chapters 3 and 4) is essential. In this context, our results also show that increasing the number of subjects has a clear impact on the quality of the decomposition. As such, including more subjects in the analysis might further facilitate finding meaningful connections between ERP peaks and fMRI activations. This data requirement becomes especially important in the case of simultaneous recordings, where the variability across subjects is higher.

To address the issue about which modality is driving the JointICA decomposition, we performed a correlation analysis to compare similarity of components obtained from integrated and individual ERP and fMRI ICA analyses. Correlation values were significantly higher for the ERP compared to the fMRI modality. Based on this, together with the fact that for 18 subjects non-simultaneous results are

more consistent than the simultaneous ones, we hypothesize that the JointICA decomposition is more strongly driven by the ERP characteristics. This finding is not only important to understand the principles behind the JointICA method, but it also represents an additional argument for optimizing the quality of the ERP data. Nevertheless, the decomposition is not completely asymmetric either, since including fMRI also influences the ERP component separation.

The poor results when randomly connecting ERP and fMRI data over subjects, confirm the importance of subject variability for JointICA. The hypothesis that the activations in ERP and fMRI data are indeed highly correlated is further also supported by results from other integration approaches, based on the same principle. In [176], e.g., visual brain activation was studied by examining correlations between ERP and fMRI face-selectivity measures. In this way, they not only found that face-selective ERP and fMRI responses were highly correlated, but also that these correlations were specific for distinct ERP latencies and brain regions. Following the same logic, we believe that these findings hold for all brain activations and that different ERP peak components are highly connected to different fMRI regions. This was also confirmed in a similar study with auditory stimulation [144].

The successful application of methods like JointICA on averaged ERP and fMRI data, might suggest that this approach should be preferred over trial-by-trial integration methods. However, as explained in the previous chapter, understanding trial-by-trial variability in neural activity is an important aspect of cognitive neuroscience [23]. For this reason, we believe that methods like JointICA and the above explained correlation over subjects, should not replace the single trial based methods, but rather considered as a valuable alternative for certain applications.

6.5 Conclusion

In this study, we investigated the performance of JointICA as an alternative method to integrate the EEG-fMRI data from the visual detection task. More specifically, we evaluated the meaningfulness of the resulting components both for simultaneously and non-simultaneously measured data and examined the necessity of several data requirements to obtain good results. Our findings extend the outcome of earlier studies, in that not only activations in accordance with literature are found, but also the importance of including enough data of sufficient quality is shown. In addition, it is demonstrated that a similar variability across subjects between ERPs and fMRI is the key element to a successful performance of JointICA.

Chapter 7

Conclusions and further research

In this final chapter, findings and conclusions of the presented work are summarized in Section 7.1 and suggestions for future research directions are given in Section 7.2.

7.1 General conclusions

Obtaining a complete and meaningful spatiotemporal picture from the integration of simultaneously recorded EEG and fMRI data, requires a series of analysis steps that need to be carefully performed. In this thesis, some of these steps were discussed in detail and specific approaches that can be used to address them, were presented and validated. The most important findings from these analyses will be briefly recapitulated in this section.

7.1.1 Optimization of data quality

As explained in Chapter 1 and further discussed in Chapter 2, the MR scanner can be seen as a hostile environment for the acquisition of EEG data. For this reason, a careful preparation and setup of the recording equipment are crucial. Based on our own experience, a set of detailed instructions on this matter have been described in a comprehensive EEG-fMRI manual, available through our K.U.Leuven EEG-fMRI website (www.esat.kuleuven.be/scd/eegfmri). However, besides requiring a specifically adapted recording equipment, the highly static and changing magnetic

fields that are present, also induce severe scanner-related artifacts that need to be removed prior to further analyses. The most challenging of these scanner-related artifacts is the BCG artifact, because of its complex origin and dynamic spatial behavior. A wide range of methods was proposed to remove this artifact, but no consensus had yet been reached. In this thesis, some of the most widely used BCG removal approaches were, therefore, applied and validated. The parameters of these methods (OBS, ICA and OBS-ICA) were optimized by verifying several specific validation criteria based on both average and single trial ERP components. Both OBS and ICA yielded similar results, but since for OBS much less parameter tuning was needed, it was preferred over ICA for reasons of user-friendliness. OBS-ICA, however, showed even better results, but there, careful parameter tuning was even more crucial.

In any case, most of the removal approaches require the detection of the QRS peaks on the ECG channel to have more detailed information about the occurrence of the BCG artifact. In this thesis, the QRS detection and correction from the FMRIB toolbox [163] were used, but results revealed several problems when applying this toolbox. For this reason, we proposed a step-by-step procedure to be followed for obtaining a good QRS detection. This procedure also includes an improved version of the correlation-based correction. Despite the simplicity of this approach, it is believed to be complementary to the FMRIB analyses and its effectiveness was illustrated on several examples.

7.1.2 Extraction of single trial ERP information

After optimizing the ERP data quality based on the above-mentioned analyses, the aim was to find a relationship between the ERP and fMRI data. One approach for this purpose, is to relate both modalities on a single trial level. However, there is no consensus yet on how to extract meaningful trial-to-trial variability from ERPs and fMRI. In this work, we therefore investigated the possibilities of source extraction with PARAFAC to distinguish between task-related ERP variability and noise. To this end, PARAFAC was applied to the ERP data from the visual detection task, arranged in $channels \times time \times trials$ arrays. Our analyses revealed that PARAFAC was indeed able to yield task-specific information in the trial modes of its resulting components. We validated this outcome by using the trial modes to differentiate between different conditions present in the task. As such, we were able to show both the possibilities and limitations of the PARAFAC approach, the latter mainly related to datasets with a lower signal to noise ratio (due to, e.g., residual artifacts or problems during acquisition).

7.1.3 Integration of EEG and fMRI

Subsequently, two different approaches to address the issue of ERP-fMRI integration, were validated in this thesis. First, the trial-by-trial amplitude information from the trial signatures extracted with PARAFAC, was used for the analysis of the simultaneously measured fMRI data. This analysis did not reveal any significant improvement compared to standard analyses of fMRI in which no amplitude information was included. Some hypotheses for this finding were discussed based on results present in recent related studies.

Second, the JointICA method, proposed by Calhoun et al. [29], was also validated on the data from the visual detection task. As this method can be applied to average ERPs and fMRI, the SNR of the input signals is inherently better than in the single trial case. As a result of these analyses, meaningful activations that were in correspondence with the literature, were obtained. In addition, the importance of a similar variation across subjects of the ERP and fMRI characteristics was demonstrated. Nevertheless, despite the averaging, the variability across subjects will still be higher in the case of simultaneous measurements, due to the more difficult recording environment and the residual artifacts. Including more subjects will, therefore, especially in the case of data acquired inside the scanner, increase the robustness of JointICA.

7.2 Future work and open problems

Different analyses towards a better understanding of cognitive processes based on EEG and fMRI, have been presented in this thesis and their possibilities and limitations have been illustrated. Nevertheless, gaining more knowledge about such multimodal approaches, also brings along new open questions. These inspired us for the future research directions, described in this section. In particular, several aspects related to advantages of the combination of EEG and fMRI will be addressed. First, the possibility of investigating spatiotemporal patterns of specific cognitive processes can be employed to get a deeper understanding on visual perception mechanisms. Second, single trial fluctuations in certain aspects of EEG and fMRI data can be studied and combined. In addition, the benefits of the integration of EEG and fMRI can be extended to other multimodal datasets.

7.2.1 Using ERP information to create a time dimension for the fMRI spatial activations: grouping study

Throughout the different chapters of this thesis, mainly the data from the visual detection and the Go/NoGo task were used. These tasks were chosen because

they were widely established and, therefore, especially appropriate to validate artifact removal and new data analysis approaches. Nevertheless, one of the true advantages of EEG-fMRI integration, is the possibility of obtaining new insights in the spatiotemporal characteristics of cognitive processes. To really benefit from this possibility, other and more complex experimental paradigms have to be investigated. The extension of integration methods to such paradigms, is without doubt one of the most intriguing research directions for future simultaneous EEG-fMRI studies.

A typical example of cognitive processes for which the combination of EEG and fMRI is particularly useful, are the mechanisms behind perceptual grouping. Studying the spatiotemporal characteristics of such processes in fact comes down to assigning a temporal order to the different spatial activations obtained with fMRI. This is a clear advantage compared to studying the same mechanisms with fMRI alone, since this latter case only yields one general spatial activity pattern without any information about the temporal interaction between the different processes. Furthermore, this application strongly benefits from a simultaneous acquisition of EEG and fMRI since similar effects of learning and attention can otherwise not be ensured.

To investigate this in more detail, we continued our collaboration with the Laboratory of Experimental Psychology of our university. The data acquired for this study were described in Chapter 2. As explained in that chapter, the aim of this grouping study was to reveal the processes behind local and global grouping principles.

As a first attempt to link the ERP peaks to their corresponding spatial activations from fMRI, an approach based on similar principles as JointICA (cf. Chapter 6), was examined. More specifically, a correlation across subjects was calculated in order to reveal temporal properties of certain brain networks. This approach was originally proposed in [176], where it was applied to data from a face perception paradigm. As a result, strong associations between ERP peaks and face-selective brain regions were demonstrated, revealing spatiotemporal characteristics of the processes under study.

The application of the correlation method on the data from the grouping study will now be discussed and some preliminary results will be shown. Afterwards, a number of open questions will be formulated.

Preliminary study and results

An illustration of the adopted correlation procedure can be found in Figure 7.1. Briefly explained, the amplitude at a specific latency of the averaged ERP for a certain stimulus is correlated across subjects with the fMRI activation in a

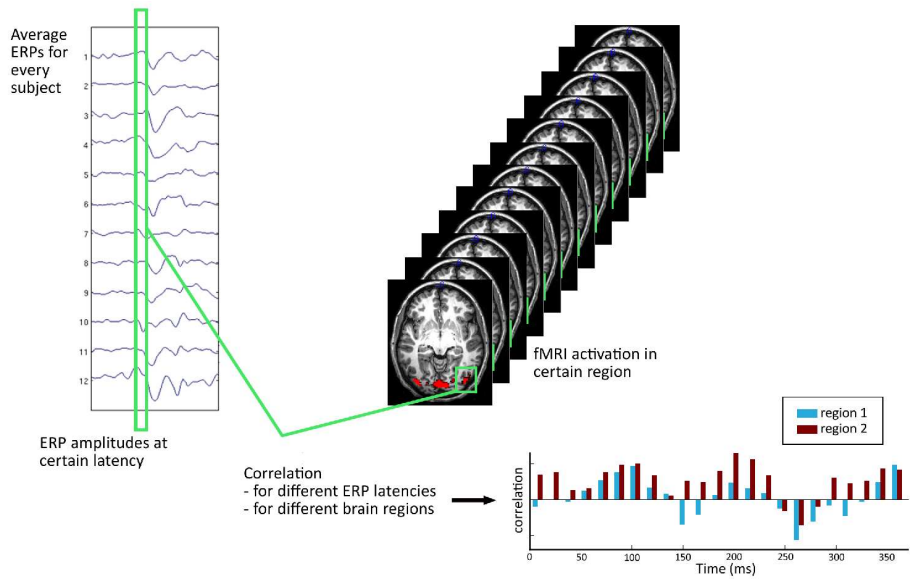

Figure 7.1: *Schematic representation of the correlation analysis performed on averaged ERP and fMRI data. The amplitude at a specific latency of the averaged ERP for a certain stimulus is correlated across subjects with a quantification of the fMRI activity in a particular brain region for this same stimulus. This analysis is then repeated for different regions and different latencies, as to finally obtain a correlation time course for each region.*

particular brain region. This analysis is then repeated for different regions and different latencies, as to finally obtain a correlation time course for each region.

The three stimuli of interest in this task were the stimuli with global and local structure, the stimuli with only global structure and the stimuli without structure (cf. Figure 2.5). To be able to calculate the correlation, average ERPs and fMRI activation maps have to be obtained.

To this end, the acquired EEG data were subjected to the same preprocessing steps as the data from the detection task in Chapter 5. To create the ERPs, data were rereferenced to the average of TP9 and TP10, segmented from 200 ms before until 600 ms after stimulus onset, baseline corrected (-200 - 0 ms) and thresholded at 150 μV. Thereafter, an average ERP for each stimulus type was computed. For the fMRI data, standard preprocessing steps were performed according to the explanation in Chapter 3. Next, the fMRI activation maps were retrieved via a GLM analysis with stick-functions based on the onset times of the different stimuli.

Correlating fMRI activation values in certain brain regions, also requires the

accurate identification of these regions. In this specific task, the ROIs were the primary and extrastriate visual cortex (known as V1, V2 until V5 or Brodmann areas 17, 18 and 19) and LOC (Brodmann area 37), involved in object detection. The best way to exactly locate these ROIs, is to ask the subjects to perform additional fMRI experiments, particularly developed to activate these areas. This procedure will not be explained in detail here, but a so-called meridian localizer task was used to locate V1, V2 and V3 and a task including objects and scrambled images (object localizer task) was employed for LOC.

In Figure 7.2, preliminary results from the correlation analysis are shown. The correlation is presented with vertical color bars for different latencies, ranging from 0 to 400 ms after stimulus onset in windows of 16 ms. Each color represents a distinct brain area, thereby differentiating between the dorsal and ventral parts of V1, V2 and V3 and LOC. In the upper panel, correlation values are shown for the global and local structure stimuli, the middle panel focuses on the global structures and the down part of the figure presents the results for the non-structure stimuli.

The results for the global stimuli in particular, compared to those including both global and local structure, reveal a higher correlation for the LOC area around 200 ms and for the visual areas around 300 ms. This is in correspondence with one of our hypotheses, implying that the global stimuli require a stronger activation in LOC in order for the contours to be fully perceived. In addition, as expected, the stimuli without any structure mainly involve a high correlation before 100 ms and only very few activation in the LOC area.

Open questions

Although a first attempt to interpret the above results was made, their relevance cannot be fully assessed without first addressing the still open methodological questions regarding the analysis. The following non-exhaustive list gives an idea what these issues are.

- **fMRI quantification:** In the current version, T-maps from SPM are used, but contrast- or beta-maps might be included as well. Another possibility is to extract the BOLD responses from the fMRI data and employ their peak amplitudes as measures for fMRI strength.
- **Regions of interest:** Do we have to look at V1 (and respectively V2 and V3) dorsal and ventral areas separately or can they be taken together? How should the large number of voxels within such an ROI be summarized?
- **Electrode selection:** Which electrode should be taken for the correlation analysis (currently: Oz) or can we take several electrodes together? Should the same selection be made for all subjects?

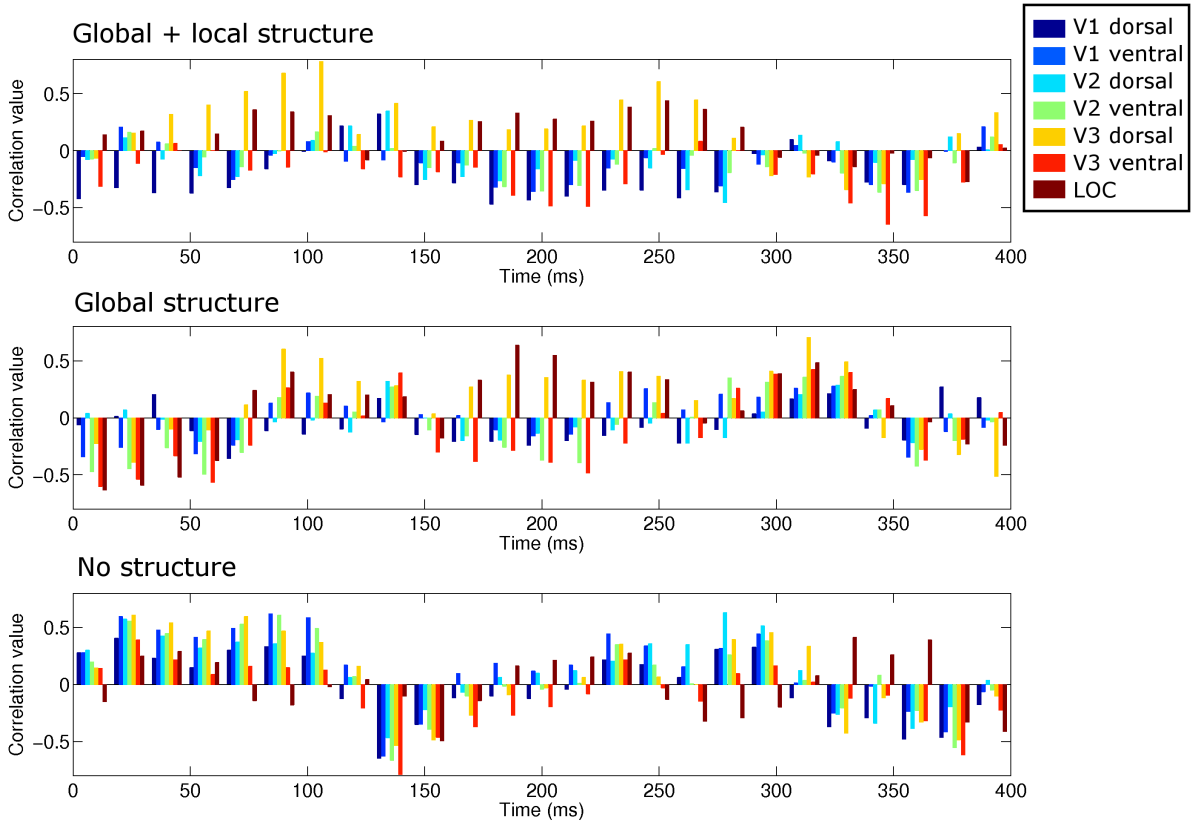

Figure 7.2: *Preliminary results of the correlation analysis applied to data from 12 subjects from the grouping study. Results are shown for the stimuli with global and local structure (upper panel), the stimuli with only global structure (middle panel) and the non-structure stimuli (below panel). For each case, correlation values are shown for latencies varying from 0 to 400 ms in windows of 16 ms. Different regions of interest are distinguished, both in the primary and extrastriate visual areas and in the lateral occipital complex (LOC).*

- **ERP preparation:** In [176], ERP peaks were used in a relative way as to represent a face-selectivity index. Can we derive a similar measure here by normalizing the ERPs? Should we compensate for different ERP latencies across subjects?
- **Statistics:** What is the correct approach to evaluate the results of this correlation analysis statistically? Should we look at a time course (as in Figure 7.2) or at specific ERP peaks? What is the correct interpretation of negative correlation results?

The principle question in the above analyses remains finding the temporal sequence in which the activation of the involved brain areas occurs. To increase the reliability of the obtained results, also other methods should be considered and their results compared with those of the correlation analysis. In addition, it can be particularly interesting to compare the results of the correlation approach with those obtained with JointICA in order to understand the underlying assumptions of both methods.

7.2.2 EEG-fMRI integration based on trial-by-trial fluctuations

In addition to unraveling fMRI spatial activations in different parts occurring in a specific order, the combination of EEG and fMRI also allows connecting single trial fluctuations of certain aspects of both modalities. Such single trial integration obviously requires the estimation of single trial ERP and fMRI characteristics, as will be explained in the next paragraphs.

Improving single trial ERP estimation

Different techniques have been proposed for the extraction of single trial information from ERP data. Among those are blind source separation techniques to analyze matrix data like PCA [70] and ICA [135, 136], and, in this thesis, source extraction based on a third-order decomposition with PARAFAC. However, as mentioned in the discussion of Chapter 5, the trilinear structure of PARAFAC might not be the most appropriate model for single trial ERP data. For this reason, another future research line could be the exploration of other higher-order decomposition techniques for use on ERP data. Because the Tucker model [198, 199] allows too many interactions and, thus, makes component interpretation almost impossible, block component decompositions [47, 48, 49] seem more suitable for this purpose. However, before starting such analyses, it is important to first decide what kind of interactions should be allowed in such a model. Including time shifts, as is done in the shifted PARAFAC approach [150], is also a good idea, but a more robust implementation of this technique is therefore needed. Obviously,

an accurate validation of the obtained single trial estimates is important. In this thesis, one possibility based on different conditions in the task was proposed, but further research should certainly also focus on more detailed validation criteria.

Improving single trial fMRI estimation

The challenges in the extraction of fMRI amplitudes on a single trial basis are in fact similar to the ones with ERP data: How can we denoise the fMRI data? How can we distinguish the fMRI event-related processes from the resting state activity? In previous years, a wide variety of methods addressing these challenges have been proposed, ranging from simple techniques fitting HRF models to preprocessed fMRI data [73], to more advanced approaches based on least-squares [223] or Bayesian-based deconvolution [85].

To our knowledge, no golden standard for fMRI estimation has yet been defined. This is also the reason why studies like [13], compare different methods to obtain the fMRI trial variability. For a sound integration of EEG and fMRI, accurate and meaningful single trial fMRI amplitude estimations would, therefore, be a real step forward. To this end, it might be important to maintain sufficiently long time periods in between consecutive stimuli (as, e.g., in the six subjects with longer ISI values, cf. Table A.1).

Connecting single trial ERP and fMRI data

Several authors (e.g., [57]) illustrate the correspondence between EEG and fMRI with the diagram shown in Figure 7.3. As such, it is assumed that part of the brain activity is revealed by both EEG and fMRI, whereas there are also processes merely visible in one or the other. Which processes belong in which part of the diagram, is still an open question. Finding a relation between the single trial ERP and fMRI estimates would, therefore, imply that these single trial fluctuations reside in the overlap between the two modalities. As such, single trial integration analyses do not only give information on neural processes but also on the potential link between EEG and fMRI fluctuations. Moreover, if a certain connection is present, these analyses can also be used to validate the accurateness of the above-mentioned single trial estimation methods.

In addition, the decomposition methods explained in the context of single trial ERP data also allow the extraction of sources from ERP and fMRI data simultaneously. One such a combined decomposition approach was explained in the method overview in Chapter 1 and is called multiway partial least squares (N-PLS). In [141], this method was applied to continuous EEG data to extract sources related to certain brain rhythms. However, since N-PLS is in fact partly based on PARAFAC, the nice performance of PARAFAC on single trial ERP

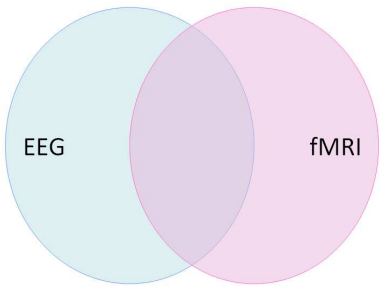

Figure 7.3: *Schematic representation of the correspondence of processes revealed with EEG and fMRI data.*

data, makes us believe that N-PLS can be extended to the ERP-fMRI application. This extension does, however, require an accurate estimation of single trial fMRI amplitudes, which brings us back to one of the above-mentioned future research lines.

7.2.3 Other multimodal approaches and applications

The main focus of the analyses and results presented in this thesis, was on the study of event-related potentials. Other applications might, however, also benefit from simultaneous EEG-fMRI measurements or from the combination of modalities other than EEG and fMRI. Future research should, therefore, also focus on these applications, as will be addressed in the list below.

- **EEG-fMRI for the study of epileptic discharges:** As explained in Chapter 1, the combination of EEG and fMRI originally emerged from the study of epileptic data. Based on the work presented in this thesis, these results can now be extended. More specifically, since PARAFAC was successfully used on epileptic spikes in [60], it should be investigated whether the resulting components could not be used for finding spike-related fMRI maps.
- **Combination of fMRI with EMG:** EMG measures the electrical activity of the muscles and can be relevant in behavioral studies focusing on, e.g., emotions. Since facial muscles can react on specific stimuli shown to a subject, their activation can be a sign of normal or abnormal behavior. For this reason, also simultaneous EMG-fMRI measurements can be useful. The higher frequencies of interest of EMG make this combination, however,

more challenging, since heavy lowpass-filtering to remove residual gradient artifacts is not allowed. Other solutions for the reduction of the gradient artifact, therefore, need to be investigated.

- **Combination of EEG with near-infrared spectroscopy (NIRS):** NIRS is a spectroscopic method that uses the near-infrared region of the electromagnetic spectrum to non-invasively assess brain function. It is based on the detection of changes in blood hemoglobin concentrations associated with neural activity and, as such, related to fMRI measures. Since the combination of EEG and NIRS has recently been made technically possible (through, e.g., the equipment of Advanced Neuro Technology B.V., Enschede, the Netherlands), integration techniques could now also be used to link these two modalities.

Appendix

In this short Appendix, a list of the acquired datasets for the detection and Go/NoGo task explained in Chapter 2, is given. For each subject, gender and age are indicated and the circumstances and location of the recording are denoted. The datasets listed here, were used for the data analyses in Chapters 3, 4, 5 and 6.

Table A.1: *Overview of available data for the detection and the Go/NoGo task. For every subject, the age and gender are shown, together with the circumstances in which the datasets have been measured (in- or outside the scanner, with or without simultaneous fMRI, in the Maastricht or in the Leuven setup). Six subjects (indicated with (long)) performed the alternative version of the detection task with longer ISI values.*

Subject	Age	Gender	Maastricht		Leuven	
			Detection task	Go/NoGo task	Detection task	Go/NoGo task
1	28	m	· with fMRI · without fMRI · outside	· with fMRI · without fMRI · outside	with fMRI	with fMRI
2	24	f	· with fMRI · without fMRI · outside	· with fMRI · without fMRI · outside	with fMRI	with fMRI
3	21	f	· with fMRI · without fMRI · outside	· with fMRI · without fMRI · outside	with fMRI	with fMRI
4	32	m	· with fMRI · without fMRI · outside	· with fMRI · without fMRI · outside	/	/
5	20	f	· with fMRI · without fMRI · outside	· with fMRI · without fMRI · outside	with fMRI	with fMRI
6	31	m	· with fMRI · without fMRI · outside	· with fMRI · without fMRI · outside	with fMRI	with fMRI
7	19	f	/	/	· with fMRI	· with fMRI

Continued on next page

Table A.1: *(continued from previous page)*

Subject	Age	Gender	Maastricht		Leuven	
			Detection task	Go/NoGo task	Detection task	Go/NoGo task
			/	/	· outside	· outside
8	25	m	with fMRI	with fMRI	· with fMRI · without fMRI · outside	· with fMRI · without fMRI · outside
9	25	m	with fMRI	with fMRI	· with fMRI · without fMRI · outside	· with fMRI · without fMRI · outside
10	28	m	/	/	· with fMRI · outside	/
11	24	f	/	/	· with fMRI · outside	/
12	25	f	/	/	· with fMRI · outside	/
13	30	m	/	/	· with fMRI · outside	/
14 (long)	25	m	/	/	· with fMRI · outside	/
15 (long)	24	f	/	/	· with fMRI · outside	/
16 (long)	24	m	/	/	· with fMRI · outside	/
17 (long)	29	f	/	/	· with fMRI	/

Continued on next page

Table A.1: *(continued from previous page)*

Subject	Age	Gender	Maastricht		Leuven	
			Detection task	Go/NoGo task	Detection task	Go/NoGo task
					· outside	
18 (long)	28	f	/	/	· with fMRI · outside	/
19 (long)	44	m	/	/	· with fMRI · outside	/
20	25	m	with fMRI	with fMRI	with fMRI	with fMRI
21	26	m	with fMRI	with fMRI	with fMRI	with fMRI
22	24	m	/	/	with fMRI	/
23	32	f	with fMRI	with fMRI	with fMRI	with fMRI
24	24	m	/	/	with fMRI	with fMRI
25	25	m	/	/	with fMRI	/
26	18	f	/	/	with fMRI	/
27	33	m	with fMRI	with fMRI	with fMRI	with fMRI

Bibliography

[1] E. Acar, C.A. Bingöl, H. Bingöl, and B. Yener. Computational Analysis of Epileptic Focus Localization. In *BioMed'06 Proceedings of the fourth IASTED International conference on Biomedical engineering*, pages 317–322, Innsbruck, Austria, 2006.

[2] A. Achim and S. Bouchard. Toward a dynamic topographic components model. *Electroencephalography and Clinical Neurophysiology*, 103:381–385, 1997.

[3] P.J. Allen, O. Josephs, and R. Turner. A method for removing imaging artifact from continuous EEG recorded during functional MRI. *NeuroImage*, 12:230–239, 2000.

[4] P.J. Allen, G. Polizzi, K. Krakow, D.R. Fish, and L. Lemieux. Identification of EEG events in the MR scanner: the problem of pulse artifact and a method for its subtraction. *NeuroImage*, 8:229–239, 1998.

[5] K. Anami, T. Mori, F. Tanaka, Y. Kawagoe, J. Okamoto, M. Yarita, T. Ohnishi, M. Yumoto, H. Matsuda, and O. Saitoh. Stepping stone sampling for retrieving artifact-free electroencephalogram during functional magnetic resonance imaging. *NeuroImage*, 19:281–295, 2003.

[6] K. Anami, O. Saitoh, M. Yumoto, F. Tanaka, Y. Kawagoe, T. Ohnishi, and H. Matsuda. Reduction of ballistocardiogram with a vacuum head-fixating system during simultaneous fMRI and multi-channel monopolar EEG recording. *International Congress Series*, 1232:427–431, 2002.

[7] C.A. Andersson and R. Bro. The N-way Toolbox for MATLAB. *Chemometrics & Intelligent Laboratory Systems*, 52(1):1–4, 2000.

[8] S. Assecondi. *Automated Subject-Specific Peak Identification and Ballistocardiographic Artifact Correction in EEG-fMRI*. PhD thesis, Faculty of Engineering, University of Ghent (Belgium), 2009.

[9] S. Assecondi, H. Hallez, S. Staelens, A. Bianchi, G. Huiskamp, and I. Lemahieu. Removal of the ballistocardiographic artifact from EEG-fMRI data: a canonical correlation approach. *Physics in Medicine and Biology*, 54(2):1673–1689, 2009.

[10] S. Assecondi, K. Vanderperren, N. Novitskiy, J. Ramautar, W. Fias, P. Stiers, S. Sunaert, S. Staelens, S. Van Huffel, and I. Lemahieu. Effect of the static magnetic field of the MR-scanner on ERPs: evaluation of visual, cognitive and motor potentials. *Clinical Neurophysiology*, 121(5):672–685, 2010.

[11] F. Babiloni, C. Babiloni, F. Carducci, G.L. Romani, P.M. Rossini, L.M. Angelone, and F. Cincotti. Multimodal integration of high-resolution EEG and functional magnetic resonance imaging data: a simulation study. *NeuroImage*, 19(1):1–15, 2003.

[12] F. Babiloni, D. Mattia, C. Babiloni, L. Astolfi, S. Salinari, A. Basilisco, P.M. Rossini, M.G. Marciani, and F. Cincotti. Multimodal integration of EEG, MEG and fMRI data for the solution of the neuroimage puzzle. *Magnetic Resonance Imaging*, 22(10):1471–1476, 2004.

[13] A.P. Bagshaw and T. Warbrick. Single trial variability of EEG and fMRI responses to visual stimuli. *NeuroImage*, 38(2):280–292, 2007.

[14] R. Becker, M. Reinacher, F. Freyer, A. Villringer, and P. Ritter. How ongoing neuronal oscillations account for variability of evoked fMRI responses. *Journal of Neuroscience*, 32(30):11016–11027, 2011.

[15] R. Becker, P. Ritter, M. Moosmann, and A. Villringer. Visual evoked potentials recovered from fMRI scan periods. *Human Brain Mapping*, 26:221–230, 2005.

[16] R. Becker, P. Ritter, and A. Villringer. Influence of Ongoing Alpha Rhythm on the Visual Evoked Potential. *NeuroImage*, 39(2):707–716, 2008.

[17] A.J. Bell and T.J. Sejnowski. An information-maximization approach to blind separation and blind deconvolution. *Neural Computation*, 7(6):1129–1159, 1995.

[18] A. Belouchrani, K. Abed-Meraim, J.F. Cardoso, and E. Moulines. Second-order blind separation of temporally correlated sources. In *Proceedings of the International Conference on Digital Signal Processing*, pages 346–351, Cyprus, 1993.

[19] C.G. Bénar, Y. Aghakhani, Y. Wang, A. Izenberg, A. Al-Asmi, F. Dubeau, and J. Gotman. Quality of EEG in simultaneous EEG-fMRI for epilepsy. *Clinical Neurophysiology*, 114:569–580, 2003.

[20] C.G. Bénar, D. Schön, S. Grimault, B. Nazarian, B. Burle, M. Roth, J.M. Badier, P. Marquis, C. Liegeois-Chauvel, and J.L. Anton. Single-trial analysis of oddball event-related potentials in simultaneous EEG-fMRI. *Human Brain Mapping*, 28:602–613, 2007.

[21] H. Berger. Uber das Electrenkephalogramm des Menschen. *Archiv fur Psychiatrie und Nervenkrankheiten*, 87:527–570, 1929.

[22] R.M. Birn, J.B. Diamond, M.A. Smith, and P.A. Bandettini. Separating respiratory-variation-related fluctuations from neuronal-activity-related fluctuations in fMRI. *NeuroImage*, 31(4):1536–1548, 2006.

[23] A. Bland, F. Mushtaq, and D.V. Smith. Exploiting Trial-to-Trial Variability in Multimodal Experiments. *Frontiers in Human Neuroscience*, 5:1–3, 2011.

[24] K. Blinowska, G. Müller-Putz, V. Kaiser, L. Astolfi, K. Vanderperren, S. Van Huffel, and L. Lemieux. Multimodal Imaging of Human Brain Activity: Rational, Biophysical Aspects and Modes of Integration. *Computational Intelligence and Neuroscience, Special Issue on Neuromath: Advanced Methods for the Estimation of Human Brain Activity and Connectivity*, 2009:1–10, 2009.

[25] H. Bokura, S. Yamaguchi, and S. Kobayashi. Electrophysiological correlates for response inhibition in a Go/NoGo task. *Clinical Neurophysiology*, 112(12):2224–2232, 2001.

[26] G. Bonmassar, P.L. Purdon, I.P. Jääskeläinen, K. Chiappa, V. Solo, E.N. Brown, and J.W. Belliveau. Motion and Ballistocardiogram Artifact Removal for Interleaved Recording of EEG and EPs during MRI. *NeuroImage*, 16(4):1127–1141, 2002.

[27] M.J. Brookes, K.J. Mullinger, C.M. Stevenson, P.G. Morris, and R. Bowtell. Simultaneous EEG source localisation and artifact rejection during concurrent fMRI by means of spatial filtering. *NeuroImage*, 40(3):1090–1104, 2008.

[28] V.D. Calhoun and T. Adali. Unmixing fMRI with independent component analysis. *IEEE Engineering in Medicine and Biology Magazine*, 25:79–90, 2006.

[29] V.D. Calhoun, T. Adali, G.D. Pearlson, and K.A. Kiehl. Neuronal chronometry of target detection: fusion of hemodynamic and event-related potential data. *NeuroImage*, 30:544–553, 2006.

[30] V.D. Calhoun, T. Adali, G.D. Pearlson, and J.J. Pekar. A Method for Making Group Inferences from Functional MRI Data Using Independent Component Analysis. *Human Brain Mapping*, 14:140–151, 2001.

[31] V.D. Calhoun, J. Liu, and T. Adali. A review of group ICA for fMRI data and ICA for joint inference of imaging, genetic, and ERP data. *NeuroImage*, 45(1 Suppl):163–172, 2009.

[32] V.D. Calhoun, L. Wu, K.A. Kiehl, T. Eichele, and G.D. Pearlson. Aberrant processing of deviant stimuli in schizophrenia revealed by fusion of fMRI and EEG data. *Acta Neuropsychiatrica*, 22(3):127–138, 2010.

[33] J.F. Cardoso and A. Souloumiac. Blind beamforming for non-Gaussian signals. *IEE Proceedings-F*, 140(6):362–370, 1993.

[34] J.D. Carroll and J. Chang. Analysis of individual differences in multidimensional scaling via an n-way generalization of 'eckartyoung' decomposition. *Psychometrika*, 35:283–319, 1970.

[35] I.I. Christov. Real time electrocardiogram QRS detection using combined adaptive threshold. *Biomedical Engineering Online*, 3(1):28, 2004.

[36] A. Cichocki, Y. Washizawa, T. Rutkowski, H. Bakardjian, A.-H. Phan, S. Choi, H. Lee, Q. Zhao, L. Zhang, and Y. Li. Noninvasive BCIs: Multiway Signal-Processing Array Decompositions. *Computer*, 41(10):34–42, 2008.

[37] V.P. Clark, S. Fan, and S.A. Hillyard. Identification of early visual evoked potential generators by retinotopic and topographic analyses. *Human Brain Mapping*, 2(3):170187, 1995.

[38] M.S. Cohen, R.I. Goldman, and J. Engel Jr. Simultaneous EEG and fMRI made easy. In *Proceedings of the seventh international conference on functional mapping of the human brain*, Brighton, England, 2001.

[39] P. Comon. Independent component analysis - a new concept? *Signal Processing*, 36:287–314, 1994.

[40] P. Comon and C. Jutten. *Handbook of Blind Source Separation: Independent Component Analysis and Applications*. Elsevier Ltd., 2010.

[41] C. Cooreman, R. Sclocco, M.G. Tana, K. Vanderperren, E. Visani, F. Panzica, S. Franceschetti, S. Van Huffel, S. Cerutti, and A.M. Bianchi. BOLD Correlates of Alpha and Beta EEG-Rhythm during a Motor Task. In *Proceedings of the* 5th *International IEEE EMBS Conference on Neural Engineering*, pages 25–28 (ThB1.1), Cancun, Mexico, 2011.

[42] N. Correa, Y.O. Li, T. Adali, and V.D. Calhoun. Canonical Correlation Analysis for Data Fusion and Group Inference. *IEEE Signal Processing Magazine*, 27(4):39–50, 2010.

[43] M. Czisch, T.C. Wetter, C. Kaufmann, T. Pollmacher, F. Holsboer, and D.P. Auer. Altered processing of acoustic stimuli during sleep: reduced auditory activation and visual deactivation detected by a combined fMRI/EEG study. *NeuroImage*, 16:251–258, 2002.

[44] I. Daubechies, E. Roussos, S. Takerkart, S. Benharrosh, C. Golden, K. DArdenne, W. Richter, J.D. Cohen, and J. Haxby. Independent component analysis for brain fMRI does not select for independence. *Proceedings of the National Academy of Sciences of the United States of America*, 106(26):10415–10422, 2009.

[45] W. De Clercq. *Advanced preprocessing techniques and nonlinear signal analysis applied to scalp electroencephalograms for the prediction of epileptic seizures*. PhD thesis, Faculty of Engineering, Katholieke Universiteit Leuven (Leuven, Belgium), 2005.

[46] W. De Clercq, A. Vergult, B. Vanrumste, W. Van Paesschen, and S. Van Huffel. Canonical Correlation Analysis applied to remove muscle artifacts from the electroencephalogram. *IEEE Transactions on Biomedical Engineering*, 53(12):2583–2587, 2006.

[47] L. De Lathauwer. Decompositions of a Higher-Order Tensor in Block Terms - Part I: Lemmas for Partitioned Matrices. *SIAM Journal on Matrix Analysis and Applications*, 30(3):1022–1032, 2008.

[48] L. De Lathauwer. Decompositions of a Higher-Order Tensor in Block Terms - Part II: Definitions and Uniqueness. *SIAM Journal on Matrix Analysis and Applications*, 30(3):1033–1066, 2008.

[49] L. De Lathauwer. Decompositions of a Higher-Order Tensor in Block Terms - Part III: Alternating Least Squares Algorithms. *SIAM Journal on Matrix Analysis and Applications*, 30(3):1067–1083, 2008.

[50] F. De Martino, A.W. de Borst, G. Valente, R. Goebel, and E. Formisano. Predicting EEG single trial responses with simultaneous fMRI and relevance vector machine regression. *NeuroImage*, 56(2):826–836, 2011.

[51] M. De Vos. *Decomposition methods with applications in neuroscience*. PhD thesis, Faculty of Engineering, Katholieke Universiteit Leuven (Leuven, Belgium), 2009.

[52] M. De Vos, S. Riès, K. Vanderperren, B. Vanrumste, F-X. Alario, S. Van Huffel, and B. Burle. Removal of muscle artifacts from EEG recordings of spoken language production. *Neuroinformatics*, 8(2):135–150, 2010.

[53] M. De Vos, A. Vergult, L. De Lathauwer, W. De Clercq, S. Van Huffel, P. Dupont, A. Palmini, and W. Van Paesschen. Canonical decomposition

of ictal scalp EEG reliably detects the seizure onset zone. *NeuroImage*, 37(3):844–854, 2007.

[54] S. Debener and M. De Vos. The benefits of simultaneous EEG-fMRI for EEG analysis. *Clinical Neurophysiology*, 122(2):217–218, 2011.

[55] S. Debener, K.J. Mullinger, R.K. Niazy, and R.W. Bowtell. Properties of the ballistocardiogram artefact as revealed by EEG recordings at 1.5, 3 and 7 Tesla static magnetic field strength. *International Journal of Psychophysiology*, 67(3):189–199, 2008.

[56] S. Debener, A. Strobel, B. Sorger, J. Peters, C. Kranczioch, A.K. Engel, and R. Goebel. Improved quality of auditory event-related potentials recorded simultaneously with 3 T fMRI: removal of the ballistocardiogram artifact. *NeuroImage*, 34:587–597, 2007.

[57] S. Debener, M. Ullsperger, M. Siegel, and A.K. Engel. Single-trial EEG-fMRI reveals the dynamics of cognitive function. *Trends in Cognitive Sciences*, 10(12):558–563, 2006.

[58] S. Debener, M. Ullsperger, M. Siegel, K. Fiehler, D.Y. von Cramon, and A.K. Engel. Trial-by-trial coupling of concurrent electroencephalogram and functional magnetic resonance imaging identifies the dynamics of performance monitoring. *The Journal of Neuroscience*, 25(50):11730–11737, 2005.

[59] W. Deburchgraeve, P.J. Cherian, M. De Vos, R.M. Swarte, J.H. Blok, G.H. Visser, P. Govaert, and S. Van Huffel. Automated neonatal seizure detection mimicking a human observer reading EEG. *Clinical Neurophysiology*, 119(11):2447–2454, 2008.

[60] W. Deburchgraeve, P.J. Cherian, M. De Vos, R.M. Swarte, J.H. Blok, G.H. Visser, P. Govaert, and S. Van Huffel. Neonatal seizure localization using PARAFAC decomposition. *Clinical Neurophysiology*, 120:1787–1796, 2009.

[61] A. Delorme and S. Makeig. EEGLAB: an open source toolbox for analysis of single-trial EEG dynamics including independent component analysis. *Journal of Neuroscience Methods*, 134:9–21, 2004.

[62] M. Demeyer and B. Machilsen. Creating perceptual grouping displays with GERT. In *Perception, 40; ECVP Abstract Supplement*, page 179, 2011.

[63] M.F. Dempsey and B. Condon. Thermal injuries associated with MRI. *Clinical Radiology*, 56:457–465, 2001.

[64] D.C. Deuchar. Ballistocardiography. *British Heart Journal*, 29(3):285–288, 1967.

[65] A. Devor, A.K. Dunn, M.L. Andermann, I. Ulbert, D.A. Boas, and A.M. Dale. Coupling of Total Hemoglobin Concentration, Oxygenation, and Neural Activity in Rat Somatosensory Cortex. *Neuron*, 39:353–359, 2003.

[66] F. Di Russo, A. Martínez, and S.A. Hillyard. Source analysis of event-related cortical activity during visuo-spatial attention. *Cerebral Cortex*, 13(5):486–499, 2003.

[67] F. Di Russo, A. Martinez, M.I. Sereno, S. Pitzalis, and S.A. Hillyard. Cortical sources of the early components of the visual evoked potential. *Human Brain Mapping*, 15:95–111, 2002.

[68] F. Di Russo, S. Pitzalis, G. Spitoni, T. Aprile, F. Patria, D. Spinelli, and S.A. Hillyard. Identification of the neural sources of the pattern-reversal VEP. *NeuroImage*, 24(3):874–886, 2005.

[69] H.H. Dietrich, Y. Kajita, and R.G. Dacey Jr. Local and conducted vasomotor responses in isolated rat cerebral arterioles. *The American Journal of Physiology*, 271(3):H1109–H1116, 1996.

[70] E. Donchin and E.F. Heffley. Multivariate analysis of event-related potential data: a tutorial review. *D.A. Otto (ed.), Multidisciplinary Perspectives in Event-Related Potential Research, U.S. Government Printing Office, Washington, DC*, pages 555–572, 1978.

[71] T. Eichele, V.D. Calhoun, and S. Debener. Mining EEG-fMRI using independent component analysis. *International Journal of Psychophysiology*, 73(1):53–61, 2009.

[72] T. Eichele, V.D. Calhoun, M. Moosmann, K. Specht, M.L.A. Jongsmae, R. Quian Quiroga, H. Nordby, and K. Hugdahl. Unmixing concurrent EEG-fMRI with parallel independent component analysis. *International Journal of Psychophysiology*, 67(3):222–234, 2008.

[73] T. Eichele, S. Debener, V.D. Calhoun, K. Specht, A.K. Engel, K. Hugdahl, D.Y. von Cramon, and M. Ullsperger. Prediction of human errors by maladaptive changes in event-related brain networks. *Proceedings of the National Academy of Sciences of the United States of America*, 105(16):6173–6178, 2008.

[74] T. Eichele, K. Specht, M. Moosmann, M.L. Jongsma, R.Q. Quiroga, H. Nordby, and K. Hugdahl. Assessing the spatiotemporal evolution of neuronal activation with single-trial event-related potentials and functional MRI. *Proceedings of the National Academy of Sciences of the United States of America*, 102:17798–17803, 2005.

[75] M.L. Ellingson, E. Liebenthal, M.V. Spanaki, T. Prieto, J.R. Binder, and K.M. Ropella. Ballistocardiogram artifact reduction in the simultaneous acquisition of auditory ERPS and fMRI. *NeuroImage*, 22:1534–1542, 2004.

[76] M. Falkenstein, J. Hoormann, and J. Hohnsbein. ERP components in Go/Nogo tasks and their relation to inhibition. *Acta Psychologica*, 101:267–291, 1999.

[77] A.S. Field and D. Graupe. Topographic component (parallel factor) analysis of multichannel evoked potentials: practical issues in trilinear spatiotemporal decomposition. *Brain Topography*, 3(4):407–423, 1991.

[78] B.J. Fisch. The source of the EEG. In *Fisch and Spelhmann's EEG Primer*, chapter 1, pages 3–17. Elsevier, third edition, 1999.

[79] M.D. Fox and M.E. Raichle. Spontaneous fluctuations in brain activity observed with functional magnetic resonance imaging. *Nature Reviews Neuroscience*, 8:700–711, 2007.

[80] M.D. Fox, A.Z. Snyder, J.M. Zacks, and M.E. Raichle. Coherent spontaneous activity accounts for trial-to-trial variability in human evoked brain responses. *Nature Neuroscience*, 9(1):23–25, 2006.

[81] A.R. Franco, J. Ling, A. Caprihan, V.D. Calhoun, R.E. Jung, G.L. Heileman, and A.R. Mayer. Multimodal and Multi-Tissue Measures of Connectivity Revealed by Joint Independent Component Analysis. *IEEE Journal of Selected Topics in Signal Processing*, 2(6):986–997, 2008.

[82] F. Freyer, R. Becker, K. Anami, G. Curio, A. Villringer, and P. Ritter. Ultrahigh-frequency EEG during fMRI: pushing the limits of imaging-artifact correction. *NeuroImage*, 48(1):94–108, 2009.

[83] O. Friman. *Adaptive Analysis of Functional MRI data*. PhD thesis, Department of Biomedical Engineering, Linköping University (Sweden), 2003.

[84] K.J. Friston, J. Ashburner, S.J. Kiebel, T.E. Nichols, and W.D. Penny. *Statistical Parametric Mapping: The Analysis of Functional Brain Images*. Academic Press, 2007.

[85] D.R. Gitelman, W.D. Penny, J. Ashburner, and K.J. Friston. Modeling regional and psychophysiologic interactions in fMRI: the importance of hemodynamic deconvolution. *NeuroImage*, 19(1):200–207, 2003.

[86] R.I. Goldman, J.M. Stern, J.Jr. Engel, and M.S. Cohen. Acquiring simultaneous EEG and functional MRI. *Clinical Neurophysiology*, 111:1974–1980, 2000.

[87] R.I. Goldman, J.M. Stern, J.Jr. Engel, and M.S. Cohen. Simultaneous EEG and FMRI of the alpha rhythm. *NeuroReport*, 13:2487–2492, 2002.

[88] S.I. Gonçalves, P.J. Pouwels, J.P. Kuijer, R.M. Heethaar, and J.C. de Munck. Artifact removal in co-registered EEG/fMRI by selective average subtraction. *Clinical Neurophysiology*, 118(11):2437–2450, 2007.

[89] J. Gotman, C.G. Bénar, and F. Dubeau. Combining EEG and FMRI in epilepsy: methodological challenges and clinical results. *Journal of Clinical Neurophysiology*, 21(4):229–240, 2004.

[90] C. Grimm, A. Schreiber, R. Kristeva-Feige, T. Mergner, J. Hennig, and C.H. Lücking. A comparison between electric source localisation and fMRI during somatosensory stimulation. *Electroencephalography and Clinical Neurophysiology*, 106(1):22–29, 1998.

[91] F. Grouiller, L. Vercueil, A. Krainik, C. Segebarth, P. Kahane, and O. David. A comparative study of different artifact removal algorithms for EEG signals acquired during functional MRI. *NeuroImage*, 38:124–137, 2007.

[92] K. Hamandi, A. Salek-Haddadi, D.R. Fish, and L. Lemieux. EEG/functional MRI in epilepsy: The Queen Square Experience. *Journal of Clinical Neurophysiology*, 21(4):241–248, 2004.

[93] N. Harel, S.P. Lee, T. Nagaoka, D.S. Kim, and S.G. Kim. Origin of negative blood oxygenation level-dependent fMRI signals. *Journal of cerebral blood flow and metabolism*, 22(8):908–917, 2002.

[94] R.A. Harshman. Foundations of the CP procedure: models and conditions for an 'explanatory' multi-modal factor analysis. *UCLA Working Papers in Phonetics*, 16:1–84, 1970.

[95] R.A. Harshman and M.E. Lundy. Data preprocessing and the extended PARAFAC model. In H.G. Law, C.W. Snyder Jr, J.A. Hattie, and R.P. McDonald, editors, *Research methods for multimode data analysis*, pages 216–284. Praeger, 1984.

[96] C.S. Herrmann and S. Debener. Simultaneous recording of EEG and BOLD responses: A historical perspective. *International Journal of Psychophysiology*, 67(3):161–168, 2008.

[97] A. Hoffmann, L. Jäger, K.J. Werhahn, M. Jaschke, S. Noachtar, and M. Reiser. Electroencephalography during functional echo-planar imaging: Detection of epileptic spikes using post-processing methods. *Magnetic Resonance in Medicine*, 44(5):791–798, 2000.

[98] `http://spot.colorado.edu/~dubin/talks/brodmann/brodmann.html`, August 2011.

[99] http://www.edoctoronline.com/medical-atlas.asp?c=4&id=21758, July 2011.

[100] http://www.brainlink.org.au/understanding-the-nervous-system.htm, August 2011.

[101] http://www.radiopaedia.org/, August 2011.

[102] http://www.revisemri.com/, August 2011.

[103] F. Huang-Hellinger, H. Breiter, G. McCormack, M. Cohen, K. Kwong, J. Sutton, R. Savoy, R. Weisskoff, T. Davis, J. Baker, J. Belliveau, and B. Rosen. Simultaneous functional magnetic resonance imaging and electrophysiological recording. *Human Brain Mapping*, 3(1):13–23, 1995.

[104] G.J. Huiskamp. Reduction of the ballistocardiogram artifact in simultaneous EEG-fMRI using ICA. In *Proceedings of the Annual International Conference of the IEEE Engineering in Medicine and Biology Society 4*, pages 3691–3694, Shanghai, China, 2005.

[105] A. Hyvärinen, J. Karhunen, and E. Oja. *Independent component analysis*. Wiley and Sons, 2001.

[106] C. Iadecola. Neurovascular regulation in the normal brain and in Alzheimer's disease. *Nature reviews. Neuroscience*, 5(5):347–360, 2004.

[107] M.H. In, S.Y. Lee, T.S. Park, T.-S. Kim, M.H. Cho, and Y.B. Ahn. Ballistocardiogram artifact removal from EEG signals using adaptive filtering of EOG signals. *Physiological Measurement*, 27(11):1227–1240, 2006.

[108] J.R. Ives, S. Warach, F. Schmitt, R.R. Edelman, and D.L. Schomer. Monitoring the patient's EEG during echo planar MRI. *Electroencephalography and Clinical Neurophysiology*, 87:417–420, 1993.

[109] H. Jasper. The Ten-Twenty Electrode System of the International Federation. *Electroencephalography and Clinical Neurophysiology*, 10(2):371–375, 1958.

[110] P. Jezzard, P.M. Matthews, and S.M. Smith. *Functional MRI : An Introduction to Methods*. Oxford University Press, 2002.

[111] D. Johanson and E. Blake. *From Lucy to Language*. New York: Simon and Schuster, 1996.

[112] C.A. Joyce, I.F. Gorodnitsky, and M. Kutas. Automatic removal of eye movement and blink artifacts from EEG data using blind component separation. *Psychophysiology*, 41(2):313–325, 2004.

[113] J.M. Kilner and K.J. Friston. Neuronal Models for EEG-fMRI integration. In C. Mulert and L. Lemieux, editors, *EEG-fMRI: Psychological Basis, Technique and Applications*, chapter 22, pages 453–464. Springer, first edition, 2010.

[114] K.H. Kim, H.W. Yoon, and H.W. Park. Improved ballistocardiac artifact removal from the electroencephalogram recorded in fMRI. *Journal of Neuroscience Methods*, 135(1-2):193–203, 2004.

[115] M. Klemm, J. Haueisen, and G. Ivanova. Independent component analysis: comparison of algorithms for the investigation of surface electrical brain activity. *Medical and Biological Engineering and Computing*, 47:413–423, 2009.

[116] K. Koffka. *Principles of Gestalt psychology.* Routledge & Kegan Paul, Ltd., 1935.

[117] K. Krakow, P.J. Allen, M.R. Symms, L. Lemieux, O. Josephs, and D.R. Fish. EEG recording during fMRI experiments: image quality. *Human Brain Mapping*, 10(1):10–15, 2000.

[118] K. Krakow, L. Lemieux, D. Messina, C.A. Scott, M.R. Symms, J.S. Duncan, and D.R. Fish. Spatio-temporal imaging of focal interictal epileptiform activity using EEG-triggered functional MRI. *Epileptic Disorders: international epilepsy journal with videotape*, 3(2):67–74, 2001.

[119] K. Krakow, D. Messina, L. Lemieux, J.S. Duncan, and D.R. Fish. Functional MRI activation of individual interictal epileptiform spikes. *NeuroImage*, 13:502–505, 2001.

[120] F. Kruggel, C.J. Wiggins, C.S. Herrmann, and D.Y. von Cramon. Recording of the event-related potentials during functional MRI at 3.0 Tesla field strength. *Magnetic Resonance in Medicine*, 44(2):277–282, 2000.

[121] H. Laufs, J. Daunizeau, D.W. Carmichael, and A. Kleinschmidt. Recent advances in recording electrophysiological data simultaneously with magnetic resonance imaging. *NeuroImage*, 40(2):515–528, 2008.

[122] H. Laufs, A. Kleinschmidt, A. Beyerle, E. Eger, A. Salek-Haddadi, C. Preibisch, and K. Krakow. EEG-correlated fMRI of human alpha activity. *NeuroImage*, 19:1463–1476, 2003.

[123] M. Lauritzen. Reading vascular changes in brain imaging: is dendritic calcium the key? *Nature Reviews Neuroscience*, 6:77–85, 2005.

[124] H. Lee, Y.D. Kim, A. Cichocki, and S. Choi. Nonnegative tensor factorization for continuous EEG classification. *International journal of neural systems*, 17(4):305–317, 2007.

[125] T.W. Lee, M. Girolami, and T.J. Sejnowski. Independent component analysis using an extended infomax algorithm for mixed sub-Gaussian and super-Gaussian sources. *Neural Computation*, 11(2):417–441, 1999.

[126] L. Lemieux, P.J. Allen, F. Franconi, M.R. Symms, and D.R. Fish. Recording of EEG during fMRI experiments: patient safety. *Magnetic Resonance in Medicine*, 38(6):943–952, 1997.

[127] L. Lemieux, P.J. Allen, K. Krakow, M.R. Symms, and D.R. Fish. Methodological Issues in EEG-correlated functional MRI Experiments. *International Journal of Bioelectromagnetism*, 1(1):87–95, 1999.

[128] L. Lemieux, K. Krakow, and D.R. Fish. Comparison of spike-triggered functional MRI BOLD activation and EEG dipole model localization. *NeuroImage*, 14:1097–1104, 2001.

[129] J. Li, L. Zhang, and Q. Zhao. Pattern Classification of Visual Evoked Potentials Based on Parallel Factor Analysis. In R. Wang, E. Shen, and F. Gu, editors, *Advances in Cognitive Neurodynamics ICCN 2007*, pages 571–575. Springer Netherlands, 2008.

[130] E. Liebenthal, M.L. Ellingson, M.V. Spanaki, T.E. Prieto, K.M. Ropella, and J.R. Binder. Simultaneous ERP and fMRI of the auditory cortex in a passive oddball paradigm. *NeuroImage*, 19:1395–1404, 2003.

[131] N.K. Logothetis, J. Pauls, M. Augath, T. Trinath, and A. Oeltermann. Neurophysiological investigation of the basis of the fMRI signal. *Nature*, 412:150–157, 2001.

[132] S.J. Luck. *An introduction to the event-related potential technique*. The MIT Press, Cambridge, MA, 2005.

[133] B. Machilsen, M. Pauwels, and J. Wagemans. The role of vertical mirror symmetry in visual shape detection. *Journal of Vision*, 9(12:11):1–11, 2009.

[134] S. Makeig, S. Debener, J. Onton, and A. Delorme. Mining event-related brain dynamics. *Trends in Cognitive Sciences*, 8(5):204–210, 2004.

[135] S. Makeig, T.-P. Juny, A.J. Bell, D. Ghahremani, and T.J. Sejnowski. Blind separation of auditory event-related brain responses into independent components. *Proceedings of the National Academy of Sciences of the United States of America*, 94:10979–10984, 1997.

[136] S. Makeig, M. Westerfield, T.-P. Jung, J. Covington, J. Townsend, T.J. Sejnowski, and E. Courchesne. Functionally independent components of the late positive event-related potential during visual spatial attention. *Journal of Neuroscience*, 19:2665–2680, 1999.

[137] J. Malmivuo and R. Plonsey. *Bioelectromagnetism: Principles and Applications of Bioelectric and Biomagnetic Fields*. Oxford University Press, New York - Oxford, 1995.

[138] H. Mandelkow, P. Halder, P. Boesiger, and D. Brandeis. Synchronization facilitates removal of MRI artefacts from concurrent EEG recordings and increases usable bandwidth. *NeuroImage*, 32:1120–1126, 2006.

[139] D. Mantini, M.G. Perrucci, S. Cugini, A. Ferretti, G.L. Romani, and C. Del Gratta. Complete artifact removal for EEG recorded during continuous fMRI using independent component analysis. *NeuroImage*, 34:598–607, 2007.

[140] A. Martínez, F. Di Russo, L. Anllo-Vento, M.I. Sereno, B.B. Buxton, and S.A. Hillyard. Putting spatial attention on the map: timing and localization of stimulus selection process in striate and extrastriate visual areas. *Vision Research*, 41(10-11):1437–1457, 2001.

[141] E. Martínez-Montes, P.A. Valdés-Sosa, F. Miwakeichi, R.I. Goldman, and M.S. Cohen. Concurrent EEG/fMRI analysis by multiway Partial Least Squares. *NeuroImage*, 22(3):1023–1034, 2004.

[142] R.A.J. Masterton, D.F. Abbott, S.W. Fleming, and G.D. Jackson. Measurement and reduction of motion and ballistocardiogram artefacts from simultaneous EEG and fMRI recordings. *NeuroImage*, 37(1):202–211, 2007.

[143] J.E. Mayhew, S. Askew, Y. Zheng, J. Porrill, G.W. Westby, P. Redgrave, D.M. Rector, and R.M. Harper. Cerebral vasomotion: a 0.1-Hz oscillation in reflected light imaging of neural activity. *NeuroImage*, 4(3):183–193, 1996.

[144] S.D. Mayhew, S.G. Dirckx, R.K. Niazy, G.D. Iannetti, and R.G. Wise. EEG signatures of auditory activity correlate with simultaneously recorded fMRI responses in humans. *NeuroImage*, 49(1):849–864, 2010.

[145] M. Mennes, H. Wouters, B. Vanrumste, L. Lagae, and P. Stiers. Validation of ICA as a tool to remove eye movement artifacts from EEG/ERP. *Psychophysiology*, 47:1142–1150, 2010.

[146] V. Meriläinen. Magnetic resonance imaging with simultaneous electroencephalography recording: safety issues. Master's thesis, Department of electrical and communications engineering, Helsinki University of Technology (Finland), 2003.

[147] A. Meyer-Lindenberg. From maps to mechanisms through neuroimaging of schizophrenia. *Nature*, 468(7321):194–202, 2010.

[148] B. Mijović, M. De Vos, K. Vanderperren, N. Novitskiy, B. Vanrumste, P. Stiers, B.R.H. Van den Bergh, J. Wagemans, L. Lagae, S. Sunaert, and S. Van Huffel. The Why and How of JointICA: Results from a

Visual Detection Task. Technical Report 10-252, ESAT-SISTA, Katholieke Universiteit Leuven, Leuven, Belgium, submitted.

[149] F. Miwakeichi, E. Martínez-Montes, P.A. Valdés-Sosa, N. Nishiyama, H. Mizuhara, and Y. Yamaguchi. Decomposing EEG data into space-time-frequency components using parallel factor analysis. *NeuroImage*, 22:1035–1045, 2004.

[150] M. Mørup, L.K. Hansen, S.M. Arnfred, L.-H. Lim, and K.H. Madsen. Shift-invariant multilinear decomposition of neuroimaging data. *NeuroImage*, 42:1439–1450, 2008.

[151] M. Mørup, L.K. Hansen, C.S. Herrmann, J. Parnas, and S.M. Arnfred. Parallel Factor Analysis as an exploratory tool for wavelet transformed event-related EEG. *NeuroImage*, 29(3):938–947, 2006.

[152] J. Möcks. Decomposing event-related potentials: a new topographic components model. *Biological Psychology*, 26:199–215, 1988.

[153] J. Möcks. Topographic components model for event-related potentials and some biophysical considerations. *IEEE Transactions on Biomedical Engineering*, 35:482–484, 1988.

[154] M. Moosmann, T. Eichele, H. Nordby, K. Hugdahl, and V.D. Calhoun. Joint independent component analysis for simultaneous EEG-fMRI: principle and simulation. *International Journal of Psychophysiology*, 67(3):212–221, 2008.

[155] M. Moosmann, P. Ritter, I. Krastel, A. Brink, S. Thees, F. Blankenburg, B. Taskin, H. Obrig, and A. Villringer. Correlates of alpha rhythm in functional magnetic resonance imaging and near infrared spectroscopy. *NeuroImage*, 20:145–158, 2003.

[156] M. Moosmann, V.H. Schonfelder, K. Specht, R. Scheeringa, H. Nordby, and K. Hugdahl. Realignment parameter-informed artefact correction for simultaneous EEG-fMRI recordings. *NeuroImage*, 45:1144–1150, 2009.

[157] C. Mulert, L. Jäger, R. Schmitt, P. Bussfeld, O. Pogarell, H.J. Möller, G. Juckel, and U. Hegerla. Integration of fMRI and simultaneous EEG: towards a comprehensive understanding of localization and time-course of brain activity in target detection. *NeuroImage*, 22:83–94, 2004.

[158] C. Mulert, G. Leicht, P. Hepp, V. Kirsch, S. Karch, O. Pogarell, M. Reiser, U. Hegerl, L. Jäger, H.J. Moller, and R.W. McCarley. Single-trial coupling of the gamma-band response and the corresponding BOLD signal. *NeuroImage*, 49(3):2238–2247, 2010.

[159] C. Mulert and L. Lemieux. *EEG-fMRI: Psychological Basis, Technique and Applications*. Springer, 2010.

[160] W. Nakamura, K. Anami, T. Mori, O. Saitoh, A. Cichocki, and S. Amari. Removal of ballistocardiogram artifacts from simultaneously recorded EEG and fMRI data using independent component analysis. *IEEE Transactions on Biomedical Engineering*, 53(7):1294–1308, 2006.

[161] M. Negishi, M. Abildgaard, T. Nixon, and R.T. Constable. Removal of time-varying gradient artifacts from EEG data acquired during continuous fMRI. *Clinical Neurophysiology*, 115(9):2181–2192, 2004.

[162] M. NessAiver. *All you really need to know about MRI Physics*. University of Maryland, Baltimore, 1996.

[163] R.K. Niazy, C.F. Beckmann, G.D. Iannetti, J.M. Brady, and S.M. Smith. Removal of FMRI environment artifacts from EEG data using optimal basis sets. *NeuroImage*, 28:720–737, 2005.

[164] J. Niessing, B. Ebisch, K.E. Schmidt, M. Niessing, W. Singer, and R.A. Galuske. Hemodynamic signals correlate tightly with synchronized gamma oscillations. *Science*, 309(5736):948–951, 2005.

[165] S. Nieuwenhuis, N. Yeung, W. Van den Wildenberg, and K.R. Ridderinkhof. Electrophysiological correlates of anterior cingulate function in a Go/NoGo task: effects of response conflict and trial-type frequency. *Cognitive, Affective and Behavioral Neuroscience*, 3:17–26, 2003.

[166] Y. Nir, L. Fisch, R. Mukamel, H. Gelbard-Sagiv, A. Arieli, I. Fried, and R. Malach. Coupling between neuronal firing rate, gamma LFP, and BOLD fMRI is related to interneuronal correlations. *Current Biology*, 17(15):1275–1285, 2007.

[167] D.G. Nishimura. *Principles of Magnetic Resonance Imaging*. Stanford University, 1996.

[168] N. Novitski, I. Anourova, S. Martinkauppi, H.J. Aronen, R. Naatanen, and S. Carlson. Effects of noise from functional magnetic resonance imaging on auditory event-related potentials in working memory task. *NeuroImage*, 20:1320–1328, 2003.

[169] N. Novitskiy, J. Ramautar, K. Vanderperren, M. De Vos, M. Mennes, B. Mijovic, B. Vanrumste, P. Stiers, B. Van den Bergh, L. Lagae, S. Sunaert, S. Van Huffel, and J. Wagemans. The BOLD correlates of the visual P1 and N1 in single-trial analysis of simultaneous EEG-fMRI recording during a spatial detection task. *NeuroImage*, 54(2):824–835, 2011.

[170] M.R. Nuwer, G. Comi, R. Emmerson, A. Fuglsang-Frederiksen, J.-M. Gue, H. Hinrichs, A. Ikeda, F. Jose, and C.Luccas. IFCN standards for digital recording of clinical EEG. *Electroencephalography and Clinical Neurophysiology*, 106(3):259–261, 1998.

[171] J. Pan and W.J. Tompkins. A real time QRS detection algorithm. *IEEE Transactions on Biomedical Engineering*, 32:230–236, 1985.

[172] O.H. Petersen. *Lecture Notes: Human Physiology, 5th Edition.* Wiley-Blackwell, 2006.

[173] D.B. Plewes and W. Kucharczyk. The Animated Physics of MRI - Spin Gymnastics. *http://www.sunnybrook.ca/files/RESH_DBP_Spin_gymnastics.pdf*, 2003.

[174] E.L. Reilly. EEG recording and operation of the apparatus. In E. Niedermeyer and F. Lopes da Silva, editors, *Electroencephalography: Basic Principles, Clinical Applications and Related Fields*, chapter 7. Urban & Schwarzenberg, Baltimore, first edition, 1987.

[175] P. Ritter and A. Villringer. Simultaneous EEG-fMRI. *Neuroscience & Biobehavioral Reviews*, 30(6):823–838, 2006.

[176] B. Sadeh, I. Podlipsky, A. Zhdanov, and G. Yovel. Event-Related Potential and Functional MRI Measures of Face-Selectivity are Highly Correlated:A Simultaneous ERP-fMRI Investigation. *Human Brain Mapping*, 31(10):1490–1501, 2010.

[177] S. Sanei and J. A. Chambers. *EEG Signal Processing.* John Wiley & Sons, Ltd, 2007.

[178] M. Schabus, T.T. Dang-Vu, G. Albouy, E. Balteau, M. Boly, J. Carrier, A. Darsaud, C. Degueldre, M. Desseilles, S. Gais, C. Phillips, G. Rauchs, C. Schnakers, V. Sterpenich, G. Vandewalle, A. Luxen, and P. Maquet. Hemodynamic cerebral correlates of sleep spindles during human non-rapid eye movement sleep. *Proceedings of the National Academy of Sciences of the United States of America*, 104:13164–13169, 2007.

[179] R. Scheeringa, A. Mazaheri, I. Bojak, D.G. Norris, and A. Kleinschmidt. Modulation of visually evoked cortical FMRI responses by phase of ongoing occipital alpha oscillations. *The Journal of Neuroscience*, 31(10):3813–3820, 2011.

[180] C. Scheibe, M. Ullsperger, W. Sommer, and H.R. Heekeren. Effects of parametrical and trial-to-trial variation in prior probability processing revealed by simultaneous electroencephalogram/functional magnetic resonance imaging. *The Journal of Neuroscience*, 30:16709–16717, 2010.

[181] M. Seeck, F. Lazeyras, C.M. Michel, O. Blanke, C.A. Gericke, J. Ives, J. Delavelle, X. Golay, C.A. Haenggeli, N. de Tribolet, and T. Landis. Non-invasive epileptic focus localization using EEG-triggered functional

MRI and electromagnetic tomography. *Electroencephalography and Clinical Neurophysiology*, 106(6):508–512, 1998.

[182] M. Seeck, C.M. Michel, L. Spinelli, and F. Lazeyras. EEG mapping and functional MRI in presurgical epilepsy evaluation. *Revue neurologique Société de neurologie de Paris*, 157(8-9 Pt. 1):747–751, 2001.

[183] H. Segers, A. Combaz, N.V. Manyakov, N. Chumerin, K. Vanderperren, S. Van Huffel, and M.M. Van Hulle. Steady state visual evoked potential (SSVEP) - based brain spelling system with synchronous and asynchronous typing modes. In *IFMBE Proceedings vol. 34 - Proceedings of the* 15th *Nordic Baltic Conference on Biomedical Engineering and Medical Physics (NBC15)*, pages 164–167, Aalborg, Denmark, 2011.

[184] A. Shmuel. Locally Measured Neuronal Correlates of Functional MRI Signals. In C. Mulert and L. Lemieux, editors, *EEG-fMRI: Psychological Basis, Technique and Applications*, chapter 4, pages 64–82. Springer, first edition, 2010.

[185] A. Shmuel and D.A. Leopold. Neuronal correlates of spontaneous fluctuations in fMRI signals in monkey visual cortex: Implications for functional connectivity at rest. *Human Brain Mapping*, 29(7):751–761, 2008.

[186] A. Shmuel, E. Yacoub, J. Pfeuffer, P.F. Van de Moortele, G. Adriany, X. Hu, and K. Ugurbil. Sustained negative BOLD, blood flow and oxygen consumption response and its coupling to the positive response in the human brain. *Neuron*, 36(6):1195–1210, 2002.

[187] J. Sijbers, J. Van Audekerke, M. Verhoye, A. Van der Linden, and D. Van Dyck. Reduction of ECG and gradient related artifacts in simultaneously recorded human EEG/MRI data. *Magnetic Resonance Imaging*, 18(7):881–886, 2000.

[188] J. Sijbers, L. Michiels, M. Verhoye, J. van Audekerke, A. van der Linden, and D. van Dyck. Restoration of MR-induced artifacts in simultaneously recorded MR/EEG data. *Magnetic Resonance Imaging*, 17(9):1383–1391, 1999.

[189] W. Skrandies. Global field power and topographic similarity. *Brain Topography*, 3(1):137–141, 1990.

[190] A. Smilde, R. Bro, and P. Geladi. *Multi-way analysis with applications in the chemical sciences*. John Wiley & Sons, 2004.

[191] M. Sorensen, L. De Lathauwer, P. Comon, S. Icart, and L. Deneire. Computation of a Canonical Polyadic Decomposition with a semi-unitary matrix factor. Technical Report 11-95, ESAT-SISTA, Katholieke Universiteit Leuven, Leuven, Belgium, submitted.

[192] G. Srivastava, S. Crottaz-Herbette, K.M. Lau, G.H. Glover, and V. Menon. ICA-based procedures for removing ballistocardiogram artifacts from EEG data acquired in the MRI scanner. *NeuroImage*, 24:50–60, 2005.

[193] J.P. Stevens. *Applied Multivariate Statistics for the Social Sciences (Third Ed.)*. Lawrence Erlbaum Associates, Inc, Mahway NJ, 1996.

[194] J.V. Stone. Independent component analysis: an introduction. *Trends in Cognitive Sciences*, 6:59–64, 2002.

[195] M.R. Symms, P.J. Allen, F.G. Woermann, G. Polizzi, K. Krakow, G.J. Barker, D.R. Fish, and J.S. Duncan. Reproducible localization of interictal epileptiform discharges using EEG-triggered fMRI. *Physics in Medicine and Biology*, 44(7):N161–N8, 1999.

[196] A.C. Tang, M.T. Sutherland, and C.J. McKinney. Validation of SOBI components from high-density EEG. *NeuroImage*, 25(2):539–553, 2005.

[197] T.S. Tenforde, C.T. Gaffey, B.R. Moyer, and T.F. Budinger. Cardiovascular alterations in Macaca monkeys exposed to stationary magnetic fields: experimental observations and theoretical analysis. *Bioelectromagnetics*, 4(1):1–9, 1983.

[198] L.R. Tucker. The extension of factor analysis to three-dimensional matrices. In H. Gulliksen and N. Frederiksen, editors, *Contributions to mathematical psychology.*, pages 110–127. Holt, Rinehart and Winston, 1964.

[199] L.R. Tucker. Some mathematical notes on three-mode factor analysis. *Psychometrika*, 31:279–311, 1966.

[200] M. Ullsperger and S. Debener. *Simultaneous EEG and fMRI: Recording, Analysis, and Application*. Oxford University Press, New York, 2010.

[201] E. Urrestarazu, J. Iriarte, M. Alegre, M. Valencia, C. Viteri, and J. Artieda. Independent component analysis removing artifacts in ictal recordings. *Epilepsia*, 45(9):1071–1078, 2004.

[202] K. Vanderperren, M. De Vos, B. Mijović, J.R. Ramautar, N. Novitskiy, B. Vanrumste, P. Stiers, B.R.H. Van den Bergh, J. Wagemans, L. Lagae, S. Sunaert, and S. Van Huffel. PARAFAC on ERP data from a visual detection task during simultaneous fMRI acquisition. In *Proceedings of the International Biosignal Processing Conference*, volume 103, pages 1–4, Berlin, Germany, 2010.

[203] K. Vanderperren, M. De Vos, J.R. Ramautar, N. Novitskiy, M. Mennes, S. Assecondi, B. Vanrumste, P. Stiers, B. Van den Bergh, J. Wagemans, L. Lagae, S. Sunaert, and S. Van Huffel. Removal of BCG artifacts from EEG recordings inside the MR scanner: a comparison of methodological and validation-related aspects. *NeuroImage*, 50(3):920–934, 2010.

[204] K. Vanderperren, B. Hunyadi, M. De Vos, M. Mennes, H. Wouters, B. Vanrumste, P. Stiers, L. Lagae, and S. Van Huffel. Reduction of alpha distortion in event related potentials. In *Proceedings of* 4th *European Congress of the International Federation for Medical and Biomedical Engineering (ECIFMBE)*, pages 1298–1301, Antwerp, Belgium, 2008.

[205] K. Vanderperren, B. Mijović, N. Novitskiy, B. Vanrumste, P. Stiers, B. Van den Bergh, J. Wagemans, L. Lagae, S. Sunaert, S. Van Huffel, and M. De Vos. Single trial ERP reading based on Parallel Factor Analysis. Technical Report 11-185, ESAT-SISTA, Katholieke Universiteit Leuven, Leuven, Belgium, submitted.

[206] K. Vanderperren, J. Ramautar, N. Novitski, M. De Vos, M. Mennes, B. Vanrumste, P. Stiers, B. Van den Bergh, J. Wagemans, L. Lagae, S. Sunaert, and S. Van Huffel. Ballistocardiogram artifacts in simultaneous EEG-fMRI acquisitions. *International Journal of Bioelectromagnetism*, 9(3):146–150, 2007.

[207] K. Vanderperren, J.R. Ramautar, N. Novitskiy, M. De Vos, M. Mennes, B. Vanrumste, P. Stiers, B.R.H. Van den Bergh, J. Wagemans, L. Lagae, S. Sunaert, and S. Van Huffel. Study of ballistocardiogram artifacts in simultaneous EEG-fMRI acquisitions. In *Proceedings of the Neuromath Workshop: Advanced Methods for the Estimation of Human Brain Activity and Connectivity (NeuroMath)*, pages 121–122, Rome, Italy, 2007.

[208] K. Vanderperren, S. Riès, M. De Vos, B. Vanrumste, F. Alario, B. Burle, and S. Van Huffel. Removal of muscle artifacts from EEG recordings of spoken language production. In *Proceedings of the Neuromath Workshop: Advanced Methods for the Estimation of Human Brain Activity and Connectivity (Neuromath)*, pages 121–122, Jena, Germany, 2008.

[209] K. Vanderperren, B. Vanrumste, and S. Van Huffel. NeuroMath: advanced methods for the estimation of human brain activity and connectivity. *Biomedizinische Technik/Biomedical Engineering*, 55(3):121, 2010.

[210] J. Vartiainen, M. Liljeström, M. Koskinen, H. Renvall, and R. Salmelin. Functional magnetic resonance imaging blood oxygenation level-dependent signal and magnetoencephalography evoked responses yield different neural functionality in reading. *The Journal of Neuroscience*, 31(3):1048–1058, 2011.

[211] J.L. Vincent, L.J. Larson-Prior, J.M. Zempel, and A.Z. Snyder. Moving GLM ballistocardiogram artifact reduction for EEG acquired simultaneously with fMRI. *Clinical Neurophysiology*, 118(5):981–998, 2007.

[212] X. Wan, K. Iwata, J. Riera, M. Kitamura, and R. Kawashima. Artifact reduction for simultaneous EEG/fMRI recording: adaptive FIR reduction of imaging artifacts. *Clinical Neurophysiology*, 117(3):681–692, 2006.

[213] X. Wan, K. Iwata, J. Riera, T. Ozaki, M. Kitamura, and R. Kawashima. Artifact reduction for EEG/fMRI recording: Nonlinear reduction of ballistocardiogram artifacts. *Clinical Neurophysiology*, 117(3):668–680, 2006.

[214] B.A. Wandell, S.O. Dumoulin, and A.A. Brewer. Visual field maps in human cortex. *Neuron*, 56:366–383, 2007.

[215] K. Wang, H. Begleiter, and B. Porjesz. Trilinear Modeling of Event-Related Potentials. *Brain Topography*, 12(4):263–271, 2000.

[216] S. Warach, J.R. Ives, G. Schlaug, M.R. Patel, D.G. Darby, V. Thangaraj, R.R. Edelman, and D.L. Schomer. EEG-triggered echo-planar functional MRI in epilepsy. *Neurology*, 47(1):89–93, 1996.

[217] R.E. Wendt, R. Rokey, G.W. Vick, and D.L. Johnston. Electrocardiographic gating and monitoring in NMR imaging. *Magnetic Resonance Imaging*, 6(1):89–95, 1988.

[218] M. Wertheimer. Untersuchungen zur Lehre von der Gestalt. *Psychologische Forschung*, 4:301–350, 1923.

[219] N.J. Wesensten, P. Badia, and J. Harsh. Time of day, repeated testing, and interblock interval effects on P300 amplitudes. *Physiology & Behavior*, 47:653–658, 1990.

[220] E.B. Wilson. Probable inference, the law of succession, and statistical inference. *Journal of the American Statistical Association*, 22(158):209–212, 1927.

[221] L. Xu, G. Pearlson, and V.D. Calhoun. Joint source based morphometry identifies linked gray and white matter group differences. *NeuroImage*, 44(3):777–789, 2009.

[222] W.X. Yan, K.J. Mullinger, G.B. Geirsdottir, and R. Bowtell. Physical modeling of the pulse artefact sources in simultaneous EEG/fMRI. *Human Brain Mapping*, 31(4):604–620, 2010.

[223] E. Zarahn. Testing for neural responses during temporal components of trials with BOLD fMRI. *NeuroImage*, 11:783–796, 2000.

Publication List

Papers in international journals

1. **K. Vanderperren**, J.R. Ramautar, N. Novitskiy, M. De Vos, M. Mennes, B. Vanrumste, P. Stiers, B.R.H. Van den Bergh, J. Wagemans, L. Lagae, S. Sunaert and S. Van Huffel. Ballistocardiogram artifacts in simultaneous EEG-fMRI acquisitions. International Journal of Bioelectromagnetism, vol. 9, no. 3, Dec. 2007, pp. 146-150.

2. K. Blinowska, G. Müller-Putz, V. Kaiser, L. Astolfi, **K. Vanderperren**, S. Van Huffel and L. Lemieux. Multimodal imaging of human brain activity: rational, biophysical aspects and modes of integration. Computational Intelligence and Neuroscience, vol. 2009, Jun. 2009, pp. 1-10.

3. **K. Vanderperren**, M. De Vos, J.R. Ramautar, N. Novitskiy, M. Mennes, S. Assecondi, B. Vanrumste, P. Stiers, B.R.H. Van den Bergh, J. Wagemans, L. Lagae, S. Sunaert and S. Van Huffel. Removal of BCG artifacts from EEG recordings inside the MR scanner: a comparison of methodological and validation-related aspects. NeuroImage, vol. 50, no. 3, Apr. 2010, pp. 920-934.

4. S. Assecondi, **K. Vanderperren**, N. Novitskiy, J.R. Ramautar, W. Fias, S. Staelens, P. Stiers, S. Sunaert, S. Van Huffel and I. Lemahieu. Effect of the static magnetic field of the MR-scanner on ERPs: evaluation of visual, cognitive and motor potentials. Clinical Neurophysiology, vol. 21, no. 5, May 2010, pp. 672-685.

5. M. De Vos, S. Riès, **K. Vanderperren**, B. Vanrumste, F. Alario, S. Van Huffel and B. Burle. Removal of muscle artifacts from EEG recordings of spoken language production. Neuroinformatics, vol. 8, no. 2, Jun. 2010, pp. 135-150.

6. N. Novitskiy, J.R. Ramautar, **K. Vanderperren**, M. De Vos, M. Mennes, B. Mijović, B. Vanrumste, P. Stiers, B.R.H. Van den Bergh, L. Lagae, S.

Sunaert, S. Van Huffel and J. Wagemans. The BOLD correlates of the visual P1 and N1 in single-trial analysis of simultaneous EEG-fMRI recordings during a spatial detection task. NeuroImage, vol. 54, no. 2, Jan. 2011, pp. 824-835.

Papers submitted to international journals

7. B. Mijović, **K. Vanderperren**, N. Novitskiy, B. Vanrumste, P. Stiers, B.R.H. Van den Bergh, J. Wagemans, L. Lagae, S. Sunaert, S. Van Huffel and M. De Vos. The Why and How of JointICA: Results from a Visual Detection Task. NeuroImage, resubmitted after major revision, Dec. 2011.

8. **K. Vanderperren**, B. Mijović, N. Novitskiy, B. Vanrumste, P. Stiers, B.R.H. Van den Bergh, L. Lagae, S. Sunaert, J. Wagemans, S. Van Huffel and M. De Vos. Single trial ERP reading based on Parallel Factor Analysis. Psychophysiology, submitted, Nov. 2011.

9. B. Mijović, **K. Vanderperren**, S. Van Huffel and M. De Vos. Improving spatiotemporal characterisation of cognitive processes with data-driven EEG-fMRI analysis. Prilozi (Macedonian Academy of Sciences and Arts), submitted, Nov. 2011.

Papers in proceedings of international conferences

10. **K. Vanderperren**, S. Vandeput, J.-B. Poullet, D. Sima and S. Van Huffel. Automatic quantification of magnetic resonance spectroscopic signals: evaluation and comparison of AQSES and QUEST. Proceedings of the 1st Annual Benelux Symposium of the IEEE Engineering in Medicine and Biology Society (EMBS), Brussels, Belgium, Dec. 2006, pp. 251-254.

11. **K. Vanderperren**, B. Hunyadi, M. De Vos, M. Mennes, H. Wouters, B. Vanrumste, P. Stiers, L. Lagae and S. Van Huffel. Reduction of alpha distortion in event related potentials. Proceedings of 4th European Congress of the International Federation for Medical and Biomedical Engineering (ECIFMBE), Antwerp, Belgium, Nov. 2008, pp. 1298-1301.

12. **K. Vanderperren**, M. De Vos, B. Mijović, J.R. Ramautar, N. Novitskiy, B. Vanrumste, P. Stiers, B.R.H. Van den Bergh, J. Wagemans, L. Lagae, S. Sunaert and S. Van Huffel. PARAFAC on ERP data from a visual detection task during simultaneous fMRI acquisition. Proceedings of the International Biosignal Processing Conference, Berlin, Germany, Jul. 2010, vol. 103, pp. 1-4.

13. C. Cooreman, R. Sclocco, M.G. Tana, **K. Vanderperren**, E. Visani, F. Panzica, S. Franceschetti, S. Van Huffel, S. Cerutti and A.M. Bianchi. BOLD Correlates of Alpha and Beta EEG-Rhythm during a Motor Task. Proceedings of the 5th International IEEE EMBS Conference on Neural Engineering, Cancun, Mexico, Apr.-May 2011, pp. 25-28 (ThB1.1).

14. H. Segers, A. Combaz, N.V. Manyakov, N. Chumerin, **K. Vanderperren**, S. Van Huffel and M.M. Van Hulle. Steady state visual evoked potential (SSVEP) - based brain spelling system with synchronous and asynchronous typing modes. IFMBE Proceedings vol. 34 - Proceedings of the 15th Nordic Baltic Conference on Biomedical Engineering and Medical Physics (NBC15), Aalborg, Denmark, Jun. 2011, pp. 164-167.

15. H. Eykens, D. Widjaja, **K. Vanderperren**, J. Taelman, M.A.K.A. Braeken, R.A. Otte, B.R.H. Van den Bergh and S. Van Huffel. Phase-rectified signal averaging for the quantification of the influence of prenatal anxiety on heart rate variability of babies. Accepted for Proceedings of the International Conference on Bio-inspired Systems and Signal Processing (BIOSIGNALS 2012), Vilamoura, Portugal, Feb. 2012.

Abstracts in proceedings of international conferences

16. **K. Vanderperren**, J.R. Ramautar, N. Novitskiy, M. De Vos, M. Mennes, B. Vanrumste, P. Stiers, B.R.H. Van den Bergh, J. Wagemans, L. Lagae, S. Sunaert and S. Van Huffel. Study of ballistocardiogram artifacts in simultaneous EEG-fMRI acquisitions. Proceedings of the Neuromath Workshop: Advanced Methods for the Estimation of Human Brain Activity and Connectivity (Neuromath), Rome, Italy, Dec. 2007, pp. 121-122.

17. M. De Vos, **K. Vanderperren**, B. Vanrumste, L. De Lathauwer and S. Van Huffel. Multiway methods and their use in neuroscience. Proceedings of the Neuromath Workshop: Advanced Methods for the Estimation of Human Brain Activity and Connectivity (Neuromath), Rome, Italy, Dec. 2007, p. 108.

18. A. Vergult, W. De Clercq, **K. Vanderperren**, B. Vanrumste, W. Van Paesschen and S. Van Huffel. Canonical Correlation Analysis to remove muscle artifacts from the EEG. Proceedings of the Neuromath Workshop: Advanced Methods for the Estimation of Human Brain Activity and Connectivity (Neuromath), Rome, Italy, Dec. 2007, p. 40.

19. **K. Vanderperren**, S. Riès, M. De Vos, B. Vanrumste, F. Alario, B. Burle and S. Van Huffel. Removal of muscle artifacts from EEG recordings of spoken language production. Proceedings of the Neuromath Workshop:

Advanced Methods for the Estimation of Human Brain Activity and Connectivity (Neuromath), Jena, Germany, April 2008, pp. 121-122.

20. M. De Vos, L. De Lathauwer, W. Deburchgraeve, **K. Vanderperren** and S. Van Huffel. A wide range of BSS applications in neuroscience. Proceedings of 4th European Congress of the International Federation for Medical and Biomedical Engineering (ECIFMBE), Antwerp, Belgium, Nov. 2008, p. 182.

21. N. Novitski, J.R. Ramautar, **K. Vanderperren**, M. De Vos, M. Mennes, B. Vanrumste, P. Stiers, B.R.H. Van den Bergh, J. Wagemans, L. Lagae, S. Sunaert and S. Van Huffel. Simultaneous fMRI-EEG study of early cortical processing of lateralized visual stimuli. Proceedings of Neuroscience & Cognitive Control, Ghent, Belgium, Dec. 2008, p. 18.

22. N. Novitski, J.R. Ramautar, **K. Vanderperren**, M. De Vos, M. Mennes, B. Vanrumste, P. Stiers, B.R.H. Van den Bergh, J. Wagemans, L. Lagae, S. Sunaert and S. Van Huffel. Detection of lateralized visual stimuli as an evaluation paradigm for simultaneous EEG/fMRI acquisition and analysis. Proceedings of the Neuromath Workshop: Advanced Methods for the Estimation of Human Brain Activity and Connectivity (Neuromath), Leuven, Belgium, March 2009, p. 26.

23. N. Novitski, J.R. Ramautar, **K. Vanderperren**, P. Stiers, B. Vanrumste, S. Sunaert, S. Van Huffel and J. Wagemans. ERP-driven analysis of simultaneously acquired fMRI data in a visual detection task. Proceedings of 15th International Congress on Event-Related Potentials of the Brain (EPIC XV), Bloomington, USA, Apr. 2009, p. 18.

24. B. Mijović, **K. Vanderperren**, M. De Vos, J.R. Ramautar, N. Novitskiy, B. Vanrumste, P. Stiers, B.R.H. Van den Bergh, J. Wagemans, L. Lagae, S. Sunaert and S. Van Huffel. Influence of the stimulus onset asynchrony in fMRI experiment to the independent component analysis results. Proceedings of the Neuromath Workshop: Advanced Methods for the Estimation of Human Brain Activity and Connectivity (Neuromath), Limassol, Cyprus, Nov.-Dec. 2009, pp. 114-115.

25. B. Mijović, **K. Vanderperren**, M. De Vos, J.R. Ramautar, N. Novitskiy, B. Vanrumste, P. Stiers, B.R.H. Van den Bergh, J. Wagemans, L. Lagae, S. Sunaert and S. Van Huffel. Influence of the stimulus onset asynchrony in fMRI experiment to the independent component analysis results. Proceedings of the 8th Belgian Day on Biomedical Engineering, Brussels, Belgium, Dec. 2009, p. 39.

26. B. Mijović, M. De Vos, **K. Vanderperren**, N. Novitskiy, B. Vanrumste, P. Stiers, B.R.H. Van den Bergh, J. Wagemans, L. Lagae, S. Sunaert and S. Van Huffel. Influence of the stimulus onset asynchrony for the analysis of

fMRI with independent component analysis. Proceedings of the 16th Annual Meeting of the Organization for Human Brain Mapping, Barcelona, Spain, Jun. 2010.

27. N. Novitski, J.R. Ramautar, **K. Vanderperren**, M. De Vos, B. Vanrumste, P. Stiers, B.R.H. Van den Bergh, L. Lagae, S. Sunaert, S. Van Huffel and J. Wagemans. Integration-by-prediction of simultaneous ERP and fMRI to peripherally presented checkerboard segments. Proceedings of the 16th Annual Meeting of the Organization for Human Brain Mapping, Barcelona, Spain, Jun. 2010.

28. N. Novitskiy, J.R. Ramautar, **K. Vanderperren**, M. De Vos, B. Vanrumste, P. Stiers, B.R.H. Van den Bergh, L. Lagae, S. Sunaert, S. Van Huffel and J. Wagemans. Simultaneous EEG-fMRI of peripheral vision. Proceedings of 7th Forum of European Neuroscience (FENS), Amsterdam, the Netherlands, Jul. 2010.

29. B. Mijović, M. De Vos, **K. Vanderperren**, N. Novitskiy, B. Vanrumste, P. Stiers, B.R.H. Van den Bergh, J. Wagemans, L. Lagae, S. Sunaert and S. Van Huffel. Combined Analysis of Electrophysiological and Hemodynamic Signals. Proceedings of the 2nd International Seminar for Magnetic Resonance Imaging in the Republic of Macedonia, Ohrid, Republic of Macedonia, Jun. 2011, p. 22.

Guest editorials

30. **K. Vanderperren**, B. Vanrumste and S. Van Huffel. NeuroMath: advanced methods for the estimation of human brain activity and connectivity. Biomedizinische Technik/Biomedical Engineering, vol. 55, no. 3, Jun. 2010, p. 121.

Curriculum vitae

Katrien Vanderperren was born in Leuven, Belgium on December 25, 1983. She received the master's degree of mechanical-electrotechnical engineering, magna cum laude from the Katholieke Universiteit Leuven, Belgium in July 2006. She was laureate Biomedical Society for her thesis 'Automatic quantification of magnetic resonance spectroscopic signals: evaluation and comparison of AQSES and QUEST'.

Since October 2006, she has been working as a researcher at the Electrical Engineering Department of the Katholieke Universiteit Leuven under the supervision of Prof. Dr. Ir. Sabine Van Huffel. During the first year, she worked on a K.U.Leuven PhD grant, and since January 2008 on an IWT grant (Flemisch Institute for Scientific and Technological Research in Industry). Her main research interests are biomedical signal processing with a focus on electroencephalography (EEG) and functional magnetic resonance imaging (fMRI) analyses. As such, she has been strongly involved in the K.U.Leuven EEG-fMRI IDO project (Interdisciplinary Research Program - 05/010), for which she created the K.U.Leuven EEG-fMRI website, available through www.esat.kuleuven.be/scd/eegfmri.

She was the main local organizer of the NeuroMath Workshop held in Leuven in March 2009 and guest editor for the special issue of the journal Biomedizinische Technik/Biomedical Engineering published on the occasion of this workshop.

In the last two years, she has been the ombudsperson for the master and postgraduate programs in biomedical engineering.

Arenberg Doctoral School of Science, Engineering & Technology
Faculty of Engineering
Department of Electrical Engineering
Research group SISTA-BIOMED
Kasteelpark Arenberg 10, B - 3001 Leuven

KATHOLIEKE UNIVERSITEIT LEUVEN

ASSOCIATIE K.U.LEUVEN